LISA

Laser Interferometer Space Antenna
for the detection and observation of gravitational waves

An international project in the field of
Fundamental Physics in Space

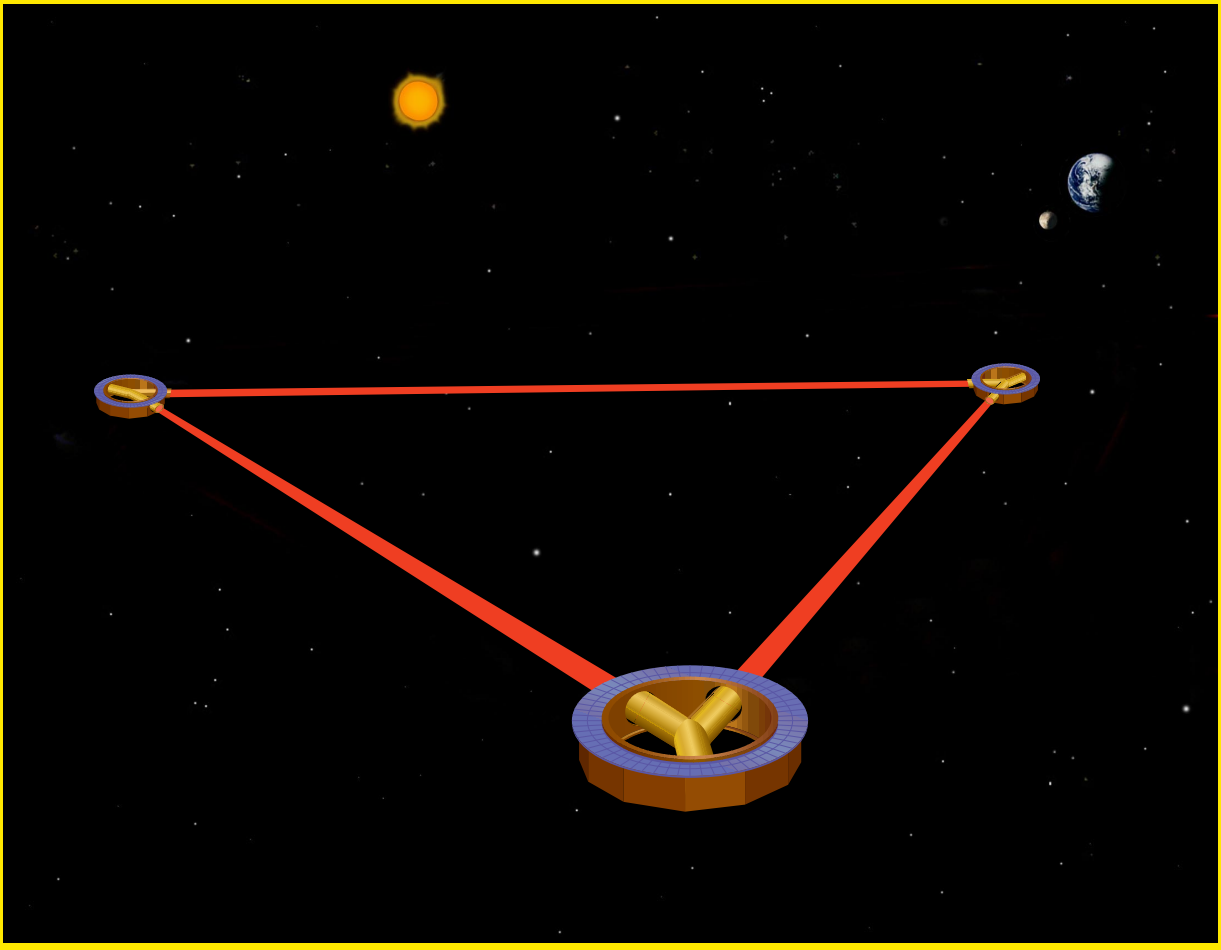

Pre-Phase A Report

Second Edition

July 1998

MPQ 233 July 1998

Front cover figure :

Artist's concept of the LISA configuration. Three spacecraft, each with a Y*-shaped payload, form an equilateral triangle with sides of 5 million km in length. The two branches of the* Y *at one corner, together with one branch each from the spacecraft at the other two corners, form one of up to three Michelson-type interferometers, operated with infrared laser beams.*

The interferometers are designed to measure relative path changes $\delta\ell/\ell$ *due to gravitational waves, so-called strains in space, down to* 10^{-23}*, for observation times of the order of 1 year.*

The drawing is not to scale, the diameters of the spacecraft are about 2 m, the distances between them 5×10^9 *m.*

LISA

Laser Interferometer Space Antenna
for the detection and observation of gravitational waves

Pre-Phase A Report

Second edition, July 1998

This report is presented by the LISA Study Team

P. Bender
A. Brillet
I. Ciufolini
A.M. Cruise
C. Cutler
K. Danzmann
F. Fidecaro
W.M. Folkner
J. Hough
P. McNamara
M. Peterseim
D. Robertson
M. Rodrigues
A. Rüdiger
M. Sandford
G. Schäfer
R. Schilling
B. Schutz
C. Speake
R.T. Stebbins
T. Sumner
P. Touboul
J.-Y. Vinet
S. Vitale
H. Ward
W. Winkler

Contact address:

Prof. Karsten Danzmann

Max-Planck-Institut für Quantenoptik
Hans-Kopfermann-Straße 1
D – 85748 Garching
Tel: +49 (89) 32905 0
Fax: +49 (89) 32905 200

or at:
Institut für Atom- und Molekülphysik
Universität Hannover
Callinstraße 38
D – 30167 Hannover
Tel: +49 (511) 762 2229
Fax: +49 (511) 762 2784

e-mail: kvd@mpq.mpg.de

Foreword

The first mission concept studies for a space-borne gravitational wave observatory began at the Joint Institute for Laboratory Astrophysics (JILA) in Boulder, Colorado. In the following years this concept was worked out in more detail by P.L. Bender and J. Faller and in 1985 the first full description of a mission comprising three drag-free spacecraft in a heliocentric orbit was proposed, then named Laser Antenna for Gravitational-radiation Observation in Space (LAGOS). LAGOS already had many elements of the present-day Laser Interferometer Space Antenna (LISA) mission.

In May 1993, the center of activity shifted from the US to Europe when LISA was proposed to ESA in response to the *Call for Mission Proposals* for the third Medium-Size Project (M3) within the framework of ESA's long-term space science programme "Horizon 2000". The proposal was submitted by a team of US and European scientists coordinated by K. Danzmann, University of Hannover. It envisaged LISA as an ESA/NASA collaborative project and described a mission comprising four spacecraft in a heliocentric orbit forming an interferometer with a baseline of 5×10^6 km.

The SAGITTARIUS proposal, with very similar scientific objectives and techniques, was proposed to ESA at the same time by another international team of scientists coordinated by R.W. Hellings, JPL. The SAGITTARIUS proposal suggested placing six spacecraft in a geocentric orbit forming an interferometer with a baseline of 10^6 km.

Because of the large degree of commonality between the two proposals ESA decided to merge them when accepting them for a study at assessment level in the M 3 cycle. The merged study was initially called LISAG and later LISA. It was one of the main objectives of the Assessment Study to make an objective trade-off between the heliocentric and the geocentric option and to find out if the two options would be feasible within the financial constraints of an ESA medium-size project. In the course of the study it turned out that the cost for both options was more or less the same: 669 MAU for four spacecraft in a heliocentric orbit, 704 MAU for six spacecraft in a geocentric orbit (ESA cost figures are inclusive of the launch vehicle and all mission operations but exclusive of the payload which is nationally funded). Because the geocentric option offered no clear cost advantage the Study Team decided to adopt the heliocentric option as the baseline. The heliocentric option has the advantage that it provides for reasonably constant arm lengths and a stable environment that gives low noise forces on the proof masses. In the geocentric orbit the telescopes are exposed to direct sunlight on every orbit and it will be a challenging task to separate the laser light (244 pW at 1064 nm wavelength) coming from the distant spacecraft from the direct sunlight, requiring a filter with 120 layers. In the heliocentric orbit this problem does not exist because the orbital plane of the LISA spacecraft is inclined with respect to the ecliptic.

Because the cost for an ESA-alone LISA (there was no expression of interest by NASA in a collaboration at that time) considerably exceeded the M 3 cost limit of 350 MAU it became clear quite early in the Assessment Study that LISA was not likely to be a successful candidate for M 3 and would not be selected for a study at Phase A level in the M 3 cycle. In December 1993, LISA was therefore proposed as a cornerstone project for "Horizon 2000 Plus", involving six spacecraft in a heliocentric orbit. Both the Fundamental Physics Topical Team and the Survey Committee realised the enormous discovery

potential and timeliness of the LISA Project and recommended it as the third cornerstone of "Horizon 2000 Plus".

Being a cornerstone in ESA's space science programme implies that, in principle, the mission is approved and that funding for industrial studies and technology development is provided right away. The launch year, however, is dictated by the availability of funding. Considering realistic funding scenarios for ESA's space science programme the launch for LISA would probably not occur before 2017 and possibly even as late as 2023. It must be expected that even the most optimistic opportunity for ESA to launch the LISA cornerstone will be pre-empted by an earlier NASA mission.

In 1996 and early 1997, the LISA team made several proposals how to drastically reduce the cost for LISA without compromising the science in any way:

- reduce the number of spacecraft from six to three (each of the new spacecraft would replace a pair of spacecraft at the vertices of the triangular configuration, with essentially two instruments in each spacecraft),
- define drag-free control as part of the payload (both the inertial sensor and the attitude detection diodes are at the heart of the payload, and the drag-free control is so intimately related to the scientific success of the mission that it has to be under PI control),
- reduce the size of the telescope from 38 to 30 cm (this reduces the size and mass of the payload and consequently of the spacecraft and the total launch mass).

With these and a few other measures the total launch mass could be reduced from 6.8 t to 1.4 t and the total cost could be as low as 300 – 400 MAU (exclusive of the payload).

Perhaps most importantly, it was proposed by the LISA team and by ESA's Fundamental Physics Advisory Group (FPAG) in February 1997 to carry out LISA in collaboration with NASA. A contribution by ESA in the range 50 – 200 MAU to a NASA/ESA collaborative LISA mission that could be launched considerably earlier than 2017 would fully satisfy the needs of the European scientific community. A launch in the time frame 2005 – 2010 would be ideal from the point of view of technological readiness of the payload and the availability of second-generation detectors in ground-based interferometers making the detection of gravitational waves in the high-frequency band very likely. It is recalled that the interplanetary radiation environment is particularly benign during solar minimum (2007 – 8) which has certain advantages (see Section 3.1.7 for details).

In January 1997, the center of activity shifted from Europe back to the US. At that time a candidate configuration of the three-spacecraft mission was developed by the LISA science team, with the goal of being able to launch the three spacecraft on a Delta-II. The three-spacecraft LISA mission was studied by JPL's Team-X during three design sessions on 4, 16 and 17 January, 1997. The purpose of the study was to assist the science team, represented by P.L. Bender and R.T. Stebbins (JILA/University of Colorado), and W.M. Folkner (JPL), in defining the necessary spacecraft subsystems and in designing a propulsion module capable of delivering the LISA spacecraft into the desired orbit. The team also came up with a grass-roots cost estimate based on experience with similar subsystem designs developed at JPL.

The result of the Team-X study was that it appeared feasible to fly the three-spacecraft LISA mission on a single Delta-II 7925 H launch vehicle by utilizing a propulsion module based on a solar-electric propulsion, and with spacecraft subsystems expected to be available by a 2001 technology cut-off date. The total estimated mission cost is $ 465M (based on FY 1997 prices), including development, construction of the spacecraft and the payload, launch vehicle, and mission operations. This revised version of the LISA mission was presented to the Structure and Evolution of the Universe Subcommittee (SEUS) in March 1997 .

Although it was not selected as one of the missions recommended for a new start during the period 2000 – 2004 under the recently adopted Office of Space Science (OSS) Strategic Plan it was included in the Technology Development Roadmap for the Structure and Evolution of the Universe Theme with the aim of recommending it for the next series of NASA missions if a technologically feasible and fiscally affordable mission can be defined. NASA would welcome substantial (50 MAU) or even equal participation (175 MAU) in LISA from ESA and European national agencies.

In June 1997, a LISA Pre-Project Office was established at JPL with W.M. Folkner as the Pre-Project Manager and in December 1997, an ad-hoc LISA Mission Definition Advisory Team was formed, involving 36 US scientists. Representatives from ESA's LISA Study Team are invited to participate in the activities of the LISA Mission Definition Team.

The revised version of LISA (three spacecraft in a heliocentric orbit, ion drive, Delta-II launch vehicle; NASA/ESA collaborative) has been endorsed by the LISA Science Team and is described in this report.

Contents

Executive Summary

The primary objective of the Laser Interferometer Space Antenna (LISA) mission is to detect and observe gravitational waves from massive black holes and galactic binaries in the frequency range 10^{-4} to 10^{-1} Hz. This low-frequency range is inaccessible to ground-based interferometers because of the unshieldable background of local gravitational noise and because ground-based interferometers are limited in length to a few kilometres.

The nature of gravitational waves

In Newton's theory of gravity the gravitational interaction between two bodies is instantaneous, but according to Special Relativity this should be impossible, because the speed of light represents the limiting speed for all interactions. If a body changes its shape the resulting change in the force field will make its way outward at the speed of light. It is interesting to note that already in 1805, Laplace, in his famous *Traité de Mécanique Céleste* stated that, if Gravitation propagates with finite speed, the force in a binary star system should not point along the line connecting the stars, and the angular momentum of the system must slowly decrease with time. Today we would say that this happens because the binary star is losing energy and angular momentum by emitting gravitational waves. It was no less than 188 years later in 1993 that Hulse and Taylor were awarded the Nobel prize in physics for the indirect proof of the existence of Gravitational Waves using exactly this kind of observation on the binary pulsar PSR 1913+16. A direct detection of gravitational waves has not been achieved up to this day.

Einstein's paper on gravitational waves was published in 1916, and that was about all that was heard on the subject for over forty years. It was not until the late 1950s that some relativity theorists, H. Bondi in particular, proved rigorously that gravitational radiation was in fact a physically observable phenomenon, that gravitational waves carry energy and that, as a result, a system that emits gravitational waves should lose energy.

General Relativity replaces the Newtonian picture of Gravitation by a geometric one that is very intuitive if we are willing to accept the fact that space and time do not have an independent existence but rather are in intense interaction with the physical world. Massive bodies produce "indentations" in the fabric of spacetime, and other bodies move in this curved spacetime taking the shortest path, much like a system of billiard balls on a springy surface. In fact, the Einstein field equations relate mass (energy) and curvature in just the same way that Hooke's law relates force and spring deformation, or phrased somewhat poignantly: spacetime is an elastic medium.

If a mass distribution moves in an asymmetric way, then the spacetime indentations travel outwards as ripples in spacetime called gravitational waves. Gravitational waves are fundamentally different from the familiar electromagnetic waves. While electromagnetic waves, created by the acceleration of electric charges, propagate IN the framework of space and time, gravitational waves, created by the acceleration of masses, are waves of the spacetime fabric ITSELF.

Unlike charge, which exists in two polarities, mass always come with the same sign. This is why the lowest order asymmetry producing *electro-magnetic* radiation is the dipole moment of the charge distribution, whereas for *gravitational* waves it is a change in the

quadrupole moment of the mass distribution. Hence those gravitational effects which are spherically symmetric will not give rise to gravitational radiation. A perfectly symmetric collapse of a supernova will produce no waves, a non-spherical one will emit gravitational radiation. A binary system will always radiate.

Gravitational waves distort spacetime, in other words they change the distances between free macroscopic bodies. A gravitational wave passing through the Solar System creates a time-varying strain in space that periodically changes the distances between all bodies in the Solar System in a direction that is perpendicular to the direction of wave propagation. These could be the distances between spacecraft and the Earth, as in the case of ULYSSES or CASSINI (attempts were and will be made to measure these distance fluctuations) or the distances between shielded proof masses inside spacecraft that are separated by a large distance, as in the case of LISA. The main problem is that the relative length change due to the passage of a gravitational wave is exceedingly small. For example, the periodic change in distance between two proof masses, separated by a sufficiently large distance, due to a typical white dwarf binary at a distance of 50 pc is only 10^{-10} m. This is not to mean that gravitational waves are weak in the sense that they carry little energy. On the contrary, a supernova in a not too distant galaxy will drench every square meter here on earth with kilowatts of gravitational radiation intensity. The resulting length changes, though, are very small because spacetime is an extremely stiff elastic medium so that it takes extremely large energies to produce even minute distortions.

Sources of gravitational waves

The two main categories of gravitational waves sources for LISA are the galactic binaries and the massive black holes (MBHs) expected to exist in the centres of most galaxies.

Because the masses involved in typical binary star systems are small (a few solar masses), the observation of binaries is limited to our Galaxy. Galactic sources that can be detected by LISA include a wide variety of binaries, such as pairs of close white dwarfs, pairs of neutron stars, neutron star and black hole ($5-20\,M_\odot$) binaries, pairs of contacting normal stars, normal star and white dwarf (cataclysmic) binaries, and possibly also pairs of black holes. It is likely that there are so many white dwarf binaries in our Galaxy that they cannot be resolved at frequencies below 10^{-3} Hz, leading to a confusion-limited background. Some galactic binaries are so well studied, especially the X-ray binary 4U1820-30, that it is one of the most reliable sources. If LISA would not detect the gravitational waves from known binaries with the intensity and polarisation predicted by General Relativity, it will shake the very foundations of gravitational physics.

The main objective of the LISA mission, however, is to learn about the formation, growth, space density and surroundings of massive black holes (MBHs). There is now compelling indirect evidence for the existence of MBHs with masses of 10^6 to $10^8\,M_\odot$ in the centres of most galaxies, including our own. The most powerful sources are the mergers of MBHs in distant galaxies, with amplitude signal-to-noise ratios of several thousand for $10^6\,M_\odot$ black holes. Observations of signals from these sources would test General Relativity and particularly black-hole theory to unprecedented accuracy. Not much is currently known about black holes with masses ranging from about $100\,M_\odot$ to $10^6\,M_\odot$. LISA can provide unique new information throughout this mass range.

Complementarity with ground-based observations

The ground-based interferometers LIGO, VIRGO, TAMA 300 and GEO 600 and the LISA interferometer in space complement each other in an essential way. Just as it is important to complement the optical and radio observations from the ground with observations from space at submillimetre, infrared, ultraviolet, X-ray and gamma-ray wavelengths, so too is it important to complement the gravitational wave observations done by the ground-based interferometers in the high-frequency regime (10 to 10^3 Hz) with observations in space in the low-frequency regime (10^{-4} to 10^{-1} Hz).

Ground-based interferometers can observe the bursts of gravitational radiation emitted by galactic binaries during the final stages (minutes and seconds) of coalescence when the frequencies are high and both the amplitudes and frequencies increase quickly with time. At low frequencies, which are only observable in space, the orbital radii of the binary systems are larger and the frequencies are stable over millions of years. Coalescences of MBHs are only observable from space. Both ground- and space-based detectors will also search for a cosmological background of gravitational waves. Since both kinds of detectors have similar energy sensitivities their different observing frequencies are ideally complementary: observations can provide crucial spectral information.

The LISA mission

The LISA mission comprises three identical spacecraft located 5×10^6 km apart forming an equilateral triangle. LISA is basically a giant Michelson interferometer placed in space, with a third arm added to give independent information on the two gravitational wave polarizations, and for redundancy. The distance between the spacecraft – the interferometer arm length – determines the frequency range in which LISA can make observations; it was carefully chosen to allow for the observation of most of the interesting sources of gravitational radiation. The centre of the triangular formation is in the ecliptic plane, 1 AU from the Sun and 20° behind the Earth. The plane of the triangle is inclined at 60° with respect to the ecliptic. These particular heliocentric orbits for the three spacecraft were chosen such that the triangular formation is maintained throughout the year with the triangle appearing to rotate about the centre of the formation once per year.

While LISA can be described as a big Michelson interferometer, the actual implementation in space is very different from a laser interferometer on the ground and is much more reminiscent of the technique called spacecraft tracking, but here realized with infrared laser light instead of radio waves. The laser light going out from the center spacecraft to the other corners is not directly reflected back because very little light intensity would be left over that way. Instead, in complete analogy with an RF transponder scheme, the laser on the distant spacecraft is phase-locked to the incoming light providing a return beam with full intensity again. After being transponded back from the far spacecraft to the center spacecraft, the light is superposed with the on-board laser light serving as a local oscillator in a heterodyne detection. This gives information on the length of one arm modulo the laser frequency. The other arm is treated the same way, giving information on the length of the other arm modulo the same laser frequency. The difference between these two signals will thus give the difference between the two arm lengths (i.e. the gravitational

wave signal). The sum will give information on laser frequency fluctuations.

Each spacecraft contains two optical assemblies. The two assemblies on one spacecraft are each pointing towards an identical assembly on each of the other two spacecraft to form a Michelson interferometer. A 1 W infrared laser beam is transmitted to the corresponding remote spacecraft via a 30-cm aperture $f/1$ Cassegrain telescope. The same telescope is used to focus the very weak beam (a few pW) coming from the distant spacecraft and to direct the light to a sensitive photodetector where it is superimposed with a fraction of the original local light. At the heart of each assembly is a vacuum enclosure containing a free-flying polished platinum-gold cube, 4 cm in size, referred to as the proof mass, which serves as an optical reference ("mirror") for the light beams. A passing gravitational wave will change the length of the optical path between the proof masses of one arm of the interferometer relative to the other arm. The distance fluctuations are measured to sub-Ångstrom precision which, when combined with the large separation between the spacecraft, allows LISA to detect gravitational-wave strains down to a level of order $\Delta\ell/\ell = 10^{-23}$ in one year of observation, with a signal-to-noise ratio of 5 .

The spacecraft mainly serve to shield the proof masses from the adverse effects due to the solar radiation pressure, and the spacecraft position does not directly enter into the measurement. It is nevertheless necessary to keep all spacecraft moderately accurately ($10^{-8}\,\mathrm{m}/\sqrt{\mathrm{Hz}}$ in the measurement band) centered on their respective proof masses to reduce spurious local noise forces. This is achieved by a "drag-free" control system, consisting of an accelerometer (or inertial sensor) and a system of electrical thrusters.

Capacitive sensing in three dimensions is used to measure the displacements of the proof masses relative to the spacecraft. These position signals are used in a feedback loop to command micro-Newton ion-emitting proportional thrusters to enable the spacecraft to follow its proof masses precisely. The thrusters are also used to control the attitude of the spacecraft relative to the incoming optical wavefronts, using signals derived from quadrant photodiodes. As the three-spacecraft constellation orbits the Sun in the course of one year, the observed gravitational waves are Doppler-shifted by the orbital motion. For periodic waves with sufficient signal-to-noise ratio, this allows the direction of the source to be determined (to arc minute or degree precision, depending on source strength).

Each of the three LISA spacecraft has a launch mass of about 400 kg (plus margin) including the payload, ion drive, all propellants and the spacecraft adapter. The ion drives are used for the transfer from the Earth orbit to the final position in interplanetary orbit. All three spacecraft can be launched by a single Delta II 7925H. Each spacecraft carries a 30 cm steerable antenna used for transmitting the science and engineering data, stored on board for two days, at a rate of 7 kB/s in the Ka-band to the 34-m network of the DSN. Nominal mission lifetime is two years.

LISA is envisaged as a NASA/ESA collaborative project, with NASA providing the launch vehicle, the Ka-band telecommunications system on board the spacecraft, mission and science operations and about 50 % of the payload, ESA providing the three spacecraft including the ion drives, and European institutes, funded nationally, providing the other 50 % of the payload. The collaborative NASA/ESA LISA mission is aimed at a launch in the 2008 – 2010 time frame.

LISA Mission Summary	
Objectives:	Detection of low-frequency (10^{-4} to 1 Hz) gravitational radiation with a strain sensitivity of $4\times10^{-21}/\sqrt{\text{Hz}}$ at 1 mHz. Abundant sources are galactic binaries (neutron stars, white dwarfs, etc.); extra-galactic targets are supermassive black hole binaries (SMBH-SMBH and BH-SMBH), SMBH formation, and cosmic background gravitational waves.
Payload:	Laser interferometry with six electrostatically controlled drag-free reference mirrors housed in three spacecraft; arm lengths 5×10^6 km. Each spacecraft has two lasers (plus two spare) which operate in a phase-locked transponder scheme. Diode-pumped Nd:YAG lasers: wavelength 1.064 μm, output power 1 W, Fabry-Perot reference cavity for frequency-stability of $10\,\text{Hz}/\sqrt{\text{Hz}}$. Quadrant photodiode detectors with interferometer fringe resolution, corresponding to $4\times10^{-5}\lambda/\sqrt{\text{Hz}}$. 30 cm diameter f/1 Cassegrain telescope (transmit/receive), $\lambda/10$ outgoing wavefront quality. Drag-free proof mass (mirror): 40 mm cube, Au-Pt alloy of extremely low magnetic susceptibility ($< 10^{-6}$); Ti-housing at vacuum $< 10^{-6}$ Pa; six-degree-of-freedom capacitive sensing.
Orbit: Launcher:	Each spacecraft orbits the Sun at 1 AU. The inclinations are such that their *relative* orbits define a circle with radius 3×10^6 km and a period of 1 year. The plane of the circle is inclined 60° with respect to the ecliptic. On this circle, the spacecraft are distributed at three vertices, defining an equilateral triangle with a side length of 5×10^6 km (interferometer baseline). This constellation is located at 1 AU from the Sun, 20° behind the Earth. Delta II 7925 H, 9.5 ft fairing. Each pair of spacecraft has its own jettisonable propulsion module to provide a ΔV of 1300 m/s using solar-electric propulsion.
Spacecraft: mass: propulsion module: propellant: total launch mass: power: dimension: Drag-free performance: Pointing performance: Payload, mass: power: Telemetry:	3-axis stabilized drag-free spacecraft (three). 203 kg, *each spacecraft in orbit.* 132 kg, *for each spacecraft.* 27 kg, *for each spacecraft.* 1407 kg 151 W, *each spacecraft in orbit.* diameter: 1.8 m, height: 0.48 m, *each spacecraft.* 10^{-15} m/s^2 (rms) in the band 10^{-4} to 10^{-1} Hz achieved with 6×4 Cesium FEEP thrusters. few nrad$/\sqrt{\text{Hz}}$ in the band 10^{-4} to 10^{-1} Hz. 70 kg, *each spacecraft.* 72 W, *each spacecraft.* 375 bps *per spacecraft* for about 5 hours. Ground stations: Villafranca (Spain), Perth (Australia).
Mission Lifetime:	2 years (nominal); 10 years (extended).

Chapter 1

Scientific Objectives

By applying Einstein's theory of general relativity to the most up-to-date information from modern astronomy, physicists have come to two fundamental conclusions about gravitational waves:

- Both the *most predictable* and the *most powerful* sources of gravitational waves emit their radiation predominantly at very low frequencies, below about 10 mHz.
- The terrestrial Newtonian gravitational field is so noisy at these frequencies that gravitational radiation from astronomical objects can only be detected by space-based instruments.

The *most predictable* sources are binary star systems in our galaxy; there should be thousands of resolvable systems, including some already identified from optical and X-ray observations. The *most powerful* sources are the mergers of supermassive black holes in distant galaxies; if they occur their signal power can be more than 10^7 times the expected noise power in a space-based detector. Observations of signals involving massive black holes (MBHs) would test general relativity and particularly black-hole theory to unprecedented accuracy, and they would provide new information about astronomy that can be obtained in no other way.

This is the motivation for the LISA Cornerstone Mission project. The experimental and mission plans for LISA are described in Chapters 3 – 10 below. The technology is an outgrowth of that developed for ground-based gravitational wave detectors, which will observe at higher frequencies; these and other existing gravitational wave detection methods are reviewed in Chapter 2. In the present Chapter, we begin with a non-mathematical introduction to general relativity and the theory of gravitational waves. We highlight places where LISA's observations can test the fundamentals of gravitation theory. Then we survey the different expected sources of low-frequency gravitational radiation and detail what astronomical information and other fundamental physics can be expected from observing them.

1.1 Theory of gravitational radiation

1.1.1 General relativity

There are a number of good textbooks that introduce general relativity and gravitational waves, with their astrophysical implications [1, 2, 3, 4]. We present here a very brief introduction to the most important ideas, with a minimum of mathematical detail. A discussion in the same spirit that deals with other experimental aspects of general relativity is in Reference [5].

Foundations of general relativity. General relativity rests on two foundation stones: the equivalence principle and special relativity. By considering each in turn, we can learn a great deal about what to expect from general relativity and gravitational radiation.

- **Equivalence principle.** This originates in Galileo's observation that all bodies fall in a gravitational field with the same acceleration, regardless of their mass. From the modern point of view, that means that if an experimenter were to fall with the acceleration of gravity (becoming a *freely falling local inertial observer*), then every local experiment on free bodies would give the same results as if gravity were completely absent: with the common acceleration removed, particles would move at constant speed and conserve energy and momentum.

  The equivalence principle is embodied in Newtonian gravity, and its importance has been understood for centuries. By assuming that it applied to light — that light behaved just like any particle — eighteenth century physicists predicted black holes (Michell and Laplace) and the gravitational deflection of light (Cavendish and von Söldner), using only Newton's theory of gravity.

  The equivalence principle leads naturally to the point of view that gravity is geometry. If all bodies follow the same trajectory, just depending on their initial velocity and position but not on their internal composition, then it is natural to associate the trajectory with the spacetime itself rather than with any force that depends on properties of the particle. General relativity is formulated mathematically as a geometrical theory, but our approach to it here will be framed in the more accessible language of forces.

  The equivalence principle can only hold locally, that is in a small region of space and for a short time. The inhomogeneity of the Earth's gravitational field introduces differential accelerations that must eventually produce measurable effects in any freely-falling experiment. These are called *tidal effects*, because tides on the Earth are caused by the inhomogeneity of the Moon's field. So tidal forces are the part of the gravitational field that cannot be removed by going to a freely falling frame. General relativity describes how tidal fields are generated by sources. Gravitational waves are time-dependent tidal forces, and gravitational wave detectors must sense the small tidal effects.

  Ironically, the equivalence principle never holds exactly in real situations in general relativity, because real particles (*e.g.* neutron stars) carry their gravitational fields along with them, and these fields always extend far from the particle. Because

of this, no real particle experiences only the local part of the external gravitational field. When a neutron star falls in the gravitational field of some other body (another neutron star or a massive black hole), its own gravitational field is accelerated with it, and far from the system this time-dependent field assumes the form of a gravitational wave. The loss of energy and momentum to gravitational radiation is accompanied by a gravitational radiation reaction force that changes the motion of the star. These reaction effects have been observed in the Hulse-Taylor binary pulsar [6], and they will be observable in the radiation from merging black holes and from neutron stars falling into massive black holes. They will allow LISA to perform more stringent quantitative tests of general relativity than are possible with the Hulse-Taylor pulsar. The reaction effects are relatively larger for more massive "particles", so the real trajectory of a star will depend on its mass, despite the equivalence principle. The equivalence principle only holds strictly in the limit of a particle of small mass.

This "failure" of the equivalence principle does not, of course, affect the self-consistency of general relativity. The field equations of general relativity are partial differential equations, and they incorporate the equivalence principle as applied to matter in infinitesimally small volumes of space and lengths of time. Since the mass in such regions is infinitesimally small, the equivalence principle does hold for the differential equations. Only when the effects of gravity are added up over the whole mass of a macroscopic body does the motion begin to deviate from that predicted by the equivalence principle.

- **Special relativity.** The second foundation stone of general relativity is special relativity. Indeed, this is what led to the downfall of Newtonian gravity: as an instantaneous theory, Newtonian gravity was recognized as obsolete as soon as special relativity was accepted. Many of general relativity's most distinctive predictions originate in its conformance to special relativity.

  General relativity incorporates special relativity through the equivalence principle: local freely falling observers see special relativity physics. That means, in particular, that nothing moves faster than light, that light moves at the same speed c with respect to all local inertial observers at the same event, and that phenomena like time dilation and the equivalence of mass and energy are part of general relativity.

  Black holes in general relativity are regions in which gravity is so strong that the escape speed is larger than c: this is the Michell-Laplace definition as well. But because nothing moves faster than c, all matter is trapped inside the black hole, something that Michell and Laplace would not have expected. Moreover, because light can't stand still, light trying to escape from a black hole does not move outwards and then turn around and fall back in, as would an ordinary particle; it never makes any outward progress at all. Instead, it falls inwards towards a complicated, poorly-understood, possibly singular, possibly quantum-dominated region in the center of the hole.

  The source of the Newtonian gravitational field is the mass density. Because of $E = mc^2$, we would naturally expect that all energy densities would create gravity in a relativistic theory. They do, but there is more. Different freely falling observers

measure different energies and different densities (volume is Lorentz-contracted), so the actual source has to include not only energy but also momentum, and not only densities but also fluxes. Since pressure is a momentum flux (it transfers momentum across surfaces), relativistic gravity can be created by mass, momentum, pressure, and other stresses.

> *Among the consequences of this that are observable by LISA are gravitational effects due to spin.*

These include the Lense-Thirring effect, which is the gravitational analogue of spin-orbit coupling, and gravitational spin-spin coupling. The first effect causes the orbital plane of a neutron star around a spinning black hole to rotate in the direction of the spin; the second causes the orbit of a spinning neutron star to differ from the orbit of a simple test particle. (This is another example of the failure of the equivalence principle for a macroscopic "particle".) Both of these orbital effects create distinctive features in the waveform of the gravitational waves from the system.

Gravitational waves themselves are, of course, a consequence of special relativity applied to gravity. Any change to a source of gravity (*e.g.* the position of a star) must change the gravitational field, and this change cannot move outwards faster than light. Far enough from the source, this change is just a ripple in the gravitational field. In general relativity, this ripple moves at the speed of light. In principle, all relativistic gravitation theories must include gravitational waves, although they could propagate slower than light. Theories will differ in their polarization properties, described for general relativity below.

Special relativity and the equivalence principle place a strong constraint on the source of gravitational waves. At least for sources that are not highly relativistic, one can decompose the source into multipoles, in close analogy to the standard way of treating electromagnetic radiation. The electromagnetic analogy lets us anticipate an important result. The monopole moment of the mass distribution is just the total mass. By the equivalence principle, this is conserved, apart from the energy radiated in gravitational waves (the part that violates the equivalence principle for the motion of the source). As for all fields, this energy is quadratic in the amplitude of the gravitational wave, so it is a second-order effect. To first order, the monopole moment is constant, so there is no monopole emission of gravitational radiation. (Conservation of charge leads to the same conclusion in electromagnetism.)

The dipole moment of the mass distribution also creates no radiation: its time derivative is the total momentum of the source, and this is also conserved in the same way. (In electromagnetism, the dipole moment obeys no such conservation law, except for systems where the ratio of charge to mass is the same for all particles.) It follows that the dominant gravitational radiation from a source comes from the time-dependent *quadrupole moment* of the system. Most estimates of expected wave amplitudes rely on the quadrupole approximation, neglecting higher multipole moments. This is a good approximation for weakly relativistic systems, but only an order-of-magnitude estimate for relativistic events, such as the waveform produced by the final merger of two black holes.

The replacement of Newtonian gravity by general relativity must, of course, still reproduce the successes of Newtonian theory in appropriate circumstances, such as when describing the solar system. General relativity has a well-defined Newtonian limit: when gravitational fields are weak (gravitational potential energy small compared to rest-mass energy) and motions are slow, then general relativity limits to Newtonian gravity. This can only happen in a limited region of space, inside and near to the source of gravity, the *near zone*. Far enough away, the gravitational waves emitted by the source must be described by general relativity.

The field equations and gravitational waves. The Einstein field equations are inevitably complicated. With 10 quantities that can create gravity (energy density, 3 components of momentum density, and 6 components of stress), there must be 10 unknowns, and these are represented by the components of the metric tensor in the geometrical language of general relativity. Moreover, the equations are necessarily nonlinear, since the energy carried away from a system by gravitational waves must produce a decrease in the mass and hence of the gravitational attraction of the system.

With such a system, exact solutions for interesting physical situations are rare. It is remarkable, therefore, that there is a unique solution that describes a black hole (with 2 parameters, for its mass and angular momentum), and that it is exactly known. This is called the Kerr metric. Establishing its uniqueness was one of the most important results in general relativity in the last 30 years. The theorem is that any isolated, uncharged black hole must be described by the Kerr metric, and therefore that any given black hole is completely specified by giving its mass and spin. This is known as the "no-hair theorem": black holes have no "hair", no extra fuzz to their shape and field that is not determined by their mass and spin.

If LISA observes neutron stars orbiting massive black holes, the detailed waveform will measure the multipole moments of the black hole. If they do not conform to those of Kerr, as determined by the lowest 2 measured moments, then the no-hair theorem and general relativity itself may be wrong.

There are no exact solutions in general relativity for the 2-body problem, the orbital motion of two bodies around one another. Considerable effort has therefore been spent over the last 30 years to develop suitable approximation methods to describe the orbits. By expanding about the Newtonian limit one obtains the *post-Newtonian* hierarchy of approximations. The first post-Newtonian equations account for such things as the perihelion shift in binary orbits. Higher orders include gravitational spin-orbit (Lense-Thirring) and spin-spin effects, gravitational radiation reaction, and so on. These approximations give detailed predictions for the waveforms expected from relativistic systems, such as black holes spiralling together but still well separated, and neutron stars orbiting near massive black holes.

When a neutron star gets close to a massive black hole, the post-Newtonian approximation fails, but one can still get good predictions using linear perturbation theory, in which the gravitational field of the neutron star is treated as a small perturbation of the field of the black hole. This technique is well-developed for orbits around non-rotating black holes (Schwarzschild black holes), and it should be completely understood for orbits around general black holes within the next 5 years.

The most difficult part of the 2-body problem is the case of two objects of comparable mass in a highly relativistic interaction, such as when two black holes merge. This can only be studied using large-scale numerical simulations. One of the NSF's Grand Challenge projects for supercomputing is a collaboration among 7 university groups in the USA to solve the problem of inspiralling and merging black holes. Within 10 years good solutions could be available.

Mathematically, the field equations can be formulated in terms of a set of 10 fields that are components of a symmetric 4×4 matrix $\{h_{\alpha\beta},\, \alpha = 0 \ldots 3,\ \beta = 0 \ldots 3\}$. These represent geometrically the *deviation* of the metric tensor from that of special relativity, the Minkowski metric. In suitable coordinates the Einstein field equations can be written

$$\left[\nabla^2 - \frac{1}{c^2}\frac{\partial^2}{\partial t^2}\right] h_{\alpha\beta} = \frac{G}{c^4}\,(\text{source}), \tag{1.1}$$

where "(source)" represents the various energy densities and stresses that can create the field, as well as the non-linear terms in $h_{\alpha\beta}$ that represent an effective energy density and stress for the gravitational field. This should be compared with Newton's field equation,

$$\nabla^2\Phi = 4\pi G\rho\,, \tag{1.2}$$

where ρ is the mass density, or the energy density divided by c^2. Since ρ is dimensionally (source)$/c^2$, we see that the potentials $h_{\alpha\beta}$ are generalisations of Φ/c^2, which is dimensionless. This correspondence between the relativistic h and Newton's Φ will help us to understand the physics of gravitational waves in the next section.

Comparing Equation 1.1 with Equation 1.2 also shows how the Newtonian limit fits into relativity. If velocities inside the source are small compared with c, then we can neglect the time-derivatives in Equation 1.1; moreover, pressures and momentum densities will be small compared to energy densities. Similarly, if h is small compared to 1 (recall that it is dimensionless), then the nonlinear terms in "(source)" will be negligible. If these two conditions hold, then the Einstein equations reduce simply to Newton's equation in and near the source.

However, Equation 1.1 is a wave equation, and time-dependent solutions will always have a wavelike character far enough away, even for a nearly Newtonian source. The transition point is where the spatial gradients in the equation no longer dominate the time-derivatives. For a field falling off basically as $1/r$ and that has an oscillation frequency of ω, the transition occurs near $r \sim c/\omega = \lambda/2\pi$, where λ is the wavelength of the gravitational wave. Inside this transition is the "near zone", and the field is basically Newtonian. Outside is the "wave zone", where the time-dependent part of the gravitational acceleration ($\nabla\Phi$) is given by Φ/λ rather than Φ/r. Time-dependent gravitational effects therefore fall off only as $1/r$, not the Newtonian $1/r^2$.

1.1.2 The nature of gravitational waves in general relativity

Tidal accelerations. We remarked above that the observable effects of gravity lie in the tidal forces. A gravitational wave detector would not respond to the acceleration produced by the wave (as given by $\nabla\Phi$), since the whole detector would fall freely in this

field, by the equivalence principle. Detectors work only because they sense the changes in this acceleration across them. If two parts of a detector are separated by a vector $\vec{L}$, then it responds to a *differential* acceleration of order

$$\vec{L} \cdot \nabla(\nabla\Phi) \sim L\Phi/\lambda^2. \tag{1.3}$$

Since we have seen that $\Phi \sim hc^2$ (dropping the indices of $h_{\alpha\beta}$ in order to simplify this order-of-magnitude argument), the differential acceleration is of order $L\omega^2 h$.

If the detector is a solid body, such as the bar detectors described in Section 2.2.1, the differential acceleration will be resisted by internal elastic stresses, and the resulting mechanical motion can be complex. Bars are made so that they will "ring" for a long time after a gravitational wave passes, making detection easier. If the detector consists of separated masses that respond to the gravitational wave like free particles, then the situation is easier to analyse. This is the case for interferometers, including LISA.

For two free masses separated by the vector $\vec{L}$, the differential acceleration given by Equation 1.3 leads to an equation for the change in their separation $\delta\vec{L}$, of order

$$\frac{d^2\delta L}{dt^2} \sim L\omega^2 h\,.$$

Since the time-derivatives on the left-hand-side just bring down factors of ω, we arrive at the very simple equation $\delta L/L \sim h$. A careful derivation shows that this is exact with a further factor of 2:

$$\frac{\delta L}{L} = \frac{1}{2}\,h\,. \tag{1.4}$$

Here we make contact with the geometrical interpretation of general relativity. The distances L and δL should be interpreted as *proper* distances, the actual distances that a meter-stick would measure at a given time. Then we see that h is indeed a metric, a distance measure: as a gravitational wave passes, it stretches and shrinks the proper distance between two free bodies. This equation also explains why interferometric detectors should be made large: the technical problem is always to measure the small distance change δL, and for a given wave amplitude h this distance change increases in proportion to L.

Polarization of gravitational waves. We have managed to discover much about gravitational waves by ignoring all the indices and the full complexity of the field equations, but this approach eventually reaches its limit. What we cannot discover without indices is how the differential accelerations depend on the direction to the source of the wave. Here there are two important results that we simply quote without proof:

- Gravitational waves are **transverse**. Like electromagnetic waves, they act only in a plane perpendicular to their direction of propagation. This means that the two separated masses will experience the maximum relative distance change if they are perpendicular to the direction to the source; if they lie along that direction there will be no change δL.
- In the transverse plane, gravitational waves are **area preserving**. This means that if a wave increases the proper distance between two free masses that lie along a given direction, it will simultaneously decrease the distance between two free masses lying along the perpendicular direction in the transverse plane. The consequence of this is illustrated in the standard polarization diagram, Figure 1.1 .

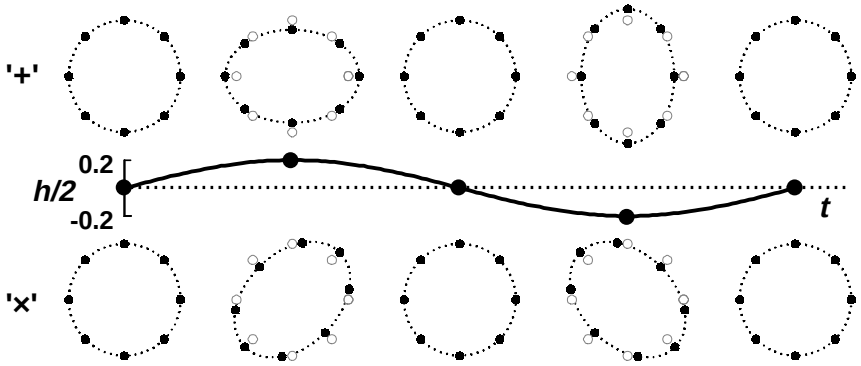

Figure 1.1 Illustration of the polarisation of a gravitational wave. *Two linearly independent polarisations of a gravitational wave are illustrated by displaying their effect on a ring of free particles arrayed in a plane perpendicular to the direction of the wave. The wave-form is shown between the two sequences, for a wave with the (large) dimensionless amplitude* $h = 0.2$ *. Shown to scale are the distortions in the original circle that the wave produces if it carries the +-polarisation (above) and the ×-polarisation (below). The motion of each particle can be discovered by comparing it to its original position, shown as the "shadow" circles. In general relativity, there are only two independent polarisations. The ones shown here are orthogonal to one another — notice that individual particles move in orthogonal directions in the two illustrations. These polarisations are transverse to the direction of the wave.*

It follows that there are only two independent linear polarizations. It is conventional to take them as the two area-preserving distortions illustrated in Figure 1.1, which are called "+" and "×". The rotation by 45° from one polarisation to the other makes them orthogonal: notice that for each particle the motion in one diagram is perpendicular to its motion in the other. In the language of quantum field theory, one expects only two independent polarisations for a pure spin-2 massless graviton, because such a particle has only two independent helicity states. But note that, despite this language, observable gravitational waves are not quantum fields: they contain such enormous numbers of "gravitons" (10^{80} or more for some sources) that they are completely classical.

Radiation and antenna patterns. We shall turn in the next section to the way waves are generated by source motions. But again we will not get directional information from our approach. We fill this gap by noting here that, happily, the directions of polarization follow closely the mass motions in the source. Suppose for simplicity that the source consists of two masses moving back and forth along a given line, as if on a spring; then the polarization ellipse of the waves will align its major axis with this line. Thus, two detector masses separated along a direction parallel to the separation of the source masses move back and forth in synchronisation with the source masses, at the same retarded time (*i.e.* allowing for the travel time of the wave from source to detector). It follows that the two oscillating source masses emit no radiation along the direction of the line joining them, because when seen from this direction they have no transverse motion at all.

It is possible from this information to build up the radiation patterns and antenna pat-

terns of more complicated sources and detectors. For example, a binary star system will emit circularly polarised radiation along its orbital angular momentum axis, since from this direction its mass motions are circular. By contrast, it will emit linearly polarised radiation along directions in the orbital plane, since from these directions the transverse mass motions are simple linear oscillations.

> *By measuring the degree of circular polarization in a wave and its orientation, LISA can determine the angle of inclination of a binary orbit, and even the direction of this inclination projected on the sky (to within a 90° ambiguity).*

This information cannot usually be obtained by conventional observations of binary systems, and is crucial to determining stellar masses. Note also that we see that the frequency of the gravitational radiation from a binary is twice the frequency of the orbital motion, since after half an orbital period the two stars have replaced one another and the mass distribution is the same as at the beginning. (This is true even if the stars have dissimilar masses, at least for the quadrupole radiation described below.)

Similarly, LISA will be most sensitive to sources located along a line perpendicular to the plane containing its spacecraft, but it will have some sensitivity to sources in its plane.

> *As LISA orbits the Sun, its orientation in space changes (see Chapter 3 and especially Section 4.4). This produces an amplitude modulation in a signal received from a long-lived source, which gives some information about its direction. Further directional information comes from LISA's changing orbital velocity. This results in a Doppler-induced phase modulation that can, for sufficiently high frequencies, give very accurate positions.*

This is similar to the way radio astronomers determine precise pulsar positions using only single radio antennas with very broad antenna patterns. These issues are discussed in detail in Section 4.4 .

For frequencies above about 3 mHz, LISA's arm length is long enough that it can measure the differences between the arrival times of the gravitational wave at the different corners. This can in principle be used to triangulate positions on the sky, provided the telemetry returns enough information to extract these timing signals. Further study is required to determine whether the added information justifies providing the extra telemetry bandwidth.

1.1.3 Generation of gravitational waves

We mentioned above the different approximation methods that are used to decide how much radiation to expect from a given source. The simplest approximation, and the one that is used for most estimates, is the lowest-order post-Newtonian formula, called the "quadrupole formula". Recall that the quadrupole radiation is the dominant radiation, because conservation of energy and momentum kill off monopole and dipole gravitational radiation. The interested reader can find a derivation of the quadrupole formula, using only the assumptions and mathematical level we have adopted here, in Reference [7].

If we define the second moment integral of the mass distribution of the source to be the integral

$$I_{jk} = \int \rho x_j x_k d^3x \,, \tag{1.5}$$

where the integral is over the entire volume of the source, then the standard trace-free quadrupole tensor is

$$Q_{jk} = I_{jk} - \frac{1}{3} I \delta_{jk} \,, \tag{1.6}$$

where I is the trace of the moment tensor. (The tensor Q is sometimes called H in textbooks. Note that I_{jk} is not the moment of inertia tensor, despite the notation.) The radiation amplitude is, for a nonrelativistic source at a distance r,

$$h = \frac{2G}{c^4} \frac{\ddot{Q}}{r} \,, \tag{1.7}$$

where we have left off indices because we have not been quantitative about the antenna and radiation patterns. The total luminosity in gravitational waves is given by

$$L_{\rm GW} = \frac{G}{c^5} \left\langle \sum_{jk} \left(\frac{d^3 Q_{jk}}{dt^3} \right)^2 \right\rangle , \tag{1.8}$$

where the angle brackets $\langle \ldots \rangle$ denote an average over one cycle of the motion of the source. In this formula we have put in all the correct factors and indices.

There are simple order-of-magnitude approximations for these formulas, which are both easy to use and instructive to look at. For example, one can write

$$\ddot{I}_{jk} = \frac{d^2}{dt^2} \int \rho x_j x_k d^3x \sim \int \rho v_j v_k d^3x \,.$$

Now, the quantity $v_j v_k$ will, by the virial theorem, be less than or of the order of the internal gravitational potential $\Phi_{\rm int}$. Combining this with Equation 1.7 gives

$$h \leq \frac{G}{c^4} \frac{\Phi_{\rm int}}{r} \int \rho d^3x = \frac{\Phi_{\rm ext}}{c^2} \frac{\Phi_{\rm int}}{c^2} \,, \tag{1.9}$$

where $\Phi_{\rm ext}$ is the external gravitational potential of the source at the observer's position, GM/r.

This simple expression provides an upper bound. It is attained for binary systems where all the mass is participating in asymmetrical motions. The exact formula was first derived by Peters and Mathews [8]. For a circular orbit the radiation is a sinusoid whose maximum amplitude can be expressed in terms of the frequency of the emitted waves and the masses of the stars by

$$h_0 = 1.5 \times 10^{-21} \left(\frac{f}{10^{-3}{\rm Hz}} \right)^{2/3} \left(\frac{r}{1\ {\rm kpc}} \right)^{-1} \left(\frac{\mathcal{M}}{M_\odot} \right)^{5/3} , \tag{1.10}$$

where f is the gravitational wave frequency (twice the binary orbital frequency), r is the distance from source to detector, and $\mathcal{M}$ is the so-called "chirp mass", defined in terms of the two stellar masses M_1 and M_2 by

$$\mathcal{M} = \frac{(M_1 M_2)^{3/5}}{(M_1 + M_2)^{1/5}} \,. \tag{1.11}$$

Equation 1.10 can be derived, to within factors of order unity, by eliminating the orbital radius from Equation 1.9 in favour of the orbital frequency and the masses using Kepler's orbit equation. For equal-mass binaries, for example, one uses

$$\omega_{\rm orbit} = \left(\frac{GM_T}{d^3}\right)^{1/2} , \tag{1.12}$$

where M_T is the total mass and d the orbital diameter. Eccentric binaries emit higher-amplitude radiation with, of course, a more complicated time-dependence.

The most important use of the luminosity formula is to discover the effect of the loss of energy on the radiating system. A binary system consisting of two equal masses M in a circular orbit of radius R emits radiation with angular frequency $\omega = (GM/R^3)^{1/2}$, amplitude $h \sim (GM/rc^2)(GM/Rc^2)$ and luminosity $L_{\rm GW} \sim GM^2R^4\omega^6/5c^5$. The time-scale for the orbit to change due to the loss of energy is the orbital energy $|E| \sim \frac{1}{2}MR^2\omega^2$ divided by the luminosity $L_{\rm GW}$:

$$\begin{aligned} \tau_{\rm GW} = \frac{|E|}{L_{\rm GW}} &\sim \frac{5c^5}{2GMR^2\omega^4} \\ &\sim \frac{5c^5}{2G^3}\frac{R^4}{M^3} \,, \qquad (1.13) \\ &\sim \frac{5}{2\omega}\left(\frac{c^3}{GM\omega}\right)^{5/3} , \qquad (1.14) \end{aligned}$$

where in the last two equations we have alternately eliminated ω or R, respectively, using the orbit equation.

Now we can draw a very important conclusion:

> *LISA can measure* distances *to binaries whose orbits "chirp"*, i.e. *which change frequency through gravitational radiation emission during the observation time.*

If we combine Equation 1.10 with Equation 1.14, we find

$$h \sim \frac{c}{\omega r}\frac{(GM\omega)^{5/3}}{c^5} \sim \frac{c}{\omega^2 \tau_{\rm GW} r} \,. \tag{1.15}$$

Now, since ω and $\tau_{\rm GW}$ are observable, a determination of the amplitude h is enough to determine the distance r to the binary system. This is a powerful way to determine distances to supermassive black-hole binaries.

Figure 1.2 summarises the content of the equations of this section in the LISA context.

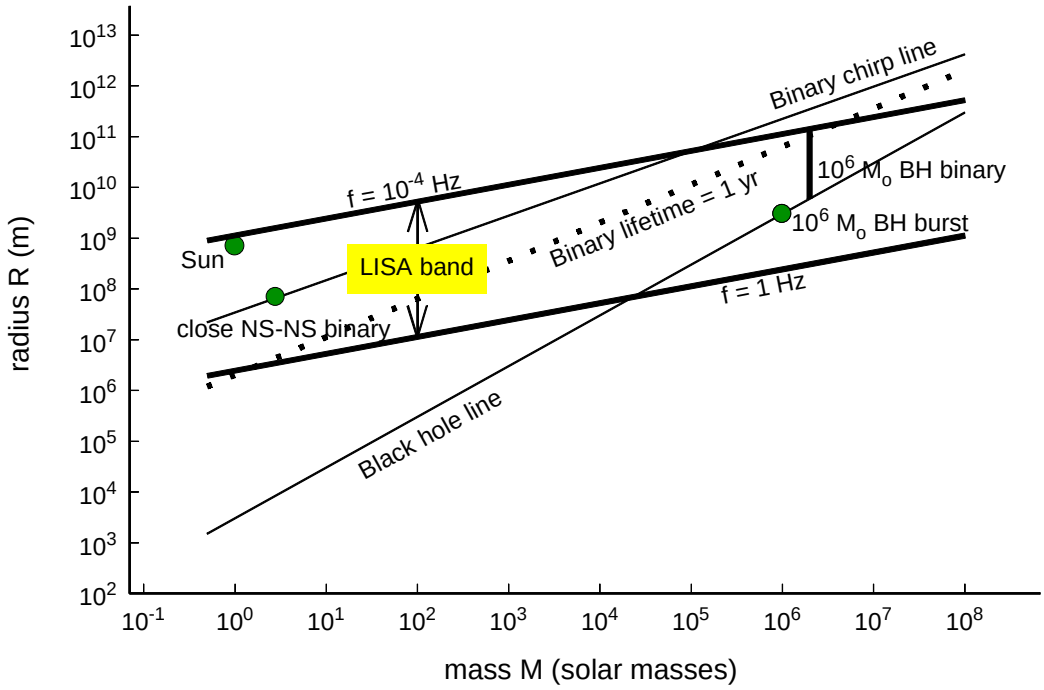

Figure 1.2 Gravitational dynamics. *This diagram shows the wide range of masses and radii of sources whose natural dynamical frequency is in the LISA band. The two heavy lines delineate the outer limits of sources accessible from space, at gravitational wave frequencies of* 10^{-4} Hz *and* 1 Hz. *They follow the formula* $f_{\rm GW} = (GM/R^3)^{1/2}/\pi$.
The "black hole line" follows $R = 2GM/c^2$*; if general relativity is correct, there are no systems below it. The "chirp line" shows the upper limit on binary systems whose orbital frequencies change (due to gravitational-wave energy emission) by a measurable amount* $(3\times10^{-8}\,\text{Hz})$ *in one year: any circular binary of total mass* M *and orbital separation* R *that lies below this line will "chirp" in LISA's observations, allowing LISA to determine its distance. (See text.) The curve labelled "binary lifetime = 1 yr" is the upper limit on binaries that chirp so strongly that they coalesce during a LISA observation. Any binaries formed of black holes above* $10^6 M_\odot$ *that are in the LISA band will coalesce as LISA observes them.*
At the lower-mass end of LISA's range we show the Sun and the shortest-period close neutron-star binary we expect LISA to see, which is on the chirp line but not the 1-year lifetime line. Near the upper mass limit we illustrate a $10^6 M_\odot$ *black hole formation burst and a* $10^6 M_\odot$ *black hole binary chirp (vertical line). Ground-based detectors operate only in the mass range between the* $f = 1$ Hz *line and the black-hole line.*

1.1.4 Other theories of gravity

When using gravitational wave observations to test general relativity, it is important to have an idea of what alternative predictions are possible. While general relativity has successfully passed every experimental and observational test so far [5, 9], it is clear that

it must fail on some level, since it is not compatible with quantum mechanics. Direct quantum effects will not be observable in such powerful gravitational waves, but side-effects of quantizing general relativity may be. For example, if by unifying gravity with the other interactions one needs to introduce massless gravitational scalar fields, these can themselves produce observable effects. One should, therefore, be alert to the possibility that some of the sources will show evidence that gravity is governed by a scalar-tensor theory.

Black holes are the same in scalar-tensor theories as in general relativity: the "no-hair" theorem demonstrates that the scalar field is radiated away when the holes are formed. So binary black holes are unlikely to show such effects, but neutron-star orbits around black holes might, as could gravitational waves emitted during the formation of a massive black hole. Not only would the dynamics in such a theory be different, but so would the radiation: scalar waves are longitudinally polarised, not transverse, and they would show a distinctive antenna pattern as LISA rotates during an observation. Perhaps the best chance to detect scalar radiation is by determining the polarization pattern of white-dwarf binaries, which ought to be abundant; some of them may have signal-to-noise ratios in excess of 1000 .

1.2 Low-frequency sources of gravitational radiation

In this section we survey some of the low-frequency sources that current astrophysical theory predicts and discuss the information that is likely to come from observations of them. The expected amplitudes will be compared with the predicted noise characteristics of LISA. The details of how these noise characteristics are estimated will be given in Chapter 3, which also discusses how the information can be extracted from the signals.

The specific types of sources that LISA will see or may see signals from are discussed in Sections 1.2.1 and 1.2.2 . However, before discussing the sources, we need to provide some information on the threshold sensitivity expected for the LISA antenna. This will be done using the example of the numerous expected signals from compact binaries in our galaxy, as shown in Figure 1.3 .

Later figures in this section will show the possible strength of signals from extragalactic sources. The search for and detailed study of such sources is the main objective of the LISA mission. Most of them involve massive black holes. If massive black holes are indeed present in most galactic nuclei, it seems likely that signals giving information about them will be observable by LISA out to cosmological distances.

The solid and roughly U-shaped curve shown in Figure 1.3 is the expected threshold sensitivity over the main observing range for LISA, which extends from 10^{-4} Hz to 1 Hz. A 1-year-long observing period is assumed. This is a reasonable length of time, but not the maximum: the nominal mission lifetime is 2 yr, but in principle it might last as long as a decade. The duration of an observation affects, of course, the effective noise in the observation. For an observation of length T, the frequency resolution is just $1/T$, and so a longer observation needs to fight against the noise in a smaller bandwidth. Since noise power is proportional to bandwidth, the *rms* noise amplitude is proportional to the square root of the bandwidth, and the result is that the noise at any frequency falls

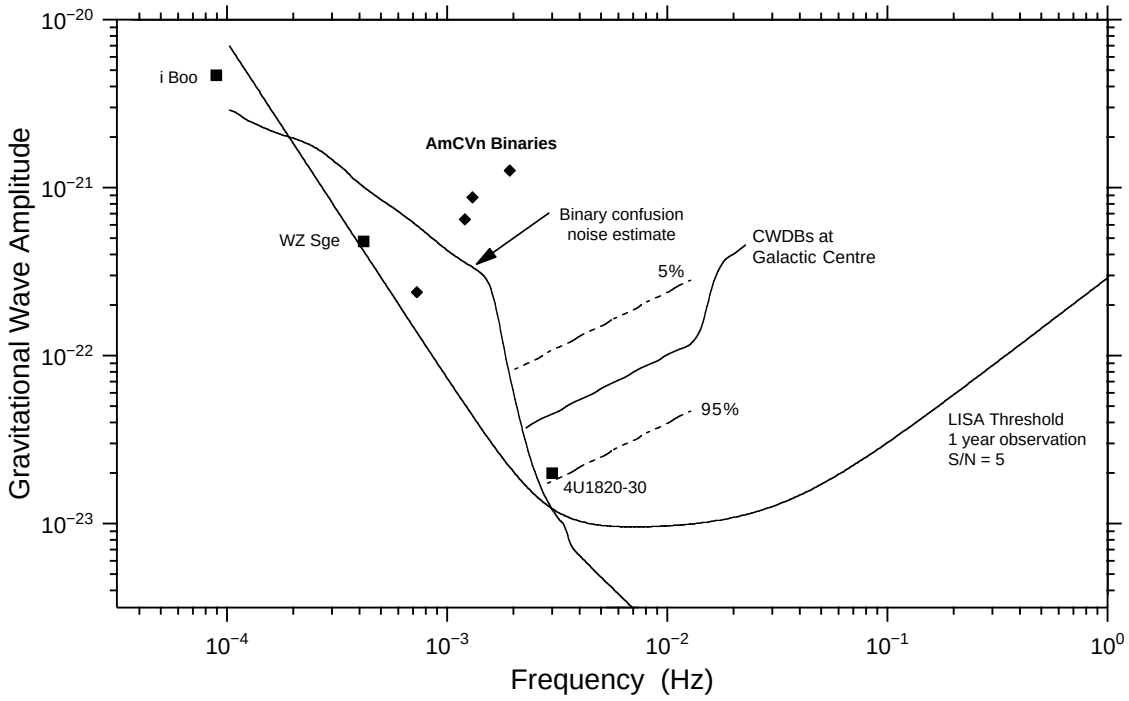

Figure 1.3 *The signal levels and frequencies are given for a few known galactic sources, along with the expected LISA threshold sensitivity and an estimate of the binary confusion noise level. In addition, the range of levels for 90 % of the expected thousands of resolvable close white dwarf binary signals from our galaxy is shown.*

as $1/\sqrt{T}$. In a 1-year observation, the frequency resolution is 3×10^{-8} Hz, and there are $(1\,\text{Hz})/(3\times10^{-8}\,\text{Hz}) = 3\times10^{7}$ resolvable frequencies in the LISA band.

For expected signals due to binaries in our galaxy, the *intrinsic* wave amplitude h is essentially constant during a 1-year observation. Such sources are placed in the diagram to show this h on the vertical scale. But because of LISA's motion, LISA almost never responds to this maximum amplitude; rather, the full signal-to-noise ratio SNR over a year is lower by a factor which depends on the exact position of the source relative to LISA's orbit. We can approximate this effect by assuming a reduction by the *rms* value of the antenna sensitivity of an interferometer averaged over the entire sky, which is a factor of $1/\sqrt{5}$ [4]. This means that, if a source lies above the 1-σ noise level by a certain factor s, the expected SNR will be typically $s/\sqrt{5}$. To be specific, the threshold sensitivity curve in Figure 1.3 is drawn to correspond to a SNR of 5 in a 1-year observation. (Accordingly, it is drawn at a factor of $5\sqrt{5}\approx 11$ above the 1-year, 1-σ noise level.) This SNR of 5 is a *confidence level*: for a 1-year observation, the probability that Gaussian noise will fluctuate to mimic a source at 5 standard deviations in the LISA search for sources over the whole sky is less than 10^{-5}, so one can be confident that any source above this threshold curve can be reliably detected. *To estimate the expected SNR for any long-lived source in the diagram, one multiplies the factor by which it exceeds the* threshold *curve by the threshold level of 5.* The threshold curve is drawn on the assumption that the dominant noise is the 1-σ instrumental noise level. If any of the random gravitational-wave backgrounds

described above are larger, then the threshold must likewise go up, remaining a factor of $5\sqrt{5}$ above the *rms* gravitational-wave noise.

It is important when looking at Figure 1.3 to realise that even sources near the threshold curve will be strongly detected: the X-ray binary 4U1820-30 is only a factor of 2 above the curve, but that implies an expected SNR in amplitude of 10, or in power of 100. Any observation by LISA above the threshold curve will not only be a detection: there will be enough signal to extract other information as well, and that will be important in our discussion below.

Note also that sources can be detected below the threshold curve if we have other information about them. For example, if a binary system is already known well enough to determine its orbital period and position, then the confidence level can be lowered to something like 3σ, where the probability would still be less than 10^{-4} that (on Gaussian statistics) the noise was responsible for the observation.

The phase-modulation of a signal produced by LISA's orbital motion will require that, in the data analysis, a compensating correction be applied to the data in order to give a signal its expected SNR as indicated in the diagram. This correction will depend on the assumed location of the source on the sky. At 0.1 Hz, there may be as many as 10^5 distinguishable locations, and so there are 10^5 different chances for noise to mimic a source at any level. This factor has been taken into account in adopting the threshold level of 5 standard deviations in the diagram: the chances that Gaussian noise will produce a false alarm anywhere in these different locations at this level is still less than 10^{-4}. The data analysis will of course test whether the noise is Gaussian, and may then set the threshold differently if necessary.

In Chapter 4 we describe in some detail how LISA's sensitivity is calculated, but here it is appropriate to note where its main features come from. The best sensitivity is between 3 and 30 mHz. In this range the sensitivity is limited by a combination of white-noise sources, including photon shot noise and noise due to variations in the beam pointing. Above 30 mHz, LISA's sensitivity begins to get worse because the wavelength of the gravitational wave becomes shorter than twice LISA's arm-length of 5×10^6 km. For such waves, light does not have time to go up and back along a LISA arm before the wave amplitude changes sign and begins to reverse its action on the arm. This increasing cancellation accounts for the rising noise at high frequencies. At low frequencies, the noise curve rises because of the effect of spurious forces on the proof masses. The acceleration noise error budget is taken to be white, so that the contribution to the instrumental noise in detecting gravitational wave signals varies as the inverse square of the frequency. The lower frequency limit at which the sensitivity curve is cut off is set by uncertainty in what the accelerometer noise will be. At some frequency below 0.1 mHz the accelerometer noise will increase rapidly unless special measures are taken to surpress it, and the instrumental uncertainty would increase even more steeply with decreasing frequency.

The sensitivities shown in Figure 1.3 are *conservative*, for three reasons:

1. The error budgets (Section 4.2) have been calculated realistically. Allowances are included for all of the substantial error sources that have been thought of since early studies of drag-free systems and since the first one was flown over 25 years ago. In most cases, except for shot noise, the error allowance is considerably larger than the expected size of the error and is more like an approximate upper limit. This means

that the performance of LISA could in principle turn out to be significantly better than shown.

2. LISA is likely to have a significantly longer lifetime than one year. The mission is planned for 2 years, but it could last up to 10 years without exhausting on-board supplies. As described above, its sensitivity to long-lived sources improves as the square root of the mission duration. Not only would this lower the noise and threshold curves, but it would also lower any gravitational-wave noise from white-dwarf binaries, since LISA would resolve more of those sources and remove them from this confusion-limited background.
3. LISA will actually have three arms, not two. LISA's third arm provides necessary redundancy for the success of the mission, but it also has an important scientific benefit: it allows LISA to detect two distinct gravitational wave observables, which can be thought of as formed from the signals of two different interferometers, with on arm common to both. This improves both the sensitivity of LISA and its ability to measure parameters, particularly the polarisation of the waves. The sensitivity shown in Figure 1.3 is only for a single interferometer.

The two interferometers are not perfectly orthogonal, since they are not oriented at 45° to each other. But they are oriented differently enough so that two distinct, linearly independent gravitational-wave observables can be formed, with similar signal-to-noise ratios. One is the difference in arm length for the two arms of the "primary" interferometer. The other is the length of the third arm minus the average of the lengths of the other two arms.

The fact that the two interfermometers share a common arm means that they will have common noise. Most of the signals in Figure 1.3 have signal-to-noise ratios that are so large that the likelihood that the signal is caused by noise will be negligible; in this case, the information from the two interferometers can be used to obtain extra polarization and direction information. This will be particularly helpful for observations of relatively short-lived sources, such as the coalescences of $10^6\,M_\odot$ black holes, where the signal does not last long enough to take full advantage of the amplitude and frequency modulation produced by LISA's orbital motion.

For signals nearer the noise limit, the second observable will still provide some increase in the confidence of detection. Using three arms could increase the effective signal-to-noise ratio by perhaps 20 %. And for stochastic backgrounds, the third arm will help to discriminate such backgrounds as produced by binaries and cosmological effects from anomalous instrumental noise. This will be considered in detail in Section 4.4 below.

The frequency of radiation emitted by a source of mass M and size R will normally be of the same order as its natural gravitational dynamical frequency, as in Equation 1.12, recalling that the gravitational wave frequency is twice the orbital frequency[1]:

$$f_{\rm GW} = \frac{1}{2\pi}\,\omega_{\rm GW} = \frac{1}{\pi}\left(\frac{GM}{R^3}\right)^{1/2} = 3.7\times10^{-3}\left(\frac{M}{1\,M_\odot}\right)^{1/2}\left(\frac{R}{1\times10^8\ \mathrm{m}}\right)^{-3/2}\ \mathrm{Hz}. \qquad (1.16)$$

[1] An exception is a system which is emitting much less radiation than the upper limit in Equation 1.9, such as a slowly rotating neutron star with a small lump on it. We do not expect any such sources to be prominent at low frequencies.

Therefore, as we can see in Figure 1.2, a source will radiate above 0.1 mHz (the main LISA band) if either (1) it is a stellar system (solar mass) with a dynamical size of order 10^9 m, about 0.01 AU or $1.4\,R_\odot$; or (2) it is supermassive, such as a pair of $5\times10^7\,M_\odot$ black holes, with a separation of about 5×10^{11} m. Since this separation is about seven times the gravitational radius of a $5\times10^7\,M_\odot$ black hole, this is essentially the largest mass that will plausibly be seen by LISA. Intermediate mass binaries, such as binaries of $300-1000\,M_\odot$ black holes, may well exist or have existed in many galactic nuclei, and their coalescences could be observed from cosmological distances.

Stellar-mass sources are weaker emitters of radiation, so they will usually be seen only in the Galaxy. Signals involving massive black holes are much stronger, and can be seen from very far away. So we discuss discrete sources in our Galaxy first, and then discrete sources in other galaxies. After that we go on to discuss primordial gravitational waves.

Oscillations of the Sun disturb its Newtonian gravitational field, and the tidal effects of this disturbance can affect LISA in the same way as gravitational waves. Estimates of the possible effects of solar g-mode oscillations on LISA indicate that they might be observable at frequencies near 0.1 mHz if they are close to the limits set by SOHO observations.

1.2.1 Galactic binary systems

After Mironowskii's [10] early and pioneering work on gravitational radiation from W UMa stars, there was a delay of nearly two decades before other studies appeared which estimated the gravitational radiation luminosity due to various types of binary stars in the galaxy. Iben [11] first described the expected signal level from close white dwarf binaries, and Hils *et al.* [12] presented a brief summary of the later results of Hils, Bender, and Webbink [13], in which other types of binaries also were included. Lipunov and Postnov [14] modelled the evolution of galactic low- and moderate-mass systems by Monte Carlo methods and gave the expected signal strengths, and Lipunov, Postnov, and Prokhorov [15] extended their results to include white dwarf and neutron star binaries plus the background due to other galaxies. Evans, Iben, and Smarr [16] gave detailed calculations on white dwarf binaries. The general picture which has developed is as follows. After an initial period of observations such as 1 yr, most frequency bins below some critical frequency near 1 mHz will contain signals from more than one galactic binary. At higher frequencies, most of the signals from individual binaries can be resolved and fit to determine the source amplitude, phase, and direction. However, the unresolved sources at lower frequencies form a confusion-limited background, which makes observations of individual sources difficult, unless they are particularly strong.

The different types of galactic binaries will be discussed in the following sections. LISA's observations of these systems would have interest both for fundamental physics and for astrophysics. Because LISA is a linearly polarised detector that rotates with a 1-year period, it can measure not only the amplitude but also the polarisation of the gravitational waves. If known systems are not seen, or seen with amplitudes or polarisations not predicted by general relativity, then general relativity must be wrong. If they are seen, the polarisation measurement reveals the angle of inclination of the orbit and the orientation of the plane of the orbit on the sky. The inclination angle is usually the crucial missing datum when one tries to infer stellar masses from optical observations. With it astronomers will

have more secure models of these systems and will in addition be able to estimate the distance to the binary from the gravitational-wave amplitude and the estimated masses. The orientation angle of the plane of the orbit will be interesting if other orientation-dependent phenomena are observed, such as jets or optical/radio/X-ray polarisation. The large majority of galactic binaries will not be known in advance, but can be located on the sky from the frequency modulation that the motion of LISA produces in their signals, and to some extent also from the amplitude modulation. This is discussed in Section 4.4 .

Neutron star binaries. The best-known two-neutron-star (NS-NS) binary is the famous Hulse-Taylor binary pulsar PSR B1913+16, discovered in 1975 [17]. Its orbital period of 7.68 hrs places it below the LISA band, but it is important to LISA as the best-studied member of a class of binaries that should be important sources. The Hulse-Taylor binary is decaying due to the loss of orbital energy to gravitational waves at exactly the rate predicted by general relativity [6]. PSR B1913+16 will coalesce to a single star in 3×10^8 years. Two other very similar systems are known. By considering the selection effects in the detection of such systems, a recent detailed study [18] arrived at a conservative estimate of $N \sim 10^3$ such systems in the Galaxy, formed at a rate of about one per 10^5 yr.

Theoretical calculations of binary evolution give a wide variety of estimates of the number of such systems. Most of them [19, 20, 21] give rather higher rates than the observational estimates. It is possible, therefore, that observations give a lower bound on the number of such systems, but that some fraction of the population does not turn up in pulsar surveys. It may be that not all neutron stars turn on as pulsars, or even that binaries like PSR B1913+16 may be merely the long-period tail of a distribution of binaries that are formed with periods as short as an hour and which decay so rapidly through the emission of gravitational radiation that one would not expect to see any such systems in pulsar surveys. In this case the formation rate could be as high as one per 3 000 yr, leading to a total population of $N \sim 3 \times 10^6$ systems. Moreover, recent observations of the binary pulsar PSR J1012+5307, whose companion is a white dwarf that is much younger than the apparent age of the pulsar as estimated from is spin-down rate, have suggested that millisecond pulsar spindown may overestimate the pulsar's true age [22]. Since binary pulsars tend to be millisecond pulsars, this could also raise the binary neutron-star birthrate. For a recent overview of this subject, see [23].

Another indication of this population comes from gamma-ray bursts [24]. From optical identifications of some recent bursts, it is now known that these events occur at immense distances [25]. Although the events are not understood in detail, it seems that they could involve coalescences of neutron stars with other neutron stars or with black holes. Such events occur at the end of the gravitational-wave evolution of systems in the population of binaries we are considering here. Estimates of the size of the population from observations of gamma-ray bursts are consistent with the observational limits mentioned above. For example, the estimates above suggest that there could be of order 10^4 neutron-star/neutron-star coalescences per year out to a redshift of $z = 1$. About 1000 observable bursts are thought to occur each year, but it seems probable that bursts are beamed, so that the two rates would be consistent for a 10 % beaming factor. If bursts are spread to greater distances (one has been seen beyond $z = 3$), the rates are not consistent unless the beams are very narrow, or unless the more distant bursts come from neutron-star/black-hole mergers (see the next section), which could indeed emit stronger bursts, according

to popular models.

Progress with ground-based gravitational wave detectors makes it likely that LIGO and VIRGO will have observed a number of the rare coalescence events by the time LISA is launched. In this case we will have a much better idea of the rate to expect. But only gravitational wave observations by LISA would provide a complete census of this population in our Galaxy. This should provide a springboard for further advances in binary evolution theory.

Black hole binaries in the Galaxy. The evolutionary scenario that is expected to lead to NS-NS binaries will also form binaries of a neutron star and a black hole (NS-BH) in some cases. In fact, the formation of a black hole has much less probability of disrupting a binary system, since less mass is lost. For this reason, Narayan, Piran, and Shemi [26] estimated that there could be almost as many neutron star – black hole binaries as there are neutron star – neutron star binaries. Tutukov and Yungelson [19], considering the process in more detail, estimate that there could be about 10 % as many NS-BH binaries as NS-NS binaries. However, these estimates are very sensitive to assumptions about mass loss in giant stars during their pre-supernova evolution. If winds are very high, close binaries containing black holes may not form at all [27].

Binaries consisting of two black holes are also predicted in scenarios that lead to neutron-star/black-hole binaries, and it is possible that there are a handful of them in the Galaxy. The Virgo cluster has many more galaxies, so the shortest-period one will be faster and more powerful than expected ones in the Galaxy. If the higher birthrate estimates are correct, then the shortest-period BH-BH binary expected in Virgo might be just detectable.

Unless the binary system chirps during the LISA observation (*i.e.* unless it lies below the chirp line in Figure 1.2), then gravitational wave observations alone will not normally distinguish between NS-NS binaries and BH-BH binaries of the same orbital period, except statistically. The black-hole binaries radiate more strongly because of their larger mass, and so they will be detectable at greater distances. Again, continued work on gamma-ray bursts and future observations by LIGO and VIRGO may give us a clearer idea of the number of systems LISA might observe. But only LISA can reveal the Galaxy's black-hole population. Its spatial distribution would be a clue to the origin of the population.

X-ray and common-envelope binaries. An important stage of the evolution of close binary systems is the X-ray binary phase, where one of the stars has become compact (a neutron star or black hole) and the other feeds gas to it. At the end of this stage, the compact star can enter the envelope of its companion and disappear from view in X-rays, while remaining a strong emitter of gravitational waves. The orbits of such systems are larger than the ultimate orbits if they leave behind compact-object binary systems, so most will be below the LISA frequency range. But there should be a number of common-envelope and X-ray systems that are in the LISA range. Indeed, one low-mass X-ray binary, 4U1820-30, is so well-studied that it is one of the most secure of the known binary sources: its orbital period, companion mass, and distance are believed very reliable. Its expected signal is shown in Figure 1.3 .

Close white dwarf binaries. The situation for close white dwarf binaries (CWDBs) unfortunately is rather more complicated than for neutron-star or black-hole binaries. The normal stellar evolution calculations for close binaries indicate that such systems

pass through at least one and sometimes two stages of common envelope evolution before CWDBs are formed. However, it is not known how to calculate the loss in angular momentum during the common evolution stages, and thus the calculated space density of CWDBs with periods in the range of interest for LISA is more like an upper estimate than an expected value. These estimates suggest that LISA will suffer an embarrassment of riches from this population, so many systems that they will not be resolvable by LISA below a few millihertz frequency, and they will obscure other, rarer systems.

Until recently, searches for this type of binary with orbital periods less than a day have been unsuccessful, but the total number of known non-interacting CWDBs with periods longer than 1 day jumped not long ago from two to six, and two additional ones with periods of 3.47 hr and about 4 hr have been found [28, 29]. These last two have lifetimes before merger of roughly a quarter of the Hubble time, and so further analysis and observations may lead soon to better understanding of the binary population in the LISA range.

In view of the theoretical and observational uncertainties, the detailed estimates of Hils *et al.* [13] of the gravitational wave background that could be expected from this population used a space density for non-interacting CWDBs which was a factor 10 less than the evolutionary rough limit. These binaries give the dominat contribution to the gravitational-wave confusion noise level shown in Figure 1.3 . The part of the curve above about 3 mHz, where the level has dropped off sharply, is due to the estimated integrated effect of CWDBs in all other galaxies. It should be stressed that the actual confusion noise level might be significantly higher or lower than the level shown. LISA will be able to distinguish the galactic binary background from a cosmological background or instrumental noise because there will be a large number of "outliers" — binaries at high enough frequencies to be individually resolvable. By studying the resolvable systems, one should be able to predict what the background level is, and infer from it what the space density of CWDBs is in other parts of the Galaxy.

The strengths of the signals from the resolvable CWDBs at the galactic centre are shown by the solid curve with that label in Figure 1.3 . The curve rises with respect to a constant slope curve above 15 mHz as the lighter CWDBs consisting of two He white dwarfs coalesce, and only the heavier ones consisting of two carbon-oxygen (CO) white dwarfs are left. The dashed curve labeled 5 % gives the rms strength for CWDBs at a distance from the Earth such that only 5 % of those in the galaxy are closer, and the 95 % curve is defined in a similar way. Thus 90 % of the galactic CWDBs give signal strengths between the two dashed curves. Based on the CWDB space density assumed in calculating the binary confusion noise estimate, roughly 5000 CWDBs would be resolvable at frequencies above about 3 mHz.

Helium cataclysmic variables. These are systems where a low-mass helium star fills its Roche lobe and transfers mass onto a more massive white dwarf [30]. Such systems have close orbits that place them in the LISA frequency band. Six HeCVs within about 100 pc of the Earth are known, and all have likely gravitational-wave frequencies near 1 mHz. The He star in these cases has been reduced by mass transfer to a few hundredths of a solar mass, so that the strength of the signals is quite low. These sources frequently are called AM CVn binaries, and also interacting white dwarf binaries, even though the He star may be only semi-degenerate. The estimated signal strengths for the four which

are best understood (AM CVn, V803 Cen, CP Eri, and GP Com) are shown in Figure 1.3 as the unlabelled squares at and above 1 mHz. The frequencies are known for AM CVn and GP Com, and are probable for the other two.

The initial conditions and evolutionary paths that produce HeCVs are not well known. One plausible assumption [31] is that they evolved through a stage where a CO white dwarf had formed and the secondary was burning He when it made Roche lobe contact. The orbital period would have shortened rapidly due to gravitational radiation until it reached a minimum of about 600 s when the secondary mass was reduced to roughly 0.2 $M_\odot$. Later evolution due mainly to mass transfer would be to longer periods, and the rate of period change would become slower as the secondary mass decreased.

Hils and Bender [32] recently have estimated the HeCV signal strength under the above scenario, with the space density of the sources normalized to an estimate given by Warner [30]. Because of the rapid evolution of these binaries before they reach the AM CVn stage with low secondary masses, and the weakness of the signals from then on, the resulting contributions to the *rms* binary signal strength as a function of frequency are fairly small. However, the estimated number of such sources in the frequency range of interest is large, so they fill many of the frequency bins that otherwise would be open between roughly 1 and 3 mHz. Thus a curve for the confusion noise including the HeCV contribution as well as those from CWDBs and other binaries is given in Figure 1.3 and in later figures.

Another estimate for the HeCV space density based on a different assumption about the nature of their progenitors has been given by Tutukov and Yungelson [33]. It considers the helium star secondary to already be degenerate or semi-degenerate at the time of Roche lobe contact. The resulting estimated space density of AM CVn binaries is much higher than the estimate of Warner [30]. Until the likelyhood of the different assumptions is better understood, the uncertainty in the contribution of HeCVs to the confusion noise should be remembered. However, they will not contribute much at frequencies above about 3 mHz in any of the assumed scenarios.

Normal detached binaries, contact binaries, and cataclysmic variable binaries. These three types of binaries have been discussed in some detail [13]. By normal detached binaries we mean binaries consisting of normal, "unevolved" stars whose Roche lobes are not in contact. "Unevolved", as used here, means that the stars have not yet reached a giant phase or started helium burning. Contact binaries are the W UMa binaries studied first by Mironowskii [10], which are two unevolved stars with their Roche lobes in contact. A cataclysmic variable binary consist of a white dwarf which accretes mass spilling over from a low mass hydrogen-burning secondary.

Some individual binaries of each of these types will be close enough and at high enough frequency, so their signals will be resolvable. This includes the normal detached binary ι Boo and the cataclysmic binary WZ Sge, which are the two lowest-frequency circles shown in Figure 1.3. The expected confusion limits for the W UMa and cataclysmic binaries are comparable with the LISA noise budget level over the frequency range from 0.1 to 0.4 mHz. Thus, if the spectral amplitudes for the CWDBs and IWDBs should turn out to be low enough, the abundance of these other types of binaries could be determined.

1.2.2 Massive black holes in distant galaxies

It is clear from the preceding sections that LISA will provide valuable information concerning the populations of various types of binaries in different parts of our galaxy. However, the most exciting scientific objectives for LISA involve the search for and detailed study of signals from sources that contain massive black holes (MBHs).

The most spectacular event involving MBHs will be the coalescence of MBH-MBH binaries. Because the signal has the unique signature of a "chirp" and can be followed over many months, and because it is intrinsically very strong, LISA can recognise MBH coalescence events in its frequency band almost anywhere in the Universe they occur. If LISA sees even one such event, it would confirm beyond doubt the existence of MBHs. From the fundamental physics point of view, the waveforms of signals from such objects at times near coalescence can provide extremely sensitive tests of general relativity for very strong field conditions [34]. Because the phase of the signals over thousands of cycles or longer can be tracked accurately for even fairly weak signals, very minor errors in the predictions of the theory would be detectable [35].

From the astrophysics point of view, sources involving MBHs can provide unique new information on the numbers, mass distribution, and surroundings of MBHs.

Astronomers invoke MBHs to explain a number of phenomena, particularly quasars and active galactic nuclei. The most well-known cases involve MBHs of masses roughly 10^8 – $10^{10}\,M_\odot$. LISA is sensitive mainly to lower masses, which may be considerably more abundant.

The key question for LISA is to estimate the likely event rate (see e.g. [36] and [37]).

Identification and abundance of massive black holes. The initial arguments for the existence of MBHs in quasars and active galactic nuclei were theoretical: there seemed to be no other way of explaining the extremely high and rapidly varying luminosities that were observed in the optical and radio bands. Now, however, direct observational evidence is compelling. For example, Hubble Space Telescope observations of M87 revealed a central brightness cusp and large asymmetric Doppler shifts, indicating a BH mass of order $3\times10^9\,M_\odot$ [38, 39]. X-ray observations can see gas much closer to the MBH, and the ASCA satellite provided remarkable evidence that seems definitive. Observing the active galaxy MCG-6-30-15, it has detected an iron X-ray line that is Doppler-broadened by velocities of order $0.3\,c$ and that is strongly redshifted, indicating that the radiation is coming from within 3 to 10 Schwarzschild radii of the MBH at the galactic centre [40]. The measured radial distances and Doppler shifts for H_2O masers in orbit around the centre of NGC 4258 demonstrate the presence of a mass of $3.6\times10^7\,M_\odot$ in a region less than 0.13 pc in radius [41].

Evidence for smaller MBHs in the main LISA mass range is also strong. Recent near-IR measurements clearly indicate a $2.6\times10^6\,M_\odot$ black hole at the centre of our own galaxy [42]. Even smaller galaxies have them: HST and ground-based observations of M32 [43] imply that this, a nearby dwarf elliptical, a satellite of the Andromeda galaxy M31, contains a $2.8\times10^6\,M_\odot$ black hole at its centre. Indeed, M31 itself contains a black hole of mass $3\times10^7\,M_\odot$.

Observational evidence for black holes is turning up in every galaxy that has been studied with enough sensitivity to see them, which restricts the evidence mainly to nearby

galaxies. Confident identifications include, besides the ones mentioned above: NGC 3115 ($2\times10^9\,M_\odot$); M104 ($5\times10^8\,M_\odot$); NGC 4261 ($52\times10^8\,M_\odot$); M106 ($3.6\times10^7\,M_\odot$); and M51 ($3\times10^6\,M_\odot$). The size of the black hole seems to be roughly proportional to the mass of the galaxy [44]. For example, limits below $10^5\,M_\odot$ now exist for MBHs in the Local Group dwarf galaxies M33 and NGC 205. See the articles by Kormendy & Richstone [44] and by Rees [45, 46] for reviews and summaries.

What is particularly important for LISA is that massive black holes must be remarkably abundant, since all the confident black-hole detections are in local galaxies. When the surveys are continued to larger distances, the evidence remains strong, within the limits of the available resolution of the observations. Two recent HST surveys bear this out. Of about 50 sample galaxies outside the Local Group in two studies [47, 48], *not a single one showed a central region that is constant in surface brightness.* Instead, 70 % of the galaxies in the first study showed light profiles similar to the cusps generated by central MBHs, with inferred MBH masses of roughly 0.1 % to a few % of the galaxy core mass. And the second study similarly concluded that the cores of many galaxies appear to be similar to that of M32, with its modest-mass MBH.

Formation of massive black holes. There is still major uncertainty about how MBHs form, although a great deal has been written on this subject. One approach taken by Quinlan and Shapiro [49] is to start from an assumed dense cluster of stars in a galactic nucleus and follow the build-up of $100\,M_\odot$ or larger seed MBHs by collisions. The further growth to a MBH would then be mainly by accretion of gas made available to the hole in a number of ways. If the seed MBHs grow to $500\,M_\odot$ before they coalesce with each other, these coalescences would give signals observable by LISA out to a redshift of $z=5$. Provided that roughly 10 or more such coalescences occurred per galaxy now having a MBH at its centre, the annual number of such events observable by LISA might be substantial. If instead a number of roughly $100\,M_\odot$ seed MBHs per galaxy are formed from a very high mass tail on the initial mass function or in some other way, coalescence signals still might observable out to high redshifts.

However, a very different view concerning the formation of MBHs was presented recently by Rees [45, 46]. In this view, fragmentation and star formation in a massive and dense gas cloud at a young galactic center will stop when the opacity becomes high, and the angular momentum loss will be rapid. The gas will either form a supermassive star, which evolves rapidly to a MBH, or collapse directly to a MBH. According to such scenarios, the collapse to a MBH will be nearly Newtonian and quite spherically symmetric until right at the end, and the amount of gravitational radiation emitted in the LISA frequency band will be very low.

A similar scenario was presented somewhat earlier by Haehnelt and Rees [50]. They stated that, if a density concentration of the order of $10^8\,M_\odot$ occurs in a region 1 pc across, it will have no nonrelativistic equilibrium state that can be supported for long, and will collapse to a MBH. Assuming that this scenario is correct for roughly $10^8\,M_\odot$ and larger gas clouds, and that it leads to rapid formation of MBHs in the quasars observed at large redshifts, it still is unclear how massive and how dense the gas cloud has to be for the collapse to a MBH to occur. In particular, whether it occurs throughout the MBH mass range of roughly 10^5 to $10^7\,M_\odot$ of particular interest for LISA has not been established. Alternative ways of forming MBHs in this mass range also have been proposed [51, 52].

If sudden collapses to MBHs do occur for gas clouds large enough to give roughly 10^5 to $10^7\,M_\odot$ MBHs, an important question is how much angular momentum will be left. If the cloud hasn't lost its angular momentum rapidly enough, a bar instability may occur and cause considerable gravitational radiation in the main LISA frequency band. Thus looking for pulses lasting only a few cycles will be important for LISA, as it is for supernova pulse searches with ground-based detectors.

MBH-MBH binary coalescence. Figure 1.4 shows the expected signal strength of coalescing MBH binary events in LISA against the LISA noise curve. The signal strengths

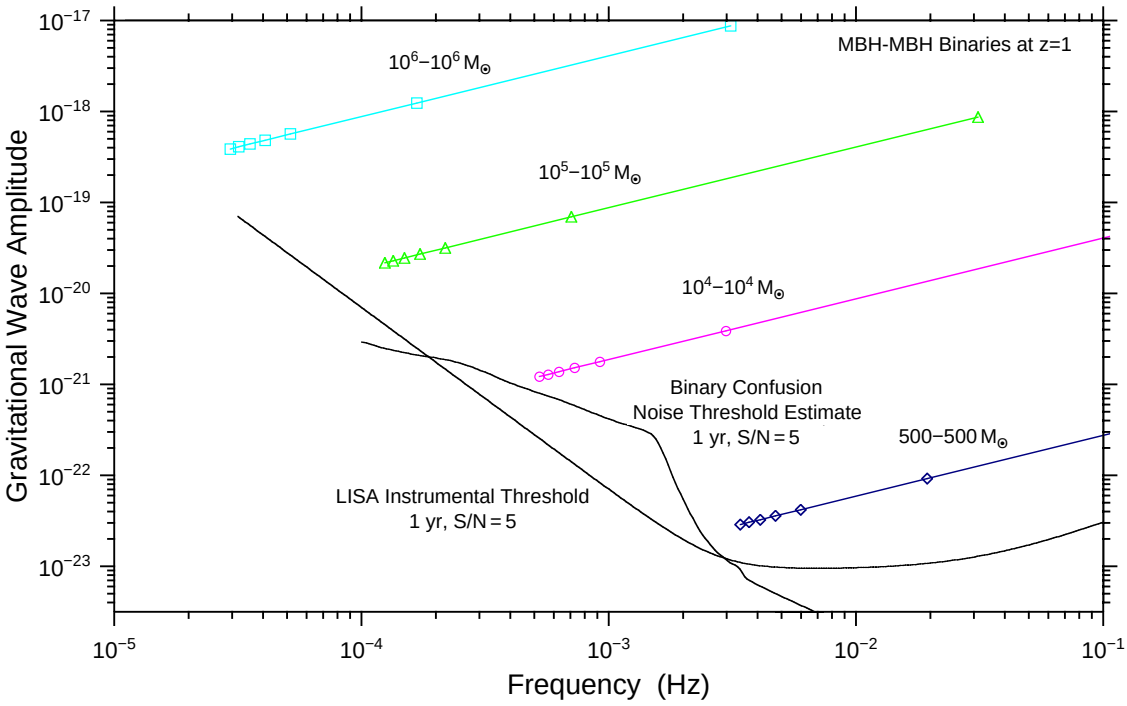

Figure 1.4 *Strain amplitude during the last year before MBH-MBH coalescence.*

and frequencies are displayed as a function of time for some possible MBH-MBH coalescence events at a redshift of 1. The Hubble constant H_0 is assumed to be $75\,\mathrm{km\,s^{-1}Mpc^{-1}}$. The straight lines sloping up to the right show the values of the gravitational wave signal strength h as a function of time during the last year before coalescence for different pairs of MBH masses. The first 5 symbols from the left correspond to times of 1.0, 0.8, 0.6, 0.4, and 0.2 yr before coalescence, while the 6th symbol is for 0.5 week before coalescence. The final symbol for the two highest mass pairs is at the approximate coalescence frequency. (Note that, at cosmological distances, the observed chirp mass of a binary is $1+z$ times its true chirp mass, its radiation is redshifted by the same factor, and its Euclidian distance is replaced by its luminosity distance. These factors are taken into account in Figure 1.4.) The case of 500 $M_\odot$ MBHs is included to correspond to possible coalescences of seed MBHs, rather than to currently plausible events resulting from galaxy mergers.

The LISA instrumental threshold curve for 1 year of observations and $S/N = 5$ is included in Figure 1.4, along with the corresponding binary confusion noise estimate. The instrumental threshold curve has been arbitrarily and optimistically extended from 0.1 mHz to 0.03 mHz with constant slope, even though there is no recommended error budget yet

for this frequency range. This is done in order for give some basis for considering the S/N ratio for the case of $10^6\,M_\odot$ MBH masses.

It is clear that the integrated S/N ratio for some time interval cannot be obtained by taking the ratio of two curve heights in Figure 1.4. This is because the instrumental and confusion noise curves correspond to 1 year of observation, and the signals of interest sweep through quite a frequency range during this time. Instead, the S/N ratio has to be integrated over time as the frequency changes, and the results are given in Figure 1.5. Here each symbol starting at the bottom left for each curve gives the integrated S/N ratio after 1 week, 2 weeks, etc., from the beginning of the last year before coalescence. The last symbol on each curve gives the total integrated S/N ratio up to roughly the last stable circular orbit, but is plotted at the frequency corresponding to 0.5 weeks before coalescence.

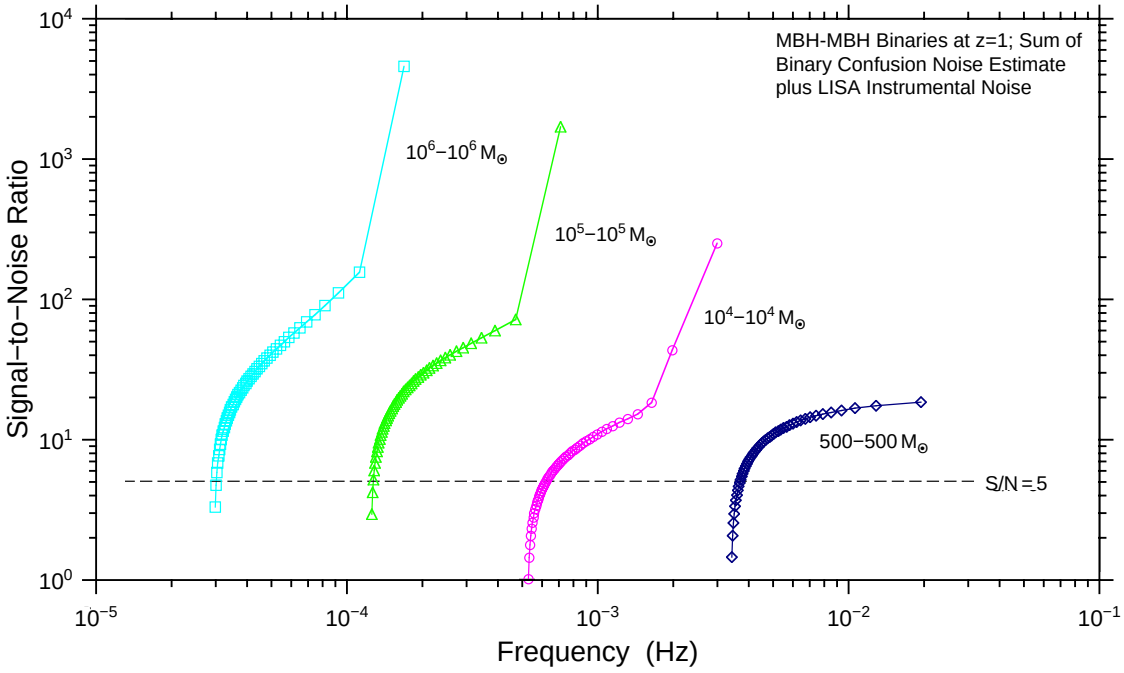

Figure 1.5 *Cumulative weekly S/N ratios during the last year before MBH-MBH coalescence.*

Moreover, by combining the amplitude, polarisation, and chirp-rate information from LISA's observations, we will be able to deduce (as in Section 1.1.3) the distance to the event. In cosmological terms, the distance measured will be the luminosity distance.

The extremely high signal-to-noise ratios that are expected in some cases are remarkable. They mean that LISA will not just detect such events; it will be able to study them in detail. The frequency modulation of the observed signal over a period of 3 months or more will locate the event on the sky, and the amplitude modulation as the plane containing LISA rotates will determine the signal's polarisation (see Section 4.4). The scientific payoff of observing such events will be great:

- Detection will confirm the existence of black holes, and details of the orbital evolution will test general relativity.

- Coalescences in the appropriate mass range will be seen essentially anywhere in the Universe they occur. In fact, gravitational lensing (see below) may multiply the event rate, so that each physical coalescence is observed tens of times or more. This would guarantee LISA an interesting rate even if physical coalescences are rare.
- Detailed comparison with numerical simulations will reveal the masses, spins and orientations of the two black holes, and this will provide important clues to the history and formation of the binary system.
- An overall test of models for when MBHs of different sizes formed with respect to the times of mergers of pregalactic and galactic structures will be obtained.
- LISA offers a slight possibility of an accurate check on both the Hubble constant H_0 and the cosmological deceleration parameter q_0. If optical signals corresponding to MBH-MBH coalescences at different cosmological distances should be observed, and if the redshifts of the associated galaxies can be obtained, comparison of the redshifts with the luminosity distances from LISA would give tight constraints on H_0 and q_0. However, this method must be used with care: gravitational lensing of distant events by nearby clusters of galaxies may be common, and could (by magnifying or de-magnifying the amplitude) distort the inferred luminosity distance. The chances of observing optical or other electromagnetic signals may be enhanced by pre-coalescence information from LISA on when and roughly where the event will occur, as suggested by Cutler [53].

If the growth of the massive holes is mainly by coalescence (rather than gas accretion), then the physical event rate will be so high that the more distant events will produce a stochastic background of signals rather like the confusion-limited white-dwarf background. An estimate is as follows: if each massive black hole contains 10^{-5} of a galaxy's baryonic mass (probably a conservative number), if the coalescence events that formed it released 10 % of the original mass in gravitational radiation, and if 10^{-3} to 10^{-2} of the infalling mass is stellar-mass black holes, then about 10^{-9} to 10^{-8} of the baryonic mass of the Universe will have been converted into gravitational radiation this way. This corresponds to an energy density greater than 10^{-11} to 10^{-10} of the closure density, a level probably detectable by LISA (see Section 1.2.3 below).

MBH – compact star binary signals. A third possible type of MBH signal is from compact stars and stellar-mass black holes orbiting around MBHs in galactic nuclei [54, 55]. MBHs in active galactic nuclei appear to be fueled partly by accreted gas from ordinary stars that were disrupted by the hole's tidal forces. But white dwarfs, neutron stars and black holes will not be disrupted, and will instead follow complex orbits near the hole. These orbits are very sensitive to relativistic effects that depend on the spin of the MBH and of the infalling star. If these events are as frequent as current thinking suggests, then they can be used not only to test general relativity but also to survey the MBH population out to redshifts beyond 1.

Estimates of the expected number and strength of signals observable by LISA in a one year period have been made by Hils and Bender [55] for the case of roughly solar-mass compact stars. Such events may well be observable if the neutron-star space density in the density cusp around the MBH is of the order of 0.1% of the total stellar density, which is not unexpected. Many more coalescence events occur, but the observable event rate

is reduced because these stars have highly eccentric orbits, which are easily perturbed by other stars in the cusp. Thus the compact stars usually plunge in rapidly, and the number of orbits one can observe in order to build up the S/N ratio usually will be small. Also, the confusion noise will obscure many of the more distant events for the higher MBH masses.

Recent calculations for $5-10\,M_\odot$ black holes orbiting MBHs indicate that these coalescence events will be more easily detected [56, 57, 32]. The signal is stronger, and the more massive black holes are less susceptible to stellar perturbations. If such black holes make up a fraction 10^{-3} of the total stellar numbers near the MBH, as they are very likely to do, then the number of signals from BH-MBH binaries observable at any time may well be substantial, and a number of such systems may coalesce each year.

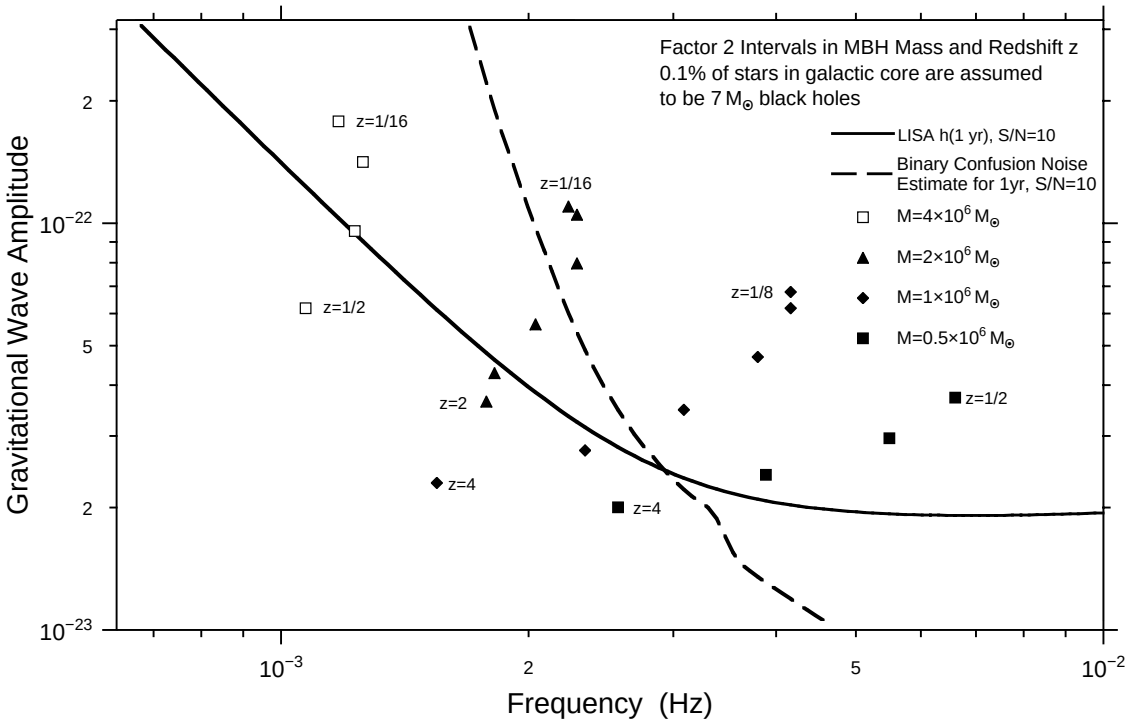

Figure 1.6 *Expected signals from BH-MBH binaries.*

Figure 1.6 shows the expected signal strengths and frequencies for $7\,M_\odot$ black holes orbiting around MBHs with different masses M and at different redshifts z [32]. For each factor-2 range in M and z about the value given, the signal strength and frequency are plotted for the strongest expected source within those ranges. For a given symbol corresponding to a given MBH mass, the plotted points correspond to values of z from the lowest to the highest value given as a label. Curves corresponding to the LISA threshold sensitivity and to the confusion noise estimate for 1 year of observation are included. However, for reasons discussed below, they are given for $S/N = 10$ instead of $S/N = 5$. The frequencies are treated as constant over a year, even though they actually will chirp strongly, and in a number of cases coalescence will occur during the year. The signals are likely to be stronger for rapidly rotating Kerr MBHs.

The orbits for such BH-MBH binaries will be highly relativistic, and observations would

test the predictions of general relativity very accurately in extremely strong fields. The orbital velocity near periapsis is roughly $0.5\,c$, and the period for the relativistic precession of periapsis is similar to the period for radial motion. In addition, if the MBH is rapidly rotating, the orbital plane will rapidly precess. In view of the complexity of the orbits, the number of parameter values to be searched for, and the expected evolution of the orbit parameters, the SNR needed to detect the signals reliably probably will be about 10.

If these events are observed, then each one will tell us the mass and spin of the central MBH, as well as its distance and position. The ensemble of events will give us some indication of the numbers of such black holes out to $z \sim 1$, and they will give us useful information about the MBH population, particularly the distribution of masses and spins.

1.2.3 Primordial gravitational waves

Just as the cosmic microwave background is left over from the Big Bang, so too should there be a background of gravitational waves. If, just after the Big Bang, gravitational radiation were in thermal equilibrium with the other fields, then today its temperature would have been redshifted to about 0.9 K. This radiation peaks, as does the microwave radiation, at frequencies above 10^{10} Hz. At frequencies accessible to LISA, or indeed even to ground-based detectors, this radiation has negligible amplitude. So if LISA sees a primordial background, it will be non-thermal.

Unlike electromagnetic waves, gravitational waves do not interact with matter after a few Planck times (10^{-45} s) after the Big Bang, so they do not thermalize. Their spectrum today, therefore, is simply a redshifted version of the spectrum they formed with, and non-thermal spectra are probably the rule rather than the exception for processes that produce gravitational waves in the early universe.

The conventional dimensionless measure of the spectrum of primordial gravitational waves is the energy density per unit logarithmic frequency, as a fraction of the critical density to close the Universe, ρ_c:

$$\omega_{\rm GW}(f) = \frac{f}{\rho_c}\frac{d\rho_{\rm GW}}{df}\,. \tag{1.17}$$

The background radiation consists of a huge number of incoherent waves arriving from all directions and with all frequencies; it can only be described statistically. The *rms* amplitude of the fluctuating gravitational wave in a bandwidth f about a frequency f is

$$h_{\rm rms}(f,\ \Delta f = f) \ = \ 10^{-15}\,[\Omega_{\rm GW}(f)]^{1/2}\left(\frac{1\,{\rm mHz}}{f}\right)\left(\frac{H_0}{75\ {\rm km\ s^{-1}\ Mpc^{-1}}}\right), \tag{1.18}$$

where H_0 is the present value of Hubble's constant. That this seems to be large in LISA's band is deceptive: we really need to compare this with LISA's instrumental noise, and this is best done over the much narrower bandwidth of the frequency resolution of a 1 yr observation, 3×10^{-8} Hz. Since the noise, being stochastic, scales as the square root of the bandwidth, this gives us the relation

$$\begin{aligned} h_{\rm rms}(f,\ \Delta f = 3\times10^{-8}{\rm Hz}) \quad &= \quad 5.5\times10^{-22}\left[\frac{\Omega_{\rm GW}(f)}{10^{-8}}\right]^{1/2}\left(\frac{1\,{\rm mHz}}{f}\right)^{3/2} \\ &\quad \times\left(\frac{H_0}{75\ {\rm km\ s^{-1}\ Mpc^{-1}}}\right), \end{aligned} \tag{1.19}$$

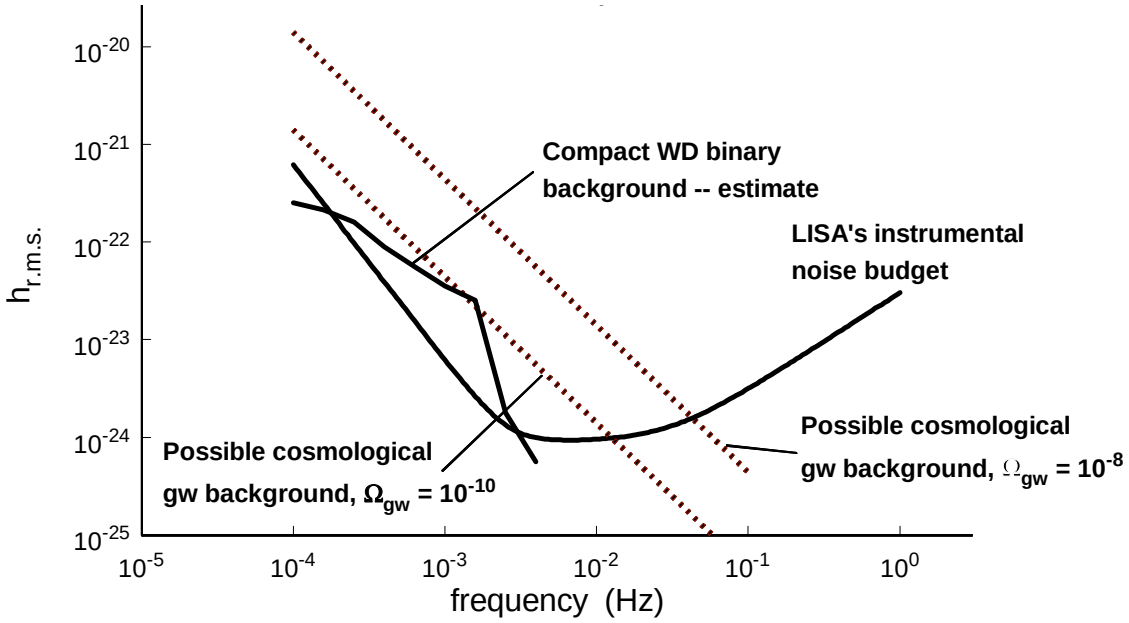

Figure 1.7 *Sensitivity to a random cosmological gravitational wave background*

where we have scaled $\Omega_{\rm GW}$ to a plausible value. This is the $\Omega_{\rm GW} = 10^{-8}$ curve that is plotted in Figure 1.7, assuming $H_0 = 75$ km s^{-1} Mpc^{-1}. Since $\Omega_{\rm GW}$ scales as h^2, curves for other constant values of $\Omega_{\rm GW}$ can be found by simply moving the given curve up or down.

A non-thermal cosmological background of gravitational waves could come from many different sources: density fluctuations produced by cosmic strings or cosmic textures have been much discussed; and there is general agreement that inflation would amplify early quantum fluctuations into a stochastic background. In all of these processes, the typical wavelength for producing gravitational waves is the cosmological horizon size at the time. After that, the waves travel freely and are redshifted by the expansion of the Universe. If we take a typical LISA frequency of 10 mHz today, and extrapolate it back in time to the point where it would have had a wavelength equal to the horizon size, we find that this occurs at a cosmological time of about 10^{-14} s, when the temperature of the Universe was 100 GeV [58]. This is a domain of physics accessible to modern particle accelerators, and it is associated with the electroweak phase transition.

This has two implications: first, if LISA measures a background, it could tell us something about electroweak physics; and second, further fundamental physics research, for example using the LHC at CERN, could make definite predictions about a gravitational wave background in the LISA frequency band.

Many processes that produce a background do not have an intrinsic scale length; when this is the case, one expects a scale-free spectrum, one whose energy density is independent of frequency. Then the curve plotted in Figure 1.7 has the shape of the expected spectrum. One such process is inflation. Since it would have occurred much earlier than the LISA "production time" of 10^{-14} s, the spectrum LISA would see consists of waves that had wavelengths much larger than the horizon size at the end of inflation, and that therefore

had no characteristic length scale. Observations of the microwave background by COBE constrain the time at which inflation occurred, and this in turn constrains the energy density today at LISA frequencies (and, incidentally, at ground-based frequencies as well) to $\Omega_{\rm GW} \leq 8 \times 10^{-14}$ [58].

The most-discussed cosmic gravitational wave background has probably been that produced by cosmic strings. These are defects that could have been left over from a GUT-scale phase transition at a much earlier epoch than the electroweak transition. Therefore, by the LISA production time, the strings would not have had any characteristic length-scale, and the spectrum today would again be essentially scale-free at LISA frequencies, rising at lower frequencies [59]. This spectrum is constrained by present observations of frequency fluctuations in millisecond pulsars. This limit suggests that, at LISA and ground-based frequencies, $\Omega_{\rm GW} \leq 10^{-8}$. This is still an interesting level for LISA, although ground-based detectors are likely to reach this level first.

One example of a process that would produce a spectrum with features in the LISA band is the collision of vacuum bubbles in the early Universe. This could occur at the end of a phase transition that occurred randomly throughout space. The expanding bubbles of the "new" vacuum state collide, and the resulting density discontinuities give off gravitational waves. If the electroweak phase transition produced such bubbles, the spectrum might peak at 0.1 mHz with a density $\Omega_{\rm GW} \sim 3 \times 10^{-7}$ [60]. This would easily be detected by LISA, and it would again be an extremely important and fundamental result. Such radiation from the electroweak transition would not be observable from the ground.

It should be emphasized that the cosmic background of gravitational waves is the least-understood prospective source for LISA. The observational constraints are few, and the predictions of possible spectra depend on relatively simple theoretical models of the early Universe and on toy models of high-energy physics. LISA's frequency band is orders of magnitude different from that which is accessible to ground-based detectors or to pulsar timing experiments, and it is very possible that LISA will find unexpected surprises here. These would give us unparalleled insight into the mechanics of the early Universe.

An interesting feature of LISA's observations of a background is that it can test its isotropy. As LISA rotates, its sensitivity to different directions changes. The low-frequency CWDB background is likely to be concentrated near the galactic plane, so by comparing two 3-month stretches of data LISA should have no difficulty seeing this background and identifying this effect. But even the cosmological background should have a dipole anisotropy caused by the motion of the solar system, just as the cosmic microwave background has. If LISA makes a 3-month observation of this background, then its frequency resolution will be about 10^{-7} Hz, and there will be about 10^5 resolvable frequencies near 10 mHz. Given random fluctuations, the strength of the background at this frequency can be estimated to a precision of something like $\sqrt{N}$, or 0.3 %. Successive periods of 3 months can then be compared to look for changes. While this is not quite precise enough to detect the expected anisotropy of about 0.1% in a single year, if the mission lasts 10 yr then LISA will be getting close to the required level. If the gravitational wave background turned out not to have the same dipole anisotropy as the cosmic microwave background, then cosmological models would have to be drastically revised.

Chapter 2

Different Ways of Detecting Gravitational Waves

2.1 Complementarity of detection on the ground and in space

Astronomical observations of electromagnetic waves cover a range of 20 orders of magnitude in frequency, from ULF radio waves to high-energy gamma-rays. Almost all of these frequencies (except for visible and radio) cannot be detected from the Earth, and therefore it is necessary to place detectors optimised for a particular frequency range (e.g. radio, infrared, ultraviolet, X-ray, gamma-ray) in space.

The situation is similar for gravitational waves. The range of frequencies spanned by ground- and space-based detectors, as shown schematically in Figure 2.1, is comparable to the range from high frequency radio waves up to X-rays. Ground-based detectors will never be sensitive below about 1 Hz, because of terrestrial gravity-gradient noise. A space-based detector is free from such noise and can be made very large, thereby opening the range from 10^{-4} Hz to 1 Hz, where both the most certain and the most exciting gravitational-wave sources radiate most of their power.

The importance of low frequencies is a consequence of Newton's laws. For systems involving solar-mass objects, lower frequencies imply larger orbital radii, and the range down to 10^{-4} Hz includes sources with the typical dimensions of many galactic neutron star binaries, cataclysmic binaries, and some known binaries. These are the most certain sources. For highly relativistic systems, where the orbital velocities approach the speed of light, lower frequencies imply larger masses ($M \propto 1/f$), and the range down to 10^{-4} Hz reaches masses of $10^7\, M_\odot$, typical of the black holes that are believed to exist in the centres of many, if not most, galaxies. Their formation and coalescences could be seen anywhere in the Universe and are among the most exciting of possible sources. Detecting them would test the strong-field limit of gravitational theory and illuminate galaxy formation and quasar models.

For ground-based detectors, on the other hand, their higher frequency range implies that even stellar-mass systems can last only for short durations, so these detectors will mainly search for sporadic short-lived catastrophic events (supernovae, coalescing neutron-star

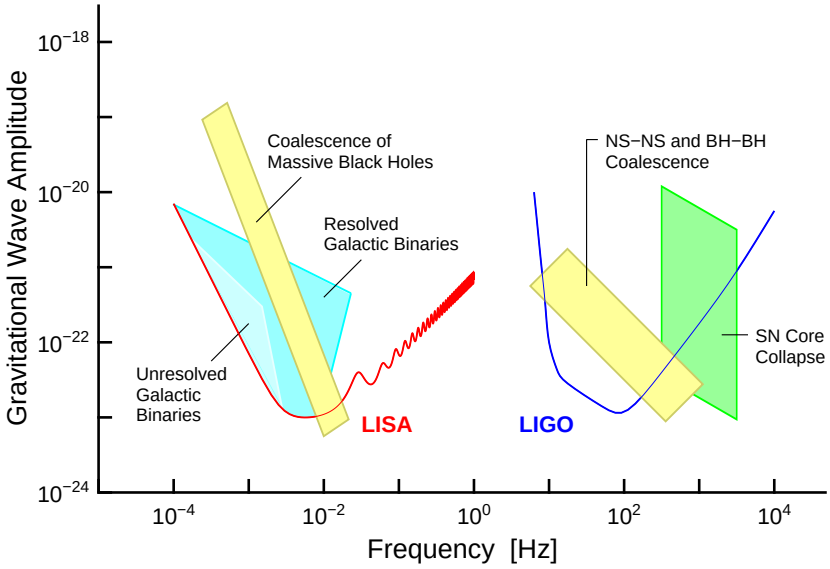

Figure 2.1 *Comparison of frequency range of sources for ground-based and space-based gravitational wave detectors. Only a few typical sources are indicated, ranging in frequency from the* kHz *region of supernovae and final mergers of binary stars down to* mHz *events due to formation and coalescence of supermassive black holes, compact binaries and interacting white dwarf binaries. The sources shown are in two clearly separated regimes: events in the range from, say,* 10 Hz *to several* kHz *(and only these will be detectable with terrestrial antennas), and a low-frequency regime,* 10^{-4} *to* 10^{-1} Hz*, accessible only with a space project. Sensitivities of LISA for periodic sources, and of (the "Advanced") LIGO for burst sources, are indicated.*

binaries). Normally, several detectors are required for directional information. If such events are not detected in the expected way, this will upset the astrophysical models assumed for such systems, but not necessarily contradict gravitation theory.

By contrast, if a space-based interferometer does not detect the gravitational waves from known binaries with the intensity and polarisation predicted by General Relativity, it will undermine the very foundations of gravitational physics. Furthermore, even some highly relativistic events, such as massive black hole coalescences with masses below $10^5\,M_\odot$, last roughly a year or longer. This allows a single space-based detector to provide directional information as it orbits the Sun during the observation.

Both ground- and space-based detectors will also search for a cosmological background of gravitational waves. Since both kinds of detectors have similar energy sensitivities, their different observing frequencies are ideally complementary: observations can supply crucial spectral information.

The space-based interferometer proposal has the full support of the ground-based detector community. Just as it is important to make observations at radio, optical, X-ray, and all other electromagnetic wavelengths, so too is it important to cover different gravitational-wave frequency ranges. Ground-based and space-based observations will therefore complement each other in an essential way.

2.2 Ground-based detectors

The highest frequencies expected for the emission of strong gravitational waves are around 10 kHz because a gravitational wave source cannot emit strongly at periods shorter than the light travel time across its gravitational radius. At frequencies below 1 Hz, observations on the ground are impossible because of an unshieldable background due to Newtonian gravity gradients on the earth. These two frequencies define the limits of the high-frequency band of gravitational radiation, mainly populated by signals from neutron star and stellar mass black hole binaries. This band is the domain of ground-based detectors: laser interferometers and resonant-mass detectors.

2.2.1 Resonant-mass detectors

The history of attempts to detect gravitational waves began in the 1960s with the famous bar experiments of Joseph Weber [61]. A resonant-mass antenna is, in principle, a simple object. It consists of a solid body that during the passage of a gravitational wave gets excited similarly to being struck with a hammer, and then rings like a bell.

The solid body traditionally used to be a cylinder, that is why resonant-mass detectors are usually called bar detectors. But in the future we may see very promising designs in the shape of a sphere or sphere-like object like a truncated icosahedron. The resonant mass is usually made from an aluminum alloy and has a mass of several tons. Occasionally, other materials are used, e.g. silicon, sapphire or niobium.

The first bar detectors were operated at room temperature, but the present generation of bars is operating below liquid-helium temperature. A new generation (NAUTILUS in Frascati and AURIGA in Legnaro) is now operating at a temperature around 100 mK.

Resonant-mass detectors are equipped with transducers that monitor the complex amplitudes of one or several of the bar's vibrational modes. A passing gravitational wave changes these amplitudes due to its frequency content near the normal mode frequencies. Present-day resonant mass antennas are fairly narrowband devices, with bandwidths of only a few Hz around centre-frequencies in the kHz range. With improved transducer designs in the future, we may see the bandwidth improve to 100 Hz or better.

The sensitivities of bar antennas have steadily improved since the first experiments of Joe Weber. Currently we see a network of antennas at Rome, Legnaro, Lousiana State and Perth with best detectors operating with a sensitivity to millisecond duration pulses of $h = 3 \times 10^{-19}$. In the first decade of the next millennium, planned sphere-like detectors operating near the standard quantum limit may reach burst sensitivities below 10^{-21} in the kHz range [62].

2.2.2 Laser Interferometers

Although the seeds of the idea can be found in early papers by Pirani [63] and Gertsenshtein and Pustovoit [64], it was really in the early 1970s that the idea emerged that laser interferometers might have a better chance of detecting gravitational waves, mainly promoted by Weiss [65] and Forward [66].

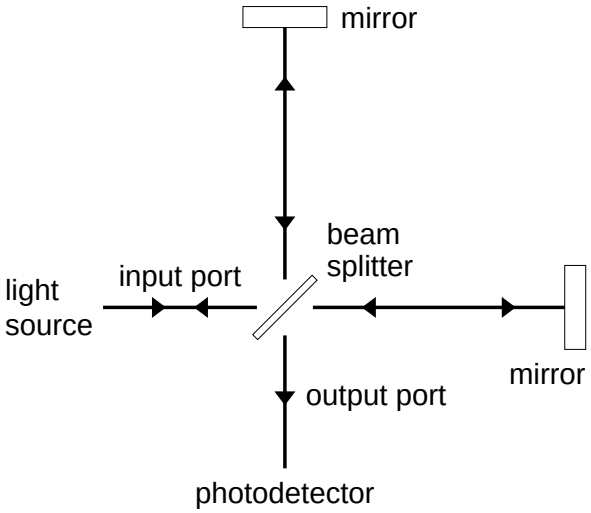

Figure 2.2 *Schematic of a two-arm Michelson interferometer. Interference of the two returning beams on the photodetector gives a measure of their relative phase. Any variation in the mirror distances caused by a passing gravitational wave will modulate this phase signal. By having two arms fed from the same light source, the phase noise inherent to the non-ideal source is the same in each arm. In essence, the interferometry amounts to a differencing of the phases from the light returning along each arm, so the common-mode noise in the light is cancelled. This is the main reason for having two arms in a Michelson interferometer.*

A Michelson interferometer measures the phase difference between two light fields having propagated up and down two perpendicular directions, i.e. essentially the length difference between the two arms (see Figure 2.2). This is the quantity that would be changed by a properly oriented gravitational wave. The phase difference measured can be increased by increasing the armlength, or, equivalently, the interaction time of the light with the gravitational wave, up to an optimum for an interaction time equal to half a gravitational wave period. For a gravitational wave frequency of 100 Hz this corresponds to five milliseconds or an armlength of 750 km. On the ground it is clearly impractical to build such large interferometers, but there are ways to increase the interaction time without increasing the physical armlength beyond reasonable limits. Several variants have been developed, all of them relying on storing and enhancing the laser light, or the gravitational-wave induced sidebands, or both.

The technology and techniques for such interferometers have now been under development for nearly 30 years. Table 2.1 gives an impression of the wide international scope of the interferometer efforts. After pioneering work at MIT, other groups at Munich/Garching, at Glasgow, then Caltech, Paris/Orsay, Pisa, and later in Japan, also entered the scene. Their prototypes range from a few meters up to 30, 40, and even 100 m.

Today, these prototype interferometers are routinely operating at a displacement noise level of the order $10^{-19}\,\mathrm{m}/\sqrt{\mathrm{Hz}}$ over a frequency range from 200 Hz to 1000 Hz, corresponding to an rms gravitational-wave amplitude noise level of $h_{\mathrm{rms}} \approx 10^{-19}$.

Plans for kilometer-size interferometers have been developed for the last 15 years. All of these large-scale projects will use low-noise Nd:YAG lasers (wavelength 1.064 μm), pumped with laser diodes, just as is intended for LISA, which will greatly benefit from their efforts for achieving extreme stability and high overall efficiency.

The US project LIGO calls for *two* facilities at two widely separated sites [67]. Both will house a 4 km interferometer, Hanford an additional 2 km interferometer. At both sites ground-work and construction have been finished, vacuum tests (of the "world's largest

Country: / *Institute:*	**USA** MIT	**USA** Caltech	**GER** MPQ	**GBR** Glasgow	**FRA** CNRS	**ITA** INFN	**JPN** ISAS	**JPN** NAO
Prototypes:								
Start:	1972	1980	1975	1977	1983	1986	1986	1991
Laser:	Ar^+	Ar^+	Ar^+	Ar^+	(Ar^+)	(Ar^+)	Ar^+	YAG
Arm length ℓ*:*	40 m		30 m	10 m	0.5 m		100 m	20 m
Strain sensitivity $\tilde{h}$ $[\mathrm{Hz}^{-\frac{1}{2}}]$ *:*	$1 \cdot 10^{-20}$ 1995		$11 \cdot 10^{-20}$ 1986	$6 \cdot 10^{-20}$ 1992			$8 \cdot 10^{-20}$ 1996	$2 \cdot 10^{-18}$ 1996
Large Interferometric Detectors:								
Planning (start):	1982	1984	1985	1986	1986	1986	1987	1994
Arm length ℓ*:*	4 km 2 km	4 km	600 m		3 km		300 m	
Site (State)	Hanford (WA)	Livingston (LA)	Hannover GER		Pisa ITA		Mitaka JPN	
Cost $(10^6$ US$)$:	292		7		90		15	
Project name:	**LIGO**		**GEO 600**		**VIRGO**		**TAMA 300**	

Table 2.1 *Funded ground-based interferometric gravitational wave detectors: List of prototypes (upper part) and long-baseline projects (lower part).*

vacuum chamber") successfully completed, and installation of optics is to begin in the latter half of 1998.

In the French-Italian project VIRGO, being built near Pisa, an elaborate seismic isolation system will allow this project to measure down to a frequency of 10 Hz or even below [68]. Construction is in full progress.

A British-German collaboration has de-scoped the project of a 3 km antenna to a length of only 600 m: GEO 600 [69]. It will employ advanced optical techniques to make up for the shorter arms. Ground work and construction at the site near Hannover are completed, the vacuum system tested.

In Japan, after a merger of efforts at ISAS and other institutions, construction and vacuum verification of a common 300 m project called TAMA 300 [70] is completed, and first optical tests in single arms have been performed.

Not included in Table 2.1 is the (not yet funded) Australian project of a 500 m detector to be built near Perth. The site would allow later extension to 3 km arms.

LIGO, VIRGO, GEO 600 and TAMA 300 are scheduled to be completed by the end of this century. Observations may begin in 2000 or 2001, although the sensitivity of the first stage detectors may be only marginally sufficient to detect gravitational waves. However, step-by-step improvements will be made, until the network finally reaches the advanced detector sensitivity sometime between 2005 and 2010. At that point, one can be confident that signals will be observed from sources such as supernovae, compact binary coalescences and pulsars, unless something is fundamentally wrong with our current estimates of their strength and distribution.

2.3 Pulsar timing

Man-made gravitational wave detectors operate by detecting the effect of gravitational waves on the apparatus. It is also possible to detect gravitational waves by observing their effect on electromagnetic waves as they travel to us from astronomical objects. Such methods of detection are like "one-arm interferometers" – the second arm is not needed if there is another way to provide a reference clock stable enough to sense the changes in propagation time produced by gravitational waves.

Pulsar timing makes use of the fact that the pulsar is a very steady clock. If we have a clock on the Earth that is as stable as the pulsar, then irregularities in the arrival times of pulses that are larger than expected from the two "clocks" can be attributed to external disturbances, and in particular possibly to gravitational waves. Since the physics near a pulsar is poorly known, it might be difficult to prove that observed irregularities are caused by gravitational waves. But where irregularities are absent, this provides an upper limit to the gravitational wave field. This is how such observations have been used so far.

All pulsars slow down, and a few have shown systematic changes in the slowing down rate. Therefore, it is safer to use random irregularities in the pulsar rate as the detection criterion, rather than systematic changes. Such random irregularities set limits on random gravitational waves: the stochastic background.

The arrival times of individual pulses from most pulsars can be very irregular. Pulsar periods are stable only when averaged over considerable times. The longer the averaging period, the smaller are the effects of this intrinsic irregularity. Therefore, pulsar timing is used to set limits on random gravitational waves whose period is of the same order as the total time the pulsar has been observed, from its discovery to the present epoch. Millisecond pulsars seem to be the most stable over these long periods, and a number of them are being used for these observations.

The best limits come from the first discovered millisecond pulsar, PSR B1937+21. At a frequency of approximately $1/(10\,\mathrm{yr})$ the pulsar sets an upper limit on the energy density of the gravitational wave background of $\Omega_{\mathrm{GW}} < 10^{-7}$ [71] (see Section 1.2.3). This is in an ultra-low frequency range that is 10^5 times lower than the LISA band and 10^{10} times lower than the ground-based band. If one believes a theoretical prediction of the spectrum of a cosmic gravitational wave background, then one can extrapolate this limit to the other bands. But this may be naive, and it is probably wiser to regard observations in the higher-frequency bands as independent searches for a background.

More-recently discovered millisecond pulsars are also being monitored and will soon allow these limits to be strengthened. If irregularities are seen in all of them at the same level, and if these are independent of the radio frequency used for the observations, then that will be strong evidence that gravitational waves are indeed responsible.

These observations have the potential of being extended to higher frequencies by directly cross-correlating the data of two pulsars. In this way one might detect a correlated component caused by gravitational waves passing the Earth at the moment of reception of the radio signals from the two pulsars. Higher frequencies are accessible because the higher intrinsic timing noise is reduced by the cross-correlation. Again, seeing the effect in many pairs of pulsars independently of the radio frequency would be strong evidence for gravitational waves.

2.4 Spacecraft tracking

Precise, multi-frequency transponding of microwave signals from interplanetary probes, such as the ULYSSES, GALILEO and CASSINI spacecraft, can set upper limits on low-frequency gravitational waves. These appear as irregularities in the time-of-communication residuals after the orbit of the spacecraft has been fitted. The irregularities have a particular signature. Searches for gravitational waves have produced only upper limits so far, but this is not surprising: their sensitivity is far short of predicted wave amplitudes. This technique is inexpensive and well worth pursuing, but will be limited for the forseeable future by some combination of measurement noise, the stability of the frequency standards, and the uncorrected parts of the fluctuations in propagation delays due to the interplanetary plasma and the Earth's atmosphere. Consequently, it is unlikely that this method will realise an *rms* strain sensitivity much better than 10^{-17}, which is six orders of magnitude worse than that of a space-based interferometer.

2.5 Space interferometer

The LISA measurement concept is, in essence, a space-borne implementation of a Michelson interferometer for the purpose of measuring the fluctuations in the distance between widely separated mirrors. There is, however, a fundamental distinction between LISA and the ground-based interferometers: LISA will search for the distinctively *low-frequency* (milli-hertz) gravitational waves (Chapter 1) which will probably *never* be detectable by any terrestrial detectors — existing or planned — because of unshieldable gravitational disturbances. These disturbances are due to the motion of bulk matter in the Earth and the atmospere which will pull gravitationally on the interferometer mirrors, producing undesirable phase shifts. Since gravity can not be shielded, and there does not seem to be a feasible way of independently measuring the gravitational effects of seismicity, these effects impose a strict lower limit on the gravitational wave frequencies observable on Earth. With its wide separation from Earth, LISA is completely free from these terrestrial disturbances.

2.6 Early concepts for a laser interferometer in space

The earliest concept for a laser gravitational wave detector in space appears to have been a Shuttle-launched monolithic Gravity Wave Interferometer (GWI). R. Weiss was informed in 1974 about NASA studies of producing such a device with up to 1 km arm lengths by using an orbiting machine to extrude aluminium beams. A NASA publication in March 1978 [72] described an interferometer with a total launch mass of 16.4 t, which included four 1000 kg test masses at the ends of a cross-shaped device (see Figure 2.3). The GWI's sensitivity was calculated as $\delta l/l = 10^{-21}$ in the frequency range from 10^{-1} to 10^2 Hz. The total cost of the project was estimated at that time to be $ 49.5 M.

The idea of a monolithic space gravitational wave interferometer presented to Weiss started discussions in 1974 with P.L. Bender, R.W.P. Drever and J.E. Faller of a much larger space interferometer. The approach considered was to send laser beams between

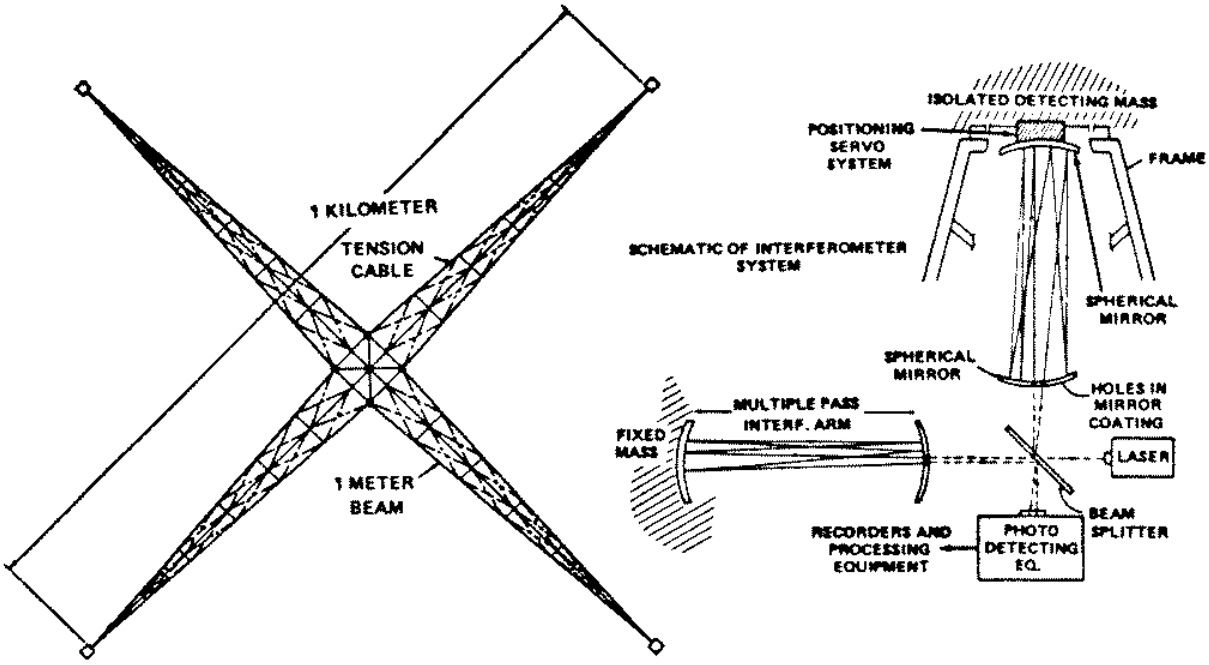

Figure 2.3 *Conceptual design of the Gravitational Wave Interferometer (GWI). Left: GWI structure after deployment in low-Earth orbit. Right: Schematic of the interferometer system.*

shielded proof masses in three widely separated drag-free spacecraft, using laser transponders rather than mirrors at the ends of the interferometer arms to greatly reduce the shot noise. Both, the separated spacecraft and monolithic approaches were mentioned in a 1976 committee report by Weiss *et al.* [73] and described by Weiss in a 1979 paper [74]. A more complete discussion of a possible separated spacecraft interferometer with 1×10^6 km arm lengths was given by Decher *et al.* [75] in 1980, but it required frequent major adjustments to the orbit of one spacecraft and had other disadvantages.

The first suggestion of a mission using spacecraft orbits similar to those planned for LISA was made in 1981 by Faller and Bender [76, 77]. It included the appraoch suggested by Faller of using the apparent changes in length of one arm to determine the laser phase noise, and then correcting the arm length difference based on the measured laser phase noise. A full description of this concept, then tentatively named the Laser Antenna for Gravitational-radiation Observation in Space (LAGOS), was given by Faller [78].

LAGOS had already many elements of the present-day LISA mission. It consisted of three drag-free satellites, one master spacecraft in the center and two auxilliary spacecraft at a distance of 10^6 km from the central spacecraft, forming a triangle with an angle of 120° at the central spacecraft (see Figure 2.4). This configuration would be placed in a circular heliocentric orbit at 1 AU from the Sun, about 4×10^7 km (15°) ahead of the Earth. With 100 mW laser power and 50 cm diameter telescopes for transmitting and receiving the laser beams a strain sensitivity of $\delta l/l = 10^{-19}$ over the frequency range from 10^{-4} to 10^{-1} Hz appeared feasible. The proof masses in the spacecraft were thought to be cylinders of about 15 cm in length and diameter, freely floating inside a housing of 25 cm. Displacements of the housing by 10 μm with respect to the proof masses would

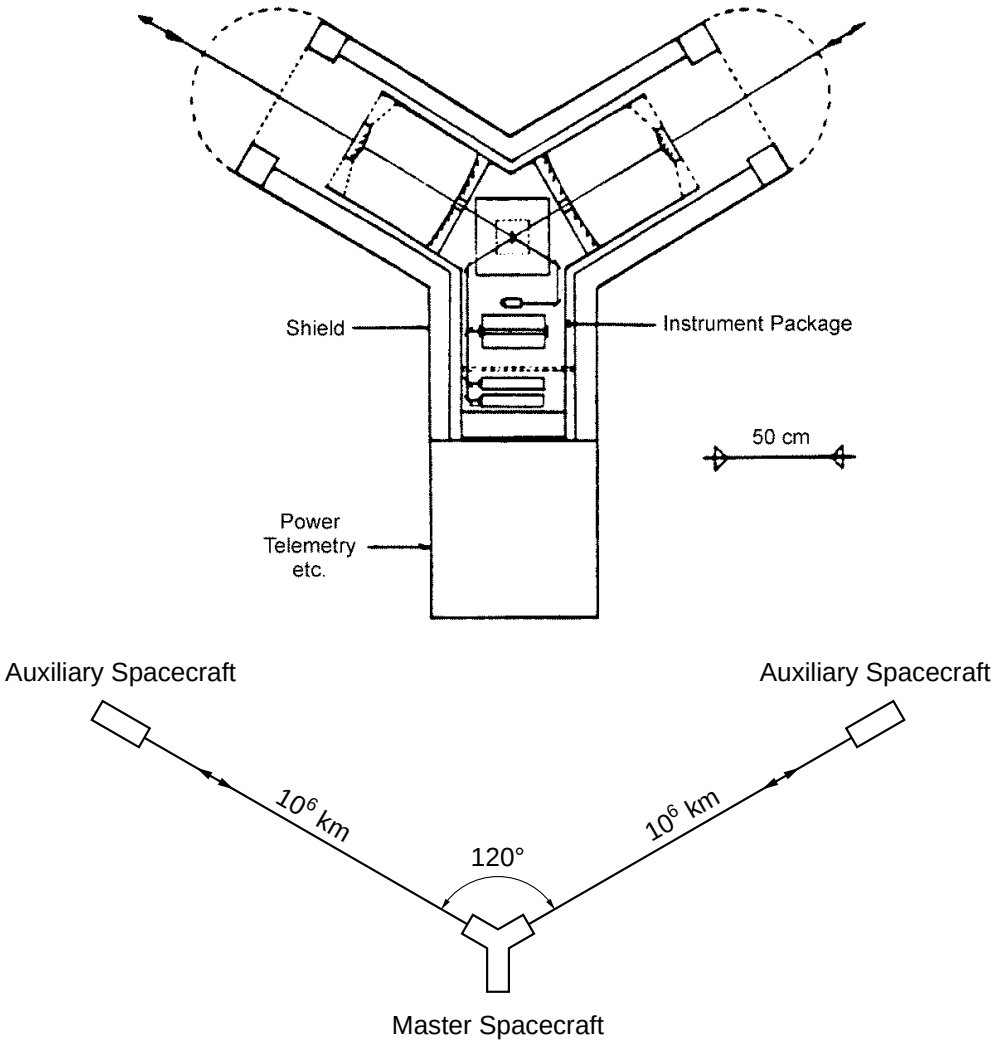

Figure 2.4 *Early version of the LAGOS concept. Top: Central spacecraft. Bottom: The configuration of three drag-free spacecraft in interplanetary space.*

be sensed optically, and the signals could be used to servo-control the position of the spacecraft against perturbations.

2.7 Heliocentric versus geocentric options

An alternate gravitational wave mission that uses geocentric rather than heliocentric orbits for the spacecraft has been suggested by R.W. Hellings. An earlier version of this mission called SAGITTARIUS was proposed to ESA in 1993 as a candidate for the M3 mission. A similar mission called OMEGA was proposed to NASA in 1996, and is expected to be proposed again in 1998 .

Our understanding is that the 1996 OMEGA proposal involved six spacecraft in retrograde coplanar geocentric orbits with semi-major axes of roughly 600 000 km and periods

of about 53 days. Two spacecraft would be close together at each corner of an equilateral triangle, as for the LISA Cornerstone proposal, but the triangle would be about 1 000 000 km on a side instead of 5 000 000 km. An inclination of 11° to the ecliptic has been mentioned for the orbits. The proposed telescope diameter was 15 cm, but we will assume a more favourable diameter of 30 cm diameter, as in LISA, for a comparison of the heliocentric and geocentric orbit options.

There are three main advantages expected for the geocentric option. One is that the propulsion requirements after the initial launch for placing the spacecraft in the desired orbits are much less. This would cut much of the cost of the interplanetary propulsion modules for LISA, and would reduce the launch vehicle cost. The second advantage is a simpler and less expensive telecommunications system for sending down the data. An S-band system with small ground antennas could be used instead of an X-band system with a large ground antenna, and the bandwidth could be much larger. This means that less or no preprocessing and data compression would be needed on the spacecraft. Finally, the time necessary to put the spacecraft in their final orbits would be considerably less than the roughly one year planned for LISA.

It unfortunately is difficult to estimate reliabily the cost savings for a geocentric mission compared with a heliocentric mission. The ESA study of both types of mission during the first half of the M3 study led to an estimated cost difference of only about 15 %, and the LISA mission was chosen for consideration in the rest of the study. However, the same launch vehicle was assumed for both types of mission, so the actual savings could be higher. Our present rough estimate is perhaps 20 % for the cost difference.

In terms of expected scientific results, a major question is the error budget allowed for the inertial sensor. For LISA, the currently adopted requirement is $3 \times 10^{-15}\,\mathrm{m\,s^{-2}}/\sqrt{\mathrm{Hz}}$ from 0.1 to 10 mHz for an individual sensor. If a geocentric mission had the same requirement, the overall interferometer sensitivity below about 3 mHz would be five times worse than for LISA. In addition, the cross-over point between mainly inertial-sensor noise and mainly distance-measurement noise would move up from 3 to about 7 mHz. If our present estimate of the confusion-noise level due to unresolved galactic and extragalactic binaries is correct, the loss in instrumental sensitivity would be serious for several types of signals that are of high scientific importance. In addition, the potential information on some types of galactic binaries would be degraded. The sensitivity at frequencies above roughly 30 mHz would be improved for the geocentric mission because of the baseline staying shorter than the gravitational wavelength up to higher frequencies. However, there are no sources expected at present for which the frequency region from 30 mHz to the top of the LISA band at 1 Hz would be important for detection.

If instead a factor five lower noise level is required for the inertial sensors in a geocentric mission, then the question becomes how difficult it is to meet that requirement. While it is possible that a lower noise level can be achieved if several of the potential noise sources are on the lower end of their potential ranges, it appears difficult at present to design the inertial sensors in such a way as to be sure of this. Thus, we regard a substantially tighter inertial sensor requirement as a major technological hurdle that the mission would have to overcome.

A second important technological issue for a geocentric mission is the need to keep sunlight from getting into the telescopes when the optical axes point close to the sun. With six

telescopes and 11° inclination of the orbits to the ecliptic, the optical axis of one of the telescopes will pass within 15° of the sun roughly 40 % of the time. Earlier theoretical studies of this problem indicated that a combination of multilayer UV and IR reflecting filters plus a narrowband optical transmitting filter could reduce incident sunlight by a sufficient amount, but such filters have not been designed in detail or constructed. The problem of constructing such filters appears to be made even more difficult if they need to be 30 cm in diameter, rather than the 15 cm diameter assumed in the earlier studies.

A third technological issue concerns the need for generating an extremely stable clock frequency for use in cancelling out the Doppler shifts in the observed signals. For the geocentric mission, the Doppler shifts vary with about 27 day period between plus and minus 300 MHz. This is more than two orders of magnitude larger than the difference in Doppler shifts for the two preferred arms of the LISA interferometer, for which the initial orbit conditions are chosen to keep the Doppler shifts low, and a factor 20 higher than for the third arm in LISA. Thus, while LISA can determine the phase noise in its Ultra Stable Oscillators (USOs) to sufficient accuracy by fairly simple means, as discussed later, this task is considerably more difficult for the geocentric mission.

For LISA, roughly 200 MHz sidebands generated from the USO are modulated onto the laser beams, with roughly 10 % of the power in the sidebands. Measurements of phase jitter in the beats between the sidetones and the carrier after transmission over an interferometer arm determine the phase noise in the USO. However, for the geocentric mission, two separate lasers with a difference frequency of perhaps 5 GHz probably would need to be used. Thus, the number of lasers that must survive in at least four of the spacecraft is doubled, since the accuracy of the results would be very strongly degraded if accurate corrections for the Doppler shifts were not available. If optical modulators with 5 GHz or higher frequencies and substantial sideband power are used instead of two separate lasers, the efficiency and long term reliability of the modulators are much more significant technological challenges than for the roughly 200 MHz modulators needed for LISA.

In view of the three important technological issues discussed above and the loss in sensitivity for a geocentric mission if tighter requirements are not imposed on the inertial sensors, we believe that the LISA approach of using heliocentric orbits should be preferred. Cost is clearly a very important issue, but we expect that the main cost drivers for a gravitational-wave mission will continue to be the design and construction of the individual spacecraft and payloads, and in insuring the reliability of all of the systems that have to work simultaneously in at least four of the six optical assemblies.

2.8 The LISA concept

2.8.1 Overview

Conceptually, the idea of implementing an interferometer in space is straightforward, but the practical realisation requires an intricate blend of optical technology, spacecraft engineering and control. For a start, the interferometer mirrors can not simply float freely in space — they must be contained inside spacecraft. Nonetheless, they can be arranged to be floating almost freely inside the spacecraft, protected from external disturbances by

the spacecraft walls. As long as the spacecraft do not disturb the mirrors, then, ideally, only gravitational waves would perturb their relative motion. "Drag-free control" can be employed to ensure that the spacecraft always remain centred on the mirrors.

A Michelson interferometer in space could be realised using three spacecraft: one at the "corner" to house the light source, beam splitter, and detector, plus one at each "end" to house the remote mirrors. But for practical reasons the actual implementation is slightly different. Each spacecraft contains two telescopes, each one pointing at one of the distant spacecraft at the other two corners of the triangle, and two lasers, one per telescope. Each laser is phase-locked either to its companion on the same spacecraft, forming the equivalent of a beam-splitter, or to the incoming light from the distant spacecraft, forming the equivalent of an amplifying mirror, or light transponder. Together the three spacecraft function as a Michelson interferometer with an additional redundant third arm. (Figure 2.5). Each spacecraft is located at the vertex of a large triangle whose sides measure

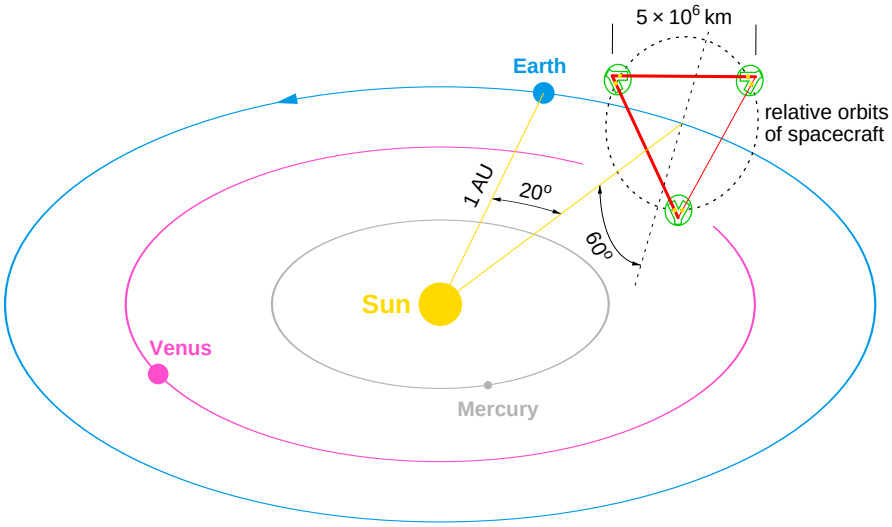

Figure 2.5 *Three spacecraft in a triangle, with one at each vertex.*

5×10^6 km in length. This arm length has been chosen to optimise the sensitivity of LISA at the frequencies of known and expected sources. A factor of 2 increase may be desirable. However, an arm length increase beyond that would begin to compromise the high-frequency sensitivity when the light in the arms experiences more than half of the gravitational wave period. An interferometer shorter than 5×10^6 km would begin to lose the interesting low-frequency massive blackhole sources. It would give less scientific information but would not be any easier to build or operate because the spacecraft and the interferometry would be essentially the same.

Each spacecraft is actually in its own orbit around the Sun. The three individual orbits have their inclinations and eccentricities arranged such that, relative to each other, the spacecraft rotate on a circle 'drawn through' the vertices of the giant triangle which is tilted at 60° with respect to the ecliptic. With this special choice of orbits, the triangular geometry of the interferometer is largely maintained throughout the mission. The centre of the triangle is located on the ecliptic — 20° behind the Earth — and follows the Earth on its orbit around the Sun. Ideally, the constellation should be as far from Earth as

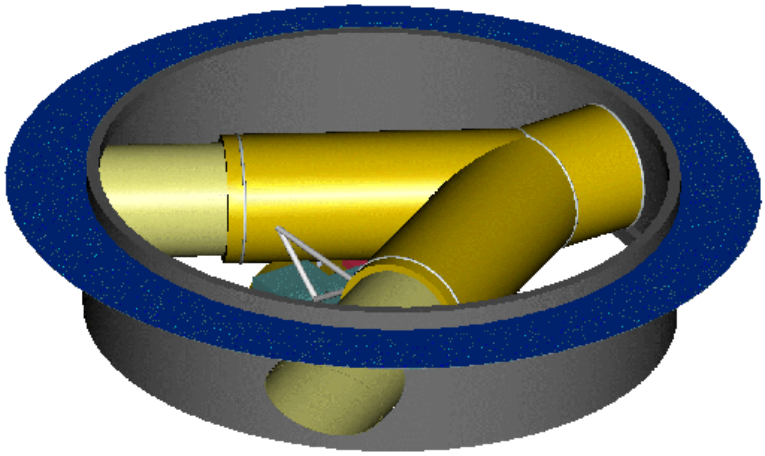

Figure 2.6 *One of the three identical LISA spacecraft. The main structure is a ring with a diameter of* 1.8 m, *and a height of* 0.48 m, *made from graphite-epoxy for low thermal expansion. A lid on top of the spacecraft is removed to allow view at the* Y*-shaped thermal shield encasing the two payload arms.*

possible in order to minimise gravitational disturbances. The choice of 20° is a practical compromise based on launch vehicle and telemetry capabilities.

The once-per-year orbital rotation of the LISA constellation around the Sun provides the instrument with angular resolution, i.e. the ability to pin-point the particular direction to a source. An interferometer is rather omnidirectional in its response to gravitational waves. In one sense this is advantageous — it means that more sources can be detected at any one time — but it has the disadvantage that the antenna cannot be "aimed" at a particular location in space. For a given source direction, the orbital motion of the interferometer Doppler-shifts the signal, and also affects the observed amplitude. By measuring these effects the angular position can thus be determined (see Section 4.4.2). This is analogous to the technique used by radio astronomers to determine pulsar locations.

It is expected that the strongest LISA sources (from very distant supermassive black holes) should be resolvable to better than an arcminute; and even the weaker sources (galactic binaries) should be positioned to within one degree throughout the entire galaxy.

A LISA spacecraft is shown in Figure 2.6. Each spacecraft has two 1 W lasers (actually four, two for redundancy), and two identical payload assemblies, each comprising a two-mirror telescope for sending and receiving light, and an optical bench which is a mechanically-stable structure on which various sensitive optical components are mounted. An optical assembly is shown in Figure 3.2. The mirrors enclosed in each spacecraft are actually 40 mm gold-platinum cubes (also referred to as the 'proof masses'). Each one is located inside a titanium vacuum can at the centre of the respective optical bench. Quartz windows allow access for the laser light.

Within the corner spacecraft, one laser is the 'master', and a fraction of its light (10 mW) is bounced off the back surface of its cube, and used as a reference to 'slave' the other local laser. In this way, the main ($\sim$ 1 W) beams going out along each arm can be considered as having originated from a single laser.

The light sent out along an arm is received by the end spacecraft telescope, bounced off

its cube, then amplified using its local laser, in such a way as to maintain the phase of the incoming light. The amplified light is then sent to the corner spacecraft. Amplification at the end spacecraft is required due to divergence of the beam over the very large distances. Even though each outgoing beam is extremely narrow — a few micro radians — it is about 20 km wide when it reaches the distant spacecraft. This diffraction effect, together with unavoidable optical losses, means that only a small fraction of the original output power ($\sim 10^{-10}$) finally reaches the end diode. If this was simply reflected and sent all the way back, only about 200 photons per hour would reach the corner diode after the round-trip. The phase-signals they carry would be swamped by shot noise, the quantum-mechanical fluctuations in the arrival times of the photons. The amplification brings the number back up to over 10^8 photons per second — which makes the signal detection straightforward using standard photodiodes. The phase precision requirement for this measurement is seven orders of magnitude less demanding than is routinely achieved (at higher frequencies) in ground-based prototype interferometers ([79, 80, 81]).

The resulting round-trip journey from the corner to the end and back, defines one arm of the large interferometer. On its return to the corner spacecraft, the incoming light is bounced off the cube and then mixed with a fraction of the outgoing light on a sensitive photodetector, where interference is detected. The resulting brightness variations contain the phase-shift information for one arm of the interferometer. This signal is then compared (in software on the on-board computer) with the corresponding signals from the other two arms, and some preliminary data processing is done. The results are then transmitted to Earth by radio link.

The LISA spacecraft must be designed to minimise the total mass and required power. Preliminary results yield a mass, per spacecraft, of 200 kg, and an operational power requirement, per spacecraft, of 150 W (see Chapter 7).

2.8.2 Lasers

Lasers have extremely narrow beams that can survive long journeys through space. In addition, they are very stable in frequency (and phase) which is crucial to interferometry since phase "noise" appears just like gravitational waves. Furthermore, the infrared light has a frequency of 3×10^{14} Hz which renders it immune from refraction caused by the charged particles (plasma) which permeate interplanetary space.

The lasers for LISA must deliver sufficient power at high efficiency, as well as being compact, stable (in frequency and amplitude), and reliable. The plan is to use solid-state diode-pumped monolithic miniature Nd:YAG ring lasers which generate a continuous 1 W infra-red beam with a wavelength of 1.064 μm.

2.8.3 Drag-free and attitude control

An essential task of the spacecraft is to protect the mirrors from any disturbances which could jostle them around and create phase-signals that appear as gravitational waves. For example, consider the momentum of the light from the Sun which amounts to an average pressure of about $5 \times 10^{-6}\,\mathrm{N/m^2}$. The internal dynamics of the Sun lead to small variations — less than one percent — in this photon pressure, which occur at the low

frequencies within LISA's range of interest. Although this variable photon pressure may seem rather small, if it were allowed to act on the cubical mirrors, the resulting motion would be 10^4 imes larger than the tiny motions due to gravitational waves that LISA is looking for.

By simply "wrapping a spacecraft around each one", the cubes are isolated from the solar pressure — but this is not the complete picture. When the solar pressure blows on the surface of the spacecraft, it will move relative to the freely-floating cube. Left alone, this motion would build up to unacceptable levels — in the extreme case, the cube would eventually "hit the wall". To stop this from happening, the relative motion can be measured very precisely by monitoring the change in electrical capacitance between the cube and electrodes mounted on the spacecraft. This measurement is then converted into a force-command which instructs thrusters mounted on the outer structure of the spacecraft, to fire against the solar pressure and keep the spacecraft centred on the cube.

This concept is, for historical reasons, known as "drag-free control", since it was originally invented in the 1960's to shield Earth-orbiting satellites from the aerodynamic drag due to the residual atmospheric gases. The method was first demonstrated on the TRIAD spacecraft, flown by the US Navy in 1972, where the drag-free controller designed at Stanford University in collaboration with the Johns Hopkins Applied Physics Laboratory, was effective in reducing the effects of atmospheric drag by a factor of 10^3. Since then, the technique has undergone continued development, most notably for use on NASA's Gravity Probe B mission, which is the proposed space experiment to search for the relativistic precessions of gyroscopes orbiting the Earth.

The thrusters used on conventional spacecraft are far too powerful for LISA. The drag-free system only needs to develop a force of a few micro-newtons. Furthermore, the delivered force must be smoothly controllable so that the varying disturbance forces can be matched without introducing a further disturbance from the thrust system itself. Surprisingly, it is not a trivial task to build a thruster which generates such a small force and yet operates smoothly and does not consume too much power. By good fortune, ESA has been developing them for years, as an alternative to hydrazine rockets for station-keeping of communication satellites.

They are called FEEPs, for Field Emission Electric Propulsion. They operate by accelerating ions in an electric field, and ejecting them to develop the thrust. They are decribed in Section 7.3 .

2.8.4 Ultrastable structures

The small variations in the intensity of sunlight will cause fluctuations in the heat-load applied to the spacecraft. This could lead to thermal gradients across the optical bench, which would upset the stability of the laser cavity. To obtain the required thermal stability, most structural elements are made from carbon-epoxy which has a thermal expansion coefficient of 4×10^{-7}/K and the optical bench is made from ULE, which has a temperature coefficient at least a factor 4 lower over the possible temperature range of the LISA payload. Furthermore, low emissivity coatings are used on most surfaces inside the spacecraft and a thermal shield surrounds the payload cylinder, in order to provide isolation from the temperature variations of the spacecraft skin that is exposed to the Sun. These shields

are only effective against heat fluctuations faster than a few hours to half a day. The slower variations will get through, thus making the sensitivity of LISA deteriorate rapidly below roughly 10^{-4} Hz. The use of carbon-epoxy structures also minimises any thermally-induced mechanical distortions which could produce physical changes in the optical path-length, as well as local gravitational disturbances on the mirror-cubes.

Chapter 3

Experiment Description

3.1 The interferometer

3.1.1 Introduction

When a gravitational wave passes through the plane of the LISA antenna it can be regarded as changing the geometry of the antenna. The precise length of each arm is defined by the distance between the front faces of proof masses positioned inside the three drag free spacecraft. The changes in proof-mass separations are determined by measuring the phase delays for laser beams which have traversed the arms of the interferometer. Due to the wide spread of even a well collimated laser beam over the arm length of 5×10^6 km, the beam cannot simply be reflected at the far spacecraft. Rather, the beams are 'amplified' with the help of a laser at each craft. So the interferometry is done by comparing the phase of an infra-red laser beam being transmitted out to a far mass with that of the beam transponded back.

In this section, we discuss the layout of the optical system, the performance requirements it must meet and the current plans for measuring the phase of the various heterodyne signals. In Section 4.3 we explain in more detail the planned methods for correcting for the laser phase noise and for removing the effects of clock noise.

To describe the method for measuring the distance changes, it is useful to have a nomenclature for referring to the different spacecraft, optical benches, and arms. The three spacecraft (S/C) are labelled A, B and C, and each S/C contains two optical benches, labelled A1, A2, B1, B2 and C1, C2. The arms of the interferometer are defined between the optical benches, *e.g.* arm 1 is between optical benches A1 and C2. The whole nomenclature is shown in figure 3.1. Note that all designations progress counterclockwise around the triangle.

The laser associated with optical bench A1 will serve as the master laser for the whole system and will be locked to an on-board reference cavity. All the other lasers in the system will be phase locked to this master laser. The lasers on a spacecraft can thus be considered as essentially identical and the three spacecraft can thus be thought of as forming a Michelson interferometer with an extra arm. Signal information from the other two S/C will be sent back to S/C A by modulation put on the laser beams travelling

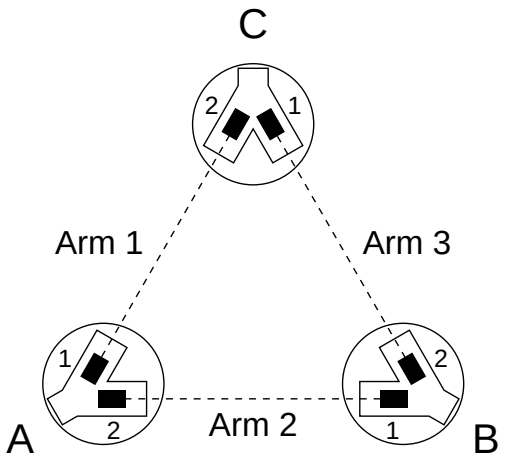

Figure 3.1 *Schematic diagram of the layout of the LISA interferometer, showing the labeling scheme adopted.*

between the spacecraft. This information is then used in S/C A to correct for laser phase noise and to determine the gravitational wave signal.

3.1.2 Phase locking and heterodyne detection

One spacecraft is designated as the master craft (S/C A) and one laser (laser A1) in this spacecraft is locked to its reference cavity. The other laser (laser A2) in this craft is offset locked to laser A1. Laser A1 points out to the spacecraft (C) at another vertex of the triangle and the relevant laser in that craft (laser C2) is offset locked to the incoming light from laser A1. Similarly laser A2 points to the remaining spacecraft (B) and laser B1 in that craft is offset locked to laser A2. Laser B2 is offset locked to laser B1 in the same space craft and laser C1 is offset locked to laser C2.

The offset frequencies, all different and around 10 kHz, for the locking are provided by numerically programmed oscillators (NPROs) on each spacecraft driven from a USO.

We assume that the spacecraft orbits are chosen so that variations in arm length for arms 1 and 2 remain fairly small without orbit adjustments over periods of several months or longer. The phases of the beat signals over the interferometric arms are determined in all three spacecraft by means of multiple input phase comparison units, (*e.g.* modified Turbostar GPS receivers from Allen Osborne Associates Inc.) at time intervals of perhaps 10 ms as discussed later. The results are then smoothed and sampled at a rate of about 0.5/s and the results from spacecraft B and C are telemetred back to spacecraft A suitable modulation of a carrier ($\sim$ 200 MHz) imposed on the laser light on each craft by the phase modulator on each optical bench. The necessary bit rate is approximately 100 bits/s. The data collected on craft A are processed on-board to essentially remove the effects of laser phase noise and of noise associated with the USOs in the system.

3.1.3 Interferometric layout

Figure 3.2 shows the payload for one of the three spacecraft. The payload consists of two identical assemblies each containing a proof mass, optical bench and telescope. The two

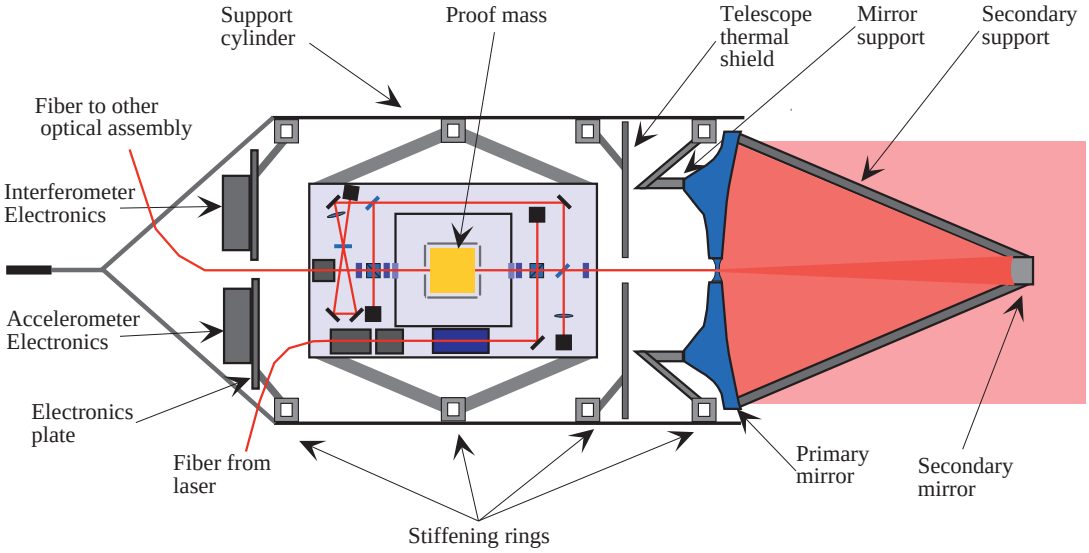

Figure 3.2 *The payload assembly, two identical structures joined by a flexure at their base (see Figure 7.2). Each structure consists of a thermal shield from which are mounted: the 30 cm transmit/receive telescope; a disk shaped thermal shield; the optical bench with laser-injection, cavity for laser stabilisation, beam-shaping optics, photodetectors, and drag-free accelerometer (containing the interferometer "mirror"); a preamplifier disk which carries the accelerometer preamplifiers, the USO and the small steerable mirror for the laser-link between the two optical benches.*

assemblies are joined at the junction of the 'Y' by a flexure. The front of each assembly is mounted from the thermal shield by an adjustable strut, allowing the angle between the two telesopes to be adjusted. By varying the length of this strut and the orientation of the spacecraft the pointing of each telescope may independently optimised. At the rear of each optical bench is a steerable mirror to direct light from one optical bench to the other.

The optical bench. The main optical components are located on an 'optical bench', containing the laser beam injection, detection and beam shaping optics, and the drag-free sensor (or "accelerometer"). The proof mass of the drag-free sensor acts as the mirror at the end of the interferometer arm. The bench consists of a solid ULE plate to which all components are rigidly attached. The components are shown schematically in Figure 3.3. Most components on this structure are passive. Exceptions are a motorised positioner for fibre selection and focusing, photodiodes for signal detection and a phase modulator that allows transfer of information between craft. Light from the laser is delivered to the optical bench by a single-mode fibre. A second fibre coupled to the back-up laser is also provided and may be selected if required.

About 1 mW is split off the main light beam to serve as the local reference for the heterodyne measurement of the phase of the transponded beam returning from the far spacecraft. This splitting is performed by the finite transmission of the polarising beamsplitter in front of the main mirror. Also, in each craft, a few mW is split off and directed towards

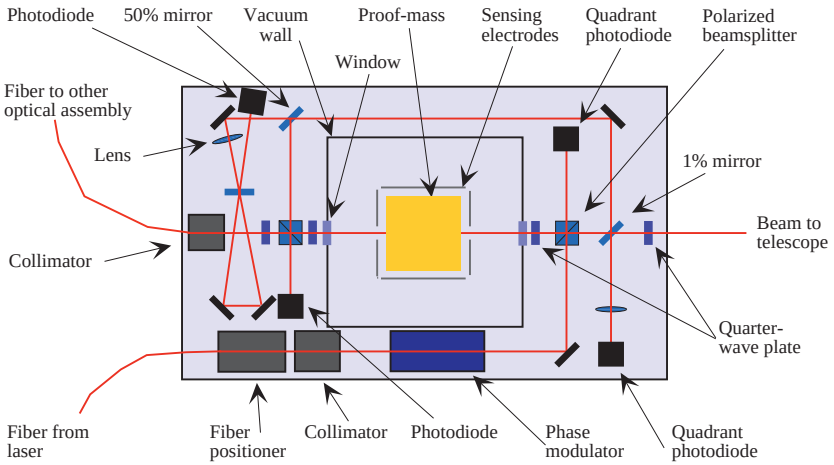

Figure 3.3 *Diagram of the optical bench. The chosen light path renders the measurement insensitive to movement on the spacecraft. The light from the local laser passes through a collimator, a phase modulator and a polarizing beamsplitter to the expanding telescope. The light beam received by the telescope from the distant spacecraft first gets reflected at the proof mass and then interferes with a small fraction of the local laser light at a (quadrant) photodiode (upper right). The diode in the lower left senses the signal for the phase locking between the two lasers at the same spacecraft. The diode in the upper left locks the laser to the reference cavity and the quadrant diode in the lower right is used in pointing the spacecraft.*

a triangular cavity. This cavity is used as a frequency reference in the master craft, with those in the other craft being available for backup purposes.

The incoming light from the telescope is reflected off the proof mass and superimposed with the local laser on the phase measuring diode. An optical isolating arrangement consisting of a polarising beamsplitter and a quarter-wave plate is used to allow the required transmission, reception and phase comparison functions to be carried out in a compact way. On the two optical benches in a spacecraft a small fraction (100 μW) of the laser light is reflected off the back of the proof mass and sent to the other optical bench for phase-comparison via the steerable aft-mirror of 1 cm diameter. This mirror is servoed using the signal from an auxiliary quadrant photodiode which senses both the phase difference between the two beams and the direction of the incoming beam. By bouncing the laser beams off the proof mass in the manner described, the interferometric measurement of proof-mass position is, to first order, unaffected by motion of the surrounding spacecraft. This allows a relaxation of its relative motion specification (though the requirement on proof-mass residual motion with respect to inertial space remains unchanged).

Telescope assembly. The receiving and transmitting telescope is a Cassegrain system with integral matching lens mounted from the payload support cylinder and protected by a thermal shield. The primary mirror is a double-arch light-weight ultra-low expansion (ULE) design with a diameter of 30 cm. The mirrors are aspherics and need careful positioning. For more details see Section 5.8.

3.1.4 System requirements

Laser power and shot noise. To attain the desired gravitational wave sensitivity the system must keep the noise in measuring the differences in round trip path length between two arms below $40 \times 10^{-12}\,\mathrm{m}/\sqrt{\mathrm{Hz}}$, over a frequency range from 10^{-3} to 10^{-1} Hz. A number of noise sources limit the performance, as will be seen in the noise budget given in Section 4.2. However the fundamental, and most significant, noise source will be due to photoelectron shot noise in the detected photocurrents. Consideration of the noise budget suggests that the limitation due to photoelectron shot noise in each detector should not exceed about $10 \times 10^{-12}\,\mathrm{m}/\sqrt{\mathrm{Hz}}$. The amount of light used in the measurment depends both on the laser power and the efficiency of the transmission of light from the emitting laser to the detection diode on the far spacecraft. This efficiency is limited by the divergence of the laser beam as it is transmitted over the 5×10^6 km arm and losses in the various components in the optical chain.

Beam divergence. Even the best collimated laser beam will still have some finite divergence governed by the size of the final optic. With a Gaussian beam optimised for transmission between mirrors of diameter D, with an arm length L, and a transmitted power P, the power received at the far craft is given by

$$P_\mathrm{r} = 0.50\,\frac{D^4}{\lambda^2 L^2}\,P\,. \tag{3.1}$$

This is the case when the Gaussian beam has a waist (of radius w) at the transmitting craft that almost fills the final telescope mirror, $w = 0.446\,D$.

Efficiency of the optical chain. There are a large number of components in the optical chain. The main ones contributing to a loss of transmitted power are listed below, beside an estimate of the likely achievable power transmission. All other components in the optical chain are assumed to be perfect.

Component	*Efficiency*
Fibre	.70
Isolator	.96
Modulator	.97
Splitter plate	.90
Splitter plate	.90
Mirrors + lenses	.88
Interference	.81
Quantum efficiency	.80
Total	.30

The term for interference is to allow for the fact that some signal is lost due to the imperfect matching of the local reference beam and the received light from the far craft: the local reference beam is Gaussian and the received beam is a 'Top Hat' mode.

Shot noise limit. Single frequency laser light of significant power from a lightweight reliable system is best provided by a monolithic Nd:YAG laser pumped by laser diodes. With this type of laser up to 2 W of light is currently achievable. In order to obtain high reliability from such a system in a space environment it is reasonable to derate the laser by a factor of two and use only $P = 1\,\mathrm{W}$ of output power. The laser system is described in detail in Section 3.1.5. Using this laser and taking into account the overall optical efficiency we find that shot noise limits the minimum detectable change[1] to

$$\widetilde{\delta x} = 11 \times 10^{-12} \left(\frac{\lambda}{1064\,\mathrm{nm}}\right)^{\frac{3}{2}} \left(\frac{0.3\,\mathrm{W}}{\epsilon P_\mathrm{o}}\right)^{\frac{1}{2}} \left(\frac{L}{5 \times 10^9\,\mathrm{m}}\right) \left(\frac{30\,\mathrm{cm}}{D}\right)^2 \mathrm{m}/\sqrt{\mathrm{Hz}}\,, \qquad (3.2)$$

where L is the arm length, λ the wavelength and P_o the power of the laser, the efficiency of the optical chain is ϵ, and D is the diameter of the transmitting and receiving optics. Thus with an optical chain with a realistic efficiency of $\epsilon = 0.3$ and a mirror of diameter of $D \approx 30\,\mathrm{cm}$ the target shot-noise performance can be achieved.

3.1.5 Laser system

Introduction. The laser system to be used in the LISA mission is a diode-laser-pumped monolithic miniature Nd:YAG ring laser which can generate a continuous diffraction-limited infra-red beam at 1064 μm of up to 2 W.

Diode-pumped solid-state lasers, operating in a single transverse mode, are well known as compact, reliable and highly efficient sources of stable radiation. In the case of the NPRO (Non Planar Ring Oscillator), TEM 00 mode operation is achieved by focussing the diode-laser beam into the crystal (see below). When the beamwidth of the diode laser radiation is smaller than the diameter of the TEM 00 mode in the absorption length of the pump radiation, the laser is forced to operate in a single transverse mode.

Homogeneously broadened solid-state lasers oscillate on several longitudinal modes even at low output power because of the spatial hole-burning effect. To enforce single-frequency operation, resonator internal elements can be applied. However, the additional intracavity elements strongly reduce the efficiency and stability of the laser system. The monolithic Nd:YAG ring laser enables single-frequency operation at high output power without intracavity elements. Unidirectional and hence single-frequency oscillation is enforced by an intrinsic optical diode.

The optical beam path in the crystal is determined by three total reflections and one reflection at the negatively curved front surface. The front surface is dielectrically coated, reflecting about 97 % of the 1064 nm laser radiation and highly transmitting the pump radiation at 808 nm (see Figure 3.4). The high frequency stability required for the LISA mission can only be achieved because of the high intrinsic stability of the NPRO (see Section 3.1.6). This stability results from the monolithic and compact design of the resonator and from the outstanding properties of host material YAG (Yttrium Aluminum Garnet $Y_3Al_5O_{12}$). Low CTE ($7 \times 10^{-6}\,\mathrm{K}^{-1}$) and low temperature dependence of the

[1] The convention above and throughout this paper is that a 'tilde' over a quantity indicates that it is a linear spectral density, *e.g.* $\widetilde{\delta x}$ is the linear spectral density of δx.

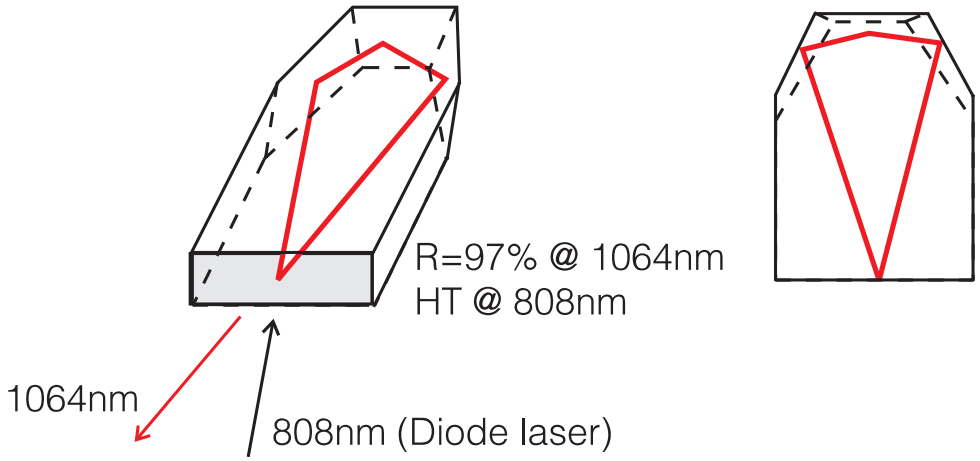

Figure 3.4 *The beampath in the monolithic, nonplanar ringresonator is determined by three total reflections and one reflection at the dielectrically coated front surface.*

index of refraction ($9.05 \times 10^{-6}\,\mathrm{K}^{-1}$) make the laser rather insensitive to temperature fluctuations.

The hardness of the YAG material makes it possible to reduce form errors of the crystal surface below $\lambda/10$. Typically 1 % of the Y^{3+}-ions are replaced by Nd^{3+}-ions. Higher doping rates would be desireable, but would cause mechanical stresses. The active ion Nd^{3+} absorbs the radiation of the pumping diode lasers at 808 nm and emits radiation at 1064 nm. Due to that quantum limit the efficiency of the laser ist limited to $\approx 75\,\%$. The 25 % energy loss is dissipated into the crystal.

To date there are few alternatives to Nd:YAG. Ytterbium can be used as the active ion, because the efficiency is higher than for Nd^{3+}(Neodymium)-ions, but the pump power requirements are also higher because Yb is a three level-atom rather then the four level Nd. Yttrium vanadate (YVO_4) is an alternative candidate for the host material, because it supports the optical diode by introducing an extra polarization selective element, but the thermal properties are much worse than those of the YAG. So it is unlikely that the active material of the NPRO will be changed from Nd:YAG to some alternative material.

Laser system components. The complete laser system consists of four major components: the laserhead, the supply unit, the electro-optic modulator and the stabilization photodiode. Each component has its own housing and the block diagram of the system is shown in Figure 3.5 for identification of the different interfaces. Both the laserhead and the supply unit are mounted on a carbon-carbon radiator, whereas the modulator and the photodiode are mounted directly onto or near the optics bench.

The **laserhead** consists of a Nd:YAG crystal pumped by two long life aluminum-free InGaAsP laser diodes. These single stripe devices have maximum cw output power of 2000 mW. The nominal single-mode, cw output power of the NPRO in this configuration is 1500 mW, but this is downrated for LISA to 1000 mW to improve lifetime and reliability properties. The nominal constant power consumption for the 1000 mW of output power of the complete laser system will be approxemately 10 W.

The pumplight from each laser diode is transferred into the crystal by imaging the emitting

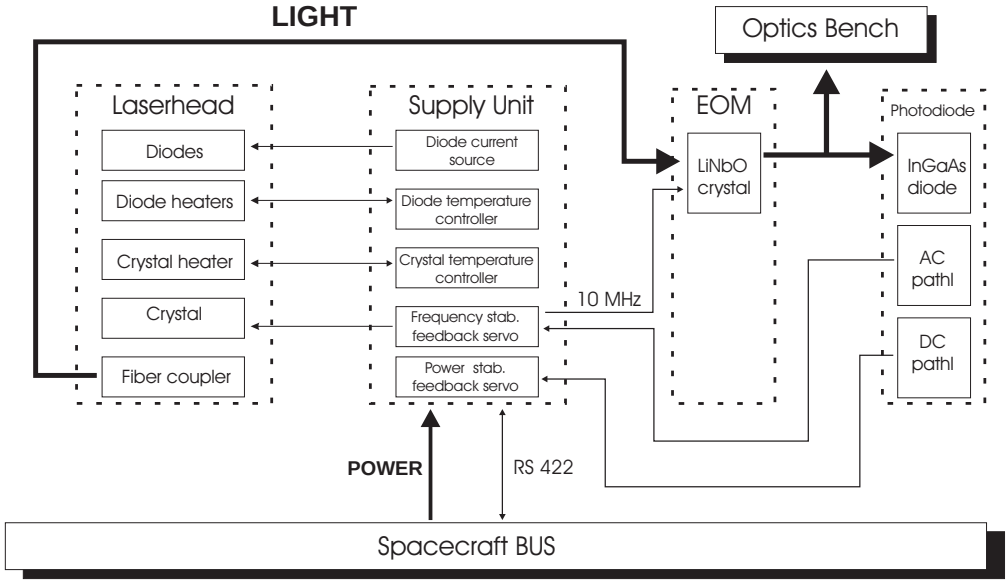

Figure 3.5 *Laser system block diagramm for the identification of the components and interfaces.*

area of $1\,\mu\text{m} \times 200\,\mu\text{m}$ at unit magnification onto the entrance surface of the crystal, using two identical lenses with plano-convex surfaces to minimize spherical aberration (best form lens shape). A polarizing beamsplitter is inserted between the two lenses to combine the pump light from the two diodes, which are orthogonal in polarization.

All of the above mentioned components are glued to a solid fused silica spacer to ensure mechanical stability. Glued to that spacer are three heat sinks, which serve as the mechanical and thermal interface to the radiator plate. There is a heater integrated in each heat sink to control the operating temperature of the diodes and the crystal.

The **supply unit** mainly contains two current sources for the laser diodes, three temperature controllers, two for the diodes and one for the crystal, the mixer and feedback servo for the frequency stabilisation and the feedback circuit for power stabilisation. The supply unit power interface to the S/C power subsystem shall be the only power interface between the laser system and the S/C.

The **electro-optic modulator** (EOM) is a resonant phase modulator. These devices use lithium niobate crystals as the electro-optic medium, where a few volts drive voltage induce a change in the crystal‘s refractive index. The only electrical interface to the EOM is the *rf* supply.

The **stabilisation photodiode** is a InGaAs diode operated with a few volts reverse voltage in order to reduce its capacitance. That capacitance is part of a LC-circuit that resonantly enhances the *rf* signal modulated on the the laser beam. The ac-signal from the photodiode is taken as a voltage from the LC-circuit. The dc-signal is obtained by converting the photocurrent into a voltage with a transimpedance operational amplifier.

3.1.6 Laser performance

Laser frequency noise. The presence of laser frequency noise can lead to an error in the measurement of each arm length. If the arms are equal these errors cancel out but if they are unequal, the comparison of lengths used to search for gravitational waves may be dominated by frequency noise.

For an arm of length L the phase difference between the outgoing and returning light of frequency ν is given by:

$$\phi = \frac{4\pi\nu L}{c}\,. \tag{3.3}$$

Thus, for slow changes in L and ν,

$$\delta\phi = \left[\frac{4\pi}{c}\right](L\delta\nu + \nu\delta L) = \frac{4\pi\nu L}{c}\left(\frac{\delta\nu}{\nu} + \frac{\delta L}{L}\right), \tag{3.4}$$

where $\delta\phi$ is a phase fluctuation resulting from either a change δL in arm length or a change $\delta\nu$ in frequency of the laser. In fact a fractional change in frequency of $\delta\nu/\nu$ gives a signal equivalent to a fractional change in length of $\delta L/L$. Thus if the difference in two arm lengths is Δx and the relative frequency stability of the laser is $\widetilde{\delta\nu}/\nu$ the smallest relative displacement which can be measured is given by:

$$\widetilde{\delta x} = \Delta x \frac{\widetilde{\delta\nu}}{\nu}\,. \tag{3.5}$$

For the 5×10^6 km arms of LISA, a maximum value of Δx of the order of 10^5 km is likely. For a relative arm length measurement of $2\times10^{-12}\,\mathrm{m}/\sqrt{\mathrm{Hz}}$, which is needed to achieve the desired overall sensitivity, a laser stability of $6\times10^{-6}\,\mathrm{Hz}/\sqrt{\mathrm{Hz}}$ is required.

The monolithic structure of the nonplanar Nd:YAG ring laser and the low technical noise of the supply electronics offer a high intrinsic frequency stability of this laser system. In order to reach the desired sensitivity that intrinsic stability has to be even improved and a high precision frequency stabilisation has to be provided. The primary method of stabilisation is to lock the frequency of one laser in the system on to a Fabry-Perot cavity mounted on one of the craft making use of a *rf* reflection locking scheme known as *Pound-Drever-Hall scheme*. This stability is then effectively transfered to other lasers in the system by phase locking techniques.

With the temperature fluctuations inside each craft limited in the region of $10^{-3}\,\mathrm{Hz}$ to approximately $10^{-6}\,\mathrm{K}/\sqrt{\mathrm{Hz}}$ by three stages of thermal insulation, a cavity formed of material of low expansion coefficient such as ULE allows a stability level of approximately $30\,\mathrm{Hz}/\sqrt{\mathrm{Hz}}$. This level of laser frequency noise is clearly much worse than the required $6\times10^{-6}\,\mathrm{Hz}/\sqrt{\mathrm{Hz}}$ and a further correction scheme is required. Such a correction is provided by comparing the mean phase of the light returning in two adjacent arms with the phase of the transmitted light. The phase difference, measured over the time of flight in the two arms, allows an estimate of laser frequency noise to be made. For each arm $\widetilde{\delta\phi} = (4\pi/c)\,L\widetilde{\delta\nu}$ (since $\nu\widetilde{\delta L} \ll L\widetilde{\delta\nu}$) and thus if the spectral density $\widetilde{\delta\phi}$ is measured, the spectral density $\widetilde{\delta\nu}$ can be estimated. A detailed analysis of this scheme is given in Section 4.3.

Laser power noise. The tolerable limit to laser power noise is to a large extent set by the radiation pressure effects of the beam to the adjacent craft at a vertex, this beam being reflected off the proof mass in the accelerometer. As will become clear from discussions in Section 3.2, we want few spurious accelerations of the proof mass above a level of $10^{-16}\,\mathrm{m\,s^{-2}}/\sqrt{\mathrm{Hz}}$. For a proof mass of 1.3 kg and a reflected light power of 100 μW, the proof mass will undergo a steady acceleration of $5\times10^{-13}\,\mathrm{m\,s^{-2}}$. To keep the fluctuating acceleration below $10^{-16}\,\mathrm{m\,s^{-2}}/\sqrt{\mathrm{Hz}}$ the power stability of the reflected light, and hence of the laser, must be better than $\widetilde{\delta P}/P = 2\times10^{-4}/\sqrt{\mathrm{Hz}}$.

The fundamental limit of the power noise for a free-running laser is set by the quantum properties of light. In principle diode-pumped solid-state lasers offer the potential to reach this quantum noise limit (QNL). However, in real systems the power fluctuations are many orders of magnitude larger. In the LISA frequency band this is mainly due to pump noise transfer.

Substantial power noise reduction has been demonstrated for Nd:YAG ring lasers by application of electronic feedback loops. A fraction of the laser light is detected with a photo diode and the AC components are appropriately amplified to generate an error signal. This signal is fed back to the pump diodes (see Figure 3.6). The noise is less than 10 dB above the quantum noise limit down to a frequency of 10 KHz, corresponding to a relative power noise of less than $5\times10^{-8}/\sqrt{\mathrm{Hz}}$. To reach the above-metioned requirements the existing noise reduction scheme has to be extended to the low frequency regime.

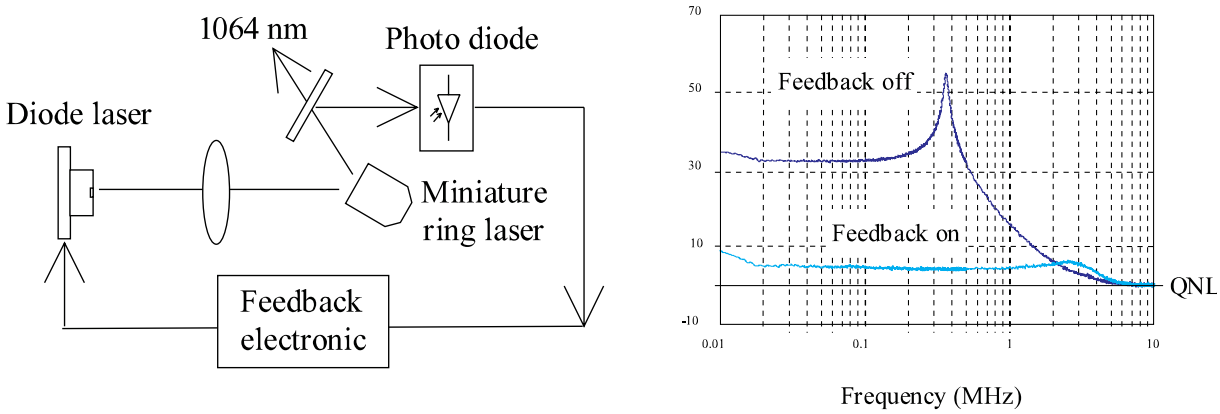

Figure 3.6 *Scheme of power noise reduction setup and intensity noise power spectrum in dB relative to quantum noise limit (1 mW optical power detected).*

On-board frequency reference. A further technical problem, that of the Doppler shift, occurs if there is a relative velocity between the two spacecraft in an arm, producing a frequency shift in the returned light and causing a beat signal when the phase comparison is made. For the particular orbits chosen (see Section 3.1.2), the relative velocities of the spacecraft in arm 3 will be up to about 15 m/s. The corresponding beat frequencies are then less than 15 MHz.

A signal from an ultra-stable oscillator (USO) is required in each arm to allow the Doppler beat frequency to be reduced to a manageable level for later signal processing. The clock

signal should be stable enough to contribute a level of phase noise less than that from an arm length change of $2\times10^{-12}\,\mathrm{m}/\sqrt{\mathrm{Hz}}$, *i.e.* $\widetilde{\delta\phi} < 1.2\times10^{-5}\,\mathrm{rad}/\sqrt{\mathrm{Hz}}$. The noise δF of the clock frequency F is related to the phase noise $\delta\phi$ at any frequency f by $\delta F = f\times\delta\phi$, so at $10^{-3}\,\mathrm{Hz}$ we require a clock with a noise $\widetilde{\delta F} \leq 1.2\times10^{-8}\,\mathrm{Hz}/\sqrt{\mathrm{Hz}}$.

If the clock frequency is, say, 15 MHz, the required relative stability of the clock is approximately $8\times10^{-16}/\sqrt{\mathrm{Hz}}$, an Allan variance[2] of 3×10^{-17} at $10^{-3}\,\mathrm{Hz}$. This demand is considerably stronger than can be fulfilled by any flight qualified USO currently available; for example the one used on the Mars Observer had an Allan variance of 2×10^{-13} at $10^{-3}\,\mathrm{Hz}$. The stability of the USO can however be improved to the desired level by modulating the clock frequency onto the laser light and stabilising this frequency to the arm length in a scheme analogous to that used to stabilise the laser frequency. To be more precise the USO in the master spacecraft is considered as the master oscillator in the system, and its phase fluctuations are measured by comparing the phase of the outgoing 200 MHz modulation sidebands with the incoming ones in one arm, the incoming ones being offset by a given frequency determined by an NPRO on the distant spacecraft. The presence of this offset is essential to allow the phase measuring system to separate the signals related to the beating of the sidebands from the signals related to the beating of the carriers. It should be noted that the phase measuring system requires an accurate measurement of the relevant Doppler signal also to be given to it.

Note that the USO on each craft is effectively phase locked to the master USO by controlling an NPRO on the output of each by means of a signal derived from the beating of the modulation sidebands on the incoming and outgoing light. This is elaborated in Section 4.3.3.

3.1.7 Thermal stability

A high level of thermal stability is required by the interferometer. Thermal variation of the optical cavity to which the lasers are stabilized introduces phase variations in the interferometer signal, which have to be corrected for by using data from the two arms separately. Thermally induced variations in the dimensions of the transmit/receive telescope will lead to changes in the optical path length. Variations in the dimensions of the spacecraft will change the positions of components which cause a change in the mass distribution and hence cause an acceleration of the proof mass.

The thermal stability needed is achieved by using structural materials with low thermal expansion coefficient and by using multiple stages of thermal isolation. The spacecraft and payload structural elements will be made of composite materials with thermal expansion coefficient less than $1\times10^{-6}/\mathrm{K}$. The optical bench and telescope are supported by the payload cylinder which is weakly thermally coupled to the payload thermal shield which in turn is weakly coupled to the spacecraft body. This provides three stages of thermal isolation for the payload from solar and spacecraft electronics thermal input.

The main source of thermal variation is due to changes in the solar intensity around its mean value of $1350\,\mathrm{W\,m^{-2}}$. Observed insolation variations from 0.1 mHz to 10 mHz can

[2]For a clock with white frequency noise, the relationship between the Allan variance and the relative frequency stability of the clock at a Fourier frequency f is given by $\sigma_{\mathrm{Allan}} = \sqrt{2\ln 2}\times\left(\widetilde{\delta F}/F\right)\times\sqrt{f}$.

be described [82] by a spectral density with a shallow frequency dependence:

$$1.75 \times \left(\frac{f}{1\,\mathrm{mHz}}\right)^{-1/3} \mathrm{W\,m^{-2}/\sqrt{Hz}}\,.$$

To quantify the effects of solar and electrical variations, a simple thermal model for the spacecraft was formed with single nodes for the spacecraft body, solar panels, optical bench, telescope, laser radiator and electronics disk. The temperature fluctuations of the optical bench due to solar fluctuations were found to be well under the value of $10^{-6}\,\mathrm{K}/\sqrt{\mathrm{Hz}}$ at 1 mHz used in the analysis of the laser phase noise. To keep the power variations from producing thermal noise in excess of this, the power dissipation of the payload electronics will have to be controlled to $10\,\mathrm{mW}/\sqrt{\mathrm{Hz}}$ and the power dissipation of the photodiodes on the optical bench will have to be controlled to better than $50\,\mu\mathrm{W}/\sqrt{\mathrm{Hz}}$. The needed control can be achieved with small heaters and voltage and current sensors. The spacecraft electronics do not need to be controlled to better than the 0.1 % typical of flight-qualified units.

The secondary mirror of the telescope is supported from the primary by a graphite-epoxy spider with length 40 cm and thermal coefficient of expansion $0.4 \times 10^{-6}/\mathrm{K}$. The thermally-induced path-length variations using the thermal model were found to be less than $2\,\mathrm{pm}/\sqrt{\mathrm{Hz}}$ at 1 mHz, and so are not a major source of noise.

The accelerations caused by changes in the mass distribution of the payload were assessed. The primary payload masses are the optical bench, the telescope, the payload electronics, and the laser/radiator combination. The proof-mass acceleration noise caused by solar fluctuations was found to be less than $1 \times 10^{-16}\,\mathrm{m\,s^{-2}}/\sqrt{\mathrm{Hz}}$ at 1 mHz. The acceleration noise due to thermal variations in the dimensions and component positions of the spacecraft body has not yet been assessed.

3.1.8 Pointing stability

The requirements of the interferometry place constraints on the allowed angular fluctuations of the various interfering beams. The level of pointing control required of each spacecraft is set by the level of phase front distortion in a transmitted beam. If the beam deviates from having perfect spherical wavefronts centred on the transmitting craft, then angular changes of the transmitting craft produce changes in the phase of the received light, and hence apparent gravitational wave signals. From diffraction arguments the largest effect is from a first order curvature error of the wavefront (equivalent to a defocus in one or the other dimension). In this case the apparent phase change, $\delta\phi$, due to movement of the beam in the far field is given by:

$$\delta\phi \;=\; \frac{1}{32}\left(\frac{2\pi}{\lambda}\right)^3 d \cdot D^2\,\theta_{\mathrm{dc}}\delta\theta\,, \tag{3.6}$$

where D is the diameter of the mirror, d is the amplitude of curvature error in the wavefront, θ_{dc} is the static offset error in the pointing and $\delta\theta$ is the angular fluctuation. In this case with an allowed phase error from this source of $\widetilde{\delta\phi} = (2\pi/\lambda) \times 10^{-12}\,\mathrm{rad}/\sqrt{\mathrm{Hz}}$

for a single transit, $d \sim \lambda/10$, and a mirror diameter $D = 30\,\mathrm{cm}$, we need to achieve

$$\theta_{\mathrm{dc}}\widetilde{\delta\theta} \;\leq\; 140\times10^{-18}\,\mathrm{rad}^2/\sqrt{\mathrm{Hz}}\,. \tag{3.7}$$

Thus if $\theta_{\mathrm{dc}} \sim 20\,\mathrm{nrad}$, the required pointing stability of the spacecraft is $\widetilde{\delta\theta} \sim 7\,\mathrm{nrad}/\sqrt{\mathrm{Hz}}$. The orientation of the spacecraft with respect to the incoming light may be determined by a wavefront sensing technique. The interference between the local laser and the received light occurs on the main quadrant diode, any angular difference between the two beams will result in a phase difference between the signals in the different quadrants and hence the orientation of the spacecraft can be measured.

3.1.9 Pointing acquisition

A star tracker would be used for initial attitude control; this should allow alignment of each of the spacecraft to $\sim 10^{-4}\,\mathrm{rad}$ (20 arcsec). The divergence of the main beam from each craft is considerably smaller than this at $4\times10^{-6}\,\mathrm{rad}$ so there is an initial problem in using the main beam for alignment. A solution is to increase the divergence of the main beam by a factor of three during the acquisition phase by a small movement of the output end of the optical fibre. (This system would also provide active focus control.) One spacecraft would use its proof mass as its pointing reference and scan through a 10×10 grid of step size 10^{-5} radians. The other spacecraft would note when it received light from the transmitter and pass this information, via the ground, to the transmitter which could then point itself appropriately. The receiving spacecraft would then align its outgoing light to the received light using the wavefront sensing technique described earlier. With light now going in both directions along the arm the original transmitter would now switch to also using wavefront sensing to maintain alignment.

3.1.10 Final focusing and pointing calibration

We saw earlier in this section that any defocus of the transmitted light, along with pointing noise, would produce a spurious signal in the interferometer. We can use this effect to optimise the focus for each of the spacecraft in turn. The pointing of one spacecraft is modulated at a known frequency, this will cause a signal at the output of the interferometer at multiples of the modulation frequency. The magnitude and sign of the focus error in the transmitting craft can be deduced from the size and phase of these signals, and hence the focus and 'dc' pointing may be optimised.

3.1.11 Point ahead

The orbits of the spacecraft, combined with the very long arm length of the interferometer and the finite speed of light, give rise to an angle between the incoming and transmitted beams in the main telescope of $3.5\times10^{-6}\,\mathrm{rad}$. This 'point ahead' angle is constant with time and would lead to the two interfering beams having an angle of $35\times10^{-5}\,\mathrm{rad}$ between them at the main diode. (This angle is the point ahead angle multiplied by the angular magnification of the telescope.) The two interfering beams can be made parallel at the

diode by offsetting the main beamsplitter from its expected angle to the optical axis of $\pi/4$ rad by an extra 9×10^{-5} rad.

3.2 The inertial sensor

3.2.1 Overview

The three LISA spacecraft each contain two inertial sensors, one for each arm forming the link to another LISA spacecraft. The proof masses of the inertial reference sensors reflect the light coming from the YAG laser and define the reference mirror of the interferometer arm. The same proof masses are also used as inertial references for the drag-free control of the spacecraft which constitute a shield to external forces. The proposed sensors (called CAESAR: Capacitive And Electrostatic Sensitive Accelerometer Reference) can be derived from existing space qualified electrostatic accelerometers already developed for the ESA projects, like the GRADIO accelerometer or the ASTRE sensor delivered to ESTEC for micro-gravity spacelab survey [83, 84, 85]. The last one has flown three times on board the COLUMBIA shuttle in 1996 and 1997. The STAR accelerometer, based on the same configuration, will also be delivered to CNES and DLR in order to be integrated on board the german geodetic satellite CHAMP to be launched in 1999. All these sensors are based on a three axis electrostatic suspension of the proof mass with capacitive position and attitude sensing.

Since the laser beam is directly reflected off the proof mass, the noise of the CAESAR proof-mass position sensing with respect to the sensor cage does not affect directly the interferometer resolution. A resolution of $10^{-9}\,\mathrm{m}/\sqrt{\mathrm{Hz}}$ is nevertheless needed to limit the disturbances induced by relative motions of the satellite with respect to the proof mass, for instance, the disturbances due to the spacecraft self gravity or to the proof-mass charge. Furthermore, this resolution is compatible with the control of the proof-mass orientation to better than $5 \times 10^{-8}\,\mathrm{rad}/\sqrt{\mathrm{Hz}}$.

What is more demanding for the definition of CAESAR is the level of the disturbing accelerations induced by the sensor back-action and by the parasitic forces that may be applied directly on the proof mass. This level must be limited to $3 \times 10^{-15}\,\mathrm{m\,s^{-2}}/\sqrt{\mathrm{Hz}}$ in the frequency domain from 10^{-4} Hz to a few 10^{-3} Hz.

Contrary to the space accelerometers, no accurate measurement of the acceleration is needed because the scientific data are obtained through the interferometer outputs. Thus, there are no very stringent requirements on the scale-factor accuracy, on stability or on the sensor linearity when the the drag compensation system of the satellite is operating.

The sensor can be considered in two ways. On the one hand, CAESAR is simply composed of an inertial reference proof mass with surrounding capacitive position sensors that provide the measurement of its attitude and its position with respect to the sensor cage and thus to the satellite. On the other hand, CAESAR can operate as an accelerometer with its proof mass servo-controlled such as to be motionless with respect to the cage, and the sensor output is then representative of the satellite acceleration. Both ways are proposed to be used during the mission to compensate the spacecraft external forces and torques.

Based on the same concept and technology as the STAR accelerometer, the CAESAR sensor

design (geometry, performances and accommodation on board the spacecraft) has to be optimised to fit the mission requirements. Fortunately, the sensor will benefit from the thermal stability of the optical-bench environment of the LISA satellite, i.e. $10^{-6}\,\mathrm{K}/\sqrt{\mathrm{Hz}}$, and of the materials that will be involved in the sensor mechanics exhibiting very low coefficient of thermal expansion (CTE) and ensuring a high geometrical stability.

3.2.2 CAESAR sensor head

As shown in Figure 3.7, the CAESAR sensor head is mainly constituted by

- a proof mass made of gold-platinum alloy,
- three gold-coated sets of electrode-plates made in ULE
- a reference base plate made also in ULE that constitutes the mechanical interface with the optical bench,
- a blocking mechanism with gold-coated fingers that should be necessary to maintain the proof mass motionless during the launch vibrations,
- a tight housing made of titanium.

The proof-mass alloy of 90% Au and 10% Pt is presently selected because of its high density of $20\,\mathrm{g/cm^3}$ and because of its weak magnetic susceptibility, in order to minimise the effects of the magnetic environment fluctuations induced by the interplanetary magnetic field or the magnetic field gradient due to the satellite itself. The drawback of a metallic

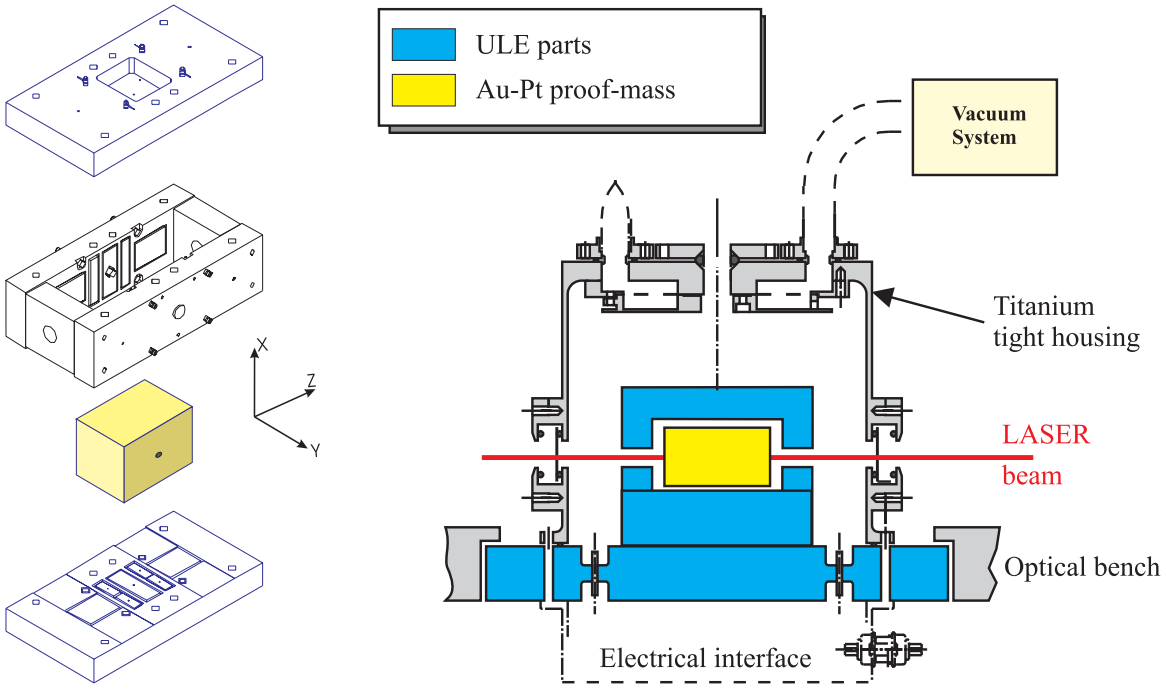

(a) ULE cage (b) Sensor configuration

Figure 3.7 *CAESAR overview.*

mass is its thermal expansion coefficient, quite one thousand times greater than the ULE cage, but it presents the advantage of a high density and a much better resistance to shocks and vibrations. Fortunately, the mass temperature fluctuations are very limited because it is well thermally decoupled and because the laser beams that are reflected off it exhibit high power stability. Furthermore, the electrode configuration is such that the mass expansion does not affect at first order the characteristics of the sensor.

Around the nearly cubic proof mass of about 4 cm side along the X and Y axes and 5 cm along Z (defined by the laser beam direction), the ULE sensor cage presents a set of six (or eight) pairs of electrodes used for capacitive sensing of its attitude and its position. The sensor could be realised with the technology developed and exploited for the production of space accelerometers. The ULE plates can be obtained by ultrasonic machining and grinding in order to benefit by a high geometrical accuracy and flatness. The gold coating necessary to define the electrode set is obtained by sputtering. In the case of CAESAR a specific effort will have to be devoted to the machining and the grinding of the proof mass: the characteristics of the capacitive sensing will depend on its geometry, on the parallelism and on the orthogonality of the faces. Two faces of the mass are also used as mirrors to reflect the laser beam.

The CTE of the ULE sensor cage is as low as a few 10^{-8}/K around 25 °C. Associated with the expected very weak thermal variations, it ensures the geometrical stability of the cage. Furthermore, the proof-mass temperature is very steady because, when electrostaticaly suspended, the thermal exchanges of the proof mass are only radiative: experiments have shown that the proof-mass temperature of the STAR accelerometer reacts with a response time of 20 hours, ensuring a very good filtering of the thermal fluctuations of the environment. With a much larger mass, the response time should be even two times larger.

The CAESAR cage must be implemented in a tight housing, and the whole sensor electronics could be accommodated on board of the satellite at a distance as large as one meter from the cage without affecting the performances too much. This allows a rather low power consumption inside the sensor head that is fixed on the satellite optical bench to the benefit from its thermal stability.

The titanium tight housing is necessary to maintain all the sensor core in a very clean vacuum after integration of the parts that will be out-gassed. In flight, the tight housing is opened to space vacuum and a very low residual pressure ($< 10^{-6}$ Pa) is expected inside the ULE cage in order to minimise the gas damping effects. A getter material can also be integrated inside the housing as it is done for the already developped space accelerometers.

3.2.3 Electronics configuration

The electronics is composed of 6 independent servo loops, each including a capacitive sensor with analog-to-digital sigma-delta converter, an electrostatic actuator and a digital control electronics. Each loop, corresponding to one pair of electrodes, can be used to control one degree of freedom of the proof mass. The proposed configuration for the electrodes is presented in Figure 3.8 .

The electrode areas are evaluated to 8 cm^2 for the Z axis and to 1.5 cm^2 for the other two directions. The gaps between the electrodes and the proof mass will result from a compromise between the position-sensor resolution, the electrostatic actuator strength

and the level of the disturbing effects resulting from the presence of the instrument cage near the mass. Currently selected are gaps of 1 to 2 mm for the Z-axis electrodes and of 0.3 mm for the X and Y axes.

Then, the setting of the configuration parameters results from the trade-off between the position sensing resolution and the back-actions induced on the proof-mass motion by the detection voltage, i.e. a negative electrostatic stiffness and an electrostatic acceleration when the configuration is not fully symmetric.

As presented in Figure 3.9, the sensitivity of the capacitive position sensor can be adjusted according to the three following parameters: the amplitude of the sine wave detection voltage, V_d, applied to the proof mass via injection electrodes, the gain of the electronics that collect the detection signal through the two sensing electrodes corresponding to the sensor, and the distance between the electrodes and the proof mass.

As a matter of fact, the capacitive sensor resolution is mainly driven by the thermodynamic noise of the capacitive bridge formed by the proof mass, the opposite sensing electrodes and the differential transformer, and it can be expressed by:

$$C_\mathrm{n}(f) = \frac{1}{V_\mathrm{d}}\sqrt{\frac{2kTC_\mathrm{e}}{\pi f_\mathrm{d} Q}} \qquad (\mathrm{F}/\sqrt{\mathrm{Hz}})\,, \tag{3.8}$$

with C_e the whole capacitance seen at the transformer input and with Q the quality factor of the LC detection circuit. With a detection voltage level of $5\,\mathrm{V_{rms}}$ and a sensitivity of $50\,\mathrm{V/pF}$ a resolution of $1.2\times10^{-7}\,\mathrm{pF}/\sqrt{\mathrm{Hz}}$ has been obtained with space qualified hybrids. Using a reduced detection voltage of only $1\,\mathrm{V_{rms}}$ and a gap of 1 mm, in order to minimise the effects of the negative electrostatic stiffness, a resolution of $2\times10^{-10}\,\mathrm{m}/\sqrt{\mathrm{Hz}}$ should be achieved. Moreover, recent improvements of the resolution of the capacitive sensor could be beneficial to the CAESAR electronics development: the corner frequency of the $1/f$ sensor noise can be lowered under certain conditions to frequencies below $10^{-4}\,\mathrm{Hz}$.

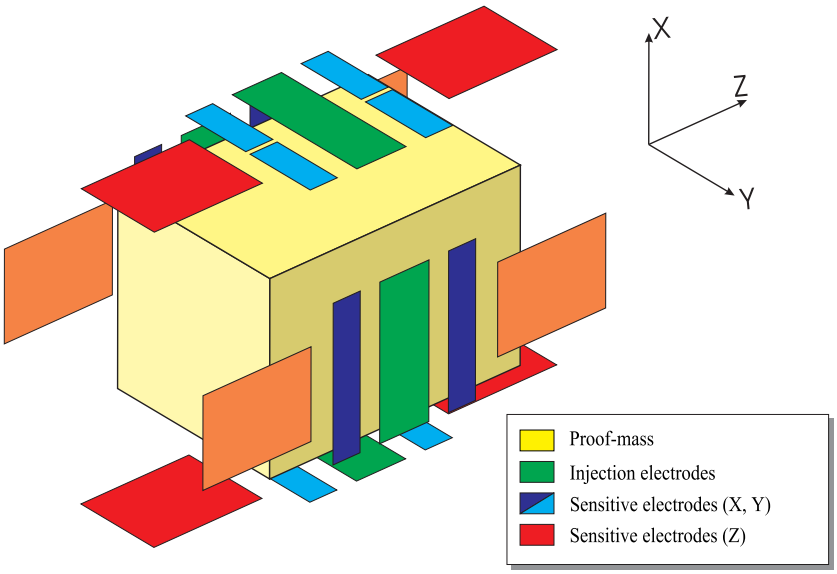

Figure 3.8 *Electrodes set configuration.*

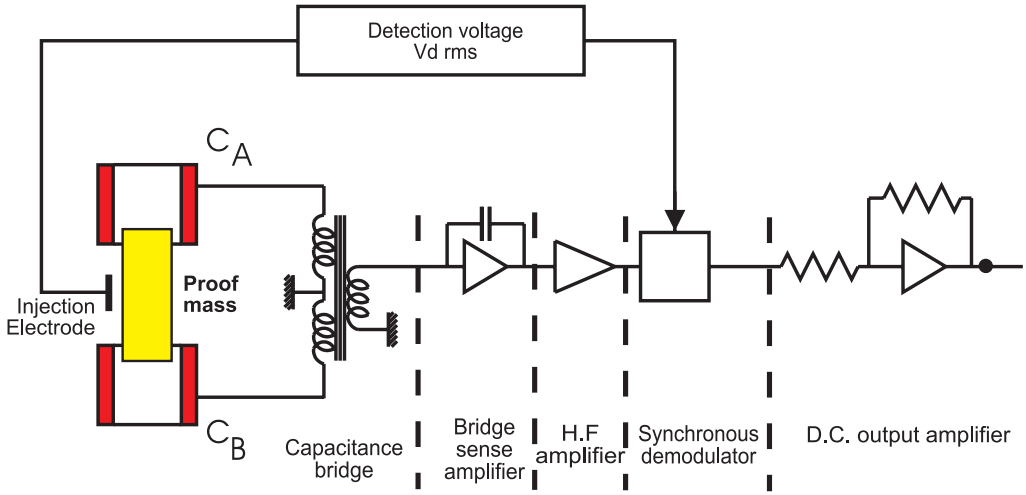

Figure 3.9 *Scheme of the capacitive sensing.*

The negative electrostatic stiffness induced by the detection voltage is reduced along the Z axis with respect to the two other ones by the electrode configuration and by the distance between the mass and the cage increased to 15 mm. The capacitance variations, measured by the sensor along this axial direction and due to the proof-mass motion, are no longer induced by the variations of the gaps between the proof mass and the sensing electrodes but by the variations of the proof-mass areas in view to these electrodes.

The electrostatic forces are generated by applying the same control voltage V on the opposite electrodes (see Figure 3.10). This control voltage is generated from the output of the corrector. Opposite DC voltages $\pm V_{\rm p}$ are added in order to linearise the electrostatic forces that become proportional to $V_{\rm p}$ when the configuration is symmetric. Both electrodes attract the proof mass with forces $F1$ and $F2$ proportional to the gradients of the capacitances ∇C_i and to the square of the potential differences between the proof mass and the electrodes. The resultant force is expressed by

$$F = F_1 + F_2 = \frac{1}{2}\left(\nabla C_2\, V_2^2 + \nabla C_1\, V_1^2\right). \tag{3.9}$$

Because of the geometrical symmetry we have

$$\nabla C_2 = -\nabla C_1 = \nabla C\,, \tag{3.10}$$

and the resultant force F, linearised by the use of biasing voltages $\pm V_{\rm p}$, is made proportional to the control voltage V:

$$F = (2\nabla C\, V_{\rm p})\, V. \tag{3.11}$$

At low frequencies, inside the control bandwidth, the proof mass is kept motionless in the accelerometer cage, and V is representative of the acceleration $\Gamma_{\rm cage}$ of this cage:

$$(2\nabla C\, V_{\rm p})\, V \approx m\Gamma_{\rm cage}\,, \tag{3.12}$$

with m being the mass of the levitated proof mass. In the above two expressions, the terms in parentheses represent the instrument scale factor. The value of $V_{\rm p}$ is selected according

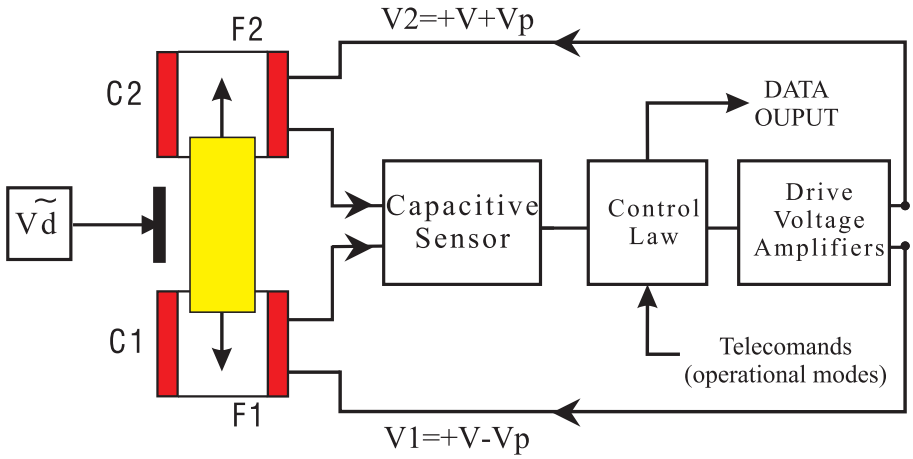

Figure 3.10 *Scheme of one channel loop.*

to the full scale range of acceleration required for the control of the proof mass. It shall be changed according to the different operation modes from tens of volts to hundreds of milli-volts.

A supplementary set of electrodes, called injection electrodes in Figures 3.8, 3.9 and 3.10, is used to control the proof-mass electrical potential, in particular at the pumping frequency of the capacitive sensing. This solution has been preferred to a thin gold wire used in other space accelerometers because of the stiffness and of the damping that the wire may generate. Experimental investigations have demonstrated that the wire is only compatible with a resolution of several $10^{-14}\,\mathrm{m\,s^{-2}/\sqrt{Hz}}$ at room temperature [86].

3.2.4 Evaluation of performances

The performances of the inertial reference sensor have been evaluated by considering the geometry and the characteristics of the sensor head, the characteristics of the electronics configuration and the environment on board the LISA satellite. In particular this last point leads to a required pressure inside the housing of less than $10^{-6}\,\mathrm{Pa}$.

The evolution of the charge Q of the isolated proof mass is one of the most critical error sources. On the one hand, the proof mass is subjected to the electrostatic forces appearing with the image charges on the electrodes in regard to the proof mass; the resultant of these forces is not null when the configuration is not perfectly symmetric, in particular for any off-centering of the proof mass with respect to the sensor cage. On the other hand, this charge Q induces a Lorentz force when it moves in the interplanetary magnetic field.

In fact Q is the sum of the charge acquired when the proof mass separates from the accelerometer cage at suspension switch-on, and of the charge resulting from the cosmic particle bombardment, especially from the proton flux over 100 MeV. When considering a charging rate of 10^{-17} to $10^{-18}\,\mathrm{C/s}$ [87, 88], the $2\times10^{-14}\,\mathrm{C}$ limit required is reached in less than one hour. Therefore the charge has to be measured exploiting the electrostatic device itself, and the proof mass has to be discharged, continuously or time by time, for instance by photo-electric emission induced by ultraviolet light [87].

Other electrostatic-force noises must be considered: they are induced either by the fluc-

tuations of the applied voltages, of the contact potential differences and of the patch effects [89], or by the proof-mass motion; they are reduced by the expected geometrical accuracy of the ULE cage and of the proof mass (1 μm), by the large gaps and by the servo-loop controls which maintain the proof mass motionless.

The parasitic effects due to the residual pressure are limited by the good vacuum and the high thermal stability. The proof-mass magnetic moment is very weak because of the choice of a material having very low magnetic susceptibility, and the magnetic behaviour of the satellite should be acceptable. Furthermore, a magnetic shield could be implemented if necessary.

This preliminary error budget shows that such a sensor concept appears compatible with the LISA mission requirements. A detailed definition of the sensor, of its operation and of the envisaged environment on board the satellite is necessary to refine and to confirm the evaluation of performances. Experimental investigations will be necessary to assess the behaviour of the sensor and to optimise the configuration. Both activities are being undertaken. The sensor configuration could be tested in the laboratory under normal gravity if a lighter proof mass, made in ULE for instance, is used, and if dedicated electronics units are employed for the one-g proof-mass suspension. Such an ULE proof mass will weight less than 100 g while the suspension of a 320 g accelerometer proof mass has already been performed with quite the same 16 cm^2 cross-section available for the electrodes used for the one-g suspension. These investigations will be performed in 1999 after the production of such a laboratory model. Even with dedicated laboratory facilities, the ground tests are limited in resolution by the seismic noise and by the coupling with the one-g suspension, but these tests can be performed over very long periods. They should be complemented by free fall tests in a drop tower that provides the micro-gravity environment, but for only very short test periods of 4.7 s. The ASTRE accelerometer, being realised in the frame of the ESA COLUMBUS program and flown on board the shuttle, has been successfully tested in the Bremen drop tower [90]. The instrument currently under development, the configuration of which is very similar and representative to the one proposed for LISA, could be much better evaluated on board a μ-satellite with a drag compensation system.

3.2.5 Sensor operation modes

The proof mass can be kept motionless in position and attitude by means of six servo-control channels acting separately. It can be shown that the operation of the drag-free control can be represented by two loops. The first loop ensures the electrostatic suspension which can maintain the proof mass at the centre of the cage with electrostatic forces. The second one is the satellite drag-free control loop which compensates the satellite external forces using thrusters.

In the LISA mission, the absolute acceleration of the proof mass should essentially depend only on the gravitational field. Three sources of disturbances can be considered: the position-sensor noise, the satellite acceleration depending on the drag-free control performances, and the parasitic forces acting directly on the proof mass that cannot be minimised by any servo loop. The first two sources can sufficiently be reduced at low frequencies, when the electrostatic loop stiffness is adequately lower than the satellite control-loop stiffness. On the contrary, the stiffness of the electrostatic loop must be

sufficient to easily control the proof-mass motion and attitude, in particular when the drag-free control is not fully operational, at the beginning of the experiment for instance. A trade-off between these requirements could be obtained with a specific configuration of the loop electronics that introduces varying control stiffnesses according to the applied acceleration.

3.2.6 Proof-mass charge control

Charge control of the proof-mass is crucial if spurious electromagnetic forces are to be kept at a level such that they do not compromise the science goals. As noted earlier the nominal requirement is to limit the free charge on the proof mass to $< 2 \times 10^{-14}$ C in the presence of a continuous charging rate of 10^{-17} to 10^{-18} C/s [91]. This charge limit comes from considering the Lorentz force acceleration noise induced in an unshielded charged proof-mass interacting with the interplanetary magnetic field and it is explained in more detail in Section 4.2.4. It is conceivable that a factor of up to 100 might be recovered by shielding provided by the metallic vacuum enclosure around the sensor. Shielding beyond that level will be very difficult, given the need for access holes in various positions, and moreover, noise caused by electrostatic interactions of the free charge with the surrounding electrode structure then becomes significant anyway (see Section 4.2.4).

The baseline charge control technique involves illuminating both the proof mass and its surrounding electrodes with ultra-violet light to release photoelectrons from both surfaces, and then to use bias voltages on the electrodes to control the nett transfer of charge. This technique has been demonstrated already for GP-B [92], albeit at a somewhat higher level of charge (10^{-9} C) and much coarser control authority than those required for LISA. Laboratory tests using 2.5 W low-power mercury discharge lamps of two different types (rf discharge for GP-B and dc electric discharge for ROSAT [93]) have shown that sufficient photoelectric emission can be achieved from gold surfaces in both direct and reflected illumination. The low magnetic susceptibility of the Au/Pt proof-mass alloy unfortunately results in a particularly high work function and it may be that a gold coating is necessary on the proof-mass.

The level of bias voltage required to effect sufficient charge control depends on the detailed electrode geometry, the gaps to be used and the mode of introducing the UV. In the current scheme, which offers the simplest mechanical solution, the UV will be introduced onto the central sections of two opposite tranverse faces of the proof-mass. The facing electrodes will then be illuminated by reflection. This scheme gives a bipolar discharging capability. However with our current understanding of the charging mechanisms the belief is that the proof-mass will charge positively and hence the bias voltage will need to work against the inherent tendancy of this implementation. An alternative scheme which would avoid the need for significant bias voltages could be to illuminate the electrode and proof mass with quasi-independently controllable UV fluxes. This is mechanically more challenging. Laboratory tests are planned to investigate these options further.

There are a number of possible operational modes for the charge control system. One is to allow the UV to illuminate the proof mass continuously and only rely on the bias voltages to control the charge. The bias voltage itself would be derived from measurements of the charge using a dither voltage applied in the transverse direction at a frequency above

the science measurement band. Alternatively it might be better to 'apply' the UV in a gated fashion only when it was necessary to discharge the proof-mass or in a timed sequence aimed at matching the charging rate. For these modes we need some means of controlling the UV intensity. This can be done using the lamp drive power over a limited range by programming its supply current. A wider dynamic range can either be achieved using a load switching technique or by using an electro-optic switch (Pockells cell). A system to control the UV intensity involving a Pockells cell has been demonstrated in the laboratory [94].

The UV discharge system incorporates 2 low-pressure mercury discharge lamps, associated optical components, power supplies and control electronics contained within a single enclosure measuring $10\,\mathrm{cm} \times 15\,\mathrm{cm} \times 7\,\mathrm{cm}$. The system is internally redundant and only 1 unit is required per spacecraft. The unit is located on the radiator plate. Two electrical connectors provide power and control function interfaces respectively. A digital control interface, including internal h/k conversion, is assumed. Four optical fibre couplings provide interfaces to fibre optic cables delivering independent UV photon fluxes to the proof-masses within the telescope structures.

3.3 Drag-free/attitude control system

3.3.1 Description

LISA requires that the acceleration noise imposed on each proof mass in the sensitive direction is smaller than

$$\widetilde{\delta a} < 10^{-15} \left[1 + \left(\frac{f}{3\times 10^{-3}\,\mathrm{Hz}}\right)^2\right] \mathrm{m\,s^{-2}}/\sqrt{\mathrm{Hz}} \tag{3.13}$$

within the measurement bandwidth (MBW) from 10^{-4} to 10^{-1} Hz. In terms of the requirements on spacecraft control, taking into account the optical referencing from both opposing faces of each proof masses, the LISA drag-free & attitude control system (DFACS) must ensure that each spacecraft is controlled in translation and orientation such that the relative displacement between the spacecraft and the proof mass in the sensitive direction of each telescope arm is less than

$$\widetilde{\delta z} < 2.5\times 10^{-9}\,\mathrm{m}/\sqrt{\mathrm{Hz}} \tag{3.14}$$

within the MBW. In the other axes, the requirement is relaxed to

$$\widetilde{\delta x} = \widetilde{\delta y} < 2.5\times 10^{-6}\,\mathrm{m}/\sqrt{\mathrm{Hz}} \tag{3.15}$$

within the MBW. The relative attitude requirement between each proof mass and the spacecraft is

$$\widetilde{\delta\theta} < 1.5\times 10^{-7}\,\mathrm{rad}/\sqrt{\mathrm{Hz}} \tag{3.16}$$

within the MBW. The attitude of the spacecraft relative to each incoming wavefront must be controlled to within the dc value of

$$\phi_{\mathrm{dc}} < 3\times 10^{-8}\,\mathrm{rad}\,, \tag{3.17}$$

with a pointing stability requirement of

$$\widetilde{\delta\phi} < 8 \times 10^{-9}\,\mathrm{rad}/\sqrt{\mathrm{Hz}} \tag{3.18}$$

within the MBW.

The DFACS on each spacecraft uses the signals from the two accelerometers and the quadrant photodiodes to generate commands to the spacecraft thrust system via the control laws implemented on the payload processor. The required computational throughput for the DFACS control laws will be less than 2 MIPS, easily accommodated on the RAD 6000-SC. Two autonomous star trackers on each spacecraft are used for coarse attitude information. Owing to the intimate relationship between the DFACS performance and the instrument sensitivity, and since the DFACS relies completely on the key payload sensors (accelerometers and photodiodes), the entire DFACS subsystem — with the exception of the spacecraft thrusters and drive electronics — will be a PI-provided contribution to the LISA payload.

3.3.2 DFACS controller modes

The spacecraft coarse attitude controller prevails upon separation from the propulsion module, maintaining a power-positive orientation. During this phase, the spacecraft has access to all of the enabled components on the bus. The coarse attitude control system establishes an inertial orientation using Sun sensors and/or the payload star trackers, plus the spacecraft thrusters. Then, from either realtime ground command or deferred store command, the payload processor is powered on and loaded from the spacecraft processor. The memory load is stored in the solid state recorder (SSR) non-volatile memory. It is fetched from the SSR by the spacecraft processor and routed to the payload processor via the 1553 interface to the payload processor bootstrap loader. Following a successful load, the payload processor is activated and enters a standby mode. Upon command from the spacecraft processor, the payload processor transitions to an intermediate mode whereby the 1553 bus control is transferred from the spacecraft processor to the payload processor. At this transition, the payload processor also takes over the coarse attitude control. Following a sequence of payload setup procedures (e.g. setting up the accelerometers and photodiodes), the payload processor transitions to successive higher modes of drag-free/fine-attitude control. For example, the next mode after coarse attitude control is the acquisition mode whereby the payload processors on each spacecraft command a sequence of manoeuvres for establishing laser links between all spacecraft. The ultimate mode of DFACS operation is the high-performance drag-free and attitude control required during science data gathering.

At all times, the spacecraft processor monitors the coarse attitude sensors and the status of the payload (by means of a watchdog signal from the payload processor) and intervenes by reclaiming bus control and coarse attitude control if a significant problem is detected. If the payload detects a problem (which is not yet severe enough to warrant the spacecraft processor to reclaim control), the payload processor will attempt to deal with it by dropping back to intermediate mode and switching from String A to String B. If not resolvable in this mode, then bus control and coarse attitude control is returned to the spacecraft processor, remaining there until commanded from the ground.

3.3.3 Autonomous star trackers

Each LISA payload will include four star tracker heads, mounted in pairs on the outside of the thermal shield, one pair aligned with each of the two telescopes. Only two are nominally operational – one on each telescope – the others serve as backups. Each has a field of view of $22° \times 16°$ and can provide attitude knowledge of about 2 arcsec in two axes and 16 arcsec in their boresight roll axis. Star processing at an update rate of 1 Hz will require a total of 16 MIPS of throughput for both operational trackers. This is provided by a dedicated processor shared by the two optical heads. The processor unit must be mounted remotely, away from the payload thermal shield. (An alternative option is to use the payload processor instead of a dedicated processor, but this is not the current baseline.)

The star trackers will be fully autonomous, and can tolerate direct Sunlight without damage.

Field of view	$22° \times 16°$	
Pitch, yaw accuracy	2 arcsec	$\approx 10\,\mu$rad
Roll accuracy	16 arcsec	$\approx 80\,\mu$rad
Update rate	1 Hz	
Tracking rate	$0.2°\,s^{-1}$	≈ 3.5 mrad/s
Number of stars tracked	≤ 50	
Tracking sensitivity	$7.5\,m_v$	
Guide stars in database	5650	
Auxiliary stars in database	22600	
Communications I/F	1553 or RS 422	
Output format	quaternions, Euler angles	
Operating temperature	$-30°$ to $+50°$ C	
Radiation tolerance	1 kJ/kg	

Table 3.1 *Star tracker specifications (per optical head).*

The performance specifications of the star trackers are summarised in Table 3.1. The mass, power, and volume budgets are summarised in Table 3.2. The data in these tables is based on the system under development for the Oersted mission. Since the payload star trackers are on the 1553 bus, they may also be accessed by the spacecraft computer for coarse attitude control.

Items	*Number of Units*	*Unit Mass* (kg)	*Total Mass* (kg)	*Power per Unit* (W)
Optical head + immediate electr.	4	0.25	1	5
Baffle	4	0.5	2	–
Data processing unit incl. shielding	2	1.5	3	3
Totals			**6 kg**	**13 W** (2 heads + 1 proc.)

Dims. of each optical head plus baffle: $100 \times 100 \times 300\,\mathrm{mm}^3$ = 3 litres
Dims. of proc. unit (housing both processors): $100 \times 100 \times 100\,\mathrm{mm}^3$ = 1 litre

Table 3.2 *Star tracker mass, power, volume budgets (for one spacecraft).*

Chapter 4

Measurement Sensitivity

4.1 Sensitivity

The sensitivity of the LISA mission is determined by the response, i.e. the *'output signal'*, of the interferometer to a gravitational wave of strength h on the one hand, and the effects of various noise sources that fake such gravitational wave signals on the other. We shall specify that relationship, as well as the terms "sensitivity" and "signal-to-noise ratio" SNR, in this section.

4.1.1 The interferometer response.

An interferometer of the Michelson type measures the phase difference between the two beams after they have returned from the two arms of length L, i.e. after each has traversed a total optical path of $\mathcal{L} = 2\,L$. Some noise effects (e.g. shot noise) will also fake such differences in phase (or optical path), and it is therefore a natural choice to express all effects in terms of this total optical path $\mathcal{L}$.

The strength of a gravitational wave is described by the "dimensionless amplitude" h, which, for normal incidence onto the light path, is defined as *twice* the relative change δL of a given distance L:

$$h \;:=\; 2\,\frac{\delta L}{L}\,, \tag{4.1}$$

or, in other words, a given length L will undergo an apparent strain $\delta L/L$ of $h/2$. If we assume a Michelson interferometer with orthogonal arms, a gravitational wave coming from the normal of the interferometer's plane, and with the appropriate polarization, would cause single-pass changes δL of opposite polarity in the two arms (having nearly equal geometrical lengths L_1 and L_2), and the *path length difference* $\delta\mathcal{L} = 2\,(\delta L_2 - \delta L_1)$, divided by the path length becomes

$$\frac{\delta\mathcal{L}}{\mathcal{L}} \;=\; h\,. \tag{4.2}$$

The difference scheme makes the response of a Michelson interferometer by a factor of two larger than that of a single arm.

For gravitational wave frequencies $f_{\rm GW}$ at which the interferometer path length $2L$ becomes an appreciable part of the gravitational wavelength $\Lambda = c/f_{\rm GW}$, the relation Eq. (4.2) has to be modified to

$$\frac{\delta\mathcal{L}}{\mathcal{L}} \;=\; h\,\mathrm{sinc}\left(\frac{2\pi L}{\Lambda}\right), \tag{4.3}$$

again assuming normal incidence and optimum polarization of the gravitational wave.

In the case of LISA, the two arms do not subtend a right angle, but one of only 60°, thus decreasing the response by a factor $\sin 60° = 0.8660$. Furthermore, the angle of incidence depends on the position of the source at the sky and on the momentary orientation of LISA which undergoes a continuous change during its orbit around the Sun. Figure 4.1 gives an example of the rather complex dependence of the LISA response while orbiting the Sun. Shown are, at a gravitational-wave frequency of 45 mHz and a source declination of 30 ° above the ecliptic, the orbit dependence for four different source azimuths $\alpha_{\rm s}$ and six different polarisations each [95].

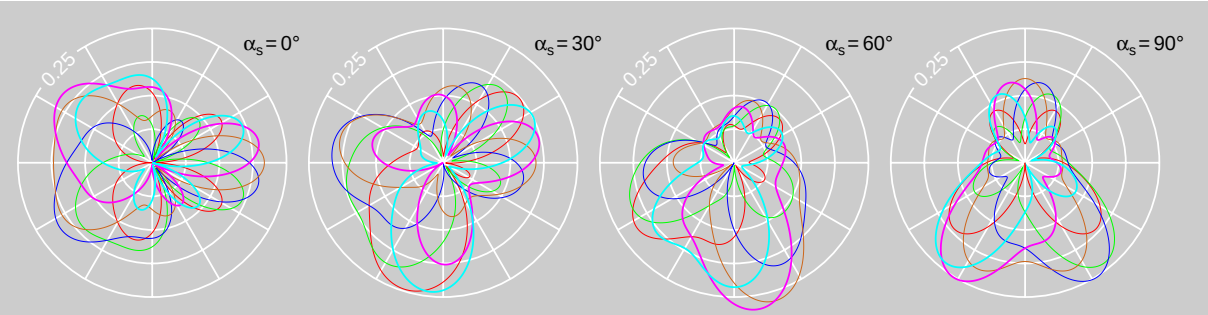

Figure 4.1 *Magnitude of the normalised LISA transfer function in dependence upon the orbit azimuth for a source at declination* 30° *and azimuths of* 0°, 30°, 60° *and* 90°, *at a frequency of 45 mHz. Six curves for different polarisation angles are shown in each diagram:* 0° *(red),* 15° *(green),* 30° *(blue),* 45° *(yellow),* 60° *(magenta) and* 75° *(cyan).*

When averaged over the different angles of incidence of the gravitational wave in the course of one year, the antenna response is smoothed out considerably, and the nulls in Eq. (4.3) disappear. Figure 4.2 shows the frequency response of LISA for four different source declinations δ after averaging over the orbit and all possible source azimuths and polarisations.

4.1.2 The noise effects.

Let us consider noise that will fake path differences $\delta\mathcal{L}_{\rm noise}$, then the level at which true gravitational wave signals can be reliably detected must be sufficiently above this noise level.

The required *signal-to-noise ratio* (SNR) will be dependent on a multitude of features of the expected signal, the characteristics of the noise, the duration of the measurement, etc. It has become practice to specify a SNR of 5, and a geometric factor of $\sqrt{5}$ to allow for less

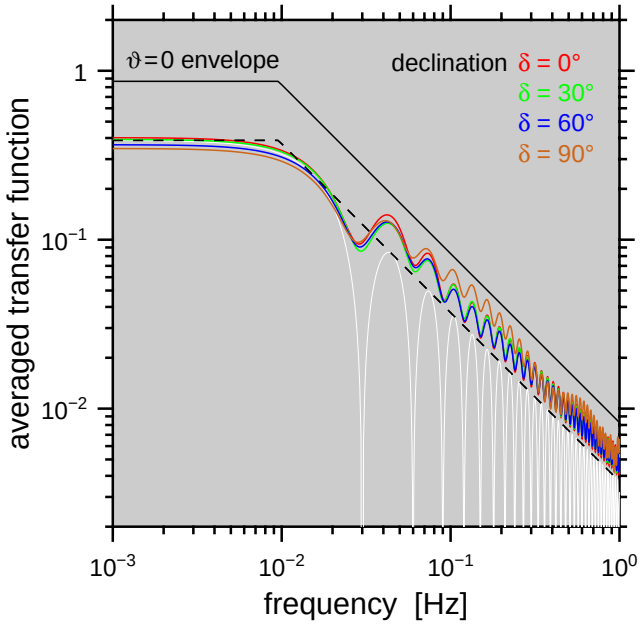

Figure 4.2 *Magnitude of the normalised LISA transfer function in dependence upon frequency after averaging over the orbit and all possible source azimuths and polarisations, shown for source declinations of* 0° *(red),* 30° *(green),* 60° *(blue) and* 90° *(yellow). For comparison, also shown are the envelope for normal incidence (black), the same line reduced by* $\sqrt{5}$ *(black, broken line) and the transfer function proper for such a case (white).*

optimal directions and polarizations. The measurement time is generally assumed to be 1 year, even though the lifetime of LISA would make longer measurement times possible. It is with these assumptions that the sensitivity curves in the figures of Section 1.2 have been drawn.

4.1.3 The noise types.

The sensitivity of LISA is determined by a wide variety of noise sources, and by the degree to which their effects can be kept small. There are two main categories of such sensitivity-limiting noise effects:

- A first one that fakes fluctuations in the lengths of the optical paths, which we will call *optical-path noise*. This category of disturbances includes different types of noise discussed earlier, such as shot noise and beam pointing instabilities. These contributions will, in general, be uncorrelated, and therefore adding quadratically the four contributions from the four passes gives the final (apparent) fluctuation in optical path difference.
- The second category is due to forces (or accelerations) acting on the proof masses. The drag-free environment will effectively shield the proof masses from outside influences, but some residual *acceleration noise* will remain. These accelerations will lead to displacement errors $\widetilde{\delta x}$ of the proof masses, and for each pass these errors have to be counted twice to arrive at the (real) fluctuation in optical path difference.

Considering these types of noise and the frequency dependence of the interferometer response as presented in Figure 4.2, one arrives at a typical sensitivity curve shown in Figure 4.3. In the low-frequency range, say below 2 mHz, the noise, and thus the sensitivity, is determined by the acceleration noise, leading to a decrease in sensitivity towards lower frequencies roughly propotional to f^{-2}. Above about 2 mHz the noise is dominated mainly by the shot noise, whereby the decline of the antenna transfer function above 10 mHz causes a decrease in sensitivity roughly proportional to the frequency.

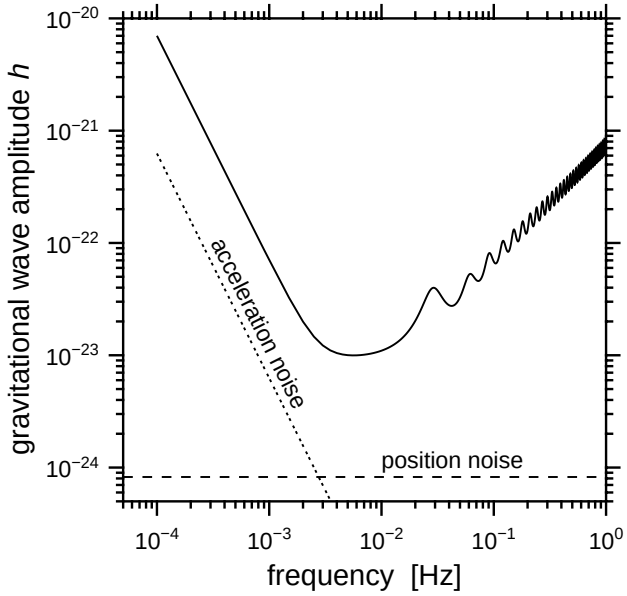

Figure 4.3 *LISA sensitivity for one year integration time and a signal-to-noise ratio of 5, averaged over all possible source locations and polarisations. Also indicated are the position noise (dashed line) and the acceleration noise (dotted line).*

The following subsections will discuss the most important noise sources, and means to suppress them. Their remaining influence is given in tabular form, separately for optical-path and acceleration noise.

4.2 Noises and error sources

4.2.1 Shot noise

Among the optical-path noise sources, a very fundamental one is *shot noise*, which for each *single* passage through an arm of length L leads to a *power* spectral density of apparent optical-path fluctuations

$$\mathcal{S}_{\delta L}(f) := \left(\widetilde{\delta L}(f)\right)^2 = \frac{\hbar c}{2\pi}\frac{\lambda}{P_{\text{avail}}}. \tag{4.4}$$

There are four such single paths, their uncorrelated contributions adding up quadratically to the final shot noise value $\widetilde{\delta\mathcal{L}}$, the apparent variation of the total path difference $\mathcal{L}_2 - \mathcal{L}_1$ in one LISA interferometer (see also Section 3.1.4).

The light power available, P_{avail}, is extremely low, due to the beam spreading ($P/P_0 < 2\times10^{-10}$) and the poor efficiency η of optics and photodiode ($\eta \approx 0.3$). Shot noise would therefore set a limit for the smallest detectable single arm-length variation of $\widetilde{\delta L} \approx 11\times10^{-12}\,\mathrm{m}/\sqrt{\mathrm{Hz}}$, assuming 1 W of laser power, or $\widetilde{\delta\mathcal{L}} \approx 22\times10^{-12}\,\mathrm{m}/\sqrt{\mathrm{Hz}}$, for the total path-length variation.

This fluctuation has to be set in relation to the path length $\mathcal{L} = 2\,L = 10^{10}\,\mathrm{m}$ over which the light has been subjected to the gravitational wave strain.

4.2.2 Optical-path noise budget

It will be our aim to keep all other *optical-path* noise contributions at a level comparable with the shot-noise induced sensitivity limit. A goal of an accumulated path-length noise of $\widetilde{\delta\mathcal{L}} \approx 40\times10^{-12}\,\mathrm{m}/\sqrt{\mathrm{Hz}}$ currently seems to be realistic, and this has led to error allocations as indicated in Table 4.1 .

Table 4.1 *Major sources of optical-path noise, and schemes to suppress their effects.*

Error Source	*Error**	*Number*	*Error Reduction Approach*
Detector shot noise 1 W laser; 30 cm optics	11	4	Optimise efficiency of optical chain
Master clock noise	10	1	Ultra-stable oscillators (USO) and correction procedure
Residual laser phase noise after correction	10	1	Use of phase noise correction algorithm
Laser beam-pointing instability	10	4	Active stabilisation of angular orientation of proof masses and spacecraft
Laser phase measurement and offset lock	5	4	Low noise electro-optic design
Scattered-light effects	5	4	Frequency offset; frequency stabilisation of laser to cavity
Other substantial effects	3	32	Careful mechanical and optical design
Total path difference	**40**	= measurement error in $\mathcal{L}_2 - \mathcal{L}_1$	

*) *Errors given in units of* $10^{-12}\,\mathrm{m}/\sqrt{\mathrm{Hz}}$

Detailed noise budgets have been set up, showing what error contributions can be allowed from the different effects. Such error allocations lead to specifications for the structural design, or for the control of various parameters. Many of the design features shown in Sections 3.1 and 3.2 are the result of these noise reduction considerations.

Table 4.1 gives the current error allocation budget, listing the cause of the spurious optical-path fluctuations, the allowed value (in units of $10^{-12}\,\mathrm{m}/\sqrt{\mathrm{Hz}}$), the number of such effects entering in one interferometer of four optical assemblies, and in the last column the means to cope with the problem.

Adding all these contributions quadratically, one arrives at the total path length variation of $40 \times 10^{-12}\,\mathrm{m}/\sqrt{\mathrm{Hz}}$ in the bottom line. It is this estimate of $40\,\mathrm{pm}/\sqrt{\mathrm{Hz}}$ that formed the basis of the sensitivity curves in the figures of Section 1.2.

The shot noise contribution in Table 4.1 was calculated assuming a 1 W laser and a diameter of 0.30 m for the optics (see Section 3.1).

Some of the major noise effects are discussed in more detail in the remainder of this section or in earlier sections.

Laser phase noise. Another optical noise source creating spurious optical-path signals is the *phase fluctuations* of the master laser. The four lasers on the four spacecraft are phase-locked with each other, but with about 17 s time delays for two of them because of the length of the interferometer arms. The requirements for measuring and correcting for the laser phase noise are discussed in Section 4.3.2.

Thermal vibrations. The proof masses and the optical structures have their resonant frequencies orders of magnitude above the frequency range of the gravitational wave signals. Nevertheless, thermal vibrations (*Brownian noise*) can produce spurious signals. We are searching for signals whose frequencies are well below the lowest resonant frequencies of the optical structure. The (kT) thermal vibration noise is composed of the sub-resonant tails of the (various) structural resonances. These vibrations, per proof mass, have *linear* spectral densities $\widetilde{\delta L}(f)$ of apparent arm-length fluctuations of a general form

$$\widetilde{\delta L}(f) \;=\; \left(\frac{4\,k\,T}{M\,Q\,\omega_0^2\,\omega}\right)^{1/2} \tag{4.5}$$

if we assume the (noisier) displacement-dependent 'structural damping' (imaginary spring constant) [96]. These noise sources will be very small for LISA, so they are not included in Table 4.1.

4.2.3 Acceleration noise budget

Table 4.2 gives the error allocation for spurious *accelerations*, mainly of the individual proof masses, the allowed value (in units of $10^{-15}\,\mathrm{m\,s^{-2}}/\sqrt{\mathrm{Hz}}$ at 10^{-4} Hz), and the number of such effects entering in one inertial sensor.

The allowed total effect of acceleration noise for one inertial sensor is $3 \times 10^{-15}\,\mathrm{m\,s^{-2}}/\sqrt{\mathrm{Hz}}$. The effect on the difference in geometrical arm lengths is then $6 \times 10^{-15}\,\mathrm{m\,s^{-2}}/\sqrt{\mathrm{Hz}}$. It is with these values, after multiplication with factors 5 (SNR) and $\sqrt{5}$ (for orientation and polarisation), that the sensitivity curves of Figures 1.3 and 1.4 were drawn.

To ease comparison of these acceleration errors with the allowed errors in optical path, the total was multiplied by two in the final line, to give $12 \times 10^{-15}\,\mathrm{m\,s^{-2}}/\sqrt{\mathrm{Hz}}$. A multiplication with ω^{-2} will give the optical-path error due to the contributions in Table 4.2.

Table 4.2 *Major sources of acceleration noise, and schemes to suppress their effects.*

Error Source	*Error**	*Number*	*Error Reduction Approach*
Thermal distortion of spacecraft	1	1	Carbon epoxy construction and limited power use variations
Thermal distortion of payload	0.5	1	Carbon-epoxy construction with $\alpha = 4 \times 10^{-7}$/K, plus two-stage thermal isolation of payload
Noise due to dielectric losses	1	1	Very low electrostatic coupling
Gravity noise due to spacecraft displacement	0.5	1	$1\,\mathrm{nm}/\sqrt{\mathrm{Hz}}$ control of spacecraft displacements with FEEP thrusters
Temperature difference variations across cavity	1	1	Three stages of thermal isolation plus symmetrical heat leak paths
Electrical force on charged proof mass	1	1	Small spacecraft displacements, $> 1\,\mathrm{mm}$ position-sensor gaps, and discharging of proof mass
Lorentz force on charged proof mass from fluctuating interplanetary field	1	1	Intermittent discharging of proof mass, e.g. with UV light
Residual gas impacts on proof mass	1	1	Less than $3 \times 10^{-7}\,\mathrm{Pa}$ pressure in proof-mass cavity
Telescope thermal expansion	0.5	1	Low-expansion secondary mounting plus two-stage thermal isolation
Magnetic force on proof mass from fluctuating interplanetary field	0.5	1	10^{-6} proof-mass susceptibility plus moderate spacecraft magnetic-field gradient
Other substantial effects	0.5	4	
Other smaller effects	0.3	16	
Total effect of accelerations :	3	for one inertial sensor	
Effect in optical path :	**12**	$=$ variation in $\dfrac{\partial^2}{\partial t^2}\,(\mathcal{L}_2 - \mathcal{L}_1)$	

*) *Errors given in units of* $10^{-15}\,\mathrm{m\,s^{-2}}/\sqrt{\mathrm{Hz}}$

Thermal distortions. Special care must be taken to avoid too strong a deformation of the spacecraft (optical bench) due to partial heating. Such inhomogeneous heating could arise from changing orientation with respect to the sun (which would have been particularly worrysome in an alternative option, the geocentric configuration). Multiple thermal shielding is used to keep the optical bench at a very stable temperature (about $10^{-6}\,\mathrm{K}/\sqrt{\mathrm{Hz}}$ at 1 mHz), with small temperature gradients.

Furthermore, the mass distribution of the main spacecraft structure is designed such that gravitational effects due to homogeneous expansion and even due to inhomogeneous deformation are kept small.

Section 5.1 gives details on how these thermal considerations entered into the design of the LISA payload.

Brownian acceleration noise due to dielectric losses. Dissipation intervening in the motion of the proof mass relative to the spacecraft is a source of Brownian acceleration noise. While damping due to residual gas is made neglegible by the very low pressure, losses in the electrostatic readout remain as a serious candidate for the residual dissipation. It is easy to calculate that any mechanism that results in a loss angle δ_ϵ in the effective capacitance between the proof mass and the sensing electrodes, also provides a loss angle δ to the (negative) stiffness $m\omega_{\rm int}^2$ of the effective spring originating from the electrostatic readout. Candidate physical phenomena for such a source of dissipation are surface losses due to adsorbed molecules, to oxide layers and to hopping of electrons among different workfunction minima. In addition, leakage of the electric field into lossy dielectric parts of the apparatus may also contribute.

In simple geometries one can expect $\delta \approx \delta_\epsilon$, and the resulting acceleration noise has a spectral density

$$\mathcal{S}_{\rm a} = \frac{4kT\,|\omega_{\rm int}|^2}{m|\omega|}\,\delta_\epsilon\,. \tag{4.6}$$

$|\omega_{\rm int}|^2$ is proportional to the square of the bias voltage needed to sense the mass displacement. Thus, though $|\omega_{\rm int}|^2$ can be reduced by reducing the voltage, this also causes a loss in displacement sensitivity. Fortunately, as repeatedly stated, LISA does not need a very high displacement sensitivity. As a consequence, $|\omega_{\rm int}|$ can be made as low as $|\omega_{\rm int}| \approx 10^{-4}\,{\rm rad/s}$. The mission goal is then met for $\delta_\epsilon < 10^{-6}$.

4.2.4 Proof-mass charging by energetic particles

As described in Section 2.8, the drag-free controller provides isolation from *external* dynamic disturbances, analagous to the seismic isolation on the ground-based gravitational-wave detectors. However, the system cannot cancel any forces that *act directly on the proof masses (mirrors).*

The primary disturbance forces are summarised in the preceding subsections. Of particular importance are those due to electrostatic charging, which are now discussed in detail.

Disturbances arising from electrical charging. Proof mass charging due to cosmic rays will produce spurious forces resulting from Lorentz forces due to the motion of the charged proof mass Through the interplanetary magnetic field, and from Coulomb interaction between the charged proof mass and surrounding conducting surfaces. These must be adequately attenuated.

Figure 4.4 shows the spectra for the most abundant primary cosmic ray constituents (protons and helium nuclei) inside the heliosphere. As far as LISA is concerned, these primary fluxes can be considered to be isotropic.

Modelling the charge deposition. Charge deposition depends significantly on secondary particle generation and detailed geometry, both of which are complicated to model analytically. Consequently, the GEANT radiation transport code [98] has been used. The

code employs Monte Carlo particle ray-tracing techniques to follow all particles (incident and generated) through three-dimensional representations of the LISA spacecraft geometry, taking into account all significant interactions. Table 4.3 shows the interactions that are currently modelled by GEANT. A more detailed discussion of the use of GEANT for this type of application can be found in [99].

The geometric model constructed for LISA is summarised as follows: the 4 cm gold cubical test body is surrounded on all faces by 25 μm gold electrodes mounted on a cubically-symmetric 15 mm shell of quartz, enclosed in a 5 mm thick titanium vacuum housing, surrounded by 1 cm of carbon-epoxy representing the spacecraft structure. On two opposing faces of the cube, quartz windows (7 mm diameter) have been inserted in the titanium, quartz, and electrode layers, representing the access windows for LISA's laser beams. Although this is a somewhat simplified representation, it does contain the key elements for accurate modelling, namely, a three-dimensional description of the intervening layers of material between the proof mass and the exposed spacecraft outer surface.

Figure 4.5 shows the computed net charging of the LISA proof mass as a function of incident particle energy. To produce this curve, GEANT was used to analyse the effect of isotropic particles striking the outer spacecraft walls, for a range of energies from 100 MeV

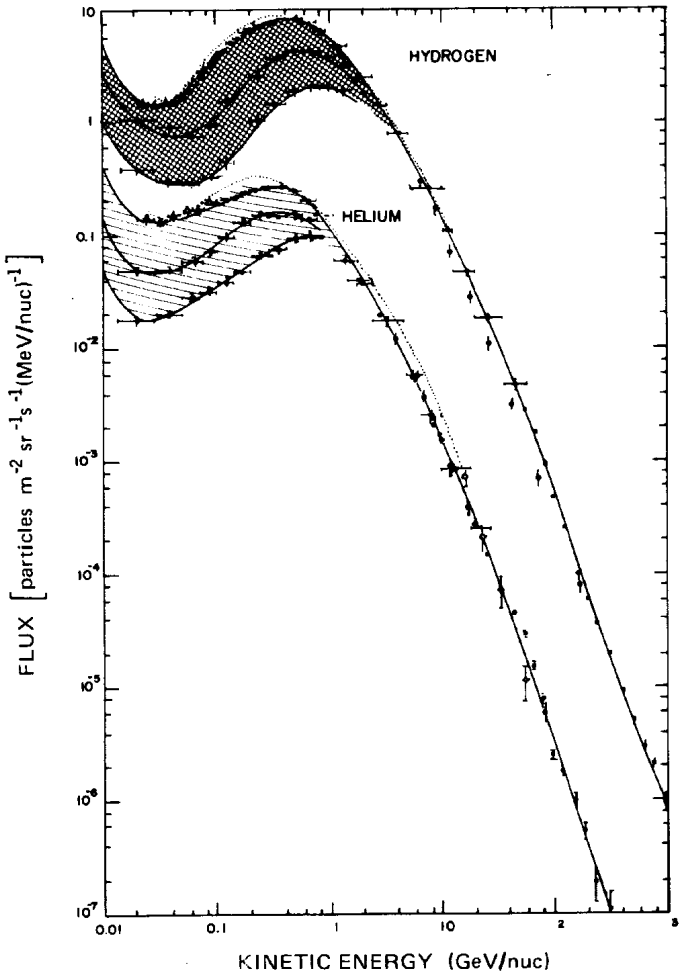

Figure 4.4 *Cosmic ray differential energy spectrum (reproduced from [97]). The hydrogen spectrum has been multiplied by a factor of 5 to avoid clutter. For each species, the upper envelope indicates the solar minimum spectrum, the lower envelope indicates the solar maximum spectrum. The shaded area indicates the range of the solar modulation over a solar cycle.*

Table 4.3 *Interactions modelled by GEANT (adapted from [98]).*

Processes involving the photon	(e^+, e^-) pair conversion Compton collision Photoelectric effect Photo fission of heavy elements Rayleigh effect
Processes involving e^+/e^-	Multiple scattering Ionisation and δ-rays production Bremsstrahlung Annihilation of positron Generation of Čerenkov light Synchrotron radiation
Processes involving μ^+/μ^-	Decay in flight Multiple scattering Ionisation and δ-rays production Ionisation by heavy ions Bremsstrahlung Direct (e^+, e^-) pair production Nuclear interaction Generation of Čerenkov light
Processes involving hadrons	Decay in flight Multiple scattering Ionisation and δ-rays production Hadronic interactions Generation of Čerenkov light

to 10 GeV. For each data point on the curve, 10^6 particles of a fixed energy were aimed randomly at the model (yielding adequate convergence of the Monte Carlo statistics). The curve contains no information on the actual spectrum of cosmic ray particles (this comes later).

In the figure, the charging has been normalised to the 'bare entry flux' which is a purely artificial number defined as *the effective isotropic flux of particles at a given energy which would enter the cube if it were freely exposed*. For example, consider the proton curve in Figure 4.5 which has a peak of 0.4 at an energy of 200 MeV. The 'bare entry flux' at this peak is defined as the number of 200 MeV particles which would enter an isolated cubical proof mass exposed to an isotropic flux of 200 MeV protons (it does not address the number of particles which then leave the body). The curve can thus be interpreted as saying that the number of 200 MeV protons stopped in the cube happens to be 0.4 of the 'bare entry flux'. These stopped protons are a combination of original (incident) protons which reach the proof mass having penetrated the intervening structure, as well as secondary protons generated somewhere along the way, which then end up reaching

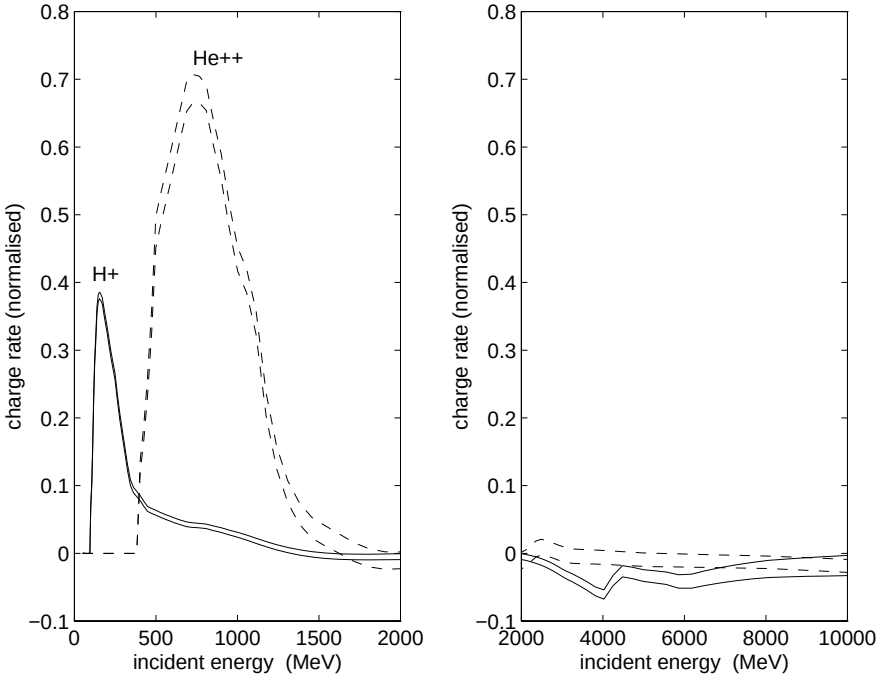

Figure 4.5 *LISA proof-mass charging versus incident particle energy. (The normalisation is described in the text.) For each species, there are two closely-spaced curves which differ only by the inclusion of low-energy electrons (see text).*

the proof mass. Therefore, the normalised plot contains information on the combined shielding power of the structure and the proof mass.

It turns out that the peak of the proton curve corresponds to the energy at which incident protons actually come to rest in the proof mass, having passed through the spacecraft structure. At higher energies, the charging is reduced but remains positive, and is due mostly to secondary protons stopping in the proof mass (most of the primary protons pass right through). At even higher energies ($> 2000\,\mathrm{MeV}$), the charging actually becomes negative, and is dominated by secondary electrons which stop in the proof mass (most protons, primary and secondary, pass right through). The curve for helium follows a similar trend, but is shifted to higher energies (by virtue of their larger size, helium nuclei require more energy to penetrate a material).

GEANT is only valid for energies in excess of 10 keV. To check whether low energy ($\leq 10\,\mathrm{keV}$) electrons unmodelled by GEANT could significantly affect the charge deposition, the ITS Monte Carlo code [100] was used to analyse the transport of low energy electrons in the near vicinity ($1\,\mu\mathrm{m}$) of surfaces. This explains the two closely-spaced curves for each species in Figure 4.5. The slight difference between the curves represents the inclusion of the effects of low-energy electrons. It is seen that the differences only become significant at high incident particle energies ($\sim 1000\,\mathrm{MeV}$) when the electrons are generated in large quantities.

The 'raw responses' in Figure 4.5 can now be 'folded in' with the cosmic ray spectra (Figure 4.4) to yield the desired result, namely, the charge rates due to cosmic rays. The

results of this convolution are shown in Figure 4.6. It can be seen that the charging is

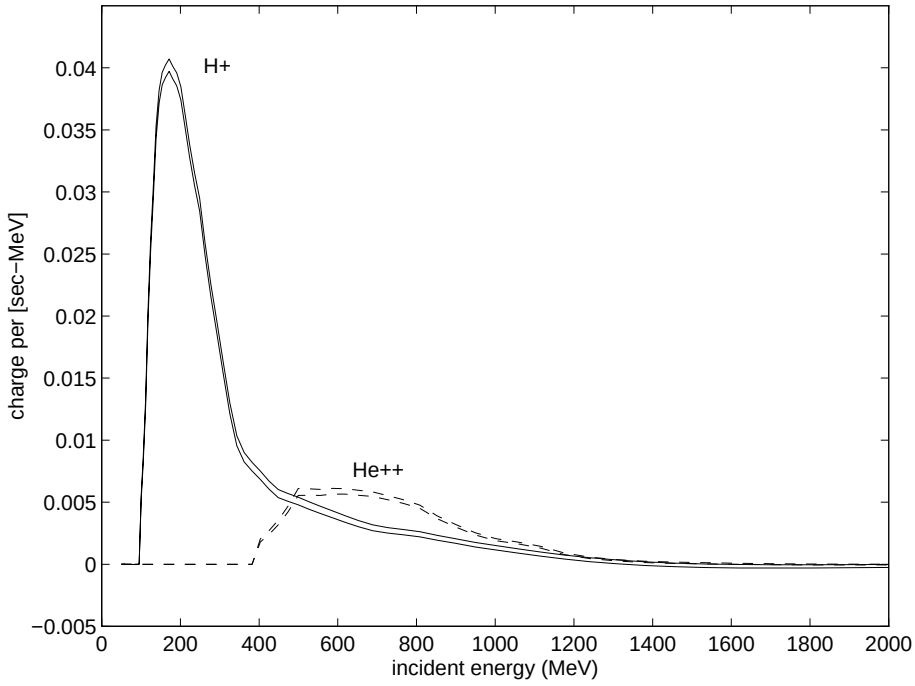

Figure 4.6 *Computed cosmic ray charging spectrum for the LISA proof mass. The results shown are for solar minimum, (and should be reduced by a factor of 4 for solar maximum).*

significant for incident particle energies up to 1000 MeV. To shield against these would require in excess of 25 cm tungsten, totally impractical for a space mission.

Integrating over energy yields a total charge rate of 11 protons/s (2×10^{-18} C/s) at solar minimum, with a discrepancy of $\pm10\%$ corresponding to the effects of low-energy electrons. Additional errors come from uncertainties in the cosmic ray spectra (error bars in Figure 4.4) which amount to $\pm30\,\%$ in computed charge rate. Therefore, the actual charge rate can be expected somewhere between 6 and 16 protons/s for solar minimum (and between 1 and 4 protons/s for solar maximum). It is interesting to note that although helium accounts for only 10 % of the cosmic ray incident flux, it is found to produce 30 % of the charging, owing to the comparatively high numbers of secondaries generated. Another interesting quantity is the ratio of stopped charge to the total rate of charges entering the proof mass if it were exposed directly to the cosmic ray flux. This ratio turns out to be 1:20 which shows that, (very) roughly speaking, 95 % percent of the cosmic rays pass straight through without any effect.

The cosmic rays are the dominant species only when the Sun is inactive. When it is active, an average solar flare will send out protons with sufficient energy to produce a charging of about 4×10^7 protons integrated over the event (calculated using GEANT with solar proton flux models from [101]). An anomalously large flare leads to 4×10^{10} protons. As discussed in [99], the frequency of flare events is skewed and asymmetric with respect to the solar cycle. In the seven-year neighbourhood of solar maximum, about eight average flares per year can be expected. In the three-year neighbourhood of solar minimum, the

frequency drops to about one per year. An anomalously large event can occur at any time in the cycle. However, a more recent reference [102] including information on solar flare cosmic rays from 1972 – 1987 with energies high enough to affect LISA indicates a considerably lower frequency of such events than the earlier data did. Although the charge rates are significant, the time history of the charging is correlated with the history of the flare event which lasts typically for a few hours, so the science data can simply be ignored during flares (as long as a subsequent discharging procedure is employed).

No account has been made for the errors in the GEANT modelling. These are difficult to assess. For conservativeness, a factor of two should be assumed.

Lorentz forces. For a given charge Q on the proof mass as it moves at velocity $\mathbf{v}$ through the interplanetary magnetic field $\mathbf{B}$, the acceleration disturbance is given by

$$\mathbf{a_n} = \frac{Q}{m}\,\mathbf{v}\times\mathbf{B}\,. \tag{4.7}$$

In order to investigate the spectral distribution of the disturbance, Eq. 4.7 can be expressed as follows,

$$\mathbf{a_n} = \frac{1}{m}\,\overline{\dot{Q}}\,t\,\mathbf{v}\times\overline{\mathbf{B}} + \frac{1}{m}\,\delta Q\,\mathbf{v}\times\overline{\mathbf{B}} + \frac{1}{m}\,\overline{\dot{Q}}\,t\,\mathbf{v}\times\delta\mathbf{B}\,, \tag{4.8}$$

where $\overline{\dot{Q}}\,t$ is the mean charge (at a given time), $\overline{\mathbf{B}}$ is the mean magnetic field, δQ are the fluctuations of charge about the mean value, and $\delta\mathbf{B}$ are the fluctuations in the magnetic field (higher order terms in δQ and $\delta\mathbf{B}$ have been neglected). The first term in Eq. 4.8 induces a drift of the proof mass, resulting in an armlength change. The rate of change of armlength is negligibly small, and, moreover, its noise components are insignificant in the measurement band.

Consider now the fluctuating terms in Eq. 4.8. In order to characterise the charge fluctuations (δQ), it can be assumed that the charging occurs in equal increments (one proton at a time) which are distributed randomly in time (a Poisson process). The (single sided) spectral density in the current flowing onto the proof mass ($\mathcal{S}_I$) is then given by [103]:

$$\mathcal{S}_I(f) = 2e\overline{\dot{Q}} \qquad (\mathrm{A}^2/\mathrm{Hz})\,. \tag{4.9}$$

(Compare this with the well-known representation for electrical 'shot noise'.) To convert from current to charge, the expressions for current must be integrated over time. This yields

$$Q(t) = \overline{\dot{Q}}\,t + \delta Q(t)\,, \tag{4.10}$$

where the first term ($\overline{\dot{Q}}\,t$) represents the average linear growth, and the second term (δQ) represents the fluctuations with a spectral density ($\mathcal{S}_Q$) given by

$$\mathcal{S}_Q = \frac{2e\overline{\dot{Q}}}{(2\pi f)^2} \qquad (\mathrm{C}^2/\mathrm{Hz})\,. \tag{4.11}$$

(The appearance of f in the denominator corresponds to the process of integration.) Substituting this into the second term in Eq. 4.8 yields the spectrum of acceleration

disturbance corresponding to δQ, namely

$$\sqrt{\mathcal{S}_a} \approx \frac{1}{m} \frac{\sqrt{2\,e\,\overline{\dot{Q}}}}{2\,\pi\,f} (\mathbf{v} \times \overline{\mathbf{B}}) \qquad (\mathrm{m\,s^{-2}}/\sqrt{\mathrm{Hz}})\,. \tag{4.12}$$

Putting in numbers, and imposing a limit of $10^{-16}\ \mathrm{m\,s^{-2}}/\sqrt{\mathrm{Hz}}$ for the acceleration, yields an upper limit of $2 \times 10^{-12}\,\mathrm{C/s}$ for the mean charge rate. This is almost six orders of magnitude above the expected charge rate, and so this effect can be neglected.

For the final term in Eq. 4.8, recent measurements of the interplanetary magnetic field variations (from the Ulysses spacecraft at 1 AU) have been used to derive $\delta\mathbf{B}$ and place limits on the allowable charge at which 10 % of the acceleration noise budget is reached. These are shown, versus frequency, in Figure 4.7. Also shown is the time taken to reach these limits, assuming the charging rates computed by GEANT (with a factor of two margin). It is clear that for low frequencies (10^{-4} Hz) the charge build-up exceeds the

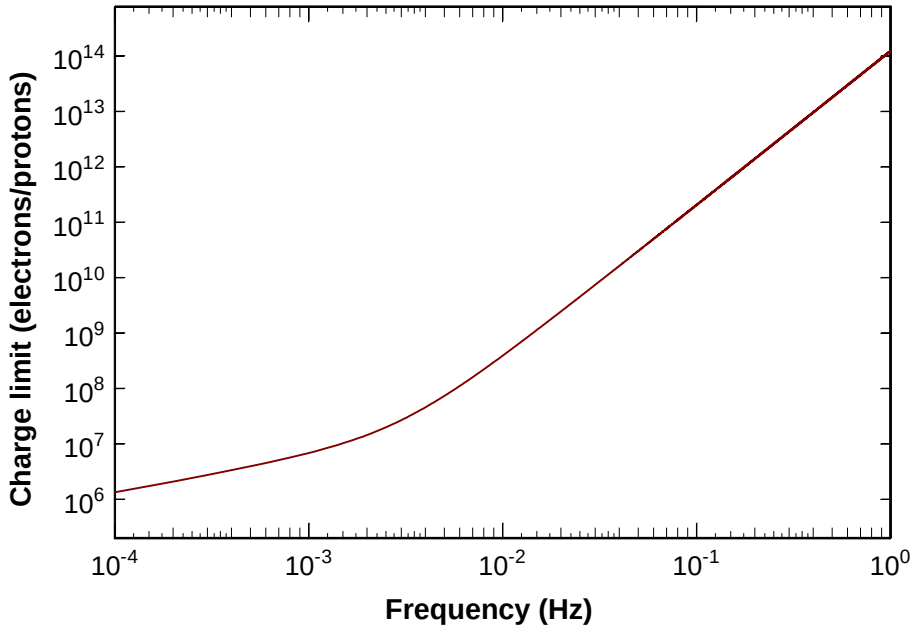

Figure 4.7 *Limit on allowable charge due to the Lorentz force disturbance as a function of frequency.*

allowable levels after an hour or so (the situation is less severe at higher frequencies), which means that the charge must be removed rather frequently. In principle this limit could be relaxed somewhat by employing closed electromagnetic shielding around the accelerometer. The precise extent to which this can be done is unclear but it is certainly reasonable to expect to be able to obtain an order of magnitude reduction in charge sensitivity. In fact it turns out that additional constraints on the charge level become the limiting factors beyond this level of shielding anyway. These are explored in the following sections.

Coulomb forces. Electrically the conducting proof mass surrounded by electrodes can be thought of as a bank of capacitors with the proof mass forming a common central

electrode. The proof-mass potential, V_T, due to any applied potentials, V_i, will be

$$V_T = \frac{1}{C}\sum_{i=1}^{n} V_i C_i \,, \tag{4.13}$$

where the summation is over all electrodes and the total capacitance is $C = \sum_{i=1}^{n} C_i$. If a free charge, Q, resides on the proof mass then the arrangement will have a total energy, E, which is a combination of stored energy in the electric fields, energy associated with the 'batteries' providing the applied potentials, and the interaction energy between the free charge and the applied potentials. This is given by

$$E = \frac{1}{2}\sum_{i} C_i \left(V_i - V_T\right)^2 + \frac{1}{2}\frac{Q^2}{C} + QV_T + \sum_{i} Q_{Bi} V_i \,. \tag{4.14}$$

Forces will act on the proof mass primarily through the capacitance gradients. In any direction, k,

$$F_k = -\frac{\partial E}{\partial k} = \frac{1}{2}\sum \frac{\partial C_i}{\partial k} V_i^2 + \frac{Q^2}{2C^2}\frac{\partial C}{\partial k} - \frac{Q}{C}\sum_{i=1}^{n} V_i \frac{\partial C_i}{\partial k} \,, \tag{4.15}$$

where we have assumed for simplicity that the electrostatic control system would normally ensure that $\sum_i C_i V_i = 0$, i.e. that

$$V_T = 0 \text{ and } \frac{\partial V_T}{\partial k} = \frac{1}{C}\sum_{i=1}^{n} V_i \frac{\partial C_i}{\partial k} \,. \tag{4.16}$$

The first term represents the electrostatic suspension and control forces, the second term is from spurious forces due to the interaction of any free charge with the surrounding electrode structures, and the third contains the interplay between the free charges and the applied potentials on the surrounding electrodes.

All terms involve the gradient of the capacitance which must be evaluated for the specific geometry of the proof mass and its surrounding electrode structure. For a simple displacement type sensor geometry, as used on the transverse degrees of freedom of the proof mass, the total capacitance gradient, $\frac{\partial C}{\partial k}$, comes from differencing the gradients from the opposing surfaces with the result that $\frac{\partial C}{\partial k} = 4\epsilon\frac{A}{g^3}\delta k$, where A is the electrode area, g is the gap between the electrode and the proof mass, ϵ is the permitivity of free space and $2\delta k$ is the difference in the gaps at the two opposing sides; i.e. the asymmetry in the arrangement. For an overlap type sensor geometry, as proposed for the sensing in the sensitive direction, the total capacitance gradient is again determined by asymmetries between the two ends. However in this case it is differences in the transverse dimensions of the electrodes and the transverse gaps which are important. For the LISA configuration each micron asymmetry in each of the critical dimensions gives rise to a capacitance gradient of typically $6 - 9\times10^{-13}\,\mathrm{F/m}$.

The total proof-mass capacitance with respect to its surroundings is $\approx 70\,\mathrm{pF}$. The electrostatic force acting on the proof mass due to free charge on it is then (using the second term in equation 4.15) $\approx 2.3\times10^{-30}\,n_\mathrm{e}^2$ $(\mathrm{N}\,\mu\mathrm{m}^{-1})$, where ne is the number of free charges on the proof mass. The corresponding acceleration is $\approx 1.8\times10^{-30}\,n_\mathrm{e}^2$ $(\mathrm{ms}^{-2}\,\mu\mathrm{m}^{-1})$.

The charge build up will be the result of the random arrival of cosmic rays, with each 'hit' depositing a variable amount of charge according to the stochastic nature of the interaction process. Following an argument similar to that already used for Lorentz force noise it turns out that the acceleration *noise* arising from this process can be approximated by

$$\tilde{a}_{\rm n} = 10^{-29.9}\, n_{\rm e} \sqrt{\dot{n}_{\rm e}}\, f^{-1} \ \ ({\rm m\,s^{-2}}/\sqrt{\rm Hz}\,)\,. \tag{4.17}$$

In order to keep this acceleration noise below its budget allocation the amount of accumulated charge must controlled such that

$$n_{\rm e} \leq 2\times 10^{13} f \left[1 + \left(\frac{f}{3\times 10^{-3}}\right)^2\right] \text{electrons/protons.} \tag{4.18}$$

This limit is much less severe than that from the Lorentz force noise. It has been based on a 1 μm 'asymmetry' assumption. Whether this is a reasonable figure to use remains to be confirmed.

Another source of acceleration noise which will occur if the proof mass becomes charged is through displacement noise modifying the electrostatic force. There are two components (arising from the second term in equation 4.15) due to changes in the total capacitance and in the asymmetry factor, which in turn affects the capacitance gradients. Adding these two in quadrature gives an acceleration noise (for the displacement type sensor geometry)

$$\tilde{a}_{\rm n} = \frac{Q^2}{mC^2}\frac{\partial C}{\partial k}\sqrt{\frac{1}{4\delta k^2} + \frac{1}{C^2}\left(\frac{\partial C}{\partial k}\right)^2}\,\tilde{k}_{\rm n} \ \ ({\rm m\,s^{-2}}/\sqrt{\rm Hz}\,)\,, \tag{4.19}$$

where $\tilde{k}_{\rm n}$ is the spatial displacement noise spectral density and all other symbols retain their earlier meanings. Putting in the numericalvalues for the LISA sensor design and using $\tilde{k}_{\rm n} = 10^{-9}{\rm m}/\sqrt{\rm Hz}$ gives $\tilde{a}_{\rm n} = 1.8\times 10^{-33}\, n_{\rm e}^2\ {\rm m\,s^{-2}}/\sqrt{\rm Hz}$.

The final noise source which will be discussed in this section arises from the interaction between any free charges on the proof mass and the applied control voltages, V_i, and any associated voltage noise, V_{ni}. Using the third term in equation 4.15 this noise component is given by

$$a_{\rm n}^2 = \frac{Q^2}{m^2C^2}\left(\sum_{i=1}^{n} V_{ni}\frac{\partial C_i}{\partial k}\right)^2 + \frac{Q^2}{m^2C^4}\left(\sum_{i=1}^{n} V_i\left(\frac{\partial C_i}{\partial k}\right)^2\right)^2 k_{\rm n}^2 \ \ ({\rm m^2\,s^{-4}}/\sqrt{\rm Hz}\,)\,. \tag{4.20}$$

The electrostatic forces which come about through the proof mass becoming charged bring with them associated effective spring constants. There are three effects, two of which involve the applied potentials and one which does not, which have been considered. The two involving the applied potentials are given by terms of the form $|K| \approx \frac{QV_{\rm cm}}{C}\,\frac{4\epsilon A}{g^3}$ and $|K| \approx \frac{2QV_{\rm cm}}{C}\,\frac{\partial^2 C_i}{\partial k^2}$, where $V_{\rm cm}$ and $V_{\rm dm}$ are the voltages applied in common mode and differential mode to electrodes on opposite sides of the proof mass. The second of these two spring constant terms is the most significant for the current sensor design. The spring constant term arising out of pure electrostatic interaction with the surrounding conducting surfaces is of the form (for displacement type sensor geometries) $|K| \approx \frac{Q^2}{2C}\,\frac{4\epsilon A}{g^3}$. This term

is not significant. A charge limit is then derived by requiring that these spring constant terms do not upset the nominal spring constant from the electrostatic control system by more than 10 %.

Summary of charge limits. The above charge limits for the LISA proof mass are summarised in Table 4.4 .. The most stringent limit comes from Lorentz force noise (note a factor of 10 is included to allow for some electromagnetic shielding from the partial titanium enclosure around the sensor). The next most critical effect is modification of the spring constant.

Table 4.4 *Summary of proof-mass charge limits and charge build up times*

Effect	*Charge Limit [electrons/protons]*	*Charging Time [days]*
Lorentz force acceleration noise	2×10^{6}	0.7
Electrostatic acceleration noise		
Stochastic charge arrival	4×10^{10}	1.4×10^{4}
Displacement noise	5×10^{8}	187
Control voltage noise	2×10^{11}	7×10^{4}
Spring Constant	10^{7}	3.7

Charge measurement using force modulation. The force modulation technique depends on applying oscillating potentials (dither voltages) to the electrode structure around the proof masses which then exert forces on the charged proof mass via the third term in equation 4.15. This induces an oscillatory motion in the proof mass which can be detected capacitively. The amplitude and phase of the response give the size of the charge and its sign. It turns out there is sufficient sensitivity in the displacement sensor for the dither to be applied in the transverse direction. If two opposing electrodes are used then the dither force is

$$F_{\rm d} = -\frac{Q}{C}\left(V_1\frac{\partial C_1}{\partial k} + V_2\frac{\partial C_2}{\partial k}\right), \tag{4.21}$$

where C is again the *total* capacitance and $\frac{\partial C_i}{\partial k}$ is the capacitance gradient associated with an individual surface. Assuming the proof mass is reasonably well centred within the two opposing electrodes, such that $\frac{\partial C_1}{\partial k} = -\frac{\partial C_2}{\partial k} = \frac{\partial C_o}{\partial k}$ and we apply equal and opposite voltages to the two sides (i.e. $V_1 = -V_2 = V_{\rm d}$) then the dither force is

$$F_{\rm d} = -\frac{2QV_{\rm d}}{C}\,\frac{\partial C_o}{\partial k}\,. \tag{4.22}$$

The charge measurement sensitivity is here defined as the charge, $Q_{\rm s}$, at which the induced acceleration just equals the system acceleration noise, $\Delta a_{\rm n}$:

$$Q_{\rm s} = \frac{m\Delta a_{\rm n} C}{2V_{\rm d}}\left(\frac{\partial C_o}{\partial k}\right)^{-1}. \tag{4.23}$$

The acceleration noise, $\Delta a_{\rm n}$, will depend on the spectral noise density, $\tilde{a}_{\rm n}$, and the measurement bandwidth of the dither sensing. The dither frequency must be high enough that the measurement time does not impinge much on the science observations. With a mean charging rate of $5\times10^{-18}\,$C/s the charge limit of 2×10^{6} electrons is reached in some $6.4\times10^{4}\,$seconds and so any charge measurement, whether it be continuous or intermittent, must have a response time small compared to this. The integration time, τ ($\sim$ inverse bandwidth), needed to achieve the required charge sensitivity is

$$\tau = \frac{m^2 a_{\rm n}^2 C^2}{4 V_{\rm d}^2 Q_{\rm s}^2} \left(\frac{\partial C_o}{\partial k}\right)^{-2} . \tag{4.24}$$

The integration times given by this equation using a 1 volt dither voltage are completely negligible compared to the charge build-up time and dither frequencies can be selected just above the science signal measurement range.

The proposed technique for control of the charge on the proof mass is described in section 3.2.6 .

Momentum transfer. Performing an analysis using poissonian statistics for arrival times to calculate the fluctuating force due to *momentum* imparted from cosmic ray interactions yields the following expression for the spectral density of momentum transfer in a given direction

$$\mathcal{S}_M \approx 2\,p^2\,\lambda \qquad (\mathrm{N^2\,s^2\,/\,Hz})\,, \tag{4.25}$$

where p is the momentum (in the given direction) per particle stopped in the proof mass, and λ is the number of particles stopped per second. Summing the effects of all particles (protons and helium), taking into account their directions, yields an acceleration of $\sim 2\times10^{-18}\,\mathrm{m\,s^{-2}/\sqrt{Hz}}$, which is two orders of magnitude below the desired sensitivity.

4.2.5 Disturbances due to minor bodies and dust

In order to provide a rough estimate of how often spurious signals might be generated by gravity forces due to minor bodies or dust grains passing by one of the LISA spacecraft, it is assumed that the disturbances take place with the point of closest approach along one of the interferometer arms. Only the acceleration of one proof mass is considered. Then the Fourier component of the proof mass acceleration at angular frequency ω is given by

$$a(\omega) = \frac{GM}{\omega R^2} \int_{-\infty}^{\infty} \frac{z^3 \cos y}{\left(z^2+y^2\right)^{3/2}}\, dy\,, \tag{4.26}$$

where R is the distance of closest approach, V is the minor body relative velocity, M is the disturbing mass, and z is defined as $z = \omega R/V$. Since

$$\int_{-\infty}^{\infty} \frac{z^2 \cos y}{z^2+y^2}\, dy = \pi z\, \mathrm{e}^{-z} \tag{4.27}$$

and

$$\int_{-\infty}^{\infty} \frac{z^4 \cos y}{(z^2+y^2)^2}\, dy = \frac{\pi}{2}\, z(1+z)\, \mathrm{e}^{-z}\,, \tag{4.28}$$

it is expected that the effective value of $a(\omega)$ will be approximately proportional to the *rms* of the above two expressions:

$$a(\omega) \approx \pi z \frac{GM}{\omega R^2}\sqrt{\frac{5}{8}+\frac{z}{4}+\frac{z^2}{8}}\ \mathrm{e}^{-z} = \frac{\pi\, GM}{RV}\sqrt{\frac{5}{8}+\frac{z}{4}+\frac{z^2}{8}}\ \mathrm{e}^{-z}\,. \tag{4.29}$$

We take the signal of interest to be the second derivative of the difference in length of two of the interferometer arms. For frequencies higher than the corner frequency f_c for the LISA antenna of about 3 mHz, the expected acceleration noise level $\tilde{a}_\mathrm{n}$ for LISA is given roughly by

$$\tilde{a}_\mathrm{n} = \tilde{a}_\mathrm{c}\left(\frac{\omega}{\omega_\mathrm{c}}\right)^2, \tag{4.30}$$

where $\tilde{a}_\mathrm{c} = 6\times10^{-15}\,\mathrm{m\,s^{-2}}/\sqrt{\mathrm{Hz}}$ and $\omega_\mathrm{c} = 2\pi f_\mathrm{c}$. Below f_c, a_n is equal to a_c down to at least 1×10^{-4} Hz, and then increases again at some lower frequency. Thus, for fixed R, since $a(\omega)$ is a monotone decreasing function of ω, the ratio of $a(\omega)$ to $\tilde{a}_\mathrm{n}$ will be a maximum somewhere below f_c. For simplicity, it is assumed below that $\tilde{a}_\mathrm{n} = \tilde{a}_\mathrm{c}$ down to zero frequency, although this won't be the case in reality.

The square of the signal-to-noise ratio S/N for detecting the disturbance is given by

$$(S/N)^2 = 2\int \frac{a(\omega)^2}{a_\mathrm{n}^2}\, df\,. \tag{4.31}$$

In terms of the dimensionless variable $z = \omega R/V$ this becomes

$$(S/N)^2 = \frac{V}{\pi R}\int \frac{a(z)^2}{a_\mathrm{n}^2}\, dz\,. \tag{4.32}$$

The integral divides naturally into two parts:

$$(S/N)^2 = \frac{\pi (GM)^2}{R^3 V a_\mathrm{c}^2}\ (I_1 + I_2)\,, \tag{4.33}$$

where

$$\begin{aligned} I_1 &= \int_0^{z_\mathrm{c}} \left(\frac{5}{8}+\frac{z}{4}+\frac{z^2}{8}\right)\mathrm{e}^{-2z}\, dz = \frac{13}{32} - \left(\frac{13}{32}+\frac{3}{16}\, z_\mathrm{c}+\frac{1}{16}\, z_\mathrm{c}^2\right)\mathrm{e}^{-2z_\mathrm{c}}, \quad \text{and} \\ I_2 &= \int_{z_\mathrm{c}}^{\infty} \frac{z_\mathrm{c}^4}{z^4}\left(\frac{5}{8}+\frac{z}{4}+\frac{z^2}{8}\right)\mathrm{e}^{-2z}\, dz = \left(\frac{5}{24}\, z_\mathrm{c} - \frac{1}{12}\, z_\mathrm{c}^2 + \frac{5}{24}\, z_\mathrm{c}^3\right)\mathrm{e}^{-2z_\mathrm{c}} - \frac{7}{12}\, z_\mathrm{c}^4\, \mathrm{E}_1(2z_\mathrm{c})\,, \end{aligned} \tag{4.34}$$

with $z_\mathrm{c} = \omega_\mathrm{c} R/V$. Here E_1 is the usual exponential integral.

It is useful to approximate $\frac{32}{13}(I_1+I_2)$ by $H(z_c)$, where $H(z_c)$ is defined as $H(z_c)=2z_c$ for $z_c<1/2$, and $H(z_c)=1$ for $z_c>1/2$. $H(z_c)$ is a maximum of 41 % too high at $z_c=0.5$, but is a very good approximation for both low and high values of z_c. Thus $(S/N)^2$ can be approximated by the following expressions:

$$\begin{aligned}(S/N)^2 &= \frac{13}{16}\pi\omega_c\left(\frac{GM}{RVa_c}\right)^2 \quad \text{for } R<V/(2\,\omega_c)\,,\\ (S/N)^2 &= \frac{13}{32}\pi\frac{(GM)^2}{VR^3(a_c)^2} \quad \text{for } R>V/(2\,\omega_c)\,.\end{aligned} \tag{4.35}$$

Even if the event time were known, the signal would not be detectable unless $S/N>3$. The differential rate $r(M)$ of small-body events with $S/N>3$ is

$$r(M)=\pi\,R^2_{(S/N=3)}F(M)\,, \tag{4.36}$$

where $F(M)$ is the differential flux of minor bodies and dust grains. From Eqs. (4.35), with $V=2\times10^4$ m/s, we get

$$\begin{aligned}\pi R^2_{(S/N=3)} &= 5.2\times10^{-3}\,M^2 \quad \text{for } R<5.3\times10^5\,\text{m}\,,\\ \pi R^2_{(S/N=3)} &= 2.9\times10^2\,M^{4/3} \quad \text{for } R>5.3\times10^5\,\text{m}\,.\end{aligned} \tag{4.37}$$

The flux of minor bodies and dust grains with masses less than about 0.1 kg is given by Grun *et al.* [104]. The results from their Table 1 can be fit for the higher part of the mass range by

$$I(M)=2.1\times10^{-19}M^{-1.34}\,\text{m}^{-2}\text{s}^{-1}, \tag{4.38}$$

where $I(M)$ is the integral flux of all bodies with masses greater than M. This expression gives a good approximation to their results down to about 10^{-9} kg, but is several orders of magnitude too high at lower masses.

For higher masses, estimates of the integral flux versus mass from Shoemaker [105] can be used. They are based on counts of impact craters versus size on the Moon, and careful analysis of the relation between crater size and the energy of the impacting body. The results appear to be consistent within the uncertainties with those from other sources of information.

Figure 1 of reference [105] gives an estimated curve represented by large black dots for the cumulative frequency per year of impacts on the Earth versus the equivalent energy of the impacts in megatons of TNT. Since 1 megaton of TNT is equivalent to 4.2×10^{15} J, for a typical impact velocity of 2×10^4 m/s, 1 megaton corresponds to an impact by a mass of 2.1×10^7 kg. Thus the results of Figure 1 of reference [105] can be converted to the integral flux of bodies with masses between roughly 2×10^4 and 2×10^{12} kg in the neighborhood of the Earth's orbit.

Shoemaker's results can be approximated by the following two power law expressions for the integral flux:

$$I(M) = 4.2\times10^{-18}M^{-0.88}\,\text{m}^{-2}\text{s}^{-1} \quad \text{for } 2\times10^4\,\text{kg}<M<2\times10^{10}\,\text{kg}, \tag{4.39}$$

$$I(M) = 1.7\times10^{-21}M^{-0.55}\,\text{m}^{-2}\text{s}^{-1} \quad \text{for } 2\times10^{10}\,\text{kg}<M<2\times10^{12}\,\text{kg}. \tag{4.40}$$

Eq. (4.39) intersects Eq. (4.38) at 1.5×10^{-3} kg, and it will be used, for simplicity, over the extended range from 1.5×10^{-3} to 2×10^{10} kg, even though it may well be too high below 2×10^{4} kg. It will turn out that this doesn't affect the final results appreciably.

From the above approximate integral flux curves, the differential flux versus mass $F(M)$ can be obtained by differentiating $I(M)$. Thus the differential rate $r(M)$ of small-body disturbances can be obtained from Eq. (4.36), using the expressions for $\pi R^2_{(S/N=3)}$ from Eq. (4.37). Integrating $r(M)$ over different mass ranges will then give the corresponding estimates of the contributions to the event rate Q.

For masses less than 1.5×10^{-3} kg, $R_{(S/N=3)}$ is much less than 3.5×10^{5} m, and

$$Q(M < 1.5\times10^{-3}) \approx 3\times10^{-23}\,\mathrm{s}^{-1}. \tag{4.41}$$

For larger masses up to 1.3×10^{7} kg, $S/N = 3$ requires $R < 5.3\times10^{5}$ km, and we get

$$Q(1.5\times10^{-3} < M < 1.3\times10^{7}) \approx 1.6\times10^{-12}\,\mathrm{s}^{-1}. \tag{4.42}$$

The next contribution, still using the integral flux from Eq. (4.39), but with a distance of $R_{(S/N=3)} > 5.3\times10^{5}$ m , yields

$$Q(1.3\times10^{7} < M < 2\times10^{10}) \approx 1.1\times10^{-10}\,\mathrm{s}^{-1}. \tag{4.43}$$

And, using Eq. (4.40) for the highest mass range, we have

$$Q(2\times10^{10} < M < 2\times10^{12}) \approx 1.5\times10^{-9}\,\mathrm{s}^{-1}. \tag{4.44}$$

From the above estimates in Eqs. (4.41-4.44), it is clear that most of the probability for an event observable by LISA comes from objects with large masses. Thus, improved estimates can be made for the important range of masses using the fact that z_c will be large. For $M > 4.1\times10^{8}$ kg, $R_{(S/N=3)}$ will be $> 5.3\times10^{6}$ m, and $z_c > 5$.

Two of the approximations made were that the point of closest approach for the disturbing body was along an interferometer arm, and that only one proof mass would be disturbed. It is estimated that removing these approximations would reduce the calculated disturbance probability by about a factor two. However, there are three spacecraft that can be disturbed, so a better estimate for the total LISA disturbance rate by masses of up to 2×10^{12} kg is about 2.4×10^{-9} per second, or roughly 8 % per year.

In considering the above estimate, it should be remembered that the instrumental acceleration noise was assumed to be constant below 3 mHz. With this assumption and for $M = 2\times10^{12}$ kg, the distance of closest approach is $R_{(S/N=3)} = 1.5\times10^{9}$ m. The time for the disturbing body to travel this distance is about 7.5×10^{4} s. Thus, if the acceleration noise level starts to rise at a shorter period than this, the probability of reaching $S/N = 3$ will be reduced. Also, as noted earlier, a S/N of 3 is adequate to observe the disturbance only if the time of the event is known.

The diameter for an asteroid with a mass of 2×10^{12} kg is roughly 1 km. At present less than 10 % of the Earth-crossing asteroids of this size or larger are believed to be known [106, 107], but future observing programs may detect most of them in the next 25 years. If LISA detected a disturbance with a period of a few hours to a few days, a rapid optical search for a nearby disturbing body should be feasible. Disturbances by comets also are possible, although their flux is believed to be somewhat lower in the mass range of interest and they generally have higher relative velocities.

4.3 Signal extraction

4.3.1 Phase measurement

Information is extracted from the beat signal as a time series of phase measurements. The phase of the beat signal between the received and transmitted beams is measured with the time base provided by the on-board USO in each of the spacecraft. The two laser beams being beat together have different frequencies because of gradual changes in arm length and because of the roughly 10 kHz offset frequencies used in the locking scheme. The expected Doppler shifts for arms 1 and 2 (see Sections 3.1.1 and 3.1.2 and Figure 3.1) are of the order of 1 MHz for annual orbit corrections, and could be kept below 20 kHz if necessary by monthly orbit corrections. For arm 3, the Doppler shifts may be as high as 15 MHz.

The phase of the laser heterodyne signals needs to be measured with an accuracy much better than the total error allocation of $40\,\mathrm{pm}/\sqrt{\mathrm{Hz}}$ and with a dynamic range of roughly 10^9 in order to perform the laser phase noise cancellation scheme. Forty picometers corresponds to 4×10^{-5} of a cycle, and the expected laser phase noise was estimated earlier to be roughly $30\,\mathrm{Hz}/\sqrt{\mathrm{Hz}}$ at 1 mHz (see Section 3.1.5). This corresponds to roughly $3000\,\mathrm{cy}/\sqrt{\mathrm{Hz}}$ for the phase noise at 1 mHz. In order to measure the phase to the necessary accuracy and with the desired dynamic range, the signal from each optical heterodyne detector is beat again against a suitable reference frequency from a comb of frequencies separated by intervals of 50 kHz, which are generated from the USO. The reference frequencies are chosen to place the final beat frequencies in the range of 75 to 125 kHz. A tracking filter is then used to remove phase noise above roughly 100 Hz in order to prevent aliasing of such noise into the phase measurements.

The resulting signals are then sent to the phase meters, where they are strongly amplified, clipped, differentiated, and clipped again to give positive-going zero-crossing pulses with standard shapes. In each measurement interval, the delay between the USO clock pulse defining the interval start and the next zero-crossing pulse is timed, and the total number of zero-crossing pulses is counted. From this information the integer and fractional numbers of zero crossings are determined for each interval. The results are then filtered to remove phase variations at frequencies above about 1 Hz, and the data set is reduced to a time delay and a count every 0.5 s.

4.3.2 Laser noise

The data are affected by the phase noise of the master laser in S/C 1, as well as orbital motions and gravitational waves affecting the long arms. However, the variations in the arm lengths in the frequency band of interest, roughly 0.1 mHz to 1 Hz, are small. Thus the apparent variations in the length of any of the arms can be analyzed to determine the laser phase noise as a function of time. For simplicity only arms 1 and 2 will be discussed here, but similar results can be obtained for observables that include arm 3 also.

The accuracy of the phase noise measurements will be degraded near harmonics of the frequencies corresponding to the round-trip travel times for the two arms. A weighted mean of the results for the two arms can be used to avoid this problem, but we assume

here that arm 1 is used and that the frequency of interest is well separated from any of the harmonics.

Following approximately the notation of Giampieri *et al.* [108], except using units of meters, the phase outputs of the diodes of spacecraft 1 and 2 are

$$\begin{aligned} s_1(t) &= p(t-2L_1/c) - p(t) + n_1(t) + h(t)\,, \\ s_2(t) &= p(t-2L_2/c) - p(t) + n_2(t) - h(t)\,, \end{aligned} \tag{4.45}$$

where $p(t)$ is the laser phase noise, L_1 and L_2 are the arm lengths, n_1 and n_2 are the separate shot noises and any other noises that are not common to the two arms, and h is the gravitational radiation signal. Transforming to the frequency domain we get

$$\begin{aligned} s_1(f) &= p(f)(\mathrm{e}^{4\pi i f L_1/c} - 1) + n_1(f) + h(f)\,, \\ s_2(f) &= p(f)(\mathrm{e}^{4\pi i f L_2/c} - 1) + n_2(f) - h(f)\,. \end{aligned} \tag{4.46}$$

An estimate of the clock signal is formed from arm 1 by

$$\widehat{p}(f) = \frac{s_1(f)}{\mathrm{e}^{4\pi i f(L_1+\delta L_1)/c} - 1}\,, \tag{4.47}$$

where our knowledge of the arm length L_1 is in error by an amount δL_1. Including the definition of s_1 we get

$$\widehat{p}(f) = p(f)\,\frac{\mathrm{e}^{4\pi i f L_1/c} - 1}{\mathrm{e}^{4\pi i f(L_1+\delta L_1)/c} - 1} + \frac{n_1}{\mathrm{e}^{4\pi i f(L_1+\delta L_1)/c} - 1} + \frac{h}{\mathrm{e}^{4\pi i f(L_1+\delta L_1)/c} - 1}\,. \tag{4.48}$$

Using the estimate $\widehat{p}$ and the definition of s_1 we define

$$\begin{aligned} \widehat{s}_1 &= \widehat{p}\,[\,\mathrm{e}^{4\pi i f(L_1+\delta L_1)/c} - 1]\,, \\ \widehat{s}_2 &= \widehat{p}\,[\,\mathrm{e}^{4\pi i f(L_2+\delta L_2)/c} - 1]\,. \end{aligned} \tag{4.49}$$

We then form the difference

$$(s_1 - s_2) - (\widehat{s}_1 - \widehat{s}_2) = P + N + H\,, \tag{4.50}$$

with

$$\begin{aligned} P &= p(f)\left[\mathrm{e}^{4\pi i f L_1/c} - \mathrm{e}^{4\pi i f L_2/c} - \frac{\mathrm{e}^{4\pi i f L_1/c} - 1}{\mathrm{e}^{4\pi i f(L_1+\delta L_1)/c} - 1}\left(\mathrm{e}^{4\pi i f(L_1+\delta L_1)/c} - \mathrm{e}^{4\pi i f(L_2+\delta L_2)/c}\right)\right] \\ N &= n_1(f) - n_2(f) - n_1(f)\,\frac{\mathrm{e}^{4\pi i f(L_1+\delta L_1)/c} - \mathrm{e}^{4\pi i f(L_2+\delta L_2)/c}}{\mathrm{e}^{4\pi i f(L_1+\delta L_1)/c} - 1} \\ H &= h(f)\left[2 - \frac{\mathrm{e}^{4\pi i f(L_1+\delta L_1)/c} - \mathrm{e}^{4\pi i f(L_2+\delta L_2)/c}}{\mathrm{e}^{4\pi i f(L_1+\delta L_1)/c} - 1}\right]. \end{aligned}$$

Expanding by using $4\pi f\delta L_1/c \ll 4\pi f L_1/c \ll 1$ and $4\pi f\delta L_2/c \ll 4\pi f L_2/c \ll 1$ these become

$$P \approx p(f)\,\frac{L_1\delta L_2 - L_2\delta L_1}{L_1}\,4\pi i f/c \tag{4.51}$$

$$N \approx \frac{n_1(f)L_2 - n_2(f)L_1}{L_1} \tag{4.52}$$

$$H \approx h(f)\,\frac{L_1 + L_2}{L_1}\,. \tag{4.53}$$

From the above expressions for $P(f)$, it is clear that the laser phase noise can be corrected for to the measurement noise level $N(f)$ if the arm lengths are known accurately enough, and if the measurement system has sufficient dynamic range.

In general, we assume that the difference in length of the two arms is known to 200 m, and the mean length to 20 km. The error in the arm length difference can then cause an error of 4×10^{-9} of the laser phase noise at $f = 1$ mHz, and 4×10^{-10} at $f = 0.1$ mHz. If the fractional difference in arm lengths is 1%, the errors in the laser phase noise corrections due to the uncertainty in the mean arm length are the same magnitude as the values given above.

Our model for the laser phase noise before correction at frequencies of 0.1 mHz to 1 Hz is based on the thermal stability of the reference cavity to which the laser in spacecraft 1 is locked for frequencies below about 3 mHz, plus the noise in locking to the cavity at higher frequencies. Our estimate for the locking noise comes from the results of Salomon *et al.* [109]. As a typical case, we take the fractional frequency noise in the laser to be $2\times10^{-11}/\sqrt{\text{Hz}}$ at 0.1 mHz, $1\times10^{-13}/\sqrt{\text{Hz}}$ at 1 mHz, and $2\times10^{-15}/\sqrt{\text{Hz}}$ at 10 mHz. As an example, the frequency noise at 1 mHz corresponds to a phase noise level of $5\times10^{-3}\,\text{m}/\sqrt{\text{Hz}}$. To correct for this to a measurement noise level of $4\,\text{pm}/\sqrt{\text{Hz}}$ requires a phase noise reduction of a factor 8×10^{-10}.

The measurement of the difference in arm length for arms 1 and 2 is then corrected for the laser phase noise, using the approximately known lengths of the arms. The requirement on knowing the difference in arm lengths is about 200 m, as assumed earlier. The arm lengths will be determined by combining ground tracking of the spacecraft with the observed arm length changes from the laser phase measurements, or, alternatively, by measuring a group delay with a modulation tone on the laser beam. If the arm lengths are very close to equal, the noise at the harmonics of the round-trip travel frequency will be less well determined, but the accuracy will still be sufficient for correcting the measured arm length difference. A similar process is used to correct the time series of the length of arm 3 minus the average for arms 1 and 2.

The advantage of on-board correction for the laser phase noise is that the data can be compressed by a factor of perhaps 5 before they are transmitted to the ground. This is because the arm length changes will be very smooth and the gravitational wave signals relatively small. The one disadvantage of having to correct for the laser phase noise is that a small fractional error will be made in the amplitude and phase of the gravitational wave signals in some cases. However, this error appears to be correctable for sources where the source direction and polarization can be determined.

4.3.3 Clock noise

An ultra-stable oscillator (USO) is required onboard for the phase measurements, for compensation of the orbital Doppler shifts, and for providing offset frequencies for laser

phase locking. Because of phase noise limitations for available space-qualified USOs, either the Doppler shifts must be kept very small or the USO phase noise must be measured. Current USOs have a stability (Allan standard deviation) of 1 to 2×10^{-13} for periods of 1 to 1000 s. At 1 mHz, this corresponds to a fractional frequency noise level of about $7\times10^{-12}/\sqrt{\text{Hz}}$. For a round-trip Doppler shift of 10 kHz and 5×10^{6} km arm lengths, the resulting noise in measuring variations in the length of one arm is $9\,\text{pm}/\sqrt{\text{Hz}}$.

As a practical matter, it would require frequent orbit corrections to keep the Doppler shifts small for even two arms of the interferometer, and the Doppler shift for the third arm would still be large. To avoid the USO stability limitation, the USO phase noise will be measured with a method suggested by Danzmann. In this method, sidebands of perhaps 200 MHz derived from the USOs will be modulated onto the laser beams sent both ways over arms 1 and 2 and one-way over the three short spacecraft separations. The received modulation signals will be used to successively phase-lock all of the USOs except the one in S/C 1 and to determine the phase noise of that USO in the same way as the laser phase noise is measured.

It is assumed that 10 % of the laser power on spacecraft 1 goes into each of two 200 MHz modulation sidetones, and that one of them is filtered out of the transmitted signal. A similar carrier and sidetone with a somewhat different offset frequency are generated on spacecraft 6 and offset phase locked to the received signals. When these signals arrive at spacecraft 1, phase measurements are made on both the carrier and the sidetone. For the carrier, the error budget allows about $\frac{1}{\sqrt{2}}\times40\,\text{pm}/\sqrt{\text{Hz}}$ for the phase error. For the sidetone, the factor 10 lower intensity will make the shot noise contribution to the error about three times larger. However, some of the systematic error sources will be common to the sidetone and the carrier, and will not affect the measurement of the sidetone frequency. As a rough estimate, we take $40\,\text{pm}/\sqrt{\text{Hz}}$ for the error in the measurement of the phase of the sidetone after the roundtrip over arm 1.

Because of the transit time over the arm, the error in determining the phase noise of the USO will be increased by a factor $1/K$, where K is the time delay factor from the previous section:

$$K = \left| \mathrm{e}^{4\pi i f L/c} - 1 \right| . \tag{4.54}$$

Here f is the frequency of the phase noise. For $f \ll 4.77\,\text{mHz}$, we get $K \sim f/(4.77\,\text{mHz})$. To reduce the phase noise in the Doppler correction signal to the level of $10\,\text{pm}/\sqrt{\text{Hz}}$ used later in our error budget, it can be shown that the following relationship is required:

$$0.25K > \nu_{\text{Doppler}}/(200\,\text{MHz}). \tag{4.55}$$

For a roundtrip Doppler shift of 1 MHz, this holds above about 0.1 mHz, except for very narrow bands around harmonics of the roundtrip travel frequency 30 mHz. For 15 MHz instead of 1 MHz, the relationship holds above 1.4 mHz, except for bands of width 3 mHz about harmonics of 30 mHz. Somewhat better performance can be obtained by using similar information from arm 2. These limitations would not seriously compromise the performance of arm 3 of LISA, and would have essentially no effect for arms 1 and 2.

4.4 Data analysis

The objective on data analysis for a gravitational wave detector is to reconstruct as far as possible the incoming gravitational wave. From the reconstruction, it is possible to make the kind of inferences about sources that we have described in Chapter 1. The parameters that describe the wave are:

- Its direction on the sky in, say, galactic coordinates (ℓ, b). These are constants that must be maintained during the observation. Proper motion and parallax are unlikely because the observations of Galactic objects are unlikely to attain better than a few arcminutes directional accuracy. (A stochastic background will not have a precise direction, but that caused by binaries may be anisotropic on the scale of tens of degrees.)
- Its amplitude and polarisation, or alternatively the amplitudes of two independent components h_+ and $h_\times$, and their relative phase. For most LISA sources, these are constant in time, or at least very slowly varying. Binary orbital precession will cause an intrinsic amplitude modulation of the signal. As LISA orbits the Sun, the projection of the wave on the detector will change, which also causes an apparent amplitude modulation, even if the intrinsic amplitude and polarisation of the signal remain constant.
- Signal phase $\Phi(t)$. Gravitational wave detectors are coherent detectors, because their operating frequencies are low enough to allow them to track the phase of the signal. The phase, as a function of time, contains interesting information if it is not regular: binaries that chirp, or even coalesce, provide important clues to their masses and distances in the phase function, and the phase function of a black-hole binary allows LISA to track the orbit to test general relativity.

The extraction of this information from the LISA data will use the same principles that have been developed for ground-based interferometers. But there are a number of important differences from ground-based instruments:

- LISA's data rate will be 10^3 times less than a ground-based detector, because LISA operates at much lower frequencies. The massive data-handling problems faced by ground-based interferometers [110] will not exist for LISA. All its data for one year will fit on a single disc, and the computational demands of the analysis are modest. In this section we will assume that the signal stream for LISA will consist of two 2-byte data samples per second. The actual data stream may be sampled more rapidly, but there is no useful gravitational wave signal data above 1 Hz, so the data stream will be anti-alias filtered and resampled at the Nyquist rate of 2 Hz.
- LISA's 3 arms form 2 independent detectors, in the sense that they record two independent components of the incoming gravitational wave. Ground-based detectors will also operate in groups of 2 or more for joint detection, but signal reconstruction and direction finding are very different, because the detectors are well-separated. LISA can, in the unfortunate event of the failure of one spacecraft, still reliably detect gravitational waves even operating as a single detector. This is possible because of the next important difference.

- LISA observes primarily long-lived sources, while ground-based detectors are expected to observe mainly bursts that are so short that frequency modulation is unimportant. LISA is able to find directions and polarisations primarily from the phase- and amplitude-modulation produced by its motion during an observation. Ground-based detectors will, of course, look for radiation from rotating neutron stars, and for this case the detection and signal reconstruction problem are similar to that for LISA, but LISA's lower data rate and lower frequency makes the analysis considerably easier.
- If LISA sees a gravitational wave background, it cannot identify it by cross-correlation with another independent detector. We will show in Section 4.4.5 below how LISA can discriminate one background from another and from instrumental noise.

In what follows we will consider in turn the methods used for data analysis and the expected manner and accuracy of extraction of the different kinds of information present in the signal.

4.4.1 Data reduction and filtering

Noise. The fundamental principle guiding the analysis of LISA data is that of *matched filtering*. Assuming that the LISA detector noise $n(t)$ is stationary (an assumption that is only a first approximation, but which will have to be tested), the noise power can be characterised by its spectral density, defined as

$$\mathcal{S}_h(f) \;= \int_{-\infty}^{\infty} \langle\, n(t)n(t+\tau)\,\rangle\; \mathrm{e}^{-2\pi i f\tau}, \tag{4.56}$$

where the autocorrelation of the noise $\langle\, n(t)n(t+\tau)\,\rangle$ depends only on the offset time τ because the noise is stationary. The subscript "h" on $\mathcal{S}_h$ refers to the gravitational wave amplitude, and it means that the detector output is assumed normalised and calibrated so that it reads directly the apparent gravitational wave amplitude.

So far we have not assumed anything about its statistics, the probability density function (PDF) of the noise. It is conventional to assume it is Gaussian, since it is usually composed of several influences, and the central limit theorem suggests that it will tend to a Gaussian distribution. However, it can happen that at some frequenciesthe noise is dominated by a single influence, and then it can be markedly non-Gaussian. This has been seen in ground-based interferometers. An important design goal of LISA will be to ensure that the noise is mainly Gaussian, and during the analysis the characterisation of the noise statistics will be an important early step.

Maximum likelihood and the matched filter. The most common way of assessing whether a signal of some expected form is present in a data stream is to use the *maximum likelihood criterion*, which is that one uses as the detection statistic the ratio of the probability that the given data would be observed if the signal were present to the probability that it would be observed if the signal were absent. This ratio has a PDF that depends on the PDF of the noise.

If the noise is Gaussian, then it can be shown that an equivalent statistic is the output of the *matched filter*. The prescription is as follows. Suppose one is searching for a signal of known form $s(t)$ (Fourier transform $\widetilde{s}(f)$). Then the matched filter for this signal is a function $q(t)$ whose transform is

$$\widetilde{q}(f) \ = \frac{\widetilde{s}(f)}{\mathcal{S}_h(f)} \, . \tag{4.57}$$

This equation shows that the filter is the signal weighted inversely by the noise *power*. This weighting cuts out frequency ranges that have excessive noise. The filter's output is simply the linear product of the filter with the data stream $x(t)$

$$c = \int_{-\infty}^{\infty} x(t) q(t) dt = \int_{-\infty}^{\infty} \widetilde{x}(f) \, \widetilde{q}^*(f) \, df \, . \tag{4.58}$$

For Gaussian noise the statistic c has a Gaussian PDF, so rare signals can be recognised at any desired confidence level by observing the standard deviation of c when the filter is applied to many data sets, and applying an appropriate decision threshold. Because this is the equivalent of the maximum likelihood criterion, the matched filter is the best linear filter that one can use to recognise signals of an expected form.

Detection in a continuous stream. In practice we don't know when to expect the signal s, so its filter must contain a time-of-arrival parameter τ: the filter must be made from the transform of $s(t - \tau)$ for an arbitrary τ. Using the shift theorem for Fourier transforms gives us the statistic that we expect to use in most cases,

$$c(\tau) = \int_{-\infty}^{\infty} \widetilde{x}(f) \, \widetilde{q}^*(f) \ \mathrm{e}^{2\pi i f \tau} \, df = \int_{-\infty}^{\infty} \frac{\widetilde{x}(f) \, \widetilde{s}^*(f)}{\mathcal{S}_h(f)} \, \mathrm{e}^{2\pi i f \tau} \, df \, . \tag{4.59}$$

This last form is simply an inverse Fourier transform. For data sets of the size of LISA's it will be efficient and fast to evaluate it using the FFT algorithm.

One recognises a rare signal in the data set by identifying times τ at which the statistic $c(\tau)$ exceeds a predetermined threshold confidence level. Of course, one must be confident that the detector was operating correctly while the data were being gathered, and this usually requires examining "housekeeping" or diagnostic data. If the data pass this test, then one has not only identified a signal $s(t)$ but also the fiducial time τ associated with it. The confidence level is set on the basis of the empirical PDF of the statistic $c(\tau)$ at times when no signal appears to be present.

Parameters. Of course, predicted signals are actually families whose members are parametrized in some way. Black-hole binaries emit waveforms that depend on the masses and spins of the two holes. Galactic binaries that do not chirp have a unique frequency (in the Solar barycentric frame). All discrete sources have a location on the sky, a polarisation, an amplitude, and a phase at the fiducial time τ. One has to construct families of filters to cover all possible parameter values. The usual covariance analysis allows us to estimate the likely errors in the determination of parameters, and this is the basis of the estimates made below of angular accuracy, polarisation, and so on.

Filtering for families of expected signals raises the possibility that the family could be so large that the computational demands would be severe. This is certainly the case

for ground-based detectors, where an all-sky all-frequency search for unknown rotating neutron stars in data sets of order one year in length will require a teraflop computer to carry out to the sensitivity limit of the detectors. But in the low-frequency range of LISA, the demands are considerably reduced. One year of data might occupy 250 MB of storage. Given what is today an easily achieved computing speed of 1 Gflop and a memory of 512 MB, a computer could perform a Fourier transform (the basis of the matched filter) in a time of order one second. Searching up to 10^4 error boxes on the sky for binaries, or 10^4 different chirp masses between 1 $M_\odot$ and 10^8 $M_\odot$ for coalescing binary systems, could be done in a day. By the time LISA is launched these will be even easier to do.

What is not trivial is searching for neutron stars and black holes falling into massive black holes. Here the parameter space is considerably larger, since even in a few orbits the signal can be dramatically affected by the spins of the objects and the amount of eccentricity of the orbit. Work is underway to estimate the computational demands of this problem, but we are confident that, by the time LISA is launched, even this filtering will not be very difficult.

Other signals. The LISA data will also be searched for unexpected signals. By definition, one cannot construct a matched filter for these. Instead, one implements a robust filter that responds to a wide range of signals of a given type. Candidates for these "discovery" filters are wavelets, fractional Fourier transforms, and nonlinear techniques like adaptive filters. These will be developed and proved intensively on the ground-based detectors, and LISA will benefit from that insight.

One source that is different from others is a possible random background of gravitational waves. This appears as an extra component of the noise $\mathcal{S}_h$. We will consider how to recognise it and determine its origin in Section 4.4.5 below.

4.4.2 Angular resolution

Introduction. The LISA mission consists of 3 spacecraft forming a laser interferometric antenna in a plane inclined 60° with respect to the ecliptic, the complete constellation describing an Earth-like orbit at a distance of $R = 1$ AU from the sun and trailing the earth in its orbit by 20° [111]. One spacecraft is placed at each corner of an equilateral triangle with baselines of 5×10^9 m, as was sketched in Figure 2.5 .

As the LISA configuration orbits around the Sun, it appears to rotate clockwise around its center, as viewed from the Sun, with a period of one year. This is indicated in Figure 4.8. As a nonmoving detector would reveal no information about the directional parameters of the source of the gravitational wave, all the information about the source parameters is contained in the variation of the detector response that results from LISA's orbital motion.

Firstly, the detector's sensitivity pattern is not isotropic; rather it projects a quadrupolar beam pattern onto the sky, which rotates with the detector. This rotating beam pattern modulates both the amplitude and phase of the measured waveform.

Secondly, the detector is moving relative to the source due to the periodic motion of its center around the Sun. This Doppler-shifting of the measured gravitational wave frequency of the results in a further phase modulation of the detector output. Both the beam-pattern

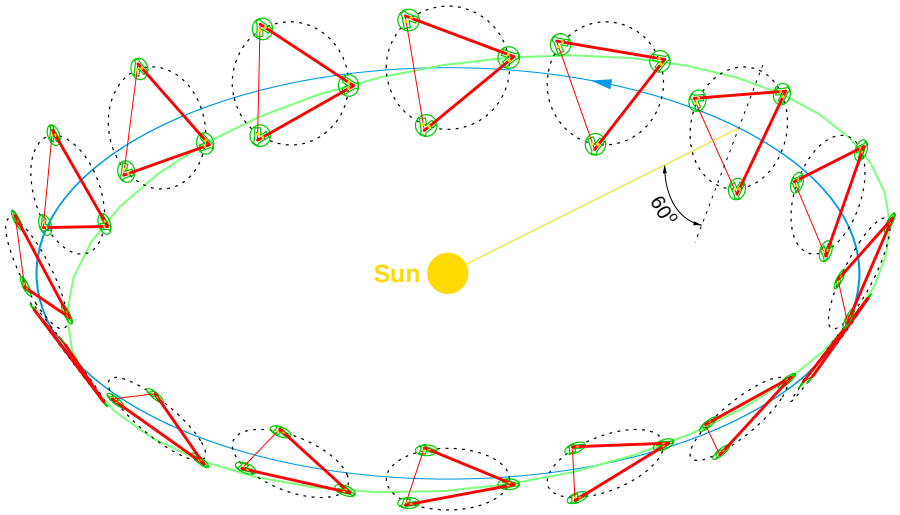

Figure 4.8 *Annual revolution of LISA configuration around the Sun, describing a cone with 60° half opening angle. One selected 2-arm interferometer is highlighted by heavier interconnecting laser beams. The "tumbling" motion of a single LISA interferometer allows the determination of the position of the source as well as of the polarisation of the wave. The (heavier) trajectory of one individual spacecraft is shown, inclined with respect to the (fainter) Earth orbit.*

modulation and Doppler modulation will spread a sharply peaked monochromatic signal into a set of sidebands separated from the carrier at integer multiples of the fundamental frequency $(1\ \text{year})^{-1}$. It is easy to see that the effects of the beam-pattern modulation and Doppler modulation are of roughly the same size. Consider a monochromatic signal with frequency f_0. In Fourier space, the effect of the beam-pattern modulation is to spread the measured power over (roughly) a range $f_0 \pm 2/T$, where T is one year. (The factor of 2 arises because the beam pattern is quadrupolar.) The effect of the periodic Doppler shift coming from the detector's center-of-mass motion is to spread the power over a range $f_0(1 \pm v/c)$, where $v/c \sim 10^{-4}$. These two effects are therefore of roughly equal size at $f_0 \sim 10^{-3}\,\text{Hz}$, which is near the center of the LISA band; beam-pattern modulation is more significant at lower frequencies and Doppler modulation is more significant at higher frequencies.

In the following chapters we review the way the source position, polarisation and intrinsic amplitude are encoded in the LISA datastream. After reviewing some standard methods of parameter estimation, we then present results on how accurately these physical parameters can be determined for two LISA sources of particular interest: stellar-mass binaries and merging MBH binaries. We refer the reader to [112, 113] for more details.

The beam-pattern modulation. The beam-pattern modulation can be calculated by transforming the metric-tensors

$$\mathbf{h}_\times := h_\times \begin{pmatrix} 0 & 1 & 0 \\ 1 & 0 & 0 \\ 0 & 0 & 0 \end{pmatrix} \qquad \text{and} \qquad \mathbf{h}_+ := h_+ \begin{pmatrix} 1 & 0 & 0 \\ 0 & -1 & 0 \\ 0 & 0 & 0 \end{pmatrix} \tag{4.60}$$

that are defined in the source frame, i.e. a system with its x-axis in the x-y-plane of the barycentric frame, its z-axis pointing towards the sun and the source at its origin. The transformation is split into one transforming the source system into the barycentric system and another one from the barycentric frame into the detector frame, which is rigidly fixed to the interferometer arms.

Let θ and ϕ be the Euler angles that define the source position in the barycentric frame, with its x-y-plane in the ecliptic, as indicated in Figure 4.9 .

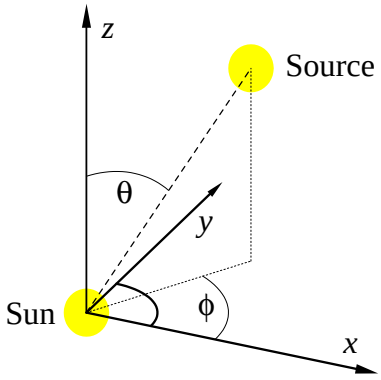

Figure 4.9 *Orientation of the source in the barycentric frame.*

The transformation into the source system is composed of two rotations. The first, realized by the rotation matrix $\mathbf{a_1}$, turns the y-axis of the barycentric frame on the projection of the line connecting sun and source on the ecliptic, that is counterclockwise through an angle $\phi - 90°$ around the z-axis,

$$\mathbf{a_1} := \begin{pmatrix} \sin\phi & -\cos\phi & 0 \\ \cos\phi & \sin\phi & 0 \\ 0 & 0 & 1 \end{pmatrix} . \tag{4.61}$$

A second rotation $\mathbf{b_1}$ turns the system counterclockwise around the new x-axis by $180° - \theta$. With $\mathbf{T_1} := \mathbf{b_1 a_1}$ the matrix $\mathbf{h}_+$ of Eq. (4.60) is transformed from the source system into the barycentric frame by

$$\mathbf{h}_+ \to \mathbf{T_1^t}\, \mathbf{h}_+\, \mathbf{T_1} . \tag{4.62}$$

The following angles are used to calculate the transformation into the detector system :

$$\psi_\mathrm{a} := 2\,\frac{\pi\, t}{T} \qquad \psi_\mathrm{b} := \frac{1}{3}\,\pi \qquad \psi_\mathrm{c} := -2\,\frac{\pi\, t}{T} + \alpha \tag{4.63}$$

where $\frac{1}{3}\,\pi$ is the angle of LISA with respect to the ecliptic and α is the phase between LISA's motion around the sun and the motion around its center of mass.

Now a rotation matrix $\mathbf{a_2}$ turns the frame of reference in the barycentric system counterclockwise around the z-axis by ψ_a, so the new y-axis points towards LISA. Then $\mathbf{b_2}$ turns it by ψ_b out of the ecliptic. Finally $\mathbf{c_2}$ turns it clockwise around the new z-axis by ψ_c. A vector is transformed from the barycentric into the detector system by $\mathbf{T_2} = \mathbf{c_2 b_2 a_2}$. Therefore e.g. the matrix $\mathbf{h}_+$ is transformed as :

$$\mathbf{h}_+ \;\to\; \underbrace{\mathbf{T_2}\,\mathbf{T_1^t}}_{=:\mathbf{T}}\, \mathbf{h}_+\, \mathbf{T_1}\,\mathbf{T_2^t} . \tag{4.64}$$

The Doppler modulation. The translational motion of the detector relative to the source leads to a phase modulation of the measured gravitational wave signal. This modulation can easily be calculated with the so-called barycentric transform between time of arrival at the Solar System and time at the detector [114]. In the former system, which can be considered to be a convenient inertial frame, the signal is not modulated and therefore of fixed frequency. Let $s_{\rm d}$ and $s_{\rm b}$ be the signals at the detector and at the barycenter, respectively; then by definition

$$s_{\rm d}(t_{\rm d}) \;=\; s_{\rm b}\left(t_{\rm b}[t_{\rm d},\theta,\phi]\right)\,, \tag{4.65}$$

where (θ,ϕ) is the angular position of the source (see Figure 4.9). The relation between the two time variables $t_{\rm b}, t_{\rm d}$ is given by

$$t_{\rm b}[t_{\rm d},\theta,\phi] = t_{\rm d} \;+\; \frac{\vec{n}(\theta,\phi)\,\vec{d}(t_{\rm d})}{c}\,, \tag{4.66}$$

with $\vec{n}$ being a unit vector pointing towards the source and $\vec{d}$ a vector connecting LISA and the sun:

$$\vec{n} = \begin{pmatrix} \cos\phi\,\sin\theta \\ \sin\phi\,\sin\theta \\ \cos\theta \end{pmatrix} \qquad \vec{d} = R\begin{pmatrix} \cos\frac{2\pi t}{T} \\ \sin\frac{2\pi t}{T} \\ 0 \end{pmatrix}. \tag{4.67}$$

Therefore the relation between the two signals $s_{\rm d}$ and $s_{\rm b}$ as functions of time is

$$s_{\rm d}(t_{\rm d}) = s_{\rm b}\left(t_{\rm d} \;+\; \frac{R\,\sin\theta}{c}\,\cos\left(\frac{2\pi t}{T} - \phi\right)\right). \tag{4.68}$$

So if the signal in the inertial frame is pure sinusodial of frequency $f_{\rm GW}$, in the detector response it appears as

$$\begin{aligned} s_{\rm d}(t_{\rm d}) \;&=\; \sin(\,2\pi f_{\rm GW} t_{\rm b}) \\ &=\; \sin\Big(\,2\pi f_{\rm GW} t_{\rm d} \;+\; \underbrace{\frac{2\pi f_{\rm GW} R\,\sin\theta}{c}\,\cos\left(\frac{2\pi t}{T} - \phi\right)}_{\Phi(t)}\Big)\,, \end{aligned} \tag{4.69}$$

including a phase modulation $\Phi(t)$ with a modulation index m of :

$$\begin{aligned} m \;&=\; \frac{2\pi f_{\rm GW} R\,\sin\theta}{c} \\ &\approx\; \pi\,\sin\theta\,\left(\frac{f_{\rm GW}}{1\,{\rm mHz}}\right). \end{aligned} \tag{4.70}$$

The LISA response to a gravitational wave. A gravitational wave which is purely sinusoidal in the barycentric frame causes a detector response given by :

$$\mathbf{H} \;=\; \mathbf{T}\begin{pmatrix} 0 & 0 & 0 & 0 \\ 0 & h_+ & h_\times & 0 \\ 0 & h_\times & -h_+ & 0 \\ 0 & 0 & 0 & 0 \end{pmatrix} \mathbf{T^t}\,\exp\left\{i\left[\,2\pi f_{\rm GW} t + \Phi(t)\right]\right\}\,, \tag{4.71}$$

with the phase modulation $\Phi(t)$ as given in Eq. (4.69) and the modulated amplitude $\mathbf{T}\,(\mathbf{h}_+ + \mathbf{h}_\times)\,\mathbf{T^t}$ (cf. Eq. 4.64). To see how the gravitational-wave detector works, recall that General Relativity predicts that a ray of light connects a set of points by an interval of zero or

$$\mathbf{ds}^2 = 0\,. \tag{4.72}$$

For simplicity, let us consider first one arm of the the detector, which we take to lie in first quadrant of the x-y plane, at an angle α to the x-axis. The above equation then becomes

$$\begin{aligned} 0 &= \mathbf{ds}^2 \\ &= g_{\mu\nu} dx^\mu dx^\nu \\ &= -c^2dt^2 + (1 + H_{xx}(t,\vec{x}))\,dx^2 + (1 + H_{yy}(t,\vec{x}))\,dy^2 + H_{xy}(t,\vec{x})\,dxdy \\ &\qquad + H_{yx}(t,\vec{x})\,dydx \\ &= -c^2dt^2 + [(1 + H_{xx}(s))\cos^2\alpha + (1 + H_{yy}(s))\sin^2\alpha \\ &\qquad + (\,H_{xy}(s) + H_{yx}(s)\,)\sin\alpha\cos\alpha]\,ds^2\,, \end{aligned} \tag{4.73}$$

where $ds \equiv \sqrt{dx^2 + dy^2}$. In the standard deDonder gauge in which we are working, the freely falling masses at the two ends of the arm maintain fixed coordinate locations (x, y, z). Thus the light travel time τ between the two ends is determined by

$$c\int_0^\tau dt \;=\; \int_0^L \sqrt{1 + H_{xx}(s)\cos^2\alpha + H_{yy}(s)\sin^2\alpha + \tfrac{1}{2}\Big(\,H_{xy}(s) + H_{yx}(s)\,\Big)\sin 2\alpha}\;\; ds\,. \tag{4.74}$$

Equivalently, we can say the arm length has changed by an amount δL given by (treating the metric perturbation as approximately constant during the trip, and expanding the square root):

$$\delta L = \frac{1}{2} L\Big[H_{xx}\cos^2\alpha + H_{yy}\sin^2\alpha + H_{xy}\sin(2\alpha)\Big]\,. \tag{4.75}$$

LISA is designed to measure the *difference* in the arm length changes, $\delta(L_1 - L_2)$. Actually, since there are three arms, LISA can measure two independent differences. We shall refer to the combination $L_1 - L_2$ as interferometer I, and to the combination $(L_1 + L_2 - 2L_3)/\sqrt{3}$ as interferometer II. For simplicity, we let L_1 make a 15^0 angle to the x-axis, while L_2 makes a 75^0 angle (i.e., $\alpha = \pi/12$ and $5\pi/12$ for L_1 and L_2, respectively).

From Eq. (4.75) one easily shows that the strains associated with these particular combinations are

$$\begin{aligned} h_{\rm I} &= \frac{\sqrt{3}}{4}\,(H_{xx} - H_{yy})\,, \\ h_{\rm II} &= \frac{\sqrt{3}}{4}\,(H_{xy} + H_{yx})\,. \end{aligned} \tag{4.76}$$

Thus $h_{\rm I}$ and $h_{\rm II}$ directly measure the $+$ and $\times$-polarisation components of a wave travelling perpendicularly to the plane of the detector. One can therefore think of LISA

as operating effectively like a pair of two-arm interferometers that measure orthogonal polarisations.

How is the noise in interferometer I correlated with that in interferometer II? This has not yet been analyzed in detail. However one can show that if the detector noise in the three individual arms is totally symmetric (so that all three arms have the same rms noise amplitude, and the correlation between any pair of arms is also the same), then the noise correlations between interferometers I and II exactly cancel out; they can be regarded as statistically independent detectors [113]. As a first approximation, then, we treat the noises in interferometers I and II as uncorrelated. It seems unlikely that a small correlation between them would significantly affect the results presented below.

A signal that is intrinsically monochromatic will be spread into a set of sidebands by the motion of the detector. The modulation contains all the information about the source position. This is illustrated in Figures 4.10 and 4.11, which show line spectra for one year of integration, for two different source locations. The frequency of the gravitational wave is 3 mHz and the dimensionless amplitude h_+ equals one; the output of interferometer I is shown.

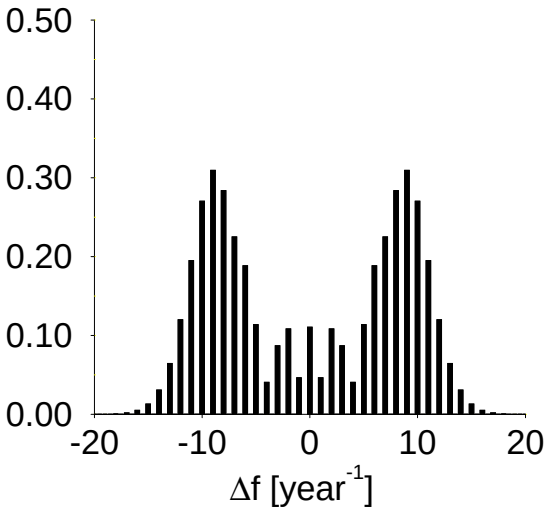

Figure 4.10 *Source at* $\theta = \frac{\pi}{2}$, $\phi = 0$.

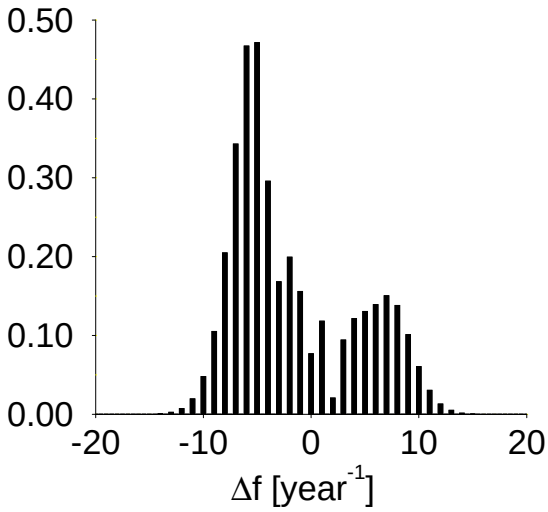

Figure 4.11 *Source at* $\theta = \frac{\pi}{4}$, $\phi = 0$.

Review of parameter estimation. The problem of measurement is to determine the values of some or all parameters of the signal [115]. It will be shown how accurately that can be done. In this section for simplicity we will consider a single datastream produced by a single interferometer (e.g., interferometer I); the generalization to a pair of outputs I and II is straightforward.

Consider a stream $s(t)$ that represents the pure detector output $h(\vec{\mu})$, parametrized by several unknown parameters μ_i collectively denoted as $\vec{\mu} = (\mu_1 = \theta, \mu_2 = \phi, \ldots)$ plus additional noise $n(t)$. Now one has to find a probability density function $\mathcal{P}(\vec{\mu}, s)$ for the parametrization $\vec{\mu}$ that characterizes the detector output $h(\vec{\mu})$. Assuming that $n(t)$ is a Gaussian process with zero mean, characterized by the one-sided power spectral

density $\mathcal{S}_n(f)$, it can be shown [116] that

$$\mathcal{P}(\vec{\mu}, s) \sim \exp\langle s, h(\vec{\mu})\rangle, \tag{4.77}$$

where the symmetric inner product is defined as

$$\langle s, h\rangle = 2\int_0^\infty \frac{\widetilde{s}(f)\widetilde{h}^*(f) + \widetilde{h}(f)\widetilde{s}^*(f)}{\mathcal{S}_h(f)}\, df\,. \tag{4.78}$$

From that definition it follows that, for a waveform $h(\vec{\mu})$, the signal-to-noise ratio is approximately given by

$$\frac{S}{N}[h(\vec{\mu})] = \frac{\langle h(\vec{\mu}), h(\vec{\mu})\rangle}{\mathrm{rms}\,(\langle h(\vec{\mu}), n\rangle)} = \sqrt{\langle h(\vec{\mu}), h(\vec{\mu})\rangle}\,. \tag{4.79}$$

The error in measurement is taken to be the width of the probability density function $\mathcal{P}(\vec{\mu}, s)$ for the measured value $\widehat{\vec{\mu}}$, i.e. the variance-covariance matrix

$$\Sigma_{ij} = \int (\mu_i - \widehat{\mu}_i)(\mu_j - \widehat{\mu}_j)\, \mathcal{P}(\vec{\mu}, s)\, d^n\mu\,. \tag{4.80}$$

For high signal-to-noise, Σ_{ij} is well approximated by $(\Gamma^{-1})_{ij}$, where Γ_{ij} is the so-called Fisher matrix, given by

$$\Gamma_{ij} = 2\int_0^\infty \frac{\partial_i\widetilde{h}(f)\,\partial_j\widetilde{h}^*(f) + \partial_j\widetilde{h}(f)\,\partial_i\widetilde{h}^*(f)}{\mathcal{S}_h(f)}\, df\,, \tag{4.81}$$

where $\partial_i \equiv \partial/\partial\mu_i$.

4.4.3 Polarization resolution and amplitude extraction

One can clearly estimate the amplitude of the waveform directly from the signal-to-noise of the detection; they are directly proportional. Given the output of both interferometers I and II, LISA should be able to extract both the amplitude and polarisation of the incoming wave, to an accuracy of order the inverse of the signal-to-noise ratio (though again the accuracy that is achievable also depends on correlations with the other parameters that one is trying to extract). Even if only a single interferometer output is available, LISA can still extract the amplitude and polarisation of the wave due to the rotation of the detector during its orbit. But clearly the yearly rotation of the detector is less helpful for determining the polarisation of shorter-lived sources such as merging MBH binaries, where most of the signal-to-noise will typically be accumulated in the final week before merger.

The same Fisher matrix calculation that tells us the angular resolution of the detector will simultaneously tell us how accurately the polarisation and amplitude of the source can be determined.

Results for monochromatic sources. In terms of sheer numbers, stellar-mass binaries will undoubtedly be the dominant LISA source. There are so many white dwarf binaries in the galaxy that they effectively form a stochastic background. In this section we consider measurements of a binary that is sufficiently close that it can be detected individually; i.e., its signal stands up above the detector noise and above the background from other binaries.

Binaries with small eccentricity are essentially monochromatic sources. To see this, note first that because the binary orbit is periodic, in Fourier space its gravitational radiation is made up of discrete lines at $f = 2/P$, $4/P$, $6/P$, etc., where P is the orbital period. (The sequence is multiples of $2/P$ instead of $1/P$ because the dominant radiation is quadrupolar.) For eccentricity $e < 0.2$, more than 60 % of the power comes out at the "fundamental" frequency $f = 2/P$, so in a first approximation we can ignore the higher harmonics. Next note that for an observation time of $T_0 \sim 1\,\mathrm{yr}$, the discrete Fourier transform sorts monochromatic signals into frequency bins of width $\Delta f = 1/T_0 \sim 3\times10^{-8}\,\mathrm{Hz}$. The typical timescale on which these binaries evolve is $\gtrsim 10^7\,\mathrm{yrs}$; so in one year's observation, a binary's emitted GW frequency changes by $\lesssim f/10^7 = 10^{-10}(f/10^{-3})\,\mathrm{H}$, i.e., much less than the width of one bin.

So a stellar-mass binary with roughly circular orbit is a monochromatic source, and conversely any monochromatic source can be thought of as a circular-orbit binary: possible polarisation states of the monochromatic source are in 1-to-1 correspondence with possible directions for the binary's angular momentum vector. Seven parameters are needed to completely characterize the waveform: its intrinsic frequency f_0, the source position θ and ϕ, the binary's orientation angles θ_L and ϕ_L, its overall amplitude $\mathcal{A}$ (proportional to $\mu(\pi M f_0)^{2/3}/D$), and its phase φ_0 at time $t = 0$. As emphasized above, one must extract all these parameters simultaneously; covariances between parameters invariably degrade the accuracy with which any particular parameter can be extracted.

The error box for the position measurement covers solid angle $\Delta\Omega$, given by

$$\Delta\Omega = 2\pi\sqrt{(\Delta\mu\,\Delta\phi)^2 - \langle\Delta\mu\,\Delta\phi\rangle^2}\ , \tag{4.82}$$

where $\mu \equiv \cos\theta$. The second term in brackets in Eq. (4.82) accounts for the fact that errors in μ and ϕ will in general be correlated, so that the error box on the sky is elliptical in general. The overall factor of 2π in the definition of $\Delta\Omega$ is chosen so that the probability $P(\beta)$ that the source lies *outside* an (appropriately shaped) error ellipse enclosing solid angle $\beta\Delta\Omega$ is just $P(\beta) = e^{-\beta}$.

Knowing the waveform's polarisation is equivalent to knowing the angular momentum direction $\widehat{L}$ of the corresponding circular-orbit binary. The accuracy with which this direction can be determined is similarly given by $\Delta\Omega_L$, where

$$\Delta\Omega_L = 2\pi\sqrt{(\Delta\mu_L\,\Delta\phi_L)^2 - \langle\Delta\mu_L\,\Delta\phi_L\rangle^2}\ . \tag{4.83}$$

Table 4.5 illustrates the accuracy LISA will have in measuring the source direction, polarisation, and amplitude of a monochromatic wave. Results are for one year of observation, normalized to total $S/N = 10$ for both interferometers I and II. (Thus, the S/N for interferometer I alone would be approximately $10/\sqrt{2} \approx 7.07$.) $\Delta\Omega$ is the size of LISA's error

box (in steradians) in source position, $\Delta\Omega_L$ the error box for the binary's orientation, and $\Delta\mathcal{A}/\mathcal{A}$ is the relative accuracy of the amplitude measurement. Cases A, B, and C refer to three representative choices of the four angles (μ, ϕ, μ_L, ϕ_L). These angles are: (0.3, 5.0, −0.2, 4.0) for A; (−0.3, 1.0, −0.2, 4.0) for B; and (−0.3, 1.0, 0.8, 0.0) for C. Each case is illustrated for three gravitational wave frequencies: $f = 10^{-4}$, 10^{-3}, 10^{-2} Hz. The subscript 'I' on $\Delta_{\rm I}$ indicates that the measurement corresponds to detection by interferometer I alone. Δ without a subscript indicates the result is for a combined measurement by interferometers I and II.

f [Hz]	*Case*	$\Delta_{\rm I}\Omega$ [sr]	$\Delta_{\rm I}\Omega_L$ [sr]	$\Delta_{\rm I}\mathcal{A}/\mathcal{A}$	$\Delta\Omega$ [sr]	$\Delta\Omega_L$ [sr]	$\Delta\mathcal{A}/\mathcal{A}$
10^{-4}	A	2.15×10^{-1}	3.81×10^{-1}	3.22×10^{-1}	8.27×10^{-2}	1.99×10^{-1}	2.04×10^{-1}
	B	2.23×10^{-1}	2.81×10^{-1}	2.38×10^{-1}	7.89×10^{-2}	9.78×10^{-2}	1.53×10^{-1}
	C	1.23×10^{-1}	8.48×10^{-2}	1.57×10^{-1}	7.11×10^{-2}	4.00×10^{-2}	1.02×10^{-1}
10^{-3}	A	1.07×10^{-1}	3.38×10^{-1}	3.21×10^{-1}	3.98×10^{-2}	1.69×10^{-1}	2.04×10^{-1}
	B	1.03×10^{-1}	1.62×10^{-1}	2.21×10^{-1}	3.83×10^{-2}	7.34×10^{-2}	1.53×10^{-1}
	C	6.51×10^{-2}	6.88×10^{-2}	1.56×10^{-1}	3.14×10^{-2}	3.44×10^{-2}	1.03×10^{-1}
10^{-2}	A	2.57×10^{-3}	3.50×10^{-1}	3.12×10^{-1}	1.08×10^{-3}	1.53×10^{-1}	2.04×10^{-1}
	B	2.90×10^{-3}	1.26×10^{-1}	2.21×10^{-1}	1.15×10^{-3}	5.78×10^{-2}	1.53×10^{-1}
	C	1.95×10^{-3}	4.22×10^{-2}	1.54×10^{-1}	7.66×10^{-4}	1.94×10^{-2}	1.02×10^{-1}

Table 4.5 *LISA's measurement accuracy for monochromatic sources, for a few representative choices of angles and gravitational wave frequency. Results are normalized to a combined $S/N = 10$. Cases A, B, and C refer to source direction and orientation angles, and are defined in the text. Error boxes $\Delta\Omega$ (for source position) and $\Delta\Omega_L$ (for source orientation) are in steradians. Results for interferometer I alone have subscript 'I'; other results are for the pair of outputs I and II.*

Table 4.5 shows that for monochromatic sources, having two independent outputs improves the position and polarisation resolution, $\Delta\Omega$ and $\Delta\Omega_L$ by a factor of only ~ 2; i.e., just the improvement that comes from the increased signal-to-noise. This basically tells us that the rotation of the detector over a one year observation time does indeed allow interferometer I alone to measure both polarisations rather effectively. LISA's $\Delta\Omega$ for monochromatic sources at $f = 10^{-3}$ Hz is typically $\sim 10^{-3} - 10^{-2}$ sr; LISA's angular resolution improves at higher frequencies due to the increased impact of the Doppler shift. LISA's polarisation resolution for these sources is typically $\Delta\Omega_L \sim 0.1$ sr, and $\Delta\mathcal{A}/\mathcal{A} \sim 0.1 - 0.2$. Here, too, if only a single interferometric output is available, the degradation in measurement accuracy comes mostly just from the loss in total signal-to-noise.

4.4.4 Results for MBH coalescence

Coalescences of MBH binaries, if they occur at sufficient rates to be observable, will be an exceptionally strong LISA source, with signal-to-noise ratios of $10^3 - 10^4$. Clearly, detecting

a population of MBH binaries would teach us a great deal about the early evolution of galaxies and the processes by which massive black holes are formed in the centers of those galaxies. There is also a possibility that several detections would allow us to determine to the basic cosmological parameters, H_0, Ω_0, and Λ_0, to high accuracy. The idea is that from the gravity-wave signal one should be able to read off the luminosity distance D_L to the source to roughly 1 % accuracy. (A naive estimate is that one should determine D_L to an accuracy of order $(S/N)^{-1} \sim 0.01-0.1\,\%$, but correlations with other parameters increase the error ΔD_L to of order 1 %; see below.) If one could identify the host galaxy or galaxy cluster, then one could determine the redshift z of the source optically. Clearly a handful of such measurements would suffice to determine H_0, Ω_0, and Λ_0 to roughly 1 % accuracy. So an important question is, will LISA have sufficient angular resolution to determine the host galaxy or cluster?

In principle we can answer this question in the same way as for monochromatic sources: just calculate the Fisher matrix and invert it. However for MBH mergers the parameter space is much larger and the signals much more complex. The physical parameter space $\mathcal{N}$ for MBH mergers is 17-dimensional:

$$\mathcal{N} = \left(D_L,\, M_1,\, M_2,\, \mu,\, \phi,\, \vec{S}_{1,0},\, \vec{S}_{2,0},\, \mu_{L,0},\, \phi_{L,0},\, e_0,\, t_0,\, \psi_0,\, \varphi_0\right), \tag{4.84}$$

where D_L is the luminosity distance; M_1 and M_2 are the masses of the two BH's; $\vec{S}_1$ and $\vec{S}_2$ are the spins; μ, ϕ, μ_L, and ϕ_L give the direction and orientation of the binary; e is the eccentricity; t_0 is the instant of time at which the orbital period has some fiducial value P_0; and ψ_0 and φ_0 indicate the direction of the semi-major axis and the value of the orbital phase at $t = t_0$. The subscript '0' added to $\vec{S}_1$, $\vec{S}_2$, μ_L and ϕ_L also refer to the values of these physical quantities at $t = t_0$; these quantities will generally vary with time due to the Lense-Thirring effect,which couples the the spins of the bodies to their orbital angular momentum.

To date, the Fisher matrix for this problem has only been calculated under the following simplifying assumptions [113]: that $e = 0$, that $\vec{S}_1$ and $\vec{S}_2$ are both parallel to the orbital angular momentum $\vec{L}$ (so that there is no precession of the orbital plane), and that both these facts are known *a priori*. By essentially ignoring some parameters, this simplified calculation is likely to overestimate somewhat the accuracy with which LISA can determine the others.

From the simplified calculation the following results emerge. The angular resolution $\Delta\Omega$ achievable by interferometers I and II combined is typically of order 10^{-4} steradians, or 0.3 square degrees. The angular resolution depends strongly on the masses and the particular angles involved, however. $\Delta\Omega$ is roughly in the range $10^{-5} - 10^{-3}$ steradians for masses in the range $10^5 - 10^7 M_\odot$; it is somewhat larger than this for lower-mass black holes, because the total S/N is generally smaller for lower masses. For MBH mergers, the angular resolution achievable by interferometers I and II combined is roughly an order of magnitude better than that achievable with detector I alone. This is quite different from the case of monochromatic sources, where the improvement was only a factor of ~ 2. This is because, in the MBH case, the time-scale over which most of the signal-to-noise is accumulated is typically a few weeks. Thus during time that the source is most visible, LISA's orientation hardly changes, and so having only one interferometric output would effectively LISA restrict to measuring a single polarisation.

LISA's distance determination accuracy $\Delta D_L/D_L$ for MBH mergers will be roughly in the range $0.1\,\% - 30\,\%$, with $\sim 1\,\%$ being typical. This is much worse than the naive guess of $\Delta D_L/D_L \approx (S/N)^{-1}$, due to correlations between D_L and the various angles describing the source. Large values of $\Delta D_L/D_L$ have a strong positive correlation with large uncertainties $\Delta\Omega_L$ in the binary's orientation. However LISA should determine the masses of the two BH's to very good accuracy indeed: typically $\Delta M_i/M_i \sim 0.1\,\% - 1\,\%$.

From the simplified calculation we have described, it is clear that LISA will not have sufficient angular resolution to determine the location of the the merging MBH binary from the gravitational waveform alone. This is because one square degree contains of order $10^4\,L_*$ galaxies. However, LISA could have sufficient angular resolution to facilitate simultaneous detections in the electromagnetic spectrum. This is because for events with $S/N \sim 10^3 - 10^4$, LISA should detect the inspiral several weeks before the final merger phase, and LISA's *one-degree* error box will be available more than a day before the final merger. Thus the source position will be known in time to train a battery of optical, radio, and X-ray telescopes at the roughly the right location on the sky, at precisely the right time. One can hope that some electromagnetic flare accompanies the MBH merger (due to the remnants of an accretion disk that one or both holes might carry with them), which would then identify the source. Clearly this would revive the possibility of using LISA to measure the cosmological parameters.

4.4.5 Estimation of background signals

Several types of background signals which either will or may be observable have been discussed previously. These are:

- a confusion-limited background due to unresolved galactic binaries;
- a similar background due to extragalactic binaries;
- possible cosmic backgrounds due to phase transitions in the early universe; and
- a possible primordial cosmic background due to quantum fluctuations before inflation.

An important issue for LISA is how well we can expect to do in identifying, separating, and quantifying these types of backgrounds.

As described earlier, backgrounds due to galactic neutron star binaries and white dwarf binaries will be observed at frequencies up to about 1 mHz. Hundreds to thousands of binaries of these kinds also will be observed as resolved signals, which are considerably stronger than the background or instrumental noise. Most of these will be at frequencies of roughly 1 mHz and higher. Their distribution in different parts of the galaxy such as the disk and the bulge will be determined from the measured directions and the statistics of the signal strengths. With this information, the galactic backgrounds can be modeled quite well, and fitted to the observations. The galactic backgrounds will be quite anisotropic because of the geometry of the galaxy.

The unresolved background due to extragalactic binaries will be quite different in nature. A few individual binaries from the LMC and other nearby galaxies probably will be resolvable. However, the universal background will have comparable contributions from equal

thickness shells ranging all the way out to cosmological distances, and thus will be nearly isotropic. The small anisotropies in the background due to nearby concentrations of stars such as the LMC, M31, and the Virgo cluster, as discussed by Lipunov *et al.* [117], will be difficult to detect.

The only handle for separating the possible cosmic backgrounds from the dominant isotropic part of the extragalactic binary background is the spectrum. There is enough uncertainty in the ratios of the numbers of binaries of various kinds in other galaxies to the numbers in our galaxy so that the strength of the extragalactic binary background cannot be predicted reliably. However, since the types of binaries contributing most strongly at the frequencies of interest probably will be evolving mostly by emitting gravitational radiation, the spectrum may be known quite well. If the spectrum of a cosmic background were significantly different and the amplitude were large enough, such a background could be separated and quantified.

Perhaps the most significant question is how well all of the backgrounds can be separated from instrumental noise. To discuss this question, it is useful to divide the instrumental noise above roughly 10^{-4} Hz into three different types. One is stationary noise with steady amplitude at all frequencies of interest. The second is noise which varies at one and two cycles/year, in such a way that it mimics the interaction of the galactic background with the rotating antenna pattern. The third is noise with all other types of time variations. The first and second types cannot be separated from isotropic and galactic backgrounds, respectively, except if they are substantially higher than experimental limits which can be put on instrumental noise. The third type of noise would not be confused with real background signals.

For measuring the difference in distances between proof masses, the main noise sources are photon shot noise and phase shifts from fluctuations in laser beam pointing. The shot noise contribution can be calculated from the received light level and at least partly subtracted out. For beam pointing fluctuations, it is difficult to say how much of the noise may be of the first two types, but an estimate of a third or less of the level given in the error budget seems reasonable. Specific experiments during the mission to characterize the noise by changing the gain of the beam-pointing servo loops and temporarily defocusing the beams somewhat should be considered.

For spurious accelerations of the proof masses, there are a number of items of comparable size in the error budget. A few, like random residual gas impacts on the proof masses, may be quite stationary, although they also may have variations at annual and six month periods from spacecraft temperature variations. However, it seems likely that most of the spurious acceleration sources will not be predominantly stationary. For example, this would apply to sources such as the interaction of the average charge on the proof mass with the fluctuations in the solar wind magnetic field. Consideration will be given to including diagnostic experiments, such as changing the average proof-mass charge or changing how tightly the spacecraft follow the proof masses, in order to characterize the spurious acceleration noise sources as well as possible.

Overall, it seems reasonable to estimate that perhaps a third of the total instrumental noise in the distance measurement and spurious acceleration error budgets would be difficult to separate from real background signals. The extent to which data from the third arm of LISA would aid in searching for background signals has not yet been investigated.

Chapter 5

Payload Design

5.1 Payload structure design concept

The design objectives for the payload structure are:

1. To ensure that the structure exhibits no modes of vibration below 60 Hz during launch.
2. To ensure that the structure exhibits no modes of vibration between 0.1 Hz and 10^{-4} Hz during operation.
3. To allow independent pointing adjustment for the two laser systems.
4. To minimise gravitational and optical disturbances due to thermally induced distortions.

An iterative design study, involving 3D-CAD modelling and Finite Element Analysis, has produced a conceptual design that meets the first three requirements. The fourth requirement is met to a greater extent, but further work is required to quantify acceptable levels of distortion and to model the behaviour of the structure in more detail.

The design has a number of features that arise from the requirement specifications:

- All of the optical components are mounted together within rigid subassemblies – the *optical assemblies* – to minimise changes to critical alignment dimensions.
- These two subassemblies are enclosed within the arms of the rigid Y-shaped payload thermal shield. They are attached to the inside by flex-pivot assemblies and pointing actuators to allow the alignment of the optical assemblies to be adjusted. These adjustments are made by moving each entire optical assembly within the payload thermal shield; the shield itself does not move with respect to the spacecraft during alignment.
- The payload thermal shield acts as the main structural member. In addition to the optical assemblies, the radiator plate is supported from the Y-tube's underside. It carries the lasers and their drive electronics, along with the UV discharge unit. Mounting the radiator plate in this manner minimises the number of interfaces with the spacecraft.

- Finite Element Analysis has shown that additional load paths are required to achieve the first structural design objective. These load paths take the form of launch-locks, which are retracted after launch.

The following sections describe the structural components and launch-lock concept in more detail.

5.2 Payload structural components

5.2.1 Optical assembly

One set of optical components (telescope, optical bench and support electronics), together with a payload cylinder, make up one optical assembly, as shown in Figure 5.1 .

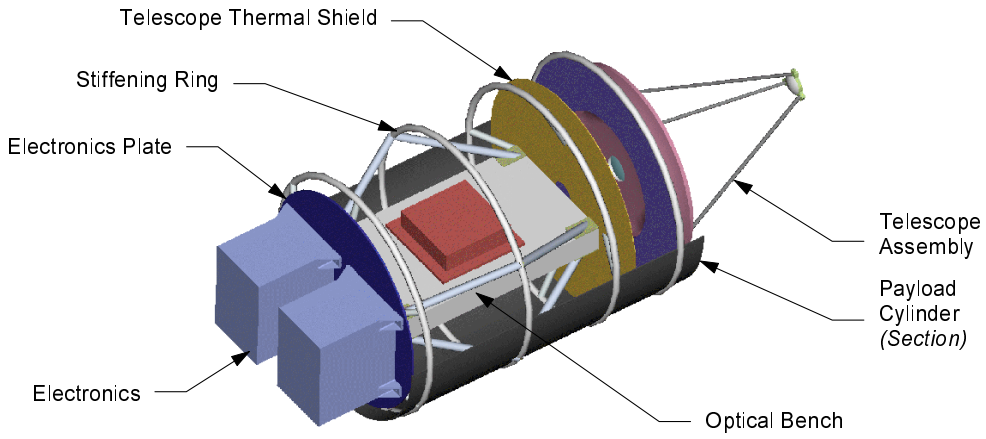

Figure 5.1 *Optical assembly, section view.*

Payload cylinder. The payload cylinder is a graphite-epoxy tube, 360 mm in diameter, 500 mm long and 2 mm thick. It is fabricated in at least two parts, so that sections can be removed in turn to allow access to the internal components after integration.

The cylinder is reinforced at intervals along its length by stiffening rings, suitably positioned to form mounting points for the optical components (see Figure 5.1). These rings are tubes, made from graphite-epoxy, 10 mm in diameter and 2 mm in wall thickness. They are either fabricated individually, then bonded onto the payload cylinder sections, or formed in sections as integral parts of the payload cylinder panels during their manufacture. Each ring is equipped with fittings into which the appropriate component support struts are attached (see descriptions to follow).

Telescope assembly. The telescope assembly is mounted from the first stiffening ring. It uses graphite-epoxy or stainless steel blade mounts to accommodate the radial thermal expansion of the ULE primary mirror and the payload cylinder. No detailed design of this assembly has been conducted to date.

Telescope thermal shield. The telescope thermal shield is mounted from the second stiffening ring. It is a disc of graphite-epoxy, 350 mm in diameter and 1 mm thick, with a 40 mm diameter hole through the centre to allow passage of the laser light. The shield is mounted to the stiffening ring with four Pyroceram support tubes, each 5 mm in diameter and 1 mm wall thickness, approximately 80 mm long.

Optical bench. The optical bench is suspended from the third stiffening ring by eight Pyroceram support tubes (each 10 mm in diameter, 2 mm wall thickness and approx. 200 mm long) to four points on the ring. The orientation of these tubes and their attachment points are indicated in Figure 5.2 .

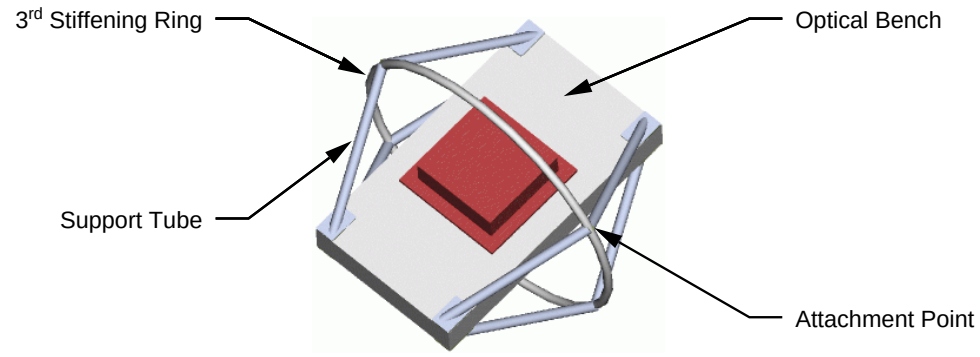

Figure 5.2 *Optical bench attachment.*

The use of four attachment points, rather than two, significantly increases the rigidity of the assembly, enabling it to meet the stiffness requirements for launch.

Electronics plate. The electronics plate (a graphite-epoxy disc, 330 mm in diameter and 3 mm thick) supports the electronics that need to be positioned near to the optical bench. It is attached to the fourth stiffening ring by six Pyroceram support tubes (each 5 mm in diameter, 1 mm wall thickness). The accommodation study conducted has shown that there is insufficient room on the electronics plate to house the ultra-stable oscillators (USOs) in addition to the other electronics units. The USOs have therefore been mounted on their own plate (see Section 5.2.3).

Flex-pivot assembly. The rear of each optical assembly is attached to the payload thermal shield by four flex-pivot beams. One end of each beam is attached to the fourth stiffening ring of the optical assembly. The other end is attached to one of two flex-pivots, situated inside the payload thermal shield where the two Y-tube arms intersect, see Figure 5.3 .

The pointing actuators and return mechanisms are mounted diametrically opposite one another, between the first stiffening rings of the optical assemblies and the payload thermal shield. Thus the flex-pivot assembly can swing the optical assemblies from side to side (in the plane of the Y) without inducing translation or roll in other directions. The flex-pivot beams are graphite-epoxy tubes, 30 mm in diameter, 460 mm long and with 2 mm wall thickness. The pointing actuators are conceptually piezo-devices attached to worm drives. They may need to be fully retractable, so that they can be stored unloaded during launch.

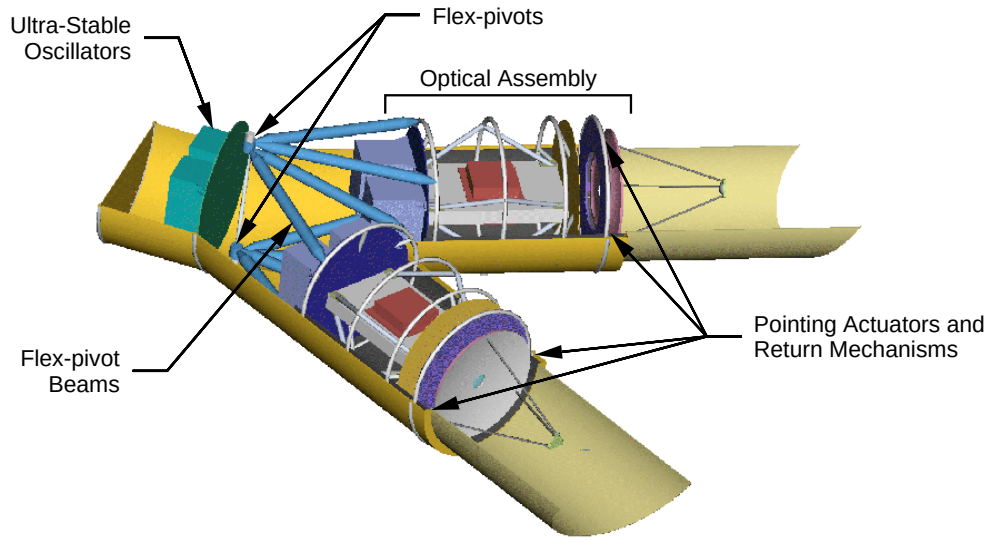

Figure 5.3 *Flex-pivot assembly, section view.*

The return mechanisms are spring-loaded to keep the optical assemblies in contact with the pointing actuators.

5.2.2 Payload thermal shield

The payload thermal shield is an assembly of graphite-epoxy cylinders (two Y-tube arms, the Y-tube stub and the two baffles), reinforced by stiffening rings at various locations, as shown in Figure 5.4 .

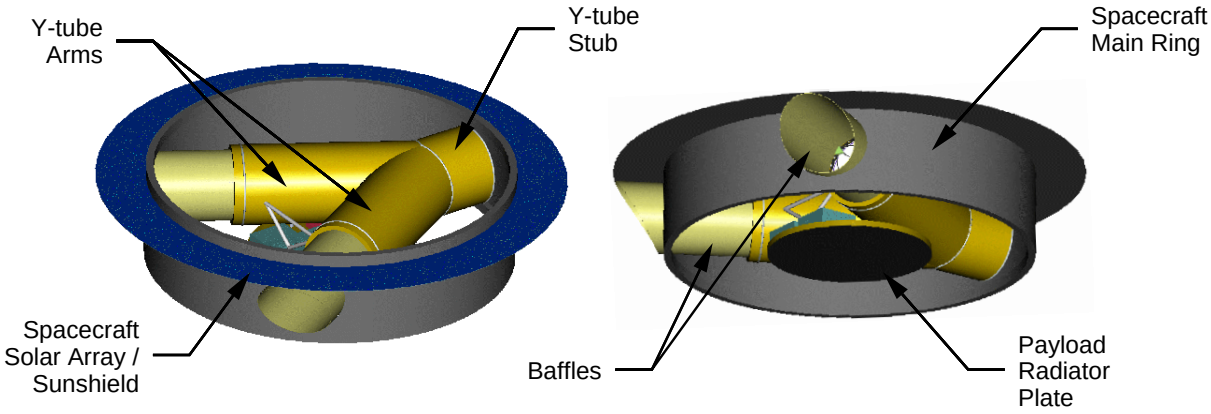

Figure 5.4 *Y-shaped payload thermal shield, viewed from above and below.*

The "stub" of the payload thermal shield houses the ultra-stable oscillators, and is connected to the Spacecraft via three stressed fibreglass bands around its circumference. Blade-mounts attach each "arm" of the payload thermal shield to the spacecraft, at the point where the baffles meet the spacecraft ring. These blade-mounts allow longitudinal expansion of the Y-tube arms (due to thermal effects), whilst preventing motion in other directions.

Launch-locks. Finite Element Analysis has shown that launch-locks will be required if the payload is to achieve the first structural design objective, i.e. to avoid resonances below 60 Hz during launch.

The first set of launch-locks reinforce the attachment of the payload to the spacecraft structure. They connect the baffles to the spacecraft ring during launch.

The second set of launch-locks attach the rear of the optical assemblies directly to the inside of the payload thermal shield. They are positioned at the top and bottom of the fourth stiffening ring.

Further detailed design and optimisation of the concept is required.

5.2.3 Ultrastable-oscillator plate

The two ultra-stable oscillators (USOs) are mounted on their own support plate, housed within the "stub" of the payload thermal shield. This graphite-epoxy plate measures 330 mm in diameter and 3 mm in thickness. It is mounted from a stiffening ring on the payload thermal shield by six Pyroceram support tubes.

The USOs have been moved to their own plate from the electronics plate due to lack of space.

5.2.4 Radiator plate

Figure 5.5 shows a possible design of the radiator plate. This radiator plate consists of a 5 mm thick, 800 mm diameter graphite-epoxy disc with a rim, 5 mm thick and 25 mm high (also made from graphite-epoxy) that helps to stiffen the plate.

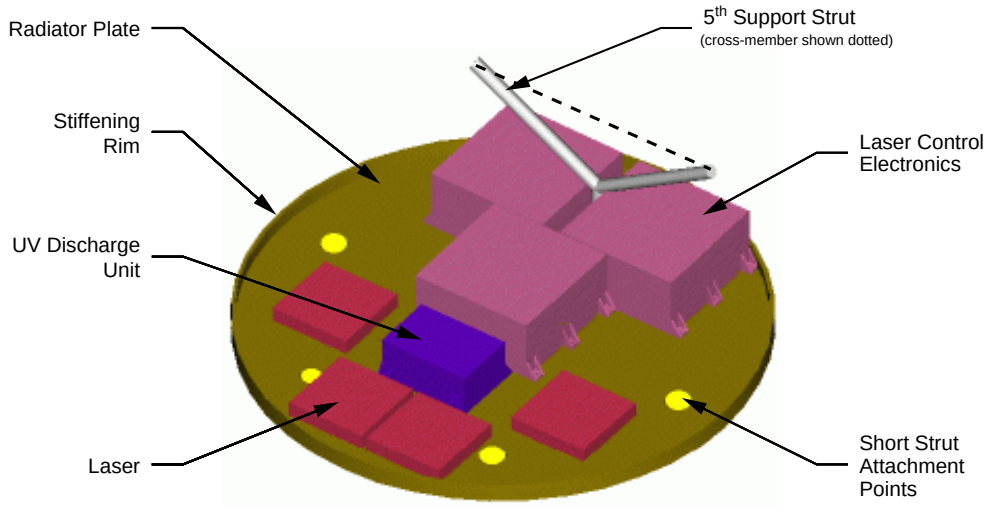

Figure 5.5 *Radiator plate assembly.*

The plate is attached to the payload thermal shield by four short graphite-epoxy support struts, 20 mm in diameter, 3 mm wall thickness and 50 mm long. A fifth graphite-epoxy strut, in the form of a Y, connects the front section of the radiator plate to the arms of

the payload thermal shield. This too is 20 mm in diameter, 3 mm wall thickness. Across the top of the Y-strut is a cross-member of the same dimensions.

Due to the limited mounting area on the plate, and to the height restriction imposed on components by the presence of the Y-tube arms above, only three laser control electronics units measuring 200 mm × 200 mm × 100 mm are accommodated (rather than the original four). The redundancy provided by only three units should be acceptable, but it is likely that the dimensions of the boxes can be reduced, thus allowing all four.

5.3 Structural design – Future work

Further improvements to the payload structure may be obtained by reassessing the design of the radiator plate (the cause of modal vibrations just above 60 Hz), and in particular its attachment to the underside of the payload. Moving the lasers and associated components to a radiator connected to the spacecraft structure would increase the modal frequencies of the payload, and reduce the loads induced in the payload structure. It would also increase their separation from the proof masses, and hence reduce their influence on the gravitational potentials within the instrument. This is currently dominated by the close proximity of the lasers and control units to the proof masses.

In addition, the launch-lock concept and telescope mounting structure must be developed in more detail.

5.4 Mass estimates

Mass estimates for the payload structural components are listed in Table 5.1 .

Item	*Number per S/C*	*Mass* (g)	*Mass* (kg)	**Mass (kg)**
Optical Assembly Structure	**2**			**< 5.8**
Payload cylinder			1.74	
Telescope support			0.64	
Support		*550*		
Stiffening ring		*87*		
Telescope thermal shield			0.32	
Shield		*145*		
Stiffening ring		*87*		
Support tubes and fittings		*92*		
Optical bench support			0.47	
Stiffening ring		*87*		
Support tubes and fittings		*385*		
Electronics Plate			0.61	
Plate		*393*		
Stiffening ring		*87*		
Support tubes and fittings		*129*		
Pointing assembly			< 2.00	
Flex-pivots		*<1000*		
Flex-pivot beams		*500*		
Pointing actuators		*<500*		
Payload Thermal Shield	**1**			**< 11.5**
Baffles			1.8	
Y-tube			7.5	
Stiffening rings			0.7	
Launch-locks			< 1.5	
Ultrastable-Oscillator Plate	**1**			**0.5**
Plate		*394*		
Support tubes and fittings		*130*		
Radiator Plate Structure	**1**			**1.3**
Plate and rim			1.0	
Support struts			0.3	
Short supports (all 4)		*48*		
Fifth support		*251*		

Table 5.1 *Estimated masses of the payload components.*

5.5 Payload thermal requirements

The major science requirement on the payload thermal control subsystem is one of temperature stability, with the optical bench fluctuations due to solar intensity variations and other sources of disturbances kept below $10^{-6}\,\mathrm{K}/\sqrt{\mathrm{Hz}}$ at $10^{-3}\,\mathrm{Hz}$. The telescope thermal stability should be below $10^{-5}\,\mathrm{K}/\sqrt{\mathrm{Hz}}$ at $10^{-3}\,\mathrm{Hz}$ to achieve the desired performance.

The optical bench part of the payload shall be maintained at $20\,^{\circ}\mathrm{C}\pm10\,^{\circ}\mathrm{C}$, but should be known with an accuracy of TBD °C at the design stage. Temperature gradients within the optical bench should be less than TBD °C. Electronics boxes need to be maintained within their operational temperature limits of TBD °C to TBD °C.

The laser diodes are to be kept at their operational temperature, and this will reduce over the mission life from 295±TBD K at BOL to 280±TBD K at EOL (beginning, end of lifetime), to accommodate changes in the diode operating wavelength.

In addition to the specific thermal requirements defined above the thermal design must, together with the thermoelastic design, prevent deformations of the structure that compromise the scientific performance of the payload.

5.6 Payload thermal design

It is clear that many thermal and system level trade-offs need to be performed before an optimised thermal design may be established. However some thermal analysis has been performed and has enabled the definition of certain design parameters.

The first stage of isolation from the sun should be provided by the spacecraft as either a solar shield with optimised α_s/ϵ or, preferably, multilayer insulation (MLI). This would probably be at the level of the top of the spacecraft structural ring. A second stage of solar isolation is provided by the Y-shaped thermal shield. This will be goldized as extensively as possible on external and internal surfaces, although if the electronics boxes are radiatively cooled then certain parts of this thermal shield will have to be blackened, and also the internal surfaces of the baffles forward of the primary mirrors will probably be blackened for control of scattered light.

The external and internal surfaces of the optical bench support cylinders are goldized to radiatively isolate them from the Y-shaped tube, thus providing a third stage of radiative isolation from the sun. The optical bench and sensor assemblies have been assumed to have their natural surface properties, but further modelling may show that these too need to have controlled low emissivity coatings.

Conductive isolation is used throughout the payload and at the interfaces with the spacecraft as defined in Section 5.2. For this purpose, Pyroceram cylinders are used to support the optical benches, the electronics plates and the telescope thermal shields off the internal support cylinders. Glass fibre reinforced bands are assumed for mounting the internal support cylinders off the Y-shaped tube and carbon fibre brackets for mounting the laser radiator off the Y-shaped tube and the primary mirror off the support cylinder.

Current modelling has indicated that the electronics boxes operate somewhat warm at about 30 °C but the current design study considered radiative losses only from the box to

the Y-shaped tube and from there to the spacecraft. It is conceivable that an additional radiator could be accommodated in plane with the laser radiator and with heat straps to the payload electronics boxes. The straps would be fairly long and a 30 K temperature drop could result, but the radiator, seeing deep space, could be operated at a cold enough temperature with little difficulty. This approach would also improve the stability of the optical bench since the whole of the Y-shaped tube could be goldized and furthermore the 'transfer function' relating payload power to optical bench temperature fluctuations would be somewhat reduced.

The laser radiator requires a radiative coupling in the order of $0.113\,\mathrm{m}^2$ to space, equivalent to an actual black painted radiator diameter of about 0.4 m. The laser diode temperatures are actively controlled using heaters.

5.7 Thermal analysis

Geometrical mathematical models of the LISA payload were established for the calculation of radiative couplings using ESARADv3.2.6 and thermal mathematical models were established using ESATANv8.2.3 . These models assume a solar shield instead of MLI on the sun facing side ($\alpha_s/\epsilon = 0.265$) and radiative cooling of the electronics boxes in the Y-shaped tube. They include major service module surfaces (the solar array, top sunshield, ring, and bottom cover) in order to calculate radiation exchanges with these, and to determine the sensitivity of the payload to changes in spacecraft temperature and solar intensity.

The thermal mesh permits the calculation of axial and circumferential gradients within the arms of the Y-shaped tube and internal support cylinders. Significant thermal components of the payload (the proof mass, sensor, titanium housing, optics bench, telescope shield, electronics plate, electronics boxes, primary mirror, secondary mirror, spider) were each represented by one node.

A detailed optical bench model was also established with the bench represented by a total of 28 nodes to allow the prediction of two-dimensional temperature gradients – those through the thickness of the bench are not calculated. A 'nominal' steady state calculation case was established using boundary conditions and payload power dissipations as given in Table 5.2 .

Item	*Value*	*Unit*
Solar constant	1370	$\mathrm{W/m^2}$
Sunshield α_s/ϵ (BOL value)	0.265	–
Spacecraft ring/base temperature	20	°C
Optics bench dissipations	2×0.9	W
USO electronics dissipations	3.0 ± 1.3	W
Analogue electronics (on plates)	2×4.0	W
Digital electronics (on plates)	2×4.5	W
Radiator plate dissipation (lasers, control, discharge)	41.4	W

Table 5.2 *Nominal model boundary conditions.*

Resulting temperatures are summarised in Table 5.3.

Location	*T* (°C)	*Location*	*T* (°C)
Optics bench	21.0	Support cylinder stiffening ring 4 (front)	2.2
Proof mass	20.4	Support cylinder middle	14.3
Sensor	20.4	USO box plate	24.7
Titanium housing	20.4	USO box	26.6
Primary mirror	−19.7	End plate of Y-shaped tube	19.8
Secondary mirror	−45.3	Y-tube apex (surrounding USO boxes)	19.8
Telescope thermal shield	4.4	Y-tube, from USO plate to electronic plate	23.0
Electronics plate	32.1	Y-tube, from electronics plate to primary mirror	11.8
Analogue electronics box on plate	33.6	Y-tube in front of primary mirror, aft end	−33.2
Digital electronics box on plate	33.8	Y-tube in front of primary mirror, middle	−49.0
Support cylinder stiffening ring 1	18.6	Y-tube in front of primary mirror, front end	−65.4
Support cylinder stiffening ring 2	16.0	Laser electronics radiator	12.2
Support cylinder stiffening ring 3	9.7	Sunshield	

Table 5.3 *Nominal case temperature distribution.*

When the results for the nominal steady state case are applied to the detailed optical bench model the maximum temperature predicted, in the region of the EOM, is 22.9 °C and the minimum temperature predicted is 20.1 °C. For the housing the maximum temperature difference between sides is 1.4 °C. The temperature sensitivity of various components compared with these nominal temperatures is given in Table 5.4 for various changes in the thermal boundary conditions.

Item	*Proof Mass*	*Optics Bench*	*Payload Electron.*	*Primary Mirror*	*Support Cylinder*
Nominal case temperature (° C)	*20.4*	*21.0*	*33.6*	*–19.7*	*14.3*
SVM Base/Ring increased by 10 °C	+4.5	+4.5	+4.8	+4.2	+4.9
Solar Constant increased by 50 W/m^2	+0.5	+0.5	+0.5	+0.5	+0.6
Shield α_s incr. by 0.052 W/m^2 (to EOL value)	+3.1	+3.1	+3.2	+2.7	+3.4
Electronics power increased by 1 W	+1.4	+1.4	+2.5	+0.9	+1.4
Optical bench power increased by 0.5 W	+9.4	+10.0	+1.3	+2.8	+4.9
CFRP conductivity doubled	–1.3	–1.3	–0.8	+4.2	–2.2

Table 5.4 *Component temperature changes* (°C) *compared with nominal case.*

The steady state results indicate that the optical bench should come to equilibrium within the required temperature range of 20 ± 10 °C under "nominal" conditions. However this temperature is sensitive to the payload power dissipation and the spacecraft temperature in particular, and to a lesser extent to a number of other parameters. If the spacecraft temperature and payload power dissipation are kept constant then seasonal and sunshield

surface degradation effects will result in long term variations limited to 3 or 4 °C (with seasonal changes alone accounting for about 0.5 °C).

Service module temperature changes could dominate the payload long term temperature variations, with a sensitivity of nearly 0.5 K/K. The electronics boxes on the electronics plate are a little on the warm side (in excess of 30 °C). Large temperature differences (nearly 80 °C) exist along the front sections of the Y-shaped tube due to the aperture seeing deep space. The payload support cylinder itself maintains a temperature difference along its length of about 18 °C.

To model the transient performance of the payload, numerical convergence criteria were set to sufficiently small values so as to allow the detection of the very small temperature changes important for LISA. Frequency response simulations were made at 10^{-4}, 10^{-3} and 10^{-2} Hz and sets of 'transfer functions' relating the *rms* temperature of various payload components to *rms* fluctuations in boundary conditions were calculated. Assuming the power spectral density for observed insolation variations $\widetilde{\delta L_\odot}$ is given as

$$\widetilde{\delta L_\odot} = 1.3\times10^{-4}\, f^{-1/3}\, L_\odot \ \ \mathrm{W\,m^{-2}/\sqrt{Hz}}\,, \tag{5.1}$$

then for the optical bench we get temperature fluctuations of $2.0\times10^{-4}\,\mathrm{K/\sqrt{Hz}}$ at 10^{-4} Hz, $4.3\times10^{-7}\,\mathrm{K/\sqrt{Hz}}$ at 10^{-3} Hz, and $< 8.0\times10^{-1}\,\mathrm{K/\sqrt{Hz}}$ at 10^{-2} Hz due to these solar fluctuations.

The requirement of $1.0\times10^{-6}\,\mathrm{K/\sqrt{Hz}}$ at 10^{-3} Hz is met, but only by a factor 2. In this case the fluctuations at 10^{-3} Hz in power dissipation for the payload electronics on the electronics plate would have to be less than $6.8\times10^{-4}\,\mathrm{W/\sqrt{Hz}}$ and variations in optical bench power dissipation would have to be less than $5.2\times10^{-6}\,\mathrm{W/\sqrt{Hz}}$. Spacecraft temperature variations would have to be less than $1.6\times10^{-3}\,\mathrm{K/\sqrt{Hz}}$ and laser electronics dissipation variations less than $1.7\times10^{-1}\,\mathrm{W/\sqrt{Hz}}$.

5.8 Telescope assembly

5.8.1 General remarks

The telescope has to fulfil two demands:

- The light power transmitted via the telescopes from the near to the far spacecraft has to be as high as possible in order to reduce the shot noise level in the optical readout system (see Eq. (3.2)).
- The wavefront of the outgoing beam has to be as flat as possible in order to minimize the coupling of beam motions to the interferometer signal (see e.g. Eq. (3.6)).

Increasing the diameter of the primary mirror allows to reduce the divergence of the outgoing beam and thus increases the intensity of the laser light at the far spacecraft. In addition, the power picked up by the far telescope is proportional to the area of the primary mirror there. The received lightpower is therefore proportional to the fourth power of the mirror diameter D (see Eq. (3.2)).

Once a particular diameter of the primary mirror is given, the intensity at the beam axis in the far field is highest when the Gaussian diameter of the outgoing beam equals the diameter of the primary mirror. The beam is then truncated at the $1/e^2$ contour line of its intensity. In this case the power picked up at the far spacecraft is given by Eq. (3.1). For reasons of cost and weight a diameter of only 30 cm for the primary mirrors was chosen; it is adequate for the envisaged sensitivity level.

Coupling of changes in beam orientation to the interferometer signal is minimal when the center of curvature of the wavefront at the receiving spacecraft sits inside the emitting spacecraft. For the wavefront of a laser beam in the far field the center of curvature coincides with the focus of the beam. The outgoing wavefront has therefore to be flat. The final quality of the plane wavefront leaving the telescope is specified as $\lambda/10$.

5.8.2 Telescope concept

The telescope widens the diameter of the beam from a few mm to 30 cm. Since the space available is very limited, spherical optics would cause huge aberrations. Therefore conical sections are used for the mirror surfaces instead of spherical ones. In this case the imaging properties for point sources can in principle be perfect, if the focus of the beam is positioned exactly at the focus of the particular mirror. This is the idea behind the original Cassegrain telescope, where the primary is chosen to be a paraboloid and the secondary a hyperboloid. Unfortunately, the tolerances for misalignments and the usable field of view are very small in this case. There are several improvements over the original Cassegrain, e.g. the Ritchey-Chretien telescope, minimising the first three Seidel aberrations.

The transmitting and receiving telescope in LISA is therefore an improved Cassegrain system, including an integral matching lens. It is mounted from the payload support cylinder and protected by a thermal shield. The primary mirror is a double-arch light-weight ultra-low expansion ULE design and has a diameter of 30 cm and also a focal length of 30 cm. The secondary mirror, supported by a three-leg carbon-epoxy spider, is mounted

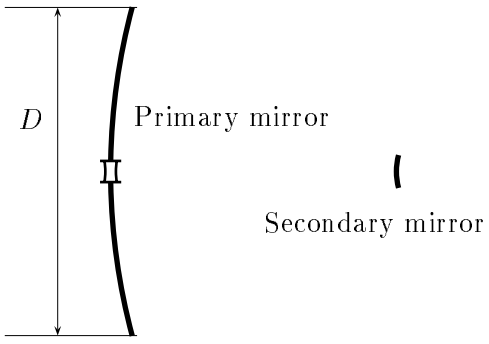

Figure 5.6 *Geometrical arrangement of the telescope components*

27.62 cm from the primary and has a diameter of 3.2 cm and a focal length of 2.6 cm. The beam from the instrument package to the secondary mirror is expanded to a diameter of approximately 3 cm by a suitable lens in the plane of the primary mirror. As just mentioned, the optical elements are aspherics to reduce aberration in the $f/1$ telescope,

and they require careful positioning. Active focus control will be necessary to compensate for any long-term deformations, caused e.g. by temperature drifts. The most critical geometrical parameter seems to be the separation between primary and secondary; a change of about one micron already deforms the outgoing wavefront by the specified tolerance of $\lambda/10$.

The temperature fluctuations at the telescope must be less than $10^{-5}\,\mathrm{K}/\sqrt{\mathrm{Hz}}$ at $10^{-3}\,\mathrm{Hz}$ to achieve the desired performance.

5.9 Payload processor and data interfaces

5.9.1 Payload processor

Each LISA spacecraft includes a PI-provided payload computer comprising a payload processor plus the associated peripherals (I/O etc.), which performs all payload management functions as well as implementation of the drag-free and fine attitude control (DFACS) laws. The current baseline is to use the RAD 6000-SC computer which is a radiation-hardened version of the IBM RS/6000 processor developed for the Mars Surveyor Program (MSP). The nominal performance is 22 MIPS. The payload computer contains 128 Mbytes of DRAM and 3 MBytes of PROM. The relatively low data rates for science and telemetry permits all data to be buffered and stored in DRAM on the payload computer. This eliminates the need for a separate mass memory board, thereby reducing the subsystem mass and power. Likewise, the spacecraft computer which will handle the telemetry (and coarse attitude control/safe modes) does not need to have storage capability for the science data.

Table 5.5 summarises the payload processor specifications. The payload computer will be fully redundant, consisting of two identical units operating in a String A and a String B fashion. String B acts as a warm backup and receives state data from String A at specified intervals. String B will contain a watchdog timer to monitor String A. If this timer runs out, String B will take over as the payload processor. The payload computer component cards will be mounted in a VME chassis.

Processor type	RAD 6000-SC, floating point included
RAM	128 Mbytes radiation tolerant DRAM
Nominal performance	22 MIPS at 10.5 W (21.6 SPECMark)
Mass	< 0.9 kg
Temperature range	$-30\,^\circ$ to $+75\,^\circ$C at the cold plate
Memory protection	on chip EDAC as well as system level EDAC
SEU bit error rate	4/MFC/year GCR (Galactic Cosmic Rays)
Processor total dose	> 20 kJ/kg Total Ionizing Dose (TID)
DRAM total dose	> 0.3 kJ/kg (TID)

Table 5.5 *Payload processor specifications.*

Payload computer mass, power, volume budgets. The mass, power, and volume budgets of the payload computer subsystem are listed in Table 5.6. The entries for mass include the VME connectors.

Units	*Number of Units*	*Total Mass* (kg)	*Power per Unit* (W)	*Notes*
Processor	2	2.3	10.5	
X-strap board	2	1.8	0.75	between A & B strings
1553 board	2	1.8	1	1553 bus controller
RS 422 board	4	1.8	2	Serial I/O for accels., etc
VME chassis	2	1.8	–	composite material
Shielding	–	1	–	
Totals		**10.5 kg**	**14.25 W**	
Dimensions of complete payload computer: $233 \times 199 \times 321\,\mathrm{mm}^3 = 14.9$ litres				

Table 5.6 *Payload computer mass, power, volume budgets.*

5.9.2 Payload data interfaces

The data interfaces between the payload subsystems and the spacecraft are shown in Figure 5.7. The baseline approach is to use a MIL-STD-1553 data bus to link all of the DFACS hardware elements to the payload processor, with the exception of the accelerometers (including UV discharge system) and interferometer electronics which are directly linked to the payload processor via an RS 422 interface. The payload processor is linked to the spacecraft processor via the 1553 bus.

If it turns out to be feasible in terms of bus management and reliability, the 1553 interfaces may be replaced throughout by RS 422 interfaces, with considerable cost benefit. For the time being, however, the 1553 protocol is the baseline choice.

Bus control. The MIL-STD-1553 protocol requires no more than one bus controller. Initially, the spacecraft processor is the bus controller for coarse attitude control. During a transition phase, after the payload processor (nominally String A) is brought on line, bus control is transferred from the spacecraft processor to the payload processor. This is accomplished by a "dynamic bus control" command which is available within the framework of the 1553 standard. (Alternatively, the spacecraft processor could retain control of the bus and use remote-terminal-to-remote-terminal transfers.)

Payload command and data handling software. The payload command and data handling (C&DH) software layer resides on the payload processor and includes the 1553 interface and data structures for normal payload operations, plus the RS 422 interface with the accelerometers and interferometer electronics. The command handler accepts and routes commands either directly from the 1553 interface, or as stored program commands loaded into the payload processor memory. These program commands may be time-tagged with absolute or relative time, or may be conditional commands. The spacecraft computer which controls the telemetry must be configured such as to accept/send data packets from/to the payload processor as commanded by the payload C&DH layer. All payload flight software will be developed using commercial compilers (C, C++, or Ada).

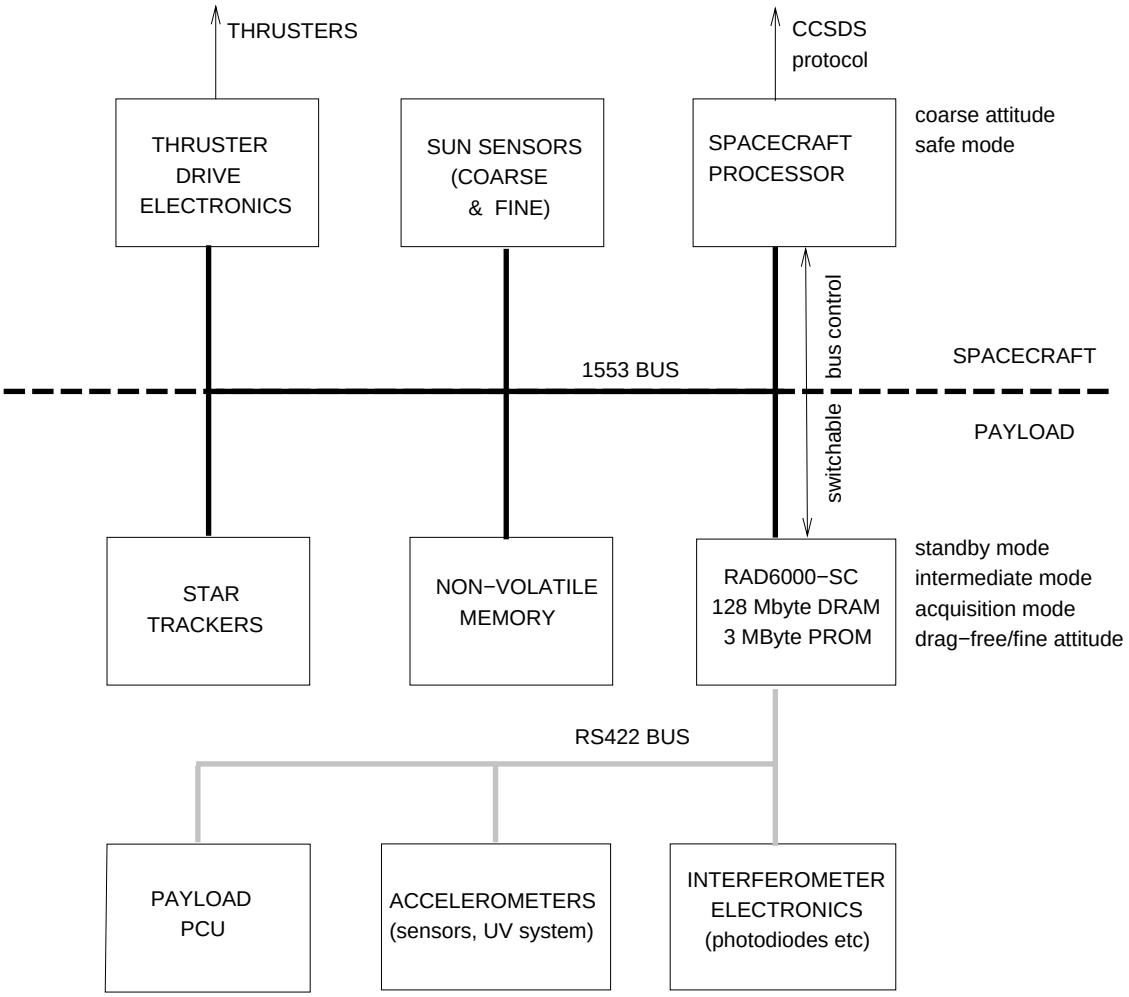

Figure 5.7 *Payload data interfaces.*

Chapter 6

Mission Analysis

6.1 Orbital configuration

The desired configuration for the LISA spacecraft is such that the three spacecraft form an equilateral triangle which changes as little as possible throughout the mission. This desire arises from instrumental noise introduced into the gravitational-wave measurement that must be dealt with if there are changes in the distances between spacecraft. The current nominal orbital configuration places the spacecraft in a triangle with a center 1 AU from the sun and trailing the Earth by 20° in its orbit (see Figure 2.5). From the Earth the triangle appears to rotate about the center with a period of one year (see Figure 4.8). The location of the center of the formation 20° behind the Earth represents a compromise between the desire to have the constellation far from the Earth, to reduce distorations caused by the Earth's gravitational pull, and the desire to be closer to the Earth, to reduce the amount of propellant needed and to ease the requirements on the telecommunications system.

Each spacecraft is in an orbit around the sun with major axis $D = 2\,\mathrm{AU}$ and eccentricity $e = d/(D\sqrt{3})$, where d is the separation between the vertices (5 million km for the nominal LISA orbits). If the spacecraft were all in the same plane then the separation between spacecraft would vary between De and $De/2$ over the course of one year. By giving the spacecraft an inclination $i = d/D$, and by appropriate choice of the node, anomaly, and argument of perihelion, the separation between spacecraft is constant to order De^2 [118].

This heliocentric orbital configuration has the property that the directions between spacecraft are always within 30° of being orthogonal to the direction to the sun. This allows the spacecraft to be designed such that sunlight never enters the interferometer optics, and also allows the spacecraft to have the sun always illuminating the same part of the spacecraft.

6.2 Launch and orbit transfer

The three spacecraft will be injected into an Earth-escape orbit by a single launch vehicle. The current spacecraft design allows the three spacecraft to fit within the payload

fairing and launch capability of a Delta II 7925 H. The Earth-escape orbit has an excess normalized energy of $C_3 = 1.1\,\mathrm{km}^2/\mathrm{s}^2$ so that the three spacecraft will slowly drift behind the Earth. After launch and injection to the Earth-escape trajectory, the three spacecraft will be separated and individually targeted to their desired operational orbit.

At launch, each spacecraft will be attached to a propulsion module. The propulsion modules will provide the capability to maneuver the spacecraft into the desired operational orbits. After reaching the operational orbits, about 13 months after launch, the propulsion modules will be separated from the spacecraft to avoid having excess mass, propellant, and/or moving parts near the proof masses within the spacecraft. After reaching the final orbits, the spacecraft positions will evolve under gravitational forces only. Micronewton ion thrusters will be used to keep the spacecraft centered about the shielded proof masses within each spacecraft. The thrusters could be used to perform small ($\Delta V < 1\,\mathrm{cm/s}$) maneuvers if required.

Maneuvers with total $\Delta V \approx 1000\,\mathrm{m/s}$ are needed to reach the desired operational orbits after launch. If a conventional chemical propulsion system was chosen, each spacecraft would perform two maneuvers of approximately 500 m/s each. The first orbit change maneuver would be a plane-change maneuver to incline the spacecraft orbit by $i \simeq 1^\circ$ with respect to the ecliptic. The plane-change maneuvers would take place at different times for each spacecraft since the three final orbits are shifted 120° from each other along the ecliptic. For example, one spacecraft might perform a plane-change maneuver shortly after launch, the second spacecraft about 4 months after launch, and the third spacecraft about 8 months after launch. Approximately 13 months after launch, each spacecraft would perform a maneuver to stop the slow drift with respect to the Earth.

The mass of chemical propellant needed to perform the orbit-change maneuvers, combined with the current masses estimated for each spacecraft, would total more than the capability of the Delta II 7925 H launch vehicle. The mass of the propellant can be considerably reduced by use of ion-engines with their much larger specific impulses (velocity with which propellant is ejected) compared with chemical systems. The solar-powered ion engines have an efficiency such that the required propellant mass can be reduced by a factor of approximately 10. This is offset partly by the mass of the additional solar panels needed to provide power for the ion engine.

The required ion-engine thrust is rather small, about 20 mN, if the engine is on during most of the orbit transfer phase. This is much smaller than the thrust of engines designed for interplanetary missions. However, ion-engines developed for station keeping of geosynchronous communications satellites are of an appropriate size. In particular, the *Hughes* XIPS thruster has a thrust of 18 mN. This engine is currently being tested in orbit on a *Hughes* communications satellite. The mass of propellant (xenon) needed for use with this engine to provide the required ΔV for the mission is only 20 kg per spacecraft compared with the $\approx 180\,\mathrm{kg}$ per spacecraft of propellant needed for the traditional chemical system. This reduction in mass is a major factor that enables the current mission design to be launched on a Delta-II class launch vehicle.

The spacecraft transfer trajectories using the ion-engines have not yet been fully optimized. A set of candidate trajectories has been found to establish the engineering feasibility. The candidate trajectories require that the ion-engines be on during approximately 80 % of the 13 month transfer phase. The angle between the thrust direction and

the direction to the sun for these trajectories ranges from 10° to 60°, making it difficult to provide power with a solar array fixed to the spacecraft body. The current spacecraft design includes steered solar arrays to provide power for the ion-engines during the transfer phase, so that the arrays can be pointed towards the sun regardless of the thrust direction. These arrays would be attached to the propulsion module for each spacecraft and jettisoned, along with the ion engine, after reaching the operational orbits.

6.3 Injection into final orbits

The spacecraft will have limited maneuvering capability once separated from the propulsion module, due to the limited impulse of the micronewton thrusters. This requires that the spacecraft be accurately delivered to the final orbits.

If chemical propellant is used in the propulsion modules, a fairly large ($\Delta V \approx 500\,\mathrm{m/s}$) insertion manuever would be needed upon reaching the desired operational orbit. With typical manuever execution errors of 1 %, the error in this maneuver would be be about 10 m/s which would be much too large to be corrected by the micronewton thrusters. Therefore, after the main insertion maneuver, the propulsion module would need to remain attached to the spacecraft while sufficient tracking information is acquired to determine the error in the orbit insertion maneuver.

The propulsion module would then perform a correction maneuver of order 10 m/s. The expected error in a maneuver of this size would be about about 10 cm/s which would still be too large for the micronewton thrusters to correct. Another period of spacecraft tracking would be needed to design a final correction maneuver to be executed by the propulsion module. After the execution of the final correction maneuver, the spacecraft would separate from the propulsion module. The separation would be effected by a spring-separation system, with a separation velocity of order 10 cm/s. The error in the separation maneuver is expected to be of order 1 cm/s which can be corrected using the micronewton thrusters.

With the use of a solar-electric propuslion module, while detailed navigation studies have not yet been performed, it is likely that a similar series of tracking periods, orbit error estimation, and orbit correction would be needed before the propulsion modules could be separated from the spacecraft.

6.4 Orbit configuration stability

Both the nature of the elliptical orbits and planetary perturbations will cause small changes in the lengths of the sides of the triangle formed by the three spacecraft. These orbital changes of distance between spacecraft will impose Doppler shifts on the interferometer signals that will have to be removed using on-board oscillators (clocks). Noise from the oscillators will then corrupt the distance measurements. The amount of noise introduced depends on the size of the Doppler shift and the performance of the oscillator.

The spacecraft are designed to be drag-free so that the only significant forces affecting the proof masses at the center of each spacecraft are gravitational. In the simplest case the

only free parameters that can be adjusted to minimize the arm rates-of-change are the initial positions and velocities of the proof masses, which then move under the influence of the gravitational field of the sun and planets. For the heliocentric configuration the typical arm-length changes due to the initial shape of the orbits are of order De^2 with a main period T of one year. For an arm length $d = 5 \times 10^6$ km, this implies a maximum arm rate-of-change of order $v = (2\pi/T)d^2/(3D) \approx 5$ m/s. Perturbations due to the Earth and other planets cause larger changes in the arm lengths after a few years. The degradation is larger when the formation is nearer the Earth.

When the initial positions and velocities for the six spacecraft are chosen to minimize the average rate-of-change of the three arm lengths over a two-year period, the arm rates-of-change are found to vary between ± 6 m/s [119]. Given the current performance of space-qualified oscillators, removing the Doppler shifts of the nominal orbits introduces more noise in the measurement than can be tolerated. The arm rates of change would have to be less than $\simeq 10$ mm/s for the noise introduced by a spacecraft clock with Allan deviation 10^{-13} to be at an acceptable level (see Section 4.3.3).

Another option studied was to include occasional maneuvers by the spacecraft to reduce the arm rates-of-change. The idea is that instead of allowing the proof masses to move under only gravitational forces for the entire nominal mission, maneuvers could be done at intervals to keep the arm rates-of-change small. The maneuvers would occur at each spacecraft mainly perpendicular to the direction between the spacecraft. The maneuvers would serve to make small adjustments in the orbit period and eccentricity such that the arm lengths remain more constant. This strategy is limited by the low level of thrust available from the micronewton thrusters planned for the spacecraft. The micronewton thrusters are currently planned to have a maximum thrust of order $100\,\mu$N, sufficient to counteract the force on the spacecraft due to the solar luminosity. With these thrusters it would take a long time to execute even small maneuvers, perhaps one day to change the velocity by 10 cm/s (given the mass of the current spacecraft design). The noise force on the proof masses during the execution of these maneuvers is assumed to be so large as to preclude accurate measurements during that time.

Analysis has been done to show that it is not possible to keep the rates-of-change of all three arms of the heliocentric formation to an acceptable level using the micronewton thrusters [119]. It is feasible to stabilize two of the three arms to an acceptable level with a practical number of small maneuvers. If one particular vertex is considered as the prime vertex, then the same spacecraft oscillator can be used to remove the Doppler shift of the two arms meeting at the prime vertex. Then it is the difference in the rate-of-change of the two arms that introduces noise into the gravitational-wave measurement. An orbit solution has been found with maneuvers taking place once each month, of magnitude 10 cm/s or less, such that the difference in rate-of-change of the two prime arms is kept to an *rms* level of 7 mm/s. The disadvantages of using maneuvers to stabilize one pair of arms is that it does not allow for using the information available from the third arm, and it involves a "dead time" of about one day each month. By not using the third arm the detector is sensitive to only one of the two possible gravitational-wave polarizations at any given time. (The rotation of the formation over the annual period will cause a given pair of arms to be sensitive to different polarizations at different times.)

Another alternative to reduce the noise caused by the Doppler shifts would be to modulate the laser beams with a signal based on the spacecraft oscillators [120]. In this scheme each arm would be essentially used as a delay line to stabilize the oscillators; the returned oscillator signal would be compared with the local oscillator signal and the difference would be used to measure fluctuations in the spacecraft oscillator. This scheme has been adopted as the nominal plan for the LISA mission.

With this scheme it is still advantageous to have the arm rates-of-change small since this reduces the dynamic range of the oscillator signal. For example, with arm rates-of-change of 15 m/s and Doppler shifts of 30 MHz, it suffices to use a 200 MHz modulation derived from the spacecraft oscillators on the laser signal [121]. The modulation can be imposed using an electro-optical modulator already planned in the spacecraft payload for other purposes. This is somewhat simpler than the two-laser scheme outlined in Hellings *et al.* [120]. With these clock-noise reduction schemes there are a variety of possible choices of nominal orbits that give acceptable ranges of Doppler shift over the period of the mission.

The nominal operational orbits selected have initial orbits that could, if necessary, be adjusted by small maneuvers each month to keep the rates-of-change of one pair of arms nearly the same throughout the mission. However, no maneuvers are planned if performance is nominal. Figure 6.1 is a plot of the arm rates of the rates-of-change of the three arm lengths for the nominal orbit configuration. (The orbits will change slightly in character depending on the chosen launch date.) The rate-of-change of arm length for two

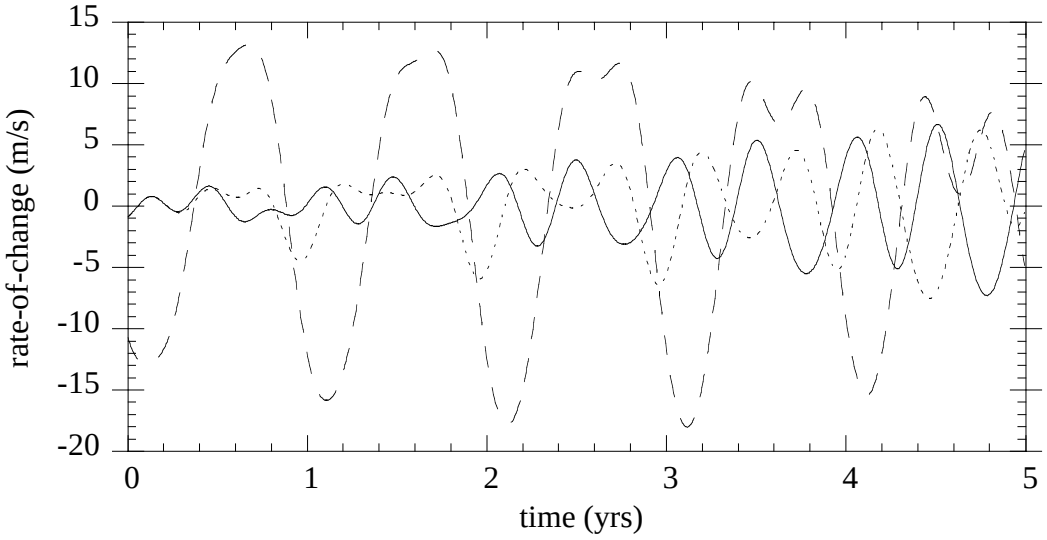

Figure 6.1 *Nominal rates-of-change for the three arms of the LISA triangular spacecraft formation, with the spacecraft orbits evolving under only gravitational forces (i.e. with no maneuvers). The rates-of-change of the lengths of arm 1 (solid line) and arm 2 (dotted line) (see Figure 3.1) are almost identical for the first six months of the mission and could be kept nearly identical, if necessary, through the use of occasional small maneuvers.*

of the arms is almost identical for the first six months of the mission. The difference in rate-of-change of these two arms could be kept small through the use of small maneuvers.

The third arm rate-of-change varies between $\pm 15\,\mathrm{m/s}$. This could be reduced if all three arms were treated equally, at the cost of not having one pair of arms with similar Doppler rates. However, the Doppler shift caused by an arm rate-of-change of $\pm 15\,\mathrm{m/s}$ is well within the capability of an electro-optical modulator to perform the clock cancellation scheme.

With the current nominal orbits, the angle between the two distant spacecraft, as seen from any one spacecraft, changes slowly through the year, by $\pm 1^\circ$ in the worst case. This requires the angle between the two telescopes on each spacecraft to be articulated. Figure 6.2 is a plot of the angle between the two distant spacecraft, as seen from any one of the spacecraft, for these orbits.

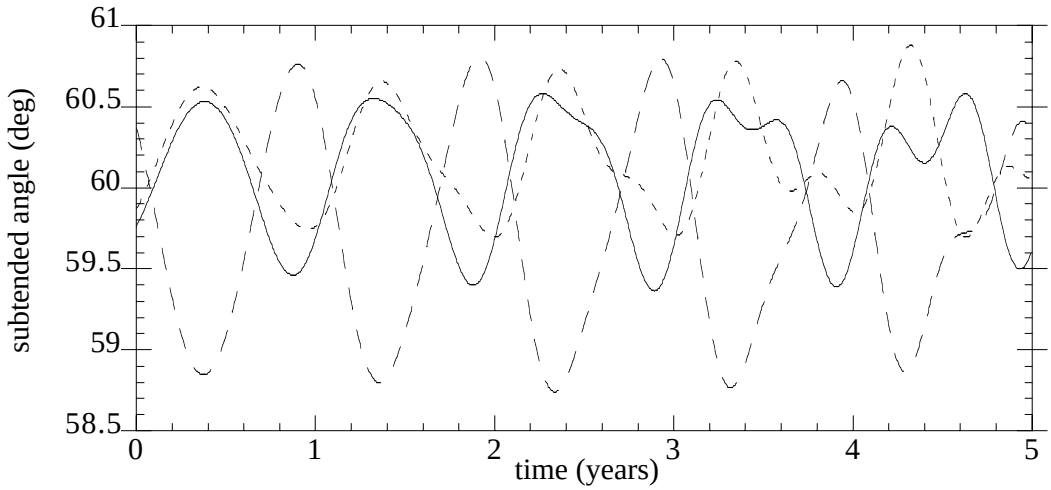

Figure 6.2 *The angle between the two distant spacecraft, as seen from any one of the spacecraft, is shown for the nominal LISA orbit configuration. The angle subtended by arm 3 (dashed line), as viewed from spacecraft A, has the most variation with the chosen nominal orbits (see Figure 3.1).*

6.5 Orbit determination and tracking requirements

Prior to the separation of the propulsion modules from the spacecraft, the spacecraft positions and velocities need to be accurately determined. The primary requirement is that the spacecraft velocity be known to about 1 cm/s, which is within the capability of the micronewton thrusters. This means that maneuvers, especially the final orbit injection maneuver and propulsion module separation, need to be determined to about 1 cm/s. The spacecraft positions should be determined well enough to know the direction to the distant spacecraft within the angle subtended by the laser primary beam width. With laser wavelength $1\,\mu$m, telescope diameter 30 cm, and spacecraft separation 5×10^6 km, this implies a position knowledge of approximately 10 km.

During the science-operations phase there are no stringent operational navigation requirements. The spacecraft orbits must be determined with modest accuracy for purposes of ground antenna pointing and frequency prediction. A more stringent requirement arises

from the on-board data reduction algorithm for the interferometer data. For this data reduction, the length of each arm needs to be known to better than 200 m at any time (see Section 4.3.2).

Table 6.1 gives a summary of the orbit determination requirements.

Table 6.1 *Required orbit determination accuracies.*

Phase	*Accuracy* ($\sigma_{\rm rms}$)	*Requirements taken into account*
Transfer	position: 10 km velocity: 1 cm/s	classical interplanetary navigation, manoeuvre dispersions
Experiment	position: $\leq$ 10 km velocity: 2 mm/s arm-length: $\leq$ 200 m	laser acquisition, on-board laser phase processing

The navigation performance for the transfer phase is relatively standard for current interplanetary missions that use X-band (8 GHz) radio systems for the acquisition of range and Doppler measurements by tracking stations of NASA's Deep Space Network (DSN). The characteristics of the assumed ground tracking accuracy are:

- Station location uncertainties $\leq$ 3 cm.
- Two-way range data (noise: $<$ 2 m; bias: $<$ 10 m) plus two-way Doppler data (max. error: $<$ 0.1 mm/s for 60 s averaging).
- Ionosphere zenith delay after calibration by means of GPS signals: $\leq$ 3 cm.
- Troposphere zenith delay after modeling: $\leq$ 4 cm.
- Earth orbit orientation error: $\leq$ 5 nrad.

These tracking assumptions are met by the DSN network, and could be met by the ESA Multi Purpose Tracking System after a few enhancements and/or modifications (X-band, GPS-calibration, highly stable frequency standards). With this type of tracking, and assuming that tracking measurements are acquired for each spacecraft throughout 8-hour tracking passes two to three times each week, the navigation requirements for the transfer phase can be met. For the injection into the final orbits, one to two weeks of tracking time may be needed between successive maneuvers until the expected error of the final pre-separation maneuver is less than 1 cm/s.

During science operations, the requirement that the arm lengths be determined to $\leq$ 200 m is not easily met using ground tracking only. However, it will be possible to augment the ground tracking data with data acquired along the interferometer arms. Each interferometer arm will include phase measurements taken every 0.1 s (see Section4.3.2). Differences in the phase measurements give information on the rate of change of the arm length (i.e. Doppler). The measurements along each arm will be noisy compared with the desired gravitational-wave performance but are sufficient to aid in the determination of the arm lengths. After the arm lengths are determined, the laser phases can be combined in a manner to cancel most of the phase measurement error and result in the desired instrument performance.

For purposes of determining the arm lengths, a short analysis was performed assuming ground tracking of each spacecraft for 8 hours every other day, and combined with phase measurements from the laser system sampled once every 30 minutes. The phase measurements were assumed to have an accuracy of $5 \times 10^{-4}\,\mathrm{m}/\sqrt{\mathrm{Hz}}$ at the frequency corresponding the round-trip light time. A phase bias needs to be estimated for each arm along with the spacecraft positions and velocities. Uncertainties in the positions of the planets, especially the Earth, have been taken into acocunt, as have uncertainties in station locations and Earth media calibrations. The analysis was performed for a configuration when the LISA constellation was at 0° declination as viewed from the Earth, which is when the poorest orbit determination is expected.

Table 6.2 shows the achievable orbit determination accuracy using combinations of ground tracking and measurements from the laser system. After 16 days of ground and laser tracking, the arm lengths can be determined to about the required 200 m accuracy. The system performance might end up being somewhat better since the assumptions on the laser-system measurements were very conservative.

Table 6.2 *Achievable orbit determination accuracy (1-σ).*

Case	*Accuracy* (σ_{rms})			
	Position	*Arm 1*	*Arm 2*	*Arm 3*
Radio tracking only over 16 days	5.94 km	3.75 km	1.49 km	5.56 km
Radio and laser tracking over 16 days	1.79 km	0.19 km	0.07 km	0.14 km

If the laser systems include some means of directly measuring the arm lengths, such as incorporation of a ranging signal in addition to the laser carrier phase, then the arm lengths would not need to be inferred from the ground tracking measurements and laser phase measurements. Further studies will need to refine the navigation analysis and determine the optimal means of determining the arm lengths.

Chapter 7

Spacecraft Design

7.1 System configuration

7.1.1 Spacecraft

The spacecraft configuration is shown in Figure 7.1. It consists of a cylinder with a height of 480 mm and a diameter of 1800 mm. It supports a Y-shaped tubular structure, the payload thermal shield, which serves to reduce the effects of changes in the solar luminosity on the optical assemblies contained in the two arms of the Y. A top lid across the cylinder (not shown in Figure 7.1) prevents sunlight from striking the payload thermal shield. The spacecraft equipment is mounted on the inside wall of the structural cylinder. Extending out from the structural cylinder is a sun shield that keeps sunlight off the cylinder wall. The main solar panels are mounted on this sun shield.

The spacecraft structural cylinder and the payload thermal shield are made of a graphite-epoxy composite chosen for its low coefficient of thermal expansion. The payload thermal shield is gold-coated and suspended by stressed fiberglass bands from the spacecraft cylinder to thermally isolate it from the spacecraft. The optical assemblies are in turn thermally isolated from the payload thermal shield. On the outside of the spacecraft cylinder the FEEP (Field Emission Electric Propulsion) thruster blocks are mounted in six clusters of four thrusters each.

Outside of the payload thermal shield, pointing parallel to the arms, star trackers are mounted on the lower side of the solar panel rim. For redundancy, a total of 4 star trackers are used. In addition Fine Sun Sensors and Sun Acquisition Sensors are mounted on the spacecraft.

Two steerable 30 cm diameter high-gain X-band antennas are mounted via suitable interface structures on the outside of the spacecraft, far enough inside the central cylinder diameter to avoid interference problems during separation. The antennas, used during the operational phase, provide the necessary 2π coverage in azimuth. Low- and medium-gain antennas are mounted on short booms at the lower side of the structural cylinder.

In the operational heliocentric orbit the spacecraft nominal orientation is such that the YZ-plane coincides with the plane of the interferometer. Thus the spacecraft X-axes make an angle of 30° with the Sun direction. The angle between the X-axis and the Earth

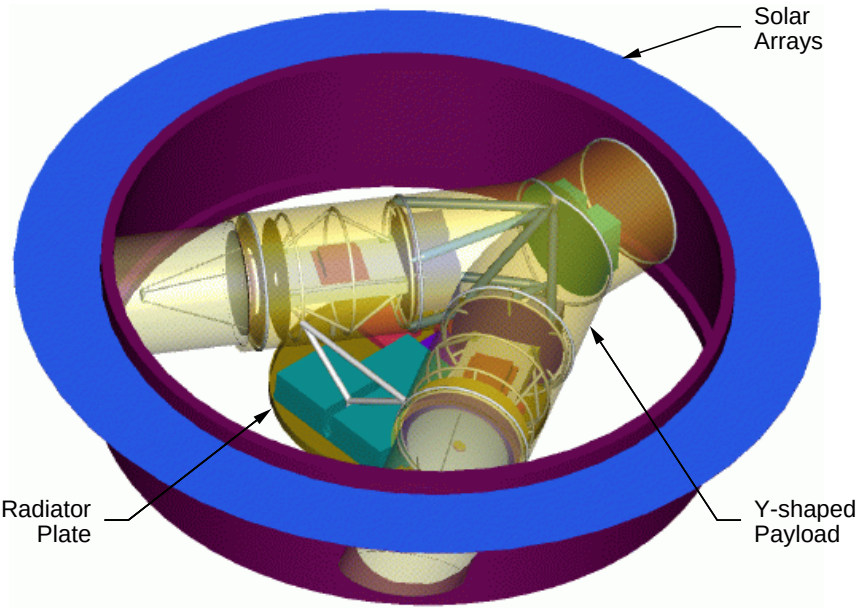

Figure 7.1 *One of the three identical LISA spacecraft. The main structure is a ring with a diameter of* 1.8 m, *and a height of* 0.48 m, *made from graphite-epoxy for low thermal expansion. A lid on top of the spacecraft is removed to allow view at the* Y*-shaped thermal shield (indicated here as semitransparent) encasing the two payload arms.*

direction varies between about 78° and 84°. The major part of this variation is due to the eccentricity of the Earth orbit. As the interferometer rotates in the apparent orbital plane, making one revolution per year, while the apparent plane moves along the Earth orbit around the Sun, the spacecraft rotate about their X-axes at a rate of about 1°/day, while the X-axes precess at about the same rate.

Figure 7.2 shows the interior of the spacecraft and the lay-out for the payload. The two optical assemblies each contain a 30 cm diameter telescope and an optical bench centered about a platinum-gold alloy proof mass. Telescope and optical bench are mounted from the payload cylinder, a graphite-epoxy cylinder which is gold-coated to thermally isolate it from the payload thermal shield. the optical bench is supported from its payload cylinder by ceramic rods with small thermal conductivity. The payload cylinders are attached at the front to two actuators (not shown) and at the rear to a flexure mount.

7.1.2 Propulsion module

At launch, each spacecraft is attached to a propulsion module. The propulsion module provides the capability to maneuver the spacecraft/propulsion module composites into the final orbits, using solar electric propulsion (SEP). The deployed configuration is shown in Figure 7.3 .

After reaching the final orbits, about 13 months after launch, the propulsion modules are separated from the spacecraft to avoid having excess mass and solar panels near the proof masses within the spacecraft.

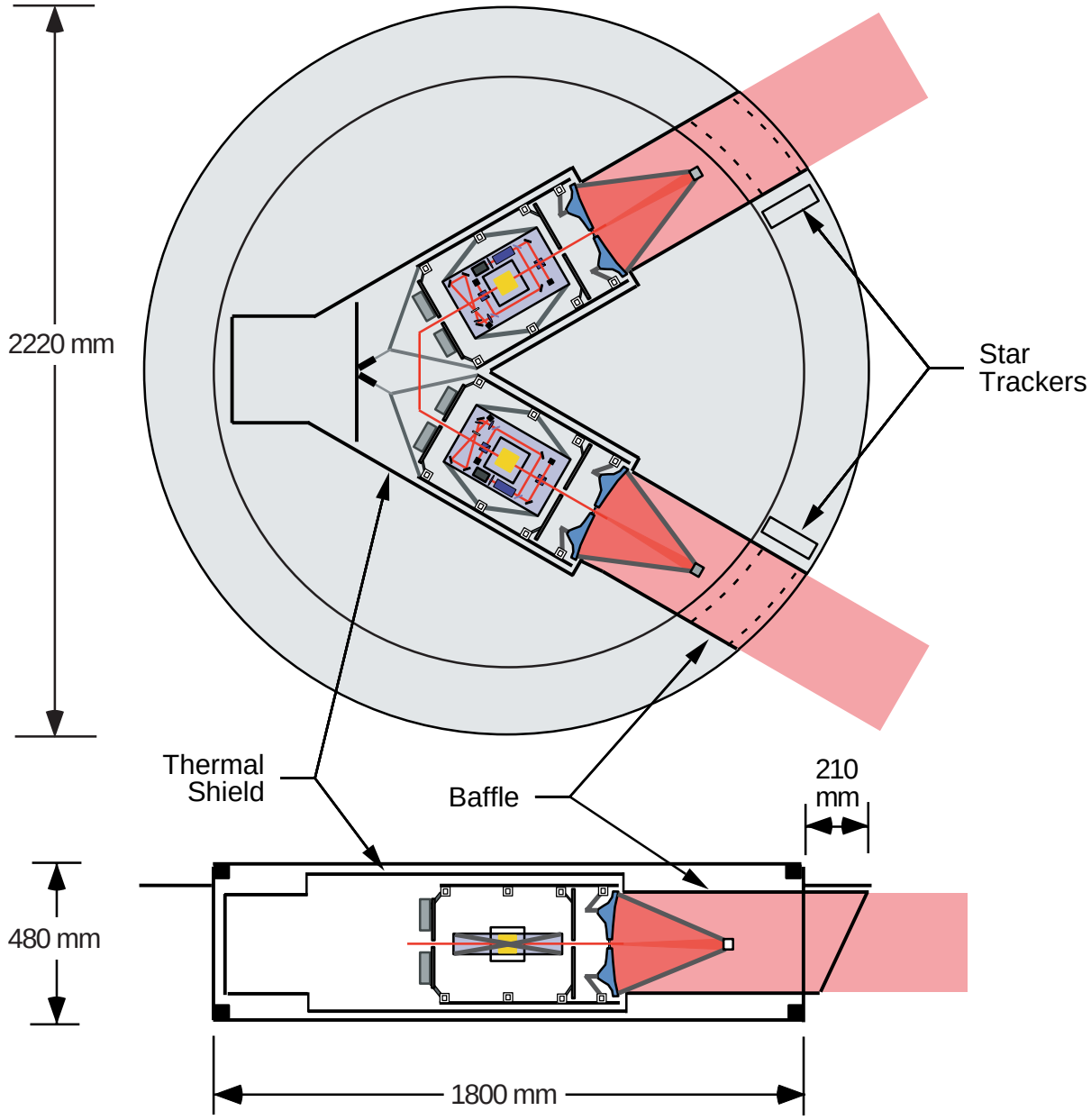

Figure 7.2 *Top and side cross sections of the LISA spacecraft.*

With the single Delta II 7925 H launch and the assumed excess energy of the initial orbit, the spacecraft will slowly drift behind the earth and a continuous low thrust will take the spacecraft to their final operations configuration in 400 days, using 19.1 kg, 13.9 kg, and 17.7 kg of xenon propellant, respectively (20 kg corresponding to a δV of 1305 m/s). The ion engine assumed is the Hughes XIPS thruster, which generates 18 mN of thrust and needs 500 W of electrical power. Two solar arrays are deployed after launch separation to generate the power needed (see Figure 7.3). The extended solar panels are mounted on one-axis gimbals to track the sun as the direction between the thrust axis and the direction to the sun change throughout the 13 months cruise phase. Two ion engines will be carried on each propulsion module, but only one will be used at a time. The second

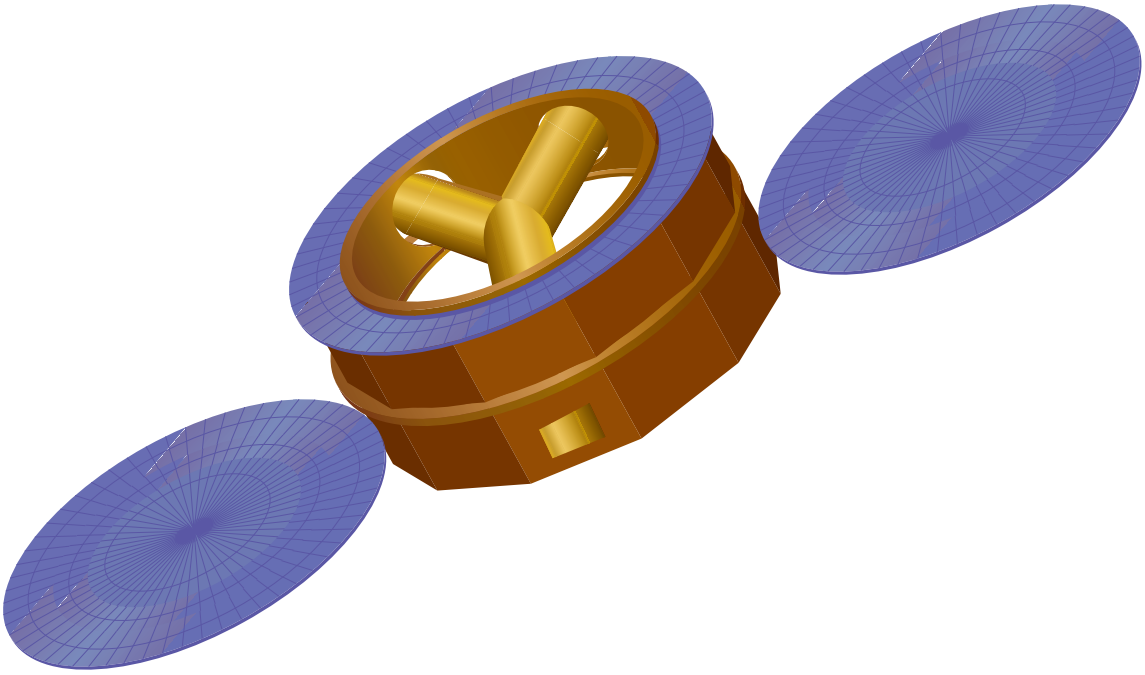

Figure 7.3 *LISA spacecraft attached to the solar electric propulsion module.*

engine is for redundancy and balances the launch load.

For attitude and small orbit trimming manoeuvres, a monopropellant hydrazine system is provided. It is a simple blowdown system with one tank and four 4.45 N and four 0.9 N thrusters, requireing about 5 kg of hydrazine.

The propulsion module structure consists of a 1800 mm diameter central cylinder and two interface rings for the separation system. The total height of the PM is 400 mm. The cylinder is constructed as a Carbon Fibre Reinforced Plastic (CFRP) honeycomb structure with a total thickness of 20 mm. The interface rings are made from aluminium.

The total nominal power provided is about 500 W. For initial acquisition, emergencies and peak power demand, two non-rechargeable batteries are included. Also the pyro firing currents for the RCS pyro valves and separation pyro's are provided from the batteries via a pyro electronics unit.

For initial rate reduction and during orbit manoeuvres, rate sensors are desirable. The PM therefore also accommodates two Inertial Reference Units (one redundant) and their electronics.

The total dry mass of the Propulsion Module is 131 kg. Mass and power budgets are given in Section 7.4.

7.1.3 Composite

Each of the three composites (Figure 7.3) consists of a propulsion module with a spacecraft mounted on top. The total composite dry mass is 333 kg.

7.1.4 Launch configuration

The spacecraft size and shape are approximately optimized to contain the two optical assemblies within the payload thermal shield. This shape combined with the desire to fit the three spacecraft with their propulsion modules into the Delta II fairing places volume constraints on the propulsion modules.

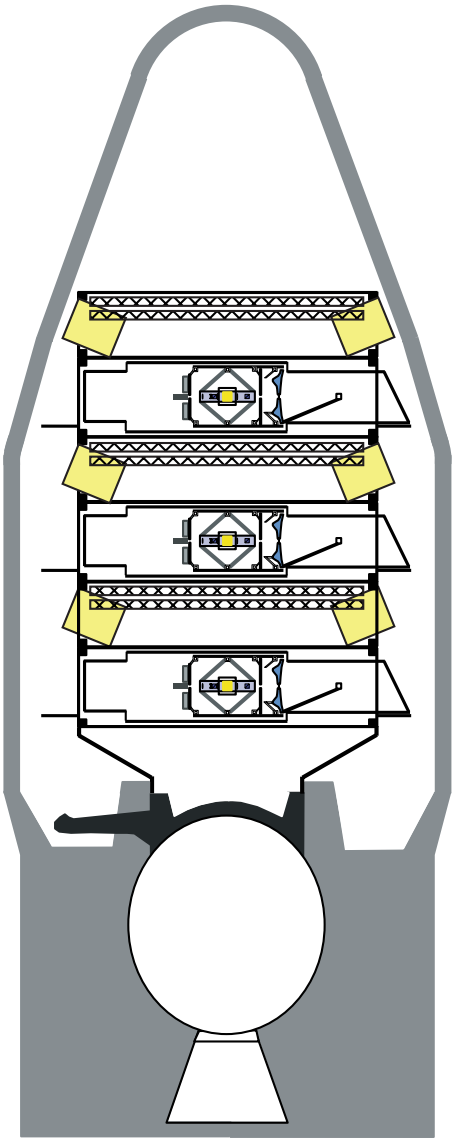

Figure 7.4 *The three LISA spacecraft, each with attached propulsion module, within the 9.5 foot fairing for the Delta II 7925 H. The launch stack is attached to the upper stage by a custom launch adapter.*

As is shown in Figure 7.4, the available static envelope within the 9.5 foot fairing allows for the accomodation of the three-composite launch stack with a propulsion module on the top. Preliminary analysis has shown that the first lateral eigenfrequency of the lower stack meets the Delta II requirement (> 15 Hz), and so does the first axial frequency (> 35 Hz).

7.2 Spacecraft subsystem design

7.2.1 Structure

The spacecraft structure is composed of the following elements:

- An exterior cylinder with top and bottom plate to stiffen the cylinder and provide mounting points for the subsystems. Made from CFRP honeycomb with 0.3 mm CFRP skins and a 10 mm CFRP core.
- Interface rings at each side of the cylinder. These interface rings are made in AFRP (Aramid Fibre Reinforced Plastic) or Carbon/Carbon material.
- Two CFRP support structures for mounting the high-gain antennas and their pointing mechanisms.

The payload module, which on the outside includes a thermal shield made of CFRP with a thickness of 1.5 mm, is attached to the central cylinder, with a system of Kevlar straps.

The two startrackers are supported by suitable interface brackets on the PLM thermal shield.

7.2.2 Thermal control

The thermal control subsystem of the spacecraft is basically a passive system with heaters and their associated controls as the only active elements. All units will have primary and redundant survival heaters controlled by thermostats. These heaters will only be used during the transfer phase or in contingency situations. During the routine operational phase, operation of the heaters will not be required. All units attached to the side panels and the internal surfaces of the side panels will have low emissivity surfaces so that most of the thermal energy is radiated to space, via radiators on the side panels.

A detailed thermal design and thermal analysis has not been performed and especially the very demanding requirements of the payload module and the optical bench in particular might require additional measures, such as a thermal shield on top of the central cylinder, thus protecting the PLM against direct Sun radiation.

Also the amount of heater power during the transfer phase, in order to ensure that the temperature of units that are switched off does not fall below their minimum survival temparature, has not been properly assessed yet and requires more detailed analysis. It is currently estimated at 17 W.

7.2.3 Coarse attitude control

The main requirements on spacecraft drag-free and attitude control derive from payload constraints. The drag-free control system must force the spacecraft to follow the proof mass to $1\,\mathrm{nm}/\sqrt{\mathrm{Hz}}$. The control signals are derived from the payload-provided electrostatic accelerometer as described in Section 3.2. The attitude control system points each spacecraft towards the spacecraft at the other end of its optical path. The pointing tolerance is $5\,\mathrm{nrad}/\sqrt{\mathrm{Hz}}$ for frequencies above about 10^{-4} Hz and 30 nrad for lower frequencies

and DC. The operational attitude control signals for pointing of the Z-axis (telescope axis) will be provided by the main signal detecting diodes, the difference between the signals from their quadrants giving information on the wavefront tilt.

Initial beam acquisition will rely on the startrackers which are co-aligned with the main telescope. A pointing accuracy of about 100 μrad is sufficient. Once this is established, the laser beam will be defocussed from its diffraction-limited divergence and imaged in the receiving spacecraft on the quadrant diodes. The resulting signal will be used to iteratively repoint the spacecraft until the laser beam divergence can be reduced to the minimum value.

The control torques and forces for the attitude and drag-free control during the operational phase are provided by the Field Emission Electric Propulsion (FEEP) subsystem. The thrusters of this subsystem are composed of an emitter, an accelerator electrode and a neutralizer and use liquid cesium as propellant. Their specific impulse is of the order of 10 000 s and they can provide a controlled thrust in the range of 1 to 100 μN, with a noise below 0.1 μN. Six clusters of four thrusters each are mounted on the spacecraft equipment panels. The major force to be compensated is the solar radiation pressure, which, if the spacecraft is completely closed on the top (thermal shield), has a magnitude of about 50 μN.

As the drag-free and attitude control is so intimately related to the experiment and payload, a more detailed description of these subsystems is given in Sections 2.8, 3.2 and 7.3, also including more details on the FEEP thrusters. Because of this close relation, the drag-free control system is a PI-provided item and described in Section 3.3 .

During the early orbit and transfer phase, the primary attitude sensors to be used are the startrackers (ST) and Fine Sun Sensors (FSS) of the top spacecraft of the composite. As the startrackers cannot measure large rates, an Inertial Reference Unit (IRU) is required as primary sensor during some phase of the early orbit and transfer phase, e.g. during rate reduction after separation from the launcher, during slew manoeuvres and during V manoeuvres. The IRU's will not be required during the operational phase and are mounted on the propulsion module.

During the initial Sun acquisition phase and during emergency safe modes, Sun Acquisition Sensors will be used.

7.2.4 On-board data handling

The spacecraft controller consists of two identical units operating in a String A and String B fashion. String B acts as a warm backup and receives state data from String A at specified intervals. String B will contain a watchdog timer to monitor String A. If this timer runs out, String B will take over as the primary spacecraft controller.

The spacecraft controller will perform the command and data handling functions, attitide determination, and control functions as well as processing science data. These functions include science and engineering data collection and data storage. Power to the controller will be supplied by the spacecraft.

A RAD 6000 flight computer as used in the Mars Surveyor Program is suggested for the spacecraft. It contains 128 Mbytes of DRAM and 3 Mbytes of PROM. The relatively low

data rates for science and telemetry permits all data to be buffered and stored in DRAM on the flight computer board, thus reducing the subsystem mass and power.

7.2.5 Tracking, telemetry and command

The TT&C functions are provided by an X-band telecommunications system, consisting of transponders, a Radio Frequency Distribution Unit (RFDU) and antennas. The transponder subsystem features two basic transponder units, each with its own solid-state power amplifier. Each transponder operates with the receivers in hot redundancy. The transmitters are configured for cold redundancy and can be switched on and off by telecommand. The function of the RFDU is to control the routing of telecommand and telemetry data between the two transponders and the antennas. The signal routing provides efficient redundancy for both telecommand and telemetry functions.

During the operational phase, two steerable high-gain antennas configured on top of the spacecraft are used. These have a diameter of 30 cm and a nominal boresight gain of 25 dBi. The 3 dB two-sided beam width of the antenna is about 8° and an elevation mechanism can be avoided. A mechanism providing 2π coverage in azimuth is required, however.

To obtain the required omni-directional coverage for telecommand, two low-gain antennas are mounted on opposite sides of the spacecraft. These, however, cannot provide for the telemetry during the transfer phase, and medium gain antennas, accommodated according to the spacecraft-Earth direction during the transfer, are required. The location of these antennas is TBD.

With 5 W transmitted RF power, the high-gain antennas allow for a telemetry rate of 375 bps into the 15 m ESA stations. For a real-time science and housekeeping data rate of 80 bps for each of the six spacecraft, a total daily contact time of 16 hours is required (e.g. two stations 8 h each) and simultaneous telemetry from the two spacecraft at one vertex.

7.2.6 Power subsystem and solar array

Each LISA composite consists of two modules. Apropulsion module jettisoned at the end of cruise, and a sciencecraft module. The sciencecraft is a flat cylinder, 1.8 m in diameter by 0.5 m thick. Anexternal sunshade is added to the outer sciencecraft edge on the sun side. This shade combined with the nominal sciencecraft flat surface provides a total sun-facing diameter of 2.2 m with a total surface area of 3.8 m^2.

The orbital configuration allows the sciencecraft to be in sunlight at all time, with a maximum off sun angle of 30 ° (during science operations). Sun facing surfaces are expected to reach 80 °C.

GaAs solar cells with 19 percent efficiency are used for power generation for both the sciencecraft and the SEP arrays. The batteries are of the Lithium-ion type, providing 80 Whr/kg specific energy density and 140 Wh/l volumetric density. Integrated Multichip Module to VME board technology is used for power control, management and distribution, and laser pyro drivers. This technology is expected to be demonstrated and qualified

before 2001 .

The sciencecraft power requirements with contingency are 195.7 W during science operations (xmit on), 76 W during cruise, and 118.5 W during launch (incl. 25.4 W for propulsion module). Cruise power for the hydrazine thrusters can be supported by the flat body mounted sciencecraft solar array. Launch power will be supported by a secondary battery. The battery will provide fault protection during flight. A 20 Ahr Li-Ion battery with 27 V will support launch for 2.7 hours. During this time, launch, separation and deployment, and sun acquisition will occur. The launch cycle depth of discharge is 80 % with few expected cycles thereafter. The mass and volume of this battery are 5.9 kg and 3.4 l, respectively.

A single body-mounted GaAs solar array of 1.57 m^2 surface area and a mass of 2.15 kg supplies the power for the sciencecraft, 237 W at BOL and 195.1 W at EOL. This array is fixed to the sun facing outer edge of the sciencecraft and is sized for a 30° off sun angle.

The power electronics system will make use of four elements. These elements are the Power Management Unit, the Power Control Unit (including the battery charger), and two laser Pyro Switching Unit slices. The power subsystem mass is based on 100 W/kg and 237 W power and is estimated at a mass of 2.9 kg.

A separate array and drive electronics are added for the solar-electric propulsion module. All pyro events conducted off the existing sciencecraft pyro drivers. The thruster requires power to be supplied at 55 V with a range from 53 to 57 Volts. Power requirement for the SEP is 558 W. SEP power must be conditioned before the SEP drive. Power contingency on the SEP is 5 %.

The SEP array makes use of 19 % efficient GaAs solar cell technology with a total surface area of 5.58 m^2 and a total mass (not including support structure and drive mechanism) of 6.97 kg. The deployed array is configured into two symmetrical panels with a single axis of freedom. The array is sized based on 100 W/m^2 specific energy density and 80 W/kg.

7.3 Micronewton ion thrusters

The very minute thrusts required in the manoeuvers for pointing (3.1.8) and drag-free operation (2.8.3) of the LISA spacecraft are best provided by the Field Emission Electric Propulsion (FEEP) thrusters. They operate by accelerating ions in an electric field, and ejecting them to develop the thrust [122]. The ions are generated by exposing a free-surface of liquid metal (cesium or indium) to an electric field.

The shape of this liquid surface is established by the counteracting forces of surface tension and electric field stress along a knife-edge slit with a width of about 1 μm, or at a Tungsten needle with a tip radius of 2 to 15 μm. With an applied voltage between 5 and 10 kV, the ions are ejected at a velocity in the range of 60 to 100 km/s, depending on the propellant and the applied voltage. The mass flow is very low, so the developed thrust is in the desired micro-Newton regime. By smoothly varying the applied voltage, the thrust can be correspondingly controlled, as desired, all the way down to fractions of a micro-Newton. The FEEPs require only about 15 W to develop the necessary thrust. The total propellant (cesium or indium) mass required for the nominal two-year mission is only a few grams per thruster.

There are mainly two designs being pursued by *Centrospazio* (Italy) and at the *Austrian Research Centre Seibersdorf* (ARC). The FEEPs originally developped by *Centrospazio* were designed for thrusts in the milli-Newton regime, as required for communication sattelites. For LISA, they had to be scaled-down by a factor of a thousand from the original design. The development at ARC, the Indium Liquid-Metal Ion Sources (In-LMIS) have originally been designed for spacecraft charge control and microanalysis instruments. They have already been flown on various missions and proven their reliability in space during more than 800 hours of operations.

The description in the following subsections mainly refer to the *Centrospazio* design. We come back to the ARC design in subsection 7.3.5 .

7.3.1 History of FEEP development

Research on Field Emission Electric Propulsion (FEEP) using liquid metals has been carried out by ESA since 1972. The thruster has evolved from a single-pin emitter configuration in 1972, through linear arrays of stacked needles in 1975, to the high-efficiency solid-slit emitter in 1979. During the past phases of the development program, all the components of the system have been designed and tested, and the emitter manufacture problems have been solved. At that time, development had entered the industrialization phase, and research was devoted to the testing of the whole system in view of an application in the milli-Newton range, mainly for North-South station-keeping operations in geostationary telecommunication satellites. The high power-to-thrust ratio of FEEPs, in comparison with other electric propulsion systems now fully developed, made FEEPs lose competitiveness for this specific application. However, a rising interest of the international scientific community in missions requiring micro-Newton thrust levels for ultra-fine pointing operations (such as in LISA) sparked the present reorientation of FEEP activities to this new thrust range.

7.3.2 The Field Emission Electric Propulsion System

In the FEEP system, ions are created directly from the surface of a liquid metal exposed to vacuum, by means of a strong electric field resulting from suitable voltages applied to an emitting unit.

When the surface of a liquid metal is subjected to a strong electric field, it distorts itself into a series of cusps that protrude more and more from the surface plane: the radius of curvature of the cusp tips becomes smaller and smaller, thus in turn increasing the strength of the local electric field. When the field reaches values of the order of 10^9 V/m, the atoms of the metal tip spontaneously ionize, and these ions are accelerated away by the electric field that has created them [123, 124].

Cesium, whose melting point is about 29 °C, has been chosen as propellant because of its low work function, high atomic mass and good properties of wetting on steel surfaces.

The basic FEEP system comprises: a single solid emitter/accelerator system or a cluster of them, a storage and feed system for the Cs propellant, a power conditioning and control unit, and a neutralizer (Figure 7.5).

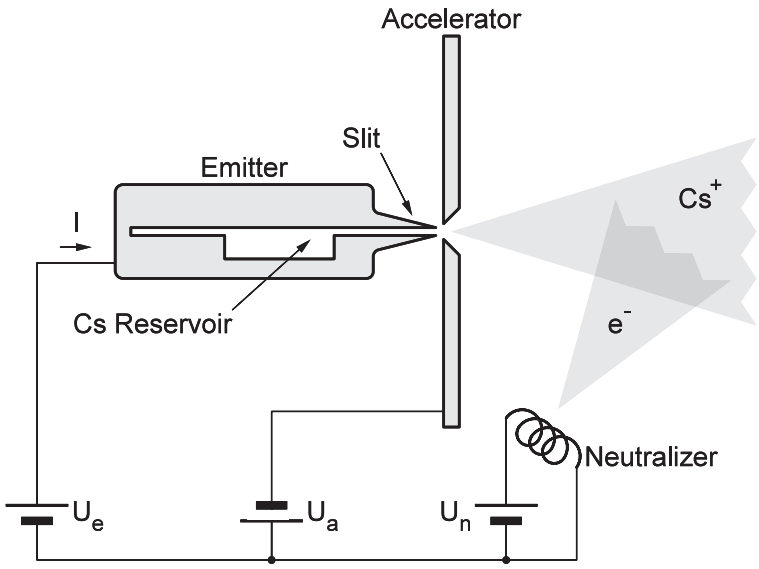

Figure 7.5 *FEEP thruster schematic.*

The main elements of the thruster are the emitter (kept at positive voltage V_e) where the ions are created, and the accelerator (kept at negative voltage V_a), a counter-electrode to establish the voltage difference $V_e - V_a$ needed for ionization and acceleration. A threshold voltage of 7 kV is necessary to start the emission.

The emitter consists of a narrow slit between two highly polished metallic plates. On certain regions of one of the inner surfaces several thin dots of Nickel ($\approx 1\,\mu$m) are deposited by sputtering. When the two halves are tightly clamped together, they are separated by only the thickness of the Ni deposits, thus forming a narrow slit through which the liquid metal is transported to the edges under the action of capillary forces. The present types of emitters have a weight of 15 g. The accelerator is a stainless steel plate placed in front of the emitter; the ion beam is extracted through an elongated slit in front of the emitter blades. The thrust produced by the FEEP system (measured in N) is given by

$$F = 1.66 \times 10^{-3}\ I_e\ V_e^{1/2}\ \frac{\sin\alpha}{\alpha}\ \frac{\sin\beta}{\beta}\,, \tag{7.1}$$

where I_e and V_e are the emitter current and voltage (measured in A and V, respectively), and α and β are the divergence angles. By varying just one parameter, the emitter voltage V_e, the thrust level can be changed.

The neutralizer will supply the electrons needed to neutralize the ion beam created in the emitter/accelerator assembly. Neutralizer concepts requiring only low current and power are currently being evaluated, such as thermionic cathodes and field emission electron sources.

The feeding system consists of a shaped reservoir directly connected to the emitter blades, requiring no external force to drive the propellant to the slit. The small amount of propellant required allows for a self-contained, integral reservoir unit, thus eliminating a complicated feeding system control and reducing the interface with the spacecraft to the electrical connections only. An engineering model of the thruster, including the propellant

reservoir, an active thermal control and monitoring system, and a sealed container is already available. This assembly weighs about 300 g and has an overall envelope of 7 cm in height and 6 cm in diameter, and may host about 40 g of propellant. The Power Conditioning and Control Unit (PCU) will provide the adequate voltage and current levels to the different subsystems of the FEEP thruster and will act as interface with the spacecraft power and data buses.

Centrospazio (Italy) and *Laben* (Italy) are currently developing the different subsystems for ESA.

7.3.3 Advantages and critical points of FEEP systems

The main advantages of the FEEP system for missions like LISA with highly demanding attitude requirements are the following [124, 125]:

- If the forces disturbing the spacecraft are of the order of $1\,\mu\text{N} - 100\,\mu\text{N}$, the FEEP thruster is the only system capable of providing this kind of thrust level with sufficient accuracy. For the LISA mission, the FEEP thrust controllability must be able to cover the range $0.1\,\mu\text{N} - 100\,\mu\text{N}$, with resolution better than $0.1\,\mu\text{N}$. The FEEP emitter performance is $300\,\mu\text{N}$ per centimeter of slit length. The power-to-thrust ratio is $50\,\text{mW}/\mu\text{N}$.
- The exhaust velocity of the ions in the FEEP thruster, $\approx 60\,\text{km/s}$, allows great mass savings compared with other propulsion systems. The total required fuel tankage for the (nominal) duration of 2 years of the LISA mission is 9 g per thruster.
- As the FEEP system requires only an insignificant amount of propellant, in a compact reservoir, disturbances due to propellant sloshing, or to tidal motion of the gravity center of the propellant under the combined Earth-Moon attraction, affecting the self gravity conditions onboard, are completely negligible.
- The FEEP sytem requires no valve or any other moving parts, and thus any problems of mechanical or gravitational compatibility are avoided.

Possible critical areas to take into consideration when using FEEP thrusters for fine attitude control are:

- Reliability: the expected lifetime in space has not been determined; however, at the ESTEC Electric Propulsion Test Laboratory, a systematic attempt will be made to determine the lifetime. An endurance test of several months will take place at ESTEC in 1998. Preliminary, non-optimal tests demonstrate that laboratory lifetime is in excess of one month in continuous operation, and at least 10^6 firings in pulsed mode.
- Repeatability: measurement techniques of FEEP micro-Newton levels must be improved in order to fully demonstrate the repeatability of the FEEP system working with the high resolution aimed at ($0.1\,\mu\text{N}$). Noise and direct thrust measurements must also be taken into consideration [126, 127].
- Major failure modes in the past have been: (1) clogging of the cesium feed by CsOH, produced by the interaction of cesium with ambient laboratory water, and

(2) sparking damage to the knife edge of the emitter when the FEEP is run at high voltages and high currents. The lower currents required for the low-thrust operation in the LISA mission should greatly reduce the danger of sparking damage. Water vapor will not be a problem in orbit or when the thrusters are firing continuously, but the process of bringing the FEEPs into space avoiding water vapour during pre-launch, launch and orbit transfer must be carefully designed.

7.3.4 Alternative solutions for FEEP systems

As the thrust level for LISA is in the range of only micro-Newtons, the old requirement of high atomic mass for the propellant is no longer so important. Therefore, alternative propellants for the FEEPs are now becoming attractive, propellants having good wetting characteristics and low ionization energy, without having the problem of reacting with water vapour. The successful operation of an indium field emitter for spacecraft charge control on the Geotail satellite and on the *Mir* station, using the same principle as the FEEPs, has focused the attention on this propellant [128, 129]. Further studies on new propellants with the selection of a suitable emitter material and/or surface treatment are being envisaged by ESA.

7.3.5 Current status

Activities at *Centrospazio*.

- To avoid contact between the water vapor and the cesium during the pre-launch, launch and orbit transfer, the thruster is placed in a gas-tight cover with an inert gas surrounding it after being operated in the vacuum chamber. This container and the ground equipment required to assemble this system has been manufactured and tested at *Centrospazio*.
- *Centrospazio* has identified the thermoionic neutralizer as the main candidate for the FEEP system due to its high reliability with a demonstrated lifetime of more than 10 000 hours. Field emission neutralizers, used in the TV-screen technology, are also being developed by *Centrospazio* because of their low power consumption and low cost.
- Under ESA contract, *Centrospazio* has designed, manufactured and tested the integrated emitter/feeding system.
- *Laben* (Italy) is manufacturing the Power Conditioning Unit for the FEEP system under ESA contract.
- *Centrospazio* and *Laben* are currently preparing a FEEP flight experiment on board the space shuttle. This will be the first time that the *Centrospazio* FEEP is operated in space.
- A lifetime test of a FEEP thruster operating at a certain thrust level ($1-50\,\mu$N) with neutralizer will take place during 1998 in the ESTEC FEEP vacuum facility under the responsibility of *Centrospazio*.

- *Centrospazio* is currently investigating the possibility of using indium as propellant for the *Centrospazio* FEEP thruster in collaboration with the *National Physics Laboratory* (United Kingdom).

Activities at the *Austrian Research Centre Seibersdorf.*

The standard Indium Liquid Metal Ion Source (In-LMIS) developed at the *Austrian Research Centre Seibersdorf* is of the central needle type, in which a sharpened tungsten needle of tip radius of a few μm is mounted in the centre of a heated indium reservoir. For operation, a potential of typically $5-7\,\mathrm{kV}$ is applied between the needle and an accelerating electrode. If the needle is well wetted by the liquified indium, the electrostatic stress of the applied field pulls the indium film towards the electrode. This stress is balanced by surface-tension forces which leads to the establishment of a characteristic equilibrium configuration, the so called Taylor cone (see Figure 7.6). Once the electric

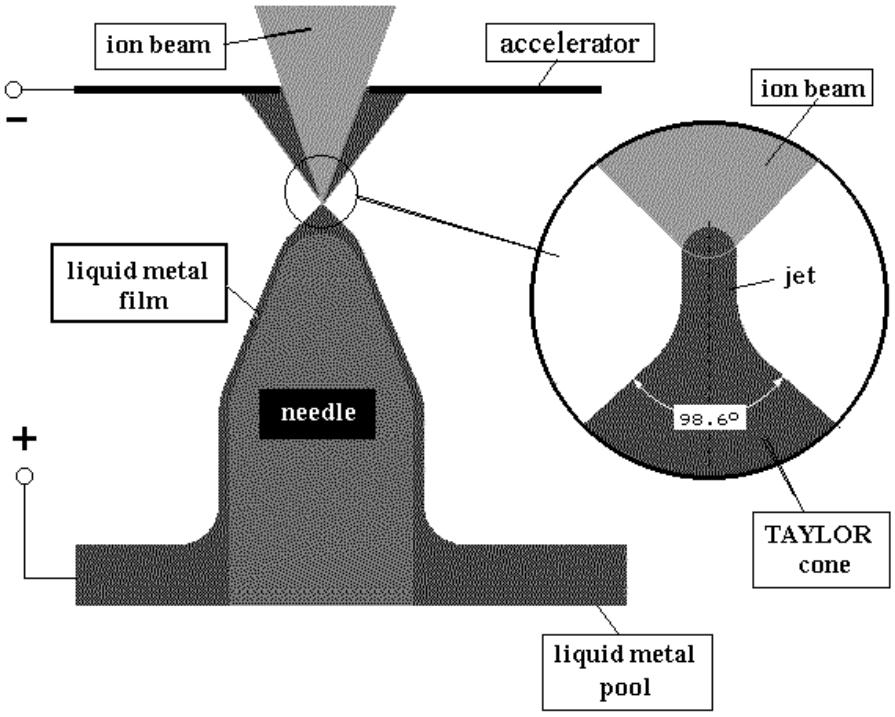

Figure 7.6 *Schematic of the operation of a needle type liquid-metal ion source.*

field at the apex of this cone gets to the order of volts per nanometer, the most protruding surface atoms are field evaporated, ionized and accelerated towards the electrode. Via hydrodynamic flow the atoms leaving the tip area are constantly replenished and a stable emission regime can thus be maintained. Figure 7.7 shows an image of the space qualified indium LMIS.

Originally developed for spacecraft potential control instruments these indium LMIS so far have been flown on four missions (GEOTAIL, EQUATOR-S and two times on MIR) and are currently scheduled to fly on CLUSTER-II, ROSETTA and again to the MIR station in the next future. A total of 35 ion sources will be used in these three projects. The reliability of the indium LMIS design up to now has been proven in more than 800 hours

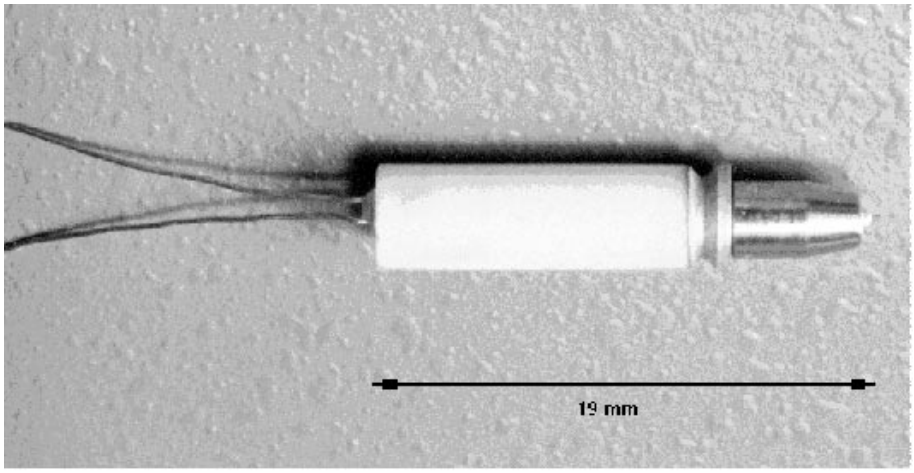

Figure 7.7 *Photograph of an indium LMIS developed at Seibersdorf.*

of operation in space. This fact together with the low emission current characteristics of these sources, which could be used to produce a highly controllable micro-thrust ion beam, highlighted the importance of this technology as a complementary low-thrust system to the cesium FEEP thrusters. Therefore a small contract for performance characterization, lifetime, reproducibility and controllability of these sources was placed by ESA with ARC in 1996. The final results showed that some areas as mass efficiency, specific impulse or thrust controllability were points still to be investigated in order to improve the thruster performance. In particular, the mass efficiency started to diminish when increasing the thrust level above $8\,\mu$N. This effect could be due to the uncompleted ionization of the indium species which induces the apparition in the beam of droplets, multi-atomic, single-charged aggregates and multiple-charge ions.

ARC is currently working in a new ESA activity dedicated to the understanding of the basic physics regulating the already mentioned phenomena. This first phase will help to optimize this device which was first designed as a charge compensator. Therefore matters such as distance between electrodes and voltage distribution will be assessed during this activity. Then, the optimized version of this thruster at engineering level will be submitted to characterization tests with thrust levels running from 1 to $25\,\mu$N.

Microthrust measurements. The *National Physics Laboratory* (United Kingdom) is currently developing a microthrust balance for the direct measurement of the FEEP thrusters. A prototype of this unit will be ready by the end of 1998. *Centrospazio* is also developping a different concept of a microthrust balance under ASI funding.

Direct measurement of FEEP thrust will be needed in order to fully characterize the FEEP thrusters, including thrust noise evaluation and validation of the theoretical formula at micro-Newton level.

Future plans. Development and qualification of a Field emission neutralizer as possible alternative to the thermoionic neutralizer. This new concept may improve some system aspects such as power consumption and redundancy.

Miniaturization of the power electronics and redundancy philosophy investigations. Power electronics is the heaviest part of the FEEP system and must be reduced.

7.4 Mass and power budgets

The spacecraft mass and power bugets are given in Table 7.1 below. Power budgets are given for two cases: power in operational orbit, and power during transfer.

Subsystem	*Mass* (kg)	*Operational Power* (W)	*Power in Transfer Orbit* (W)
Payload	70.0	72.2	
Payload Shield	14.2		
Structure	41.1		
Thermal	1.7		17.0
Attitude Measurement	6.0	2.1	12.7
Propulsion (FEEP)	22.0		
Telecommunications	9.9	26.4	12.0
Data Handling	14.5	13.1	9.9
Power Subsystem	12.2	14.8	6.8
Cabling	15.1		
Total	202.8	150.6	58.4

Table 7.1 *Spacecraft mass and power budgets.*

The mass and power budgets of the propulsion module are given in Table 7.2 .

Subsystem	*Mass* (kg)	*Power* (W)
Structure	52.0	
Thermal	3.0	17.0
Propulsion SEP	44.2	490.0
Propulsion Hydra	7.6	0.8
Power	12.6	26.9
Solar Array	4.2	1.0
Cabling	8.0	
Total	131.6	535.7

Table 7.2 *Propulsion module budgets.*

The overall launch mass budget is presented in Table 7.3.

Item	*Composite* 1	*Composite* 2	*Composite* 3	Total
S/C	203	203	203	
PM dry	132	132	132	
Propellant	27	27	27	
Total	362	362	362	1086
Adaptor				21
Contingency (30 %)	100	100	100	300
Total Launch Mass	462	462	462	1407

Table 7.3 *Total launch mass budget* (kg).

Chapter 8

Technology Demonstration in Space

To minimize the cost and risk associated with the full LISA mission it is essential to have well-understood and proven technology available. A LISA technology demonstration mission is therefore highly desirable. Such a mission should not just provide a functional test but should instead aim at testing the key technologies required for LISA to within an order of magnitude of the final performance in the relevant mHz frequency range.

8.1 ELITE – The European LISA Technology Demonstration Satellite

8.1.1 Introduction

The proposed *E*uropean *LI*sa *TE*chnology demonstration satellite (ELITE) aims to test the key technologies of inertial sensing, drag-free control, and low-frequency laser interferometry required for LISA.

The single ELITE spacecraft will contain two isolated proof masses which will be used as references for the drag-free/attitude control system. The proof masses will also serve as reference mirrors for the laser interferometer package. The interferometer will provide an independent measurement of relative displacement between the masses, allowing a direct assessment of the relative acceleration between the masses. Field emission (ion) thrusters will be the primary actuators for the drag-free/attitude control. An autonomous star-tracker plus Sun sensor will be used for coarse attitude control/safe-mode. A cold-gas system will be used for coarse-attitude control.

The target launch year is 2002 (pending the timely development of the key technologies), with a nominal mission duration of six months.

Various candidate orbits and launch options are being considered. It is desirable to have an orbit altitude above 10 000 km in order to avoid the charging of the proof masses due to interaction with trapped protons in the Van Allen Belts. The baseline choice is a Geostationary orbit (GEO) which avoids the proton belts completely, but which necessitates an apogee kick motor for orbit injection. Another option would be to utilise a shared launch into a suitable orbit without the need for an apogee kick motor. One

possibility is to partner with the proposed Kronos mission which has an orbit perigee of 10 Earth radii and an apogee of 60 Earth radii. Other suitable sharing options should be investigated. In the worst case, a "de-scoped" option would be a Geostationary transfer orbit (GTO) which would eliminate the need for a large apogee kick motor, but which would incur much higher charging rates due to traversal of the proton belts. The charge management system would thus have to be enhanced in this option, but the spacecraft and launch costs could be minimised compared with the alternative options.

8.1.2 Mission goals

The primary goals of the ELITE mission are summarised as follows:

1. To demonstrate drag-free/attitude control in a spacecraft with two proof masses in order to isolate the masses from inertial disturbances. The aim will be to demonstrate the drag-free system with a performance on the order of than $10^{-14}\,\mathrm{m\,s^{-2}}/\sqrt{\mathrm{Hz}}$ in the bandwidth from $10^{-3}\,\mathrm{Hz}$ to $10^{-1}\,\mathrm{Hz}$, bearing in mind the LISA requirement of $10^{-15}\,\mathrm{m\,s^{-2}}/\sqrt{\mathrm{Hz}}$ for each proof mass (see below).
2. To demonstrate the feasibility of performing laser interferometry in the required low-frequency regime with a performance as close as possible to $10^{-12}\,\mathrm{m}/\sqrt{\mathrm{Hz}}$ in the bandwidth from $10^{-3}\,\mathrm{Hz}$ to $10^{-1}\,\mathrm{Hz}$, as required by the LISA mission (see below). Of course, this test only demonstrates the *displacement* sensitivity of the interferometer, not the *strain* sensitivity, which would require large separations ($5\times10^{6}\,\mathrm{km}$) between the proof masses.
3. To assess the longevity and reliability of the capacitive sensors, thrusters, lasers, and optics in the space environment.

In addition to these primary goals, the ELITE mission will enable systematic tests to be performed on the technology. For example, the characteristics of the thrusters and sensors can be determined over their dynamic range, for use in future design refinements; and the effects of known disturbances (e.g. due to electrical charging of the proof masses) can be assessed. Likewise, various control and calibration strategies can be compared (e.g. using one proof mass as the translational reference, the other as an attitude reference; or defining a virtual drag-free reference from a combination of sensor outputs, etc.)

8.1.3 Background requirements

It is useful to consider the requirements of the full-blown LISA gravitational-wave mission in order to put the ELITE goals into perspective The baseline LISA requirements are summarised as follows:

1. In order to achieve the basic gravitational wave strain sensitivity, each proof mass must be free of spurious accelerations (relative to inertial space) along the interferometer axis to better than

$$10^{-15}\left[1+\left(\frac{f}{3\times10^{-3}\,\mathrm{Hz}}\right)^{2}\right]\,\mathrm{m\,s^{-2}}/\sqrt{\mathrm{Hz}}$$

within the measurement bandwidth (MBW) of 10^{-4} to 10^{-1} Hz. The requirements along the other axes are relaxed by approximately two orders of magnitude.

2. In order to suppress the effects of motion-modulation of local (spacecraft-induced) disturbance fields (magnetic, electrostatic, gravitational, etc.) and to suppress the effects of optical-path fluctuations, the relative displacement between each proof mass and the spacecraft, along the intereferometer axis, must be less than

$$5 \times 10^{-9}\,\mathrm{m}/\sqrt{\mathrm{Hz}}$$

within the MBW. This corresponds to a relative acceleration of

$$\approx 10^{-13}\,\mathrm{m\,s^{-2}}/\sqrt{\mathrm{Hz}} \quad (\text{at } 10^{-3}\,\mathrm{Hz})\,,$$

which is seen to be two orders of magnitude above the requirement on the inertial acceleration of the proof mass (item 1). This means that the spacecraft drag-free control requirement (i.e. relative to the proof mass) is relaxed compared with the requirement on the inertial isolation of the proof mass. This relaxation is made possible by the optical arrangement whereby the light is effectively referenced to opposing surfaces on each proof mass.

The corresponding relative displacement requirements along the non-sensitive axes arise only from the need to suppress nonlinearities and to avoid sensor saturation (e.g. of the op-amps in the capacitive circuits) which suggests that the displacements must be less than

$$5 \times 10^{-6}\,\mathrm{m}/\sqrt{\mathrm{Hz}}$$

within the MBW. However, since each spacecraft contains two proof masses, and since the interferometer axes for each arm are not parallel, the more rigid requirements will prevail in two planar directions, and only the out-of-plane direction will be relaxed.

3. The spacecraft attitude must be precisely controlled for two reasons: (i) to ensure that the receiving spacecraft remains locked-on to the same portion of the incoming, non-perfectly-spherical optical wavefront; and (ii) to ensure that the attitude motion does not yield excessive translational motion at the location of each proof mass (which are spatially separated by tens of centimetres). For nominal parameters, (i) imposes that the pointing must be controlled to within

$$\theta_{\mathrm{dc}}\,\widetilde{\delta\theta} \leq 3 \times 10^{-16}\,\mathrm{rad}^2/\sqrt{\mathrm{Hz}}\,,$$

where θ_{dc} represents the dc pointing error, and $\widetilde{\delta\theta}$ represents the pointing jitter across the MBW. Assuming that θ_{dc} can be controlled to $\approx 3 \times 10^{-8}$ rad (depending on photodiode drift, etc.), this imposes a jitter requirement of

$$\widetilde{\delta\theta} \leq 10^{-8}\,\mathrm{rad}/\sqrt{\mathrm{Hz}}$$

within the MBW. Depending on the actual geometrical layout, condition (i) will be more or less demanding than condition (ii). For example, assuming that the proof masses are spatially separated by 0.2 m, and that the drag-free null passes through

the location of one proof mass, then the jitter of $10^{-8}\,\mathrm{rad}/\sqrt{\mathrm{Hz}}$ corresponds to a displacement of $2\times10^{-9}\,\mathrm{m}/\sqrt{\mathrm{Hz}}$ at the location of the other proof mass. This is within the allowable limit of item 2, so condition (i) on attitude is more restrictive than condition (ii), etc.

4. In order to achieve the target strain sensitivity across the armlength of $5\times10^{6}\,\mathrm{km}$, the interferometer displacement noise must be lower than approximately

$$10^{-11}\,\mathrm{m}/\sqrt{\mathrm{Hz}}$$

across the MBW. This includes all optical effects, as well as spurious proof-mass motions. Allowing for reasonable apportioning of errors across the various contributions, the requirement on the optics alone becomes

$$10^{-12}\,\mathrm{m}/\sqrt{\mathrm{Hz}}$$

over the MBW.

8.2 ELITE Mission profile

8.2.1 Orbit and disturbance environment

Baseline option. For the baseline GEO option (and for a shared launch into higher orbits), the main disturbance will be radiation pressure with a nominal force magnitude of $\approx$ 10 μN (solar pressure $4.644\times10^{-6}\,\mathrm{N/m^2}$; Earth albedo plus IR pressure $\approx$ 0.2 of solar pressure), modulated at the orbit frequency due to the variation in the direction of the line-of-sight to the Sun. This disturbance will be essentially uniform, with only slight stochastic variations due to solar fluctuations amounting to a few percent of the nominal values. The largest stochastic disturbance is likely to be noise in the thrusters which may be on the order of $1\,\mu$N (*rms* across the MBW).

De-scoped option. For the de-scoped option which may be necessary due to cost, the most accessible orbit would be GTO (Geostationary Transfer Orbit). For example, from a nominal Ariane 5 launch into GTO, the resulting orbit will be low-inclination, highly eccentric, with a perigee altitude of $\approx 600\,\mathrm{km}$ (velocity $\approx 9.9\,\mathrm{km/s}$), an apogee altitude of 35786 km (velocity $\approx 1.6\,\mathrm{km/s}$), and an orbit period of $\approx$ 10.6 hours. In the vicinity of perigee, aerodynamic drag will dominate, with a nominal magnitude of $\approx 0.1\,\mathrm{mN}$ opposite the direction of travel (atmospheric density $\approx 5\times10^{-13}\,\mathrm{kg/m^3}$ at 600 km, solar maximum; drag coefficient $\approx$ 2.2, spacecraft projected surface area $\approx 1\,\mathrm{m^2}$). For most of the orbit, the altitude will exceed 1000 km, and the aerodynamic drag will be negligible compared with radiation pressure ($\approx 10\,\mu$N). The comparitively large drag at perigee will saturate the electric thrusters and the inertial sensors, requiring an undesirable switching of electrostatic suspension forces and a corresponding reset and calibration every orbit. It would thus be desirable to boost the orbit perigee to above 1000 km in order to overcome this problem. Furthermore, the GTO trajectory traverses the trapped radiation belts twice per orbit, leading to an integrated electric charge build-up on each proof mass of about $10^{-10}\,\mathrm{C}$ per orbit. However, ground tests have shown that this high charge rate can be managed by enhancing the performance of the discharge system.

8.2.2 Coarse attitude control

It is necessary to perform a continuous slewing motion in order to keep the solar array pointed at the Sun to within $\approx 1\,\mathrm{deg}$. This will require a continuously-varying angular acceleration with a peak value of $\approx 10^{-7}\,\mathrm{rad/s^2}$ which corresponds to a torque of $\approx 10^{-5}\,\mathrm{Nm}$ for nominal spacecraft dimensions. This torque could be supplied by the ion thrusters [TBD]. However, a cold-gas attitude control system will also be required for safe-modes and for the spin-up/down procedure required for stabilising the satellite during the apogee boost (if a solid apogee boost motor is used to minimise the costs in the baseline option).

The nominal mission lifetime is six months. This is sufficient for testing the performance of the accelerometers, lasers, interferometer, and thrusters, and for partially assessing their longevity and reliability in the space environment. The mission could be extended at the expense of higher operations costs.

8.3 ELITE Technologies

8.3.1 Capacitive sensor

The capacitive sensors must be designed to meet the appropriate requirements on proof-mass isolation and readout (for control) along all three translational axes. The three attitude degrees-of-freedom of each proof mass must also be measurable and controllable. Existing spaceborne accelerometer technology falls short of the LISA requirements by many orders of magnitude. It is necessary to develop the sensor technology dedicated to LISA's requirements. The aim is to test this sensor on ELITE.

8.3.2 Laser interferometer

Current ground-based laser interferometry more than meets the requirements of ELITE (and LISA), *but only in a much higher frequency regime (*kHz *instead of* mHz*).* It is necessary to demonstrate the technology required for low-frequency operation, and to test the functionality in the space environment.

8.3.3 Ion thrusters

The main requirements for the ELITE thrust system is to provide sufficient steady-state thrust to offset the external disturbance forces and to provide the six-degree-of-freedom drag-free/attitude control. Existing field-effect ion thrusters operating in the micro-Newton regime are the most suitable technology but have to be further developed for LISA. It is known that the thruster noise characteristics play a key role in the noise budget for LISA so the thrusters must be developed and flight-tested with these considerations in mind.

8.3.4 Drag-free control

Verification of the performance of the drag-free control system is a key element of the ELITE mission concept. Since the spacecraft contains two inertial sensors (as with the new LISA baseline), it cannot be manoeuvred to centre each proof mass within its housing electrodes. Instead, there will be a single location (the "drag-free null") within the spacecraft where the acceleration is minimised by the drag-free control system. Forces will have to be applied on the proof masses to compensate for any force gradients relative to this drag-free null. ELITE will test various control strategies. For example, perhaps the simplest approach is to have the spacecraft translation controlled to centre, in all three components, on one of the two proof masses (i.e. locating the drag-free null at the centre of one proof mass). The attitude of the spacecraft could then be controlled using the information from the other proof mass. The other proof mass will need to have forces applied to it to follow the primary proof mass. These forces would be applied electrostatically by means of its sensing electrodes. The magnitude of the applied force in each component would be comparable to the expected forces on the primary proof mass, i.e. corresponding to an acceleration of order $10^{-10}\,\mathrm{m\,s^{-2}}$. A key objective for ELITE will be to demonstrate that these forces can be applied in such a way that the noise introduced within the measurement band is acceptable. Also, the orientation of each proof mass needs to be controlled to match the orientation of its housing at the nanoradian level.

8.4 ELITE Satellite design

The ELITE system will consist primarily of institute-provided payload elements (e.g. inertial sensors, thrusters, lasers/optical package, flight computer, etc.). The spacecraft, which comprises the structure, power, communication etc. subsystems will be 'built around the payload' using commercially-available off-the-shelf components as far as possible. In order to minimise costs, the satellite will be single-string (in terms of failure modes) with limited functional redundancy and graceful degradation of all items.

8.4.1 Power subsystem

For the six-month duration, the GEO orbit can be chosen to be free of eclipses. Then the nominal continuous power requirement is $\approx 150\,\mathrm{W}$, including $\approx 25\,\mathrm{W}$ for battery charging (for safe-mode).

8.4.2 Command and Data Handling

A main central processor unit (CPU, e.g. RAD 6000) will be responsible for all command & data handling, and computation of control laws. A smaller backup processor will be used for initial set-up and safe-modes. Command and data I/F between the processors and all sensors and actuators will be via a 1553 bus with maximum throughput of 100 kbps. RS 422 serial communication may also be an option for some payload items [TBD]. Control of the 1553 bus can be software-switched between the processors. The main CPU will

incorporate its own warm reset/reboot capability. The backup processor will provide a cold boot capability for the main CPU. Both the main and back-up processors will have anomaly detection and safing functions.

8.4.3 Telemetry and mission operations

For the GEO-type orbit, the nominal operations can be performed via a single ground-station, essentially in real-time. NORAD and on-board GPS [TBD for GEO] (to $\approx 100\,\mathrm{m}$) will provide sufficiently accurate orbit determination so ground-based tracking/ranging will not be required.

Telemetry will be packetised according to CCSDS standards and managed by either the main or backup processor [TBD]. Standard S-band telemetry rates are: 2 Mbps S-band downlink (11 m ground-station), 1 kbps uplink. If a 1 m portable station is used, the available downlink rate is reduced by an order of magnitude (i.e. to 1.4 kbps) which is, nevertheless, sufficient for ELITE (see Table 8.1). For the GEO orbit, an on-board solid-state storage capability would not be required.

Data Items	*Word size* (bits)	*Words per Data Item*	*Data size* (bits)	*Nominal rate* (bits/sec)
2 accelerometers				
readout	16	2 x 6 (6 dof per mass)	192	192
servo command	16	2 x 6 (6 dof per mass)	192	192
discharge	16	2 x 2 (V, I per mass)	64	64
interferometer system				
lasers	16	6 [TBD] (e.g. power, etc)	96	96
readout	16	6 [TBD] (photodiodes)	96	96
Payload thermometers	12	5 [TBD] (different locations)	60	60
Drag-free control vector	16	3 (3 axes)	48	48
Attitude control vector	16	3 (3 axes)	48	48
Star-tracker readout	16	3 (3 axes)	48	48
Thruster commands	16	16 (different thrusters)	256	256
GPS	32	6	192	192
Magnetometers	12	3 (axes)	36	16
Torque rod command	12	1 (axis)	12	12
Sun sensor	12	2 (axes)	24	24
Spacecraft housekeeping	8	4	32	32
		Totals:	∼1396	∼1396

Table 8.1 *ELITE data rates, assuming uniform sample rate of 1 Hz for all data items.*

Chapter 9

Science and Mission Operations

9.1 Science operations

9.1.1 Relationship to spacecraft operations

Science operations includes all operations related to the operation of the interferometers including the checkout and setting up of the experiment sub-systems. Science operations also includes the following operations that are traditionally regarded to be spacecraft operations, because they affect control loops which directly affect the science data and so need to be under the direct supervision of the experimenters:

- Pointing measurement by startrackers and telescope quadrant detector,
- Attitude control by FEEP thrusters,
- Acquisition of laser beams,
- Adjustment of spacecraft velocity by means of the FEEPs to maintain Doppler shifts within the bandwidth of the detector system,
- Control of the scheduling of spacecraft operations in order to maintain thermal stability and avoid sources of systematic noise.

In a traditional space experiment, the need to assure the fundamental safety of the mission would normally result in the above topics being assigned to spacecraft operations. For LISA the fundamental mission safety will be assured by on-board autonomous systems and ground autonomous systems which will monitor the spacecraft engineering data stream and switch to safe modes if parameters go out of limits. Within planned limits it will be completely safe for the specified spacecraft functions to be under the control of the scientific operations team.

There will be detailed procedures to recover from the various safe modes. The most complex of these will be that following a complete loss attitude and entry into the attitude recovery mode.

Spacecraft operations once the satellites are in their final orbits should be limited to this autonomous and manual monitoring and recovery from emergencies or work arounds for observed spacecraft degradation. It is thus envisaged that the spacecraft operations team

will be primarily a group of experts who, once the spacecraft and experiment have been successfully commissioned, will only take control on comparatively rare occasions.

9.1.2 Scientific commissioning

After the initial switch-on and simple verification of operation of all the scientific subsystems, the commissioning takes place which includes the following:

- Pointing acquisition using startrackers and laser beams.
- Beam profile characterisation and choice of operating pointing.
- Measurement of orbit parameters using ground stations to track spacecraft, supplemented by observed laser Doppler shifts, and orbit adjustment using FEEPs.
- Establishment of drag-free control loop using the signals from the accelerometer, the startrackers and the laser interferometer.
- Closing of the phased lock loops on the laser transceivers.

In all these cases there will be tests performed to characterise the operation of subsystems followed by analysis of the data by the experiment team and adjustment of operating parameters. The scientific commissioning will provide the information about the operating conditions which will be used for scientific data acquisition.

9.1.3 Scientific data acquisition

During scientific data acquisition the goal will be to operate the observatory with very few interruptions for long periods, typically half or one year which will provide near continuos data sets which will be analysed to separate the GW signals from many different astrophysical sources. The steady data acquisition will be interrupted for periods of adjustment such as making changes to the relative space craft velocity. It may also be interrupted by events such as solar flares which may cause result in disturbances to the drag-free sensor proof mass.

Scientific operations are will consist of long periods of routine operations during which searches for transient events will be carried out. This will be followed by computationally intensive data analysis looking for long duration signals. Since the data can be readily stored on board and transmitted to Earth during one 8 hour shift when the constellation is in view of the principal ground station it is anticipated that scientific operations can be organised remotely by networking teams in different laboratories. So the infrastructure for operations will be comparatively modest compared with many space observatories and the operations cost is likely to be modest compared to major ground based optical observatories. Thus there should be no financial barriers to exploiting any excess life that the observatory has over and above the design life used for the engineering specifications. It is thus important that if possible the mission consumables are sized to permit extended operations over 10 to 20 years.

9.2 Mission operations

In a NASA/ESA collaborative LISA mission, ground systems and mission operations could be provided by NASA. Station support will be through the DSN and so, accordingly, several software subsystems are best taken directly from the DSN Mission Ground Support Operations (MGSO), and adapted for the LISA mission. All navigation functions with the exception of maneuver design will be done by the multimission navigation services.

Some or all of the personnel from design, development, integration, and test will become part of the operations team. Command and telemetry software developed for operations will be used for support in assembly, test, and launch operations.

Upon receipt of the telemetry data, the housekeeping packets will be analysed in order to check the health of spacecraft and instruments. Payload housekeeping and science data will be forwarded to the LISA Science Centre (LSC) located at a PI institute (to be selected through the AO), where the status of the payload will be monitored. Payload Doppler data will be immediately processed, and any desired maneuvre commands will be sent to the MGSO for uplinking. The LSC will calibrate the interferometer data and distribute them to the PIs.

9.3 Operating modes

Six operational modes/mission sequences can be envisaged. During each of these modes the allowable/required payload operations are described in the followin Subsections.

9.3.1 Ground-test mode

In this mode it will be necessary to exercise as much of the payload functionality and performance as possible. Some subsystems will not be able to be used in full due to $1\,g$ operation. Tests may be carried out with payload in any arbitrary orientation. Most tests can be done on single spacecraft.

Functional tests of all electrical/mechanical subsystems, including pointing device, lasers, discharge system, drag-free sensor electronics, drag-free clamping device, USO, interferometer electronics, star trackers, FEEP electronics, CPU and PCU.

Performance tests of subset of electrical/mechanical subsystems, including pointing device, lasers, discharge system, USO, interferometer electronics, star trackers, CPU and PCU.

An end-to-end test with two/three payloads operating together would be desirable.

9.3.2 Launch mode

Access is required for late removal of telescope covers.
All payload power should be off.

9.3.3 Orbit acquisition

Spacecraft computer performs attitude control and orbit manoeuvres with direct access to star tracker data. During this orbit acquisition phase some subsystem tests are envisaged. Release of drag-sensor vacuum enclosure seal will be done (pyrotechnic device operation). Feep seals are released. These activities are initiated by the spacecraft computer.

Functional tests of all electrical/mechanical subsystems, including pointing device, lasers, discharge system, drag-free sensor electronics, drag-free clamping device, USO, interferometer electronics, star trackers, feep electronics, CPU and PCU. Performance tests of subset of electrical/mechanical subsystems, including pointing device, lasers, discharge system, drag-free sensor electronics, drag-free clamping device, USO, interferometer electronics, star trackers, CPU and PCU.

Payload orbit/attitude constraints - keep sun outside field-of-view of telescopes.

9.3.4 Attitude acquisition

This phase includes calibration activities controlled by spacecraft but where payload computer requires access to star tracker data and ACS calibration information. There will be a progressive transfer of attitude control from spacecraft computer to payload computer. Full payload functionality is required. Sequential commissioning of drag-free operation under autonomous payload computer control. Data transfer from payload computer to spacecraft computer. Telemetry and ground command is via spacecraft computer with commands passed to payload computer for implementation. Spacecraft computer monitors orbit and attitude, including sun sensor data.

9.3.5 Science mode

Attitude control solely by payload computer. Full payload functionality and performance required under autonomous payload computer control. Payload computer is collecting science and housekeeping (h/k) data. Data are transferred from payload computer to spacecraft computer. Telemetry and ground command is via spacecraft computer with commands passed to payload computer for implementation. Spacecraft computer monitors orbit and attitude.

9.3.6 Safe mode

This mode may be invoked by the spacecraft in the event of attitude disturbance beyond the range of controllability of the drag-free system putting the mission in jeopardy. In this event the spacecraft computer may invoke safety and power saving routines. Depending on the severity of the situation the power saving priorities are given in the list below:

Power saving priorities (first off to last off):

Discharge system
Drag-free sensor electronics
Payload CPU
Lasers
Laser electronics
USO
Payload PCU

Chapter 10

International Collaboration, Management, Schedules, Archiving

10.1 International collaboration

LISA is envisaged as a NASA/ESA collaborative project in an equal partnering arrangement. This allows both space agencies to participate in this project at moderate cost and also reflects the contributions to the payload and mission design made by the scientific community in the USA and in Europe and by the two space agencies.

Much of the early development work of the LISA payload and project was carried out in the US (then known as the LAGOS project, for details see Section 2.6), while more recently most of the work was done in Europe: study of a 4-spacecraft LISA mission at assessment level in 1993/94 including an in-depth trade-off between the geocentric and the heliocentric option, selection of a 6-spacecraft LISA mission as a cornerstone project in 1995, detailed payload definition and design in 1997/98 and industrial study at Phase A level in 1999.

In early 1997, NASA supported a short LISA study by JPL's Team-X, based on three spacecraft and ion drive propulsion which led to a significant mass and cost reduction (from 6.8 t launch mass and about 800 MECU for the 6-spacecraft configuration excluding the payload to 1.4 t launch mass and $ 465 M for the 3-spacecraft configuration including the ion drives, launch vehicle, operations and payload). Towards the end of 1997, NASA decided to form a LISA Pre-Project Office at JPL and in March 1998 to set up a LISA Mission Definition Team.

Currently, both ESA and NASA studies of the LISA mission proceed in parallel, with partial team membership overlap to ensure maximum commonality between the two studies.

From the very beginning, the LISA team consisted of US and European scientists working very closely together and it is difficult for the international LISA team to imagine that LISA could be carried out in any other way than in collaboration between ESA and NASA.

The original proposal of the LISA Project by an international team of scientists to ESA in May 1993 suggested a NASA/ESA collaborative project. Furthermore, in February 1997, ESA's Fundamental Physics Advisory Group (FPAG) strongly recommended to carry out LISA in collaboration with NASA and suggested that *"this collaboration should be put in*

place as soon as possible". Also in February 1997, ESA's LISA Study Team clearly stated that *"the LISA mission should be carried out in collaboration with NASA."* It is assumed that ESA and NASA will explore the possibilities of a collaboration after completion of ESA's industrial study, at a time when the feasibility and the cost of the LISA mission are better known.

Considering that a Delta II class launch vehicle is sufficient to launch the three LISA spacecraft and that a launch vehicle of that class does not exist in Europe (only the much bigger Ariane 5) it would be natural to assume that NASA would provide the launch vehicle in such a collaboration. It would also make sense for NASA to provide the mission and science operations using their Deep Space Network (DSN). ESA would then provide the three spacecraft, presumably including the ion drives. To ensure compatibility with the DSN the telecommunications system will use Ka-band transmission with the telecommunications system hardware on board the spacecraft provided by NASA. In such an "equal sharing scenario", NASA would provide 50 % of the payload while European institutes funded nationally would provide the other 50 %. In this scenario the cost to ESA should be < 175 MECU.

Possible other candidates for cooperation in the LISA mission could be Japan and Australia, where there are active communities interested in ground-based detection of gravitational waves. Discussions with individual scientists in these countries have taken place which may lead to a collaboration at a later time, presumably at a lower level of investment than the two main partners NASA and ESA.

After approval of the LISA project by NASA and ESA, a Memorandum of Understanding (MoU) and a Program Plan (PP) would be prepared jointly by NASA and ESA. The MoU would define the agreement made between NASA and ESA for the implementation of the LISA project. It would contain, inter alia, agreements, responsibilities and deliverable items. The PP is the highest level Project document which defines the objectives, requirements, organization, and management structure of the project.

10.2 Science and project management

The proposed procurement scheme for LISA is based on the concept that the payload will be provided by Principal Investigators (PIs) with funding from ESA's Member States as far as European contributions are concerned, and from NASA for possible US contributions. Payload selection would be based on proposals that would be submitted to NASA and ESA in response to a single joint NASA/ESA Announcement of Opportunity (AO). Payload elements would be selected competitively by a joint NASA/ESA selection committee after a parallel scientific and technical evaluation of the proposals.

After selection of the payload a LISA Science Working Team would be formed, comprising the US and European PIs, the NASA and ESA Project Managers and Project Scientists and the Experiment Manager. Nationally funded payload subsystems such as lasers, optical bench, telescope, accelerometer, and structure, will be constructed at PI institutes. One institute would perform the overall management, integration, and testing of the payload under the responsibility of the Experiment Manager who would be the single-point interface to the ESA Project Manager.

The ESA Project Manager would set the requirements for and procure the three spacecraft from industry. He would also be responsible for the integration of the payload into the spacecraft and the overall test programme until delivery of the integrated and tested spacecraft to the launch site.

The NASA project Manager would interface with the launch vehicle authorities and provide launch operations support. During the flight phase he would also be responsible for the mission operations. Science operations would be carried out at a science institute to be selected competitively a few years before the launch.

10.3 Schedule

The schedule for the NASA/ESA collaborative LISA Project assumes approval of the project by NASA and ESA in 2004 and a 4-year development programme leading to a launch in 2008 .

The project development phase is preceded by a 4-year technology development programme in both space agencies starting in the year 2000. In parallel with this technology development programme a joint NASA/ESA system level study is assumed which would last about a year starting in 2001.

A major element in the schedule is a dedicated small ($\sim$100 kg), low-cost (5-20 MECU) LISA Technology demonstration satellite (ELITE) which could be launched as early as 2002 and should not fly later than 5 years before the LISA launch. ELITE could be an ESA responsibility. A NASA responsibility could be a ground-based full-scale LISA simulation facility located at JPL.

10.4 Archiving

According to the ESA policy on data rights, for the first six months after the end of the mission, the team of LISA investigators will have exclusive rights over their data. Thereafter, all science data (raw, calibrated, housekeeping) will have to be submitted to two LISA Science Data Archiving Centres (LSDAC) where the data will be stored on CD-ROM and can be accessed by the wide scientific community. One candidate for the LSDAC would be ESA's Space Science Department at ESTEC, the other archiving centre would presumably be the National Space Science Data Center (NSSDC) at GSFC, Greenbelt, MD, USA. The complete LISA data set comprises:

- interferometer data,
- inertial sensor data,
- drag-free control and FEEP thruster data,
- UV control lamp discharging data.

The teams providing the various data sets have the following tasks:

- performing a thorough end-to-end error analysis,

- calibration of the science data,
- development of appropriate software for data analysis,
- production of an explanatory supplement,
- timely (i.e. 6 months after mission end) delivery of the items above to the LSDACs.

The LSDACs have the following tasks:

- ensuring timely delivery of the items above,
- verification of the contents of the CD-ROMs,
- production of an appropriate number of copies of CD-ROMs and supplements,
- responding to requests from the user community and sending out CD-ROMs and supplements as requested.

References

[1] C.W. Misner, K.S. Thorne, and J.A. Wheeler, *Gravitation* (Freeman & Co., San Francisco, 1973). Cited on page 8

[2] P.R. Saulson, *Fundamentals of Interferometric Gravitational Wave Detectors* (World Scientific, Singapore, 1994). Cited on page 8

[3] B.F. Schutz, *A First Course in General Relativity* (Cambridge University Press, Cambridge, 1985). Cited on page 8

[4] K.S. Thorne, *Gravitational Radiation*, in: S.W. Hawking and W. Israel, eds., *300 Years of Gravitation* (Cambridge University Press, Cambridge, 1987) 330–458. Cited on page 8, 20

[5] B.F. Schutz and C.M. Will, *Gravitation and General Relativity* in *Encyclopedia of Applied Physics* **7** (1993) 303–340. Cited on page 8, 18

[6] J.H. Taylor and J.M. Weisberg, *Further experimental tests of relativistic gravity using the binary pulsar PSR 1913+16*, Astrophys. J. **345** (1989) 434. Cited on page 9, 24

[7] B.F. Schutz, *Gravitational Waves on the Back of an Envelope*, Am. J. Phys. **52** (1984) 412–419. Cited on page 15

[8] P.C. Peters and J. Mathews, Phys. Rev. **131** (1963) 435. Cited on page 16

[9] C.M. Will, *Theory and Experiment in Gravitational Physics* (Cambridge University Press, Cambridge, England, 1981). Cited on page 18

[10] V.N. Mironowskii, Soviet Astron. **9** (1966) 752. Cited on page 23, 27

[11] I. Iben, paper presented at the Workshop on Gravitational Waves and Axions, Inst. for Theoretical Physics, Santa Barbara, CA (1984). Cited on page 23

[12] D. Hils, P.L. Bender, J.E. Faller, and R.F. Webbink, in *11th Int. Conf. on General Relativity and Gravitation: Abstracts of Cont. Papers, Vol. 2* (Univ. of Stockholm, 1986) 509. Cited on page 23

[13] D. Hils, P.L. Bender, and R.F. Webbink, Astrophys. J. **360** (1990) 75. Cited on page 23, 26, 27

[14] V.M. Lipunov and K.A. Postnov, Soviet Astron. **31** (1987) 228-230. Cited on page 23

[15] V.M. Lipunov, K.A. Postnov, and M.E. Prokhorov, Astron. Astrophys. **176** (1987) L1–L4. Cited on page 23

[16] C.R. Evans, I. Iben, and L. Smarr, *Degenerate Dwarf Binaries as Promising Detectable Sources of Gravitational Radiation*, Astrophys. J. **323** (1987) 129–139. Cited on page 23

[17] R.A. Hulse and J.H. Taylor, *Discovery of a pulsar in a binary system*, Astrophys. J. **195** (1975) L51. Astrophys. J. **345** (1989) 434. Cited on page 24

[18] D. Lorimer and E.P.J. van den Heuvel, *On the galactic and cosmic merger rate of double neutron stars*, Mon. Not. Roy. Astr. Soc. **283** (1996) L37–L39. Cited on page 24

[19] A.V. Tutukov and L.R. Yungelson, Mon. Not. R. Astron. Soc. **260** (1993) 675. Cited on page 24, 25

[20] H. Yamaoka, T. Shigeyama, and K. Nomoto, Astron. Astrophys. **267** (1993) 433. Cited on page 24

[21] V.M. Lipunov, *Relativistic Binary Merging Rates*, astro-ph/9711270 (to be published in the proceedings of the Joint Discussion "High Energy Transients", XXIIIrd General Assembly of the IAU, Kyoto). Cited on page 24

[22] D.R. Lorimer, A.G. Lyne, L. Festin, and L. Nicastro, Nature **376** (1995) 393. Cited on page 24

[23] F. Verbunt, *Waiting for LISA: binaries with orbital periods less than* 10^4 *s*, Class. Quantum Grav. **14** (1997) 1417–1424. Cited on page 24

[24] C.A. Meegan *et al.*, Astrophys. J. Suppl. **106** (1996) 65. Cited on page 24

[25] J. van Paradijs, P.J. Groot, T. Galama, *et al.*, Nature **386** (1997) 686. Cited on page 24

[26] R. Narayan, T. Piran, and A. Shemi, *Neutron star and black hole binaries in the Galaxy*, Astrophys. J. **379** (1991) L17. Cited on page 25

[27] L. Yungelson and S.F.P. Zwart, *Evolution of Close Binaries: Formation and Merger of Neutron Star Binaries*, astro-ph/9801127 (to appear in the proceedings of the "Second Workshop on Gravitational Wave Data Analysis", held 13-15 November 1997, Orsay, France). Cited on page 25

[28] T.R. Marsh, Mon. Not. R. Astron. Soc. **275** (1995) L1. Cited on page 26

[29] T.R. Marsh, V.S. Dhillon, and S.R. Duck, Mon. Not. R. Astron. Soc. **275** (1995) 828. Cited on page 26

[30] B. Warner, Astrophys. and Sp. Sci., in press (1995). Cited on page 26, 27, 27

[31] I. Iben and A.V. Tutukov, Astrophys. J. **370** (1991) 615. Cited on page 27

[32] D. Hils and P.L. Bender, in preparation (1998). Cited on page 27, 33, 33

[33] A. Tutukov and L. Yungelson, Mon. Not. R. Astron. Soc. **280** (1996) 1035. Cited on page 27

[34] K.S. Thorne, in *Proceedings of Snowmass 1994 Summer Study on Particle and Nuclear Astrophysics and Cosmology*, E.W. Kolb and R.D. Peccei, eds., (World Scientific, Singapore, 1995) 160–184. Cited on page 28

[35] C. Cutler, T.A. Apostolatos, L. Bildsten, L.S. Finn, E.E. Flanagan, D. Kennefick, D.M. Markovic, A. Ori, E. Poisson, G.J. Sussman, and K.S. Thorne, *The Last Three Minutes: Issues in Gravitational Wave Measurements of Coalescing Binaries*, Phys. Rev. Lett. **70** (1993) 2984. Cited on page 28

[36] M. Haehnelt, Mon. Not. R. Astron. Soc. **269** (1994) 199. Cited on page 28

[37] A. Vecchio, Class. Quantum Grav. **14** (1997) 1431. Cited on page 28

[38] H.C. Ford *et al.*, Astrophys. J. **435** (1994) L27. Cited on page 28

[39] R.J. Harms *et al.*, Astrophys. J. **435** (1994) L35. Cited on page 28

[40] Y. Tanaka *et al.*, Nature **375** (1995) 659. Cited on page 28

[41] M. Miyoshi *et al.*, Nature **373** (1995) 127. Cited on page 28

[42] A. Eckart and R. Genzel, *Observations of stellar proper motions near the Galactic Centre*, Nature **383** (1996) 415–417. Cited on page 28

[43] T.R. Lauer *et al.*, Astron. J. **104** (1992) 552. Cited on page 28

[44] J. Kormendy and D. Richstone, Ann. Rev. Astron. & Astrophys. **33** (1995) 581. Cited on page 29, 29

[45] M.J. Rees, *Astrophysical evidence for black holes*, in: R.M. Wald, ed., *Black Holes and Neutron Stars* (University of Chicago Press, Chicago, 1997). Cited on page 29, 29

[46] M.J. Rees, Class. Quantum Grav. **14** (1997) 1411–1416. Cited on page 29, 29

[47] P. Crane *et al.*, Astron. J. **106** (1993) 1371. Cited on page 29

[48] T.R. Lauer *et al.*, Astron. J., submitted (1995). Cited on page 29

[49] G.D. Quinlan and S.L. Shapiro, Astrophys. J. **356** (1990) 483. Cited on page 29

[50] M.G. Haehnelt and M.J. Rees, Mon. Not. R. Astron. Soc. **263** (1993) 168. Cited on page 29

[51] D.J. Eisenstein and A. Loeb, Astrophys. J. **443** (1995) 11. Cited on page 29

[52] M. Umemura, A. Loeb, and E.L. Turner, Astrophys. J. **419** (1993) 459. Cited on page 29

[53] C. Cutler, *Angular Resolution of the LISA Gravitational Wave Detector*, (preprint gr-gc/9703068 24 Mar 1997). Cited on page 32

[54] M. Shibata, Phys. Rev. D **50** (1994) 6297. Cited on page 32

[55] D. Hils and P.L. Bender, Astrophys. J. **445** (1995) L7. Cited on page 32, 32

[56] S. Sigurdsson and M.J. Rees, Mon. Not. R. Astron. Soc. **284** (1996) 318. Cited on page 33

[57] S. Sigurdsson, Class. Quantum Grav. **14** (1997) 1425. Cited on page 33

[58] B. Allen, private comunication (1995). Cited on page 35, 36

[59] B. Caldwell and B. Allen, Phys. Rev. D **45** (1992) 3447. Cited on page 36

[60] A. Kosowsky, M.S. Turner, and R. Watkins, *Gravitational radiation from colliding vacuum bubbles*, Phys. Rev. D **45** (1992) 4514. Cited on page 36

[61] J. Weber, Phys. Rev. **117** (1960) 306. Cited on page 39

[62] M. Bassan, Class. Quant. Grav. Supplement A **39** (1994) 11. Cited on page 39

[63] F.A.E. Pirani, Acta Physica Polonica **15** (1956) 389. Cited on page 39

[64] M.E. Gertsenshtein and V.I. Pustovoit, JETP **16** (1963) 433. Cited on page 39

[65] R. Weiss, Quarterly Progress Report of RLE, MIT **105** (1971) 54. Cited on page 39

[66] G.E. Moss, L.R. Miller, and R.L. Forward, Appl. Opt. **10** (1971) 2495. Cited on page 39

[67] A. Abramovici *et al.*, Science **256** (1992) 325. Cited on page 40

[68] G. Bradaschia *et al.*, Nucl. Instrum. and Methods A **289** (1990) 518. Cited on page 41

[69] K. Danzmann *et al.*, *GEO 600 – A 300 m laser-interferometric gravitational wave antenna*, Proc. 1st Edoardo Amaldi Conference, Frascati, June 1994;
and also: J. Hough *et al.*, Proc. MG7, Stanford, July 1994. Cited on page 41

[70] K. Tsubono and TAMA collaboration, *TAMA Project* in: K. Tsubono, M.-K. Fujimoto, K. Kuroda, (Eds.), *Gravitational Wave Detection, Proc. TAMA Intern. Workshop, Nov. 1996*, p. 183–191, Universal Academy Press (Tokyo, 1997). Cited on page 41

[71] V.M. Kaspi, J.H. Taylor, M.F. Ryba, Astrophys. J. **428** (1994) 713. Cited on page 42

[72] Report prepared by NASA Marshall Space Flight Center, US Govt. Printing Office No. 1978-261-371:11 (1978). Cited on page 43

[73] R. Weiss, P.L. Bender, C.W. Misner and R.V. Pound, in *Report of the Sub-Panel on Relativity and Gravitation, Management and Operations Working Group for Shuttle Astronomy*, (NASA, Washington, DC, 1976). Cited on page 44

[74] R. Weiss, *Gravitational Radiation – The Status of the Experiments and Prospects for the Future,* in L. Smarr (ed.), *Sources of Gravitational Radiation*, (Cambridge University Press, 1979). Cited on page 44

[75] R. Decher, J.L. Randall, P.L. Bender and J.E. Faller, *Design aspects of a laser gravitational wave detector in space,* in *Active Optical Devices and Applications,* SPIE **228** (1980) 149–153 . Cited on page 44

[76] J.E. Faller and P.L. Bender, Abstract for the Second International Conference on Precision Measurements and Fundamental Constants, Gaithersburg, MD, 8-12 June 1981 . Cited on page 44, 183

[77] J.E. Faller and P.L. Bender, *A possible laser gravitational-wave experiment in space,* in *Precision Measurements and Fundamental Constants II,* NBS Special Publication 617 (U.S. Govt. Printing Office, Washington, D.C., 1984) 689–690. (This paper is identical with the abstract given in [76].) Cited on page 44

[78] J.E. Faller, P.L. Bender, J.L. Hall, D. Hils and M.A. Vincent, *Space antenna for gravitational wave astronomy*, in Proceedings of the Colloquium on *Kilometric Optical Arrays in Space*, Cargese (Corsica), 23-25 October 1984, ESA report SP-226 (1985). Cited on page 44

[79] D. Shoemaker, R. Schilling, L. Schnupp, W. Winkler, K. Maischberger, A. Rüdiger, *Noise behavior of the Garching 30 meter prototype gravitational wave detector,* Phys. Rev. D **38** (1988) 423–432. Cited on page 50

[80] D.I. Robertson, E. Morrison, J. Hough, S. Killbourn, B.J. Meers, G.P. Newton, N.A. Robertson, K.A. Strain, H. Ward, *The Glasgow 10 m prototype laser interferometric gravitational wave detector,* Rev. Sci. Inst. **66** (1995) 4447–4451. Cited on page 50

[81] R.E. Vogt *et al.*, *The U.S. LIGO Project,* in *Proc. of the Sixth Marcel Grossmann Meeting on General Relativity, Kyoto 1991*, eds. H. Sato and T. Nakamura (World Scientific, Singapore, 1992) 244–266. Cited on page 50

[82] M. Woodard, *Short-Period Oscillations in the Total Solar Irradiance*, Thesis, University of California, San Diego, 1984. Cited on page 64

[83] M. Nati, A. Bernard, B. Foulon, P. Touboul, *ASTRE – a highly performant accelerometer for the low frequency range of the microgravity environment,* 24th International Conference on Environmental Systems, Friedrichshafen (Germany), 20–23 June 1994. Cited on page 66

[84] A. Bernard, P. Touboul, *The GRADIO accelerometer: design and development status,* Proc. ESA-NASA Workshop on the Solid Earth Mission ARISTOTELES, Anacapri (Italy), 23–24 September 1991. Cited on page 66

[85] P. Touboul *et al.*, *Continuation of the GRADIO accelerometer predevelopment,* ONERA Final Report 51/6114PY ESTEC contract (1992), ONERA Final Report 62/6114PY ESTEC contract (1993). Cited on page 66

[86] E. Willemenot, *Pendule de torsion à suspension electrostatique, trés hautes résolutions des accéléromètres spatiaux pour la physique fondamentale,* Paris-Sud University Thesis, 1997. Cited on page 71

[87] T.J. Sumner, P. Touboul, *Charge management system for STEP,* STEP Symposium, Pisa 1993 (ESA Proceedings, 1995). Cited on page 71, 71

[88] P. Touboul, M. Gay, B. Foulon, Y. Bienenfeld, T.J. Sumner, *The charge measurement and control technique for STEP experimentation,* The 2nd William Fairbank conference on Relativistic Gravitational Experiments in Space and Related Theoretical Topics, Hong Kong, 13–16 December 1993. Cited on page 71

[89] Y. Bienenfeld, *Etude des différences de potentiel de contact au coeur des acceleromètres ultrasensibles à suspension électrostatique,* Thèse de doctorat de l'Université Paris 6, 19 December 1994. Cited on page 72

[90] P. Touboul, B. Foulon, E. Willemenot, *Electrostatic space accelerometers for present and future missions,* IAF-96-J1.02, Acta Astronautica 1998, in press. Cited on page 72

[91] Y. Jafry and T.J. Sumner, *Electrostatic charging of the LISA proof masses,* Class. Quantum Grav., **14** (1997) 1567–1574. Cited on page 73

[92] S. Buchman, T. Quinn, M. Keiser, D. Gill, T.J. Sumner, *Charge measurement and control for the Gravity Probe B gyroscopes,* Rev. Sci. Instrum. **66** (1995) 120–129. Cited on page 73

[93] G.P. Adams, G.K. Rochester, T.J. Sumner, O.R. Williams, *The ultra-violet calibration system for the UK XUV telescope to be flown on the ROSAT satellite,* J. Phys. E. **20** (1987) 1261–1264. Cited on page 73

[94] T.J. Sumner and G.K. Rochester, *Technical report on charging rates and discharge studies for LISA,* in *DFSC-FR-DA-001*, Daimler-Benz Aerospace (1998). Cited on page 74

[95] R. Schilling, *Angular and frequency response of LISA,* Class. Quantum Grav. **14** (1997) 1513–1519 . Cited on page 80

[96] P.R. Saulson, *Thermal noise in mechanical experiments,* Phys. Rev. D **42** (1990) 2437–2445. Cited on page 84

[97] A.S. Jursa (ed.), Handbook of geophysics and the space environment, United States Air Force Geophysics Laboratory, Document number ADA 167000, (1985). Cited on page 87

[98] R. Brun, F. Bruyant, M. Maire, A.C. McPherson and P. Zanarini, *GEANT3 User's Guide*, DD/EE/84–1, CERN (1984). Cited on page 86, 88

[99] Y. Jafry and C. Tranquille, *An Assessment of the Charged Particle Environment during the STEP Mission, and Consequences for the Payload*, STEP Symposium, Pisa 1993 (ESA Proceedings, 1995). Cited on page 87, 90

[100] J.A. Halbleib, R.P. Kensek, T.A. Mehlhorn, G.D. Valdez, S.M. Seltzer, and M.J. Berger, *ITS Version 3.0: The Integrated TIGER Series of Coupled Electron/Photon Monte Carlo Transport Codes*, SAND91–1634· UC–405, Sandia National Laboratories, New Mexico (1992). Cited on page 89

[101] J.H. King, *Solar Proton Fluences for 1977–1983 Space Missions*, J. Spacecraft **11** (1974) 401. Cited on page 90

[102] J.N. Goswami, R.E. McGuire, R.C. Reedy, D. Lal, and R. Jha, *Solar Flare Protons and Alpha Particles During the Last Three Solar Cycles,* J. Geophys. Res. **93** (1988) A7195–A7205. Cited on page 91

[103] F. De Coulon, *Signal Theory and Processing* (Artech House, Dedham, MA, 1986). Cited on page 91

[104] E. Grun, H.A. Zook, H. Fechtig, and R.H. Giese, *Collisional Balance of the Meteoritic Complex,* Icarus **62** (1985) 244–272. Cited on page 98

[105] E.M. Shoemaker, *Asteroid and Comet Bombardment of the Earth,* Ann. Rev. Earth Planet. Sci. **11** (1983) 461–494. Cited on page 98, 98, 98

[106] E.M. Shoemaker, R.F. Wolfe, and C.S. Shoemaker, *Asteroid and Comet Flux in the Neighborhood of Earth,* in *Global Catastrophes in Earth History,* Geol. Soc. of Amer., Special Paper 247 (V.L. Sharpton and P.D. Ward, eds., 1990) 155–170. Cited on page 99

[107] D. Morrison and C.R. Chapman, *Impact Hazard and the International Spaceguard Survey,* in *Observations and Physical Properties of Small Solar System Bodies,* Proc. 30th Liege Int. Astrophys. Colloq. (A. Brahic, J.-C. Gerard and J. Surdej, eds., Univ. de Liege, 1992) 223–228. Cited on page 99

[108] G. Giampieri R.W. Hellings, M. Tinto, and J.E. Faller, *Algorithms for Unequal-Arm Michelson Interferometers,* Opt. Commun. **123** (1996) 669–678. Cited on page 101

[109] Ch. Salomon, D. Hils, and J.H. Hall, *Laser stabilization at the millihertz level,* J. Opt. Soc. Am. B **5** (1988) 1576–1587. Cited on page 102

[110] B.F. Schutz, ed., *Gravitational Wave Data Analysis* (Kluwer, Dordrecht, 1989). Cited on page 104

[111] K. Danzmann *et al.*, *LISA – Proposal for a Laser-Interferometric Gravitational Wave Detector in Space,* Max-Planck-Institut für Quantenoptik, Report MPQ 177 (1993). Cited on page 107

[112] M. Peterseim, O. Jennrich, and K. Danzmann, Class. Quantum Grav. **13**, (1996) 279. Cited on page 108

[113] C. Cutler, Phys. Rev. D **57** (1998). Cited on page 108, 112, 116

[114] B.F. Schutz, in D. Blair (ed.), *The detection of gravitational waves* (Cambridge University Press, Cambridge, England, 1991) 406–452. Cited on page 110

[115] C. Cutler and E. Flanagan, Phys. Rev. D **49** (1994) 2658. Cited on page 112

[116] L.S. Finn, Phys. Rev. D **46** (1992) 5236. Cited on page 113

[117] V.M. Lipunov, S.N. Nazin, I.E. Panchenko, K.A. Postnov, and M.E. Prokhorov, Astron. Astrophys. **298** (1995) 677–687. Cited on page 118

[118] M.A. Vincent and P.L. Bender, *Orbital mechanics of a space-borne gravitational wave experiment,* Proc. Astrodynamics Specialist Conference (Kalispell USA) (San Diego: Univelt, 1987) 1346. Cited on page 135

[119] F. Hechler and W.M. Folkner, *Mission Analysis for Laser Interferometer Space Antenna (LISA),* paper presented at the COSPAR Scientific Assembly, Birmingham (UK), 16-19 July 1996, to appear in *Advances in Space Research.* Cited on page 138, 138

[120] R. Hellings, G. Giampieri, L. Maleki, M. Tinto, K. Danzmann, J. Hough, D. Robertson, *Heterodyne laser tracking at high Doppler rates,* Opt. Commun. **124**, (1996) 313–320 . Cited on page 139, 139

[121] R.T. Stebbins, P.L. Bender, W.M. Folkner, *LISA data acquisition,* Class. Quantum Grav. **13** (1996) A285–A289 . Cited on page 139

[122] C. Bartoli, H. von Rohden, S. Thompson, J. Blommers, *A Liquid Caesium Field Ion Source for Plasma Propulsion,* J. Phys. D: Appl. Phys. **17** (1984) 2473–2483. Cited on page 151

[123] B.T.C. Zandbergen, *FEEP: the ESTEC Liquid Caesium Field Ion Source. An Investigative Report,* Thesis TU Delft, June 1984. Cited on page 152

[124] C. Bartoli, J. González, G. Saccoccia, M. Andrenucci, S. Marcuccio, A. Genovese, *Space-Borne Astronomical Gravity wave Interferometer Mission (SAGITTARIUS): the FEEP option,* IEPC–93–016. Cited on page 152, 154

[125] J. González, G. Saccoccia, H. von Rohden, *Field Emission Electric Propulsion: Experimental Investigations on Microthrust FEEP Thrusters,* IEPC–93–157. Cited on page 154

[126] M. Andrenucci, S. Marcuccio, L. Spagli, A. Genovese and F. Repola, *Experimental Study of FEEP Emitter Starting Characteristics,* IEPC–91–104. Cited on page 154

[127] A. Ciucci, G. Genuini and M. Andrenucci, *Experimental Investigation of Field Emission Electrostatic Thrusters,* IEPC–91–103. Cited on page 154

[128] R. Schmidt, H. Arends et al., *A novel medium-energy ion emitter for active spacecraft potential control,* Rev. Sci. Instrum. **64** (1993). Cited on page 155

[129] M. Fehringer, F. Rüdenauer and W. Steiger, *Space-Proven Indium Liquid Metal Field Ion Emitters for Ion Microthruster Applications,* 33rd AIAA Joint Propulsion Conference, Seattle, WA (1997), AIAA 97-3057. Cited on page 155

List of Acronyms

– and other abbreviations and mission names

1553	(standardised interface bus)
AC	Alternating Current
ACS	Attitude Control System
Ada	(a programming language)
AFRP	Aramid Fibre Reinforced Plastic
AO	Announcement of Opportunity
ARC	Austrian Research Centre, Seibersdorf
ARISTOTELES	Applications and Research Involving Space Techniques Observing The Earth field from Low-Earth orbiting Satellite
ASCA	– satellite name –
ASI	Agenzia Spaziale Italiano
ASTRE	Accelerometre Spatial TRiaxial Electrostatique
AU	Astronomical Unit : distance Sun–Earth
AURIGA	Antenna Ultracriogenica Risonante per l'Indagine Gravitazionale Astronomica : cryogenic resonant-mass antenna, Legnaro, Italy
BH	Black Hole
BOL	Begin Of Lifetime
C	(a programming language)
C++	(an object-oriented programming language)
C&DH	Command and Data Handling
CAD	Computer Aided Design
CAESAR	Capacitive And Electrostatic Sensitive Accelerometer Reference
CASSINI	– NASA space mission (1997) to orbit Saturn –
CCSDS	Consultative Committee for Space Data Systems, telemetry standard
CD-ROM	Compact Disk – Read Only Memory
CERN	Centre Européen de la Recherche Nucléaire
CFRP	Carbon Fibre Reinforced Plastic
CHAMP	– German geodetic satellite –
CLUSTER-II	– ESA/NASA space mission (2000), 4 S/C to be launched on Ariane 5 –
CNES	Centre National d'Etude Spatiales (France)
CO	Carbon-Oxygen
COBE	COsmic Background Explorer
COLUMBIA	– NASA space shuttle –
COLUMBUS	– ESA space mission, to fly on NASA shuttle, 1996 –
COSPAR	Committee On SPAce Research

CPU	Central Processing Unit
CTE	Coefficient of Thermal Expansion
CWDB	Close White Dwarf Binaries
DC	Direct Current
DFACS	Drag-Free and Attitude Control System
DLR	Deutsches Zentrum für Luft- und Raumfahrt
DRAM	Dynamic Random Access Memory
DSN	Deep Space Network (NASA)
EDAC	Error Detection And Correction
ELITE	European LISA TEchnology demonstration satellite
EOL	End Of Lifetime
EOM	Electro-Optic Modulator
EQUATOR-S	– satellite name –
ESA	European Space Agency
ESTEC	European Space Research and Technology Centre
FEEP	Field Emission Electric Propulsion
FFT	Fast Fourier Transform
FPAG	Fundamental Physics Advisory Group
FSS	Fine Sun Sensor
GALILEO	– Spacecraft tracking mission (1989), now orbiting Jupiter –
GCR	Galctic Cosmic Rays
GEANT	– program code, CERN –
GEO	Geostationary Orbit
GEO 600	– German-British 600 m laser-interferometric GW detector –
GEOTAIL	– satellite name –
GP-B	Gravity Probe B
GPS	Global Positioning System
GRADIO	– Gravity Gradiometry mission: accelerometer sensor –
GSFC	Goddard Space Flight Center
GTO	"Geostationary Transfer Orbit" – highly eccentric orbit for transfer from low-earth orbit to geostationary orbit
GUT	Grand Unification Theory
GW	Gravitational Wave
GWI	Gravity Wave Interferometer
HeCV	Helium Cataclysmic Variables
HST	Hubble Space Telescope
I/F	Interface
I/O	Input/Output
IBM RS/6000	IBM 'risc' processor, 22 MIPS
In-LMIS	Indium Liquid Metal Ion Source
IR	InfraRed
IRU	Inertial Reference Unit
ISAS	Institute of Space and Astronautical Science (Japan)
IWDB	Interacting White Dwarf Binaries
JILA	Joint Institute for Laboratory Astophysics (Boulder, USA)
JPL	Jet Propulsion Laboratory (Pasadena, USA)

LAGOS	Laser Antenna for Gravitation-radiation Observation in Space
LHC	Large Hadron Collider (CERN)
LIGO	Laser Interferometer Gravitational wave Observatory (USA)
LISA	Laser Interferometer Space Antenna
LMC	Large Magellanic Cloud
LMIS	Liquid Metal Ion Source
LSC	LISA Science Centre
LSDAC	Lisa Science Data Archiving Centre
MAU	Million Accounting Units
MBH	Massive Black Hole
MBW	Measurement Bandwidth
MCG	– Catalogue of Galaxies –
MD	Maryland (State in USA)
MECU	Million ECU (European Currency Unit)
MGSO	Mission Ground Support Operations
MIL-STD-1553	MIL-Standard interface 1553
MIPS	Million Instructions Per Second
MIR	– Russian space station –
MIT	Massachusetts Institute of Technology (USA)
MLI	Multi-Layer Insulation
MoU	Memorandum of Understanding
MPQ	Max-Planck Institut für Quantenoptik (Germany)
MSP	Mars Surveyor Program
NASA	National Aeronautics and Space Administration (USA)
NAUTILUS	– Cryogenic resonant-mass antenna, Frascati (Italy) –
Nd:YAG	Neodymium-doped Yttrium-Aluminium Garnet
NORAD	NORth American Defense command
NPRO	Numerically PRogrammed Oscillator
NS	Neutron Star
NSF	National Science Foundation (USA)
NSSDC	National Space Science Data Center
OMEGA	Orbiting Medium Explorer for Gravitational Astrophysics
ONERA	Office National d'Etudes et de Recherches Aerospatiales (France)
OSS	Office of Space Science (USA)
PCU	Power Conditioning and Control Unit
PDF	Probability Density Function
PI	Principal Investigator
PLM	PayLoad Module
PM	Propulsion Module
PP	Program Plan
PROM	Programmable Read-Only Memory
QNL	Quantum Noise Limit
RAD 6000-SC	Radiation-hardened version of IBM RS/6000
RAM	Random Access Memory
RCS	Reaction Control Subsystem
RF	Radio Frequency

RFDU	Radio Frequency Distribution Unit
rms	root mean square
ROSAT	ROentgen SATellite
ROSETTA	– planned ESA cornerstone mission –
RS 422	(standardised interface bus)
S/C	SpaceCraft
SAGITTARIUS	Spaceborne Astronomical Gravitational-wave Interferometer To Test Aspects of Relativity and Investigate Unknown Sources
SEP	Solar Electric Propulsion
SEU	Single Event Upset
SEUS	Structure and Evolution of the Universe Subcommittee (USA)
SNR	Signal-to-Noise Ratio
SOHO	Solar Oscillation and Heliospheric Observatory (1995)
SSR	Solid State Recorder
ST	StarTracker
STAR	Space Three-axis Accelerometer for Research
STEP	Satellite Test of the Equivalence Principle
SVM	SerVice Module
TAMA 300	– Japanese 300 m GW detector built near Tama, Tokyo –
TBD	To Be Determined
TEM 00	Fundamental transverse light mode
TID	Total Ionising Dose
TNT	TriNitroToluene (an explosive)
TRIAD	– Space mission using drag free control –
TT&C	Tracking, Telemetry and Command
UK	United Kingdom
ULE	Ultra-Low Expansion glass (trade name)
ULF	Ultra Low Frequency
ULYSSES	– spacecraft tracking mission (1990), orbiting Sun –
US	United States (of America)
USA	United States of America
USO	Ultra-Stable Oscillator
UV	Ultra Violet
VIRGO	– French-Italian laser-interferometric GW detector –
VME	(interface bus type)
XIPS	Xenon Ion Propulsion System
XUV	eXtreme Ultra Violet
YAG	Yttrium-Aluminium Garnet

Max-Planck-Institut für Quantenoptik
D – 85748 Garching, Germany

Rear cover figure :

Schematic diagram of LISA configuration. Three spacecraft form an equilateral triangle with sides of 5 million km in length. The plane of this triangle is tilted by 60° out of the ecliptic. The center of this triangle moves around the Sun in an Earth-like orbit, about 20° behind the Earth.
The spacecraft each house a Y*-shaped payload, with the two telescopes aligned (60° from another) towards the other spacecraft. A full* Y *at one corner, together with one* Y *branch each from the other spacecraft, form one of up to three Michelson-type interferometers, operated with infrared laser beams.*
The drawing is not to scale, the diameters of the celestial bodies as well as that of the LISA interferometer are blown up by more than an order of magnitude.

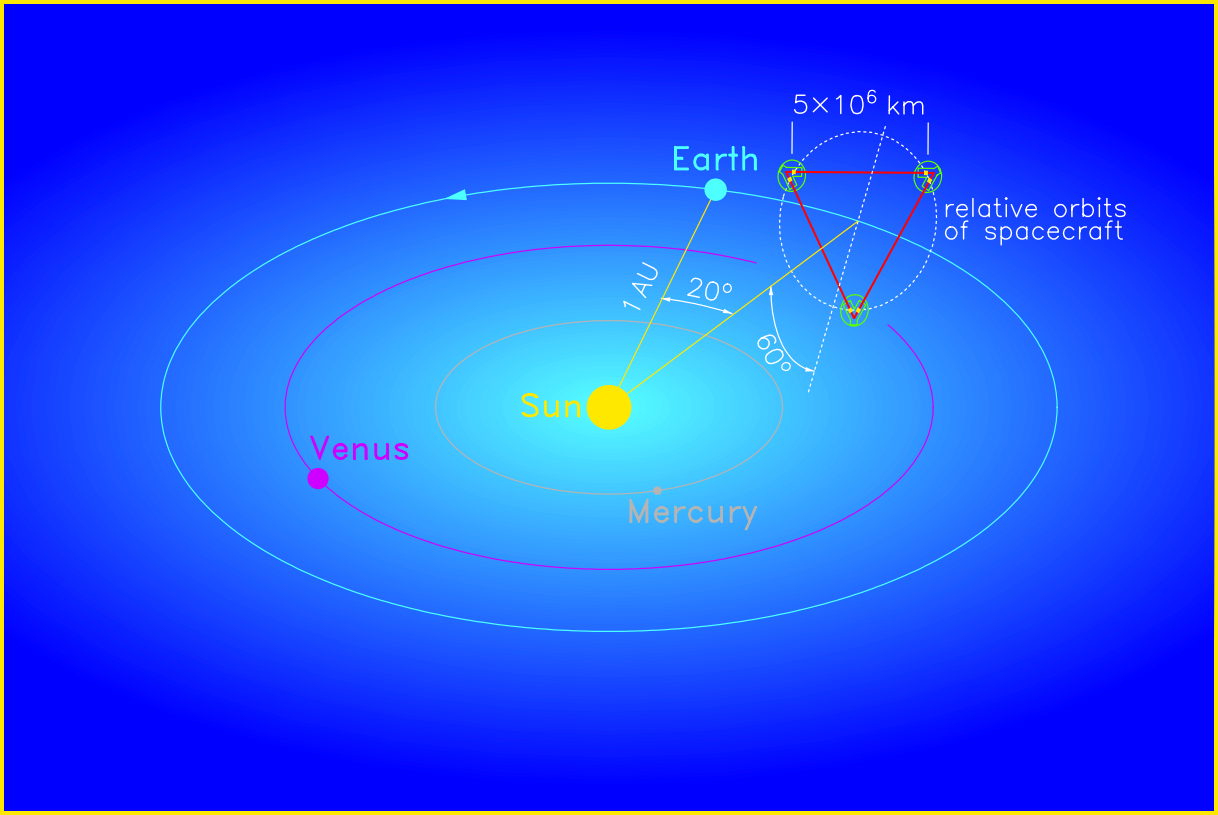
5×10^6 km
Earth
relative orbits
of spacecraft
1 AU
20°
60°
Sun
Venus
Mercury